

**LIFE MODEL FOR ROLLING CONTACT, APPLIED TO THE OPTIMIZATION OF A
TRIPODE CONSTANT VELOCITY JOINT**

By

Eduardo Raul Mondragon-Parra

A DISSERTATION

Submitted to
Michigan State University
in partial fulfillment of the requirements
for the degree of

DOCTOR OF PHILSOPHY

Mechanical Engineering

2010

ABSTRACT

LIFE MODEL FOR ROLLING CONTACT, APPLIED TO THE OPTIMIZATION OF A TRIPODE CONSTANT VELOCITY JOINT

By

Eduardo R. Mondragon-Parra

A Constant Velocity Joint (CVJ) is a mechanical device capable of transmitting torque and motion between two rotating shafts that are misaligned. Most front wheel drive vehicles have torque and motion transmitted to the driven wheels through a set of inboard CVJ's (transmission side) and a set of outboard CVJ's (wheel side). One of the most common types of inboard joints is the Tripode Joint, which is composed of a housing, a spider and three sets of roller assemblies that connect the spider to the housing and allow for stroking motion and rotation of the joint at an angle. Wear fatigue-life in a Tripode Joint is defined by how many rotation cycles a Joint can complete before experiencing spalling or flaking of the internal surfaces subject to contact forces. Similarities and differences between a Tripode Joint and roller bearings are discussed. Internal contacts are treated as non-Hertzian and the state of stress is determined based on the kinematics of the joint, the geometry of the interacting components and the way internal forces are distributed when a torque is applied.

A rolling contact wear fatigue-life model for Tripode Joints, that relates the critical shear stress in the contacts to the number of cycles a joint can perform before spalling, is proposed and compared to actual test data. Residual stresses were considered to obtain the stress-life exponent of the Tripode equation.

Optimization of the geometric form of the contact surfaces in the spider is performed, aimed to minimize the peak contact load and to minimize the load differences between adjacent needle rollers. Reduction of the peak contact load allows an increment in durability of the Tripode Joint. The optimized profile in the contact surfaces of the spider is compared against traditional geometric forms, such as perfect circular and elliptical. The proposed model has a direct application in the auto-industry.

Copyright by

EDUARDO R. MONDRAGON-PARRA

2010

Para Carolina, mi hija amada.

(To Carolina, my beloved daughter)

“... Of making many books there is no end, and much study wearies the body. Now all has been heard; here is the conclusion of the matter: Fear God and keep his commandments, for this is the whole duty of man.”

Ecclesiastes 12:12-13

ACKNOWLEDGMENTS

Conducting the research that led to this document was a unique experience. I would like to thank the persons that contributed to this work in different manners and at different stages.

To Dr. Patrick Kwon, my advisor, who risked to take me as his off-campus student and guided me through the entire research. The time he dedicated reviewing my work, his wisdom and valuable feedback made this possible. To my committee members Dr. Ronald Averill, Dr. Dashin Liu and Dr. K. N. Subramanian, for their patience, for serving on my committee and for their teaching inside and outside of the classroom.

To Mr. Jerry Eaton, Mr. William Skvarla and Mr. Robin Milavec, for their support, encouragement and for granting me the flexibility and resources to combine work in industry with my studies. To Dr. Keith Kozlowski, who led me by example when I started to work in industry, encouraged me and planted the seeds of curiosity about contact stress and fatigue-life.

To my parents, sister and friends, who made me laugh and laughed with me, fished with me, brewed beer with me, allowed me to share their family time and prayed with me and for me to help me be on track and keep things in perspective.

To JESUS, thank you for being my LORD and my HIDING PLACE.

TABLE OF CONTENTS

LIST OF TABLES.....	ix
LIST OF FIGURES.....	xi
LIST OF SYMBOLS.....	xviii
CHAPTER 1	
INTRODUCTION.....	1
1.1 Background.....	1
1.2 Fixed center constant velocity joints.....	3
1.3 Stroking constant velocity joints.....	5
1.4 Rolling bearings and tripod joints.....	6
1.5 Benefits of a life model.....	10
1.6 Joint size and packaging.....	10
1.7 Project description.....	11
CHAPTER 2	
KINEMATIC ANALYSIS OF A STROKING TRIPODE JOINT.....	12
2.1 Introduction.....	12
2.2 Assumptions.....	14
2.3 Definitions.....	14
2.4 Spherical roller positions.....	18
2.5 Numerical examples of spherical roller positions and displacements.....	23
2.6 Needle roller positions and displacements.....	31
2.7 Critical joint angle.....	47
2.8 Critical joint angle, when ball tilting is neglected and $\psi = \phi$	48
CHAPTER 3	
QUASI-STATIC ANALYSIS OF A STROKING TRIPODE JOINT.....	56
3.1 Introduction.....	56
3.2 Normal forces at spider trunnions.....	57
3.3 Normal forces at ball bores.....	59
3.4 Numerical examples and GAF experimental results.....	64
CHAPTER 4	
LOAD DISTRIBUTION ON A TRUNNION.....	71
4.1 Introduction.....	71
4.2 Normal load distribution on needles (axial direction).....	72
4.3 Normal load distribution on needles (radial direction).....	92
4.4 Numerical examples of load distribution on trunnions.....	99
4.5 Making trunnion load distribution a function of joint angle.....	105

CHAPTER 5	
STATE OF STRESS AT THE ROLLER-TRUNNION CONTACT.....	109
5.1 Introduction.....	109
5.2 Hertzian formulation for line (cylindrical) contacts.....	110
5.3 Non-Hertzian formulation for line (cylindrical) contacts.....	114
5.4 Non-Hertzian formulation for contact of rollers with crowning.....	122
5.5 Sub-surface stress distribution.....	135
CHAPTER 6	
FATIGUE-LIFE THEORIES.....	146
6.1 Introduction.....	146
6.2 Weibull equation.....	146
6.3 Lundberg-Palmgren equation.....	148
6.4 Ioannides-Harris equation.....	149
6.5 Zaretsky equation.....	150
6.6 Tripode equation.....	151
6.7 Testing and prototypes to validate the Tripode model.....	153
6.8 Load and stress conditions per test schedule.....	157
6.9 Test results.....	178
CHAPTER 7	
TRUNNION FORM OPTIMIZATION.....	191
7.1 Introduction.....	191
7.2 Elliptical vs. circular trunnion.....	191
7.3 Optimized vs. elliptical trunnion.....	194
CHAPTER 8	
CONCLUSIONS.....	200
APPENDICES.....	206
REFERENCES.....	214

LIST OF TABLES

Table 3.1	Properties of CVJ greases. (*) stands for “Extreme Pressure”.....	67
Table 4.1	Load distribution (N) at different proportions of yield torque.....	100
Table 5.1	Convergence of maximum pressure and deflection.....	119
Table 5.2	Convergence of maximum pressure and deflection.....	121
Table 5.3	Convergence of maximum pressure and deflection.....	126
Table 5.4	Convergence of maximum pressure and deflection.....	129
Table 6.1	Summary of wear tests conditions.....	155
Table 6.2	Needle-trunnion load as a function of joint angle at 272Nm.....	163
Table 6.3	Needle-trunnion load as a function of applied torque.....	163
Table 6.4	Inputs to calculate non-Hertzian contacts.....	165
Table 6.5	Key characteristics of non-Hertzian contacts.....	167
Table 6.6	Key characteristics of Hertzian contacts.....	168
Table 6.7	Sub-surface Critical shear stresses at the center of the contact.....	169
Table 6.8	Sub-surface Critical shear stresses at the point of maximum pressure.....	170
Table 6.9	Ratio of yield shear strength to critical shear stress.....	172
Table 6.10	Elastic stress and residual stress components at $z = 0.047\text{mm}$	177
Table 6.11	Elastic stress and residual stress components at $z = 0.042\text{mm}$	179
Table 6.12	Test results summary.....	181
Table 6.13	Inputs to best-fit life equation.....	185
Table 6.14	Life prediction summary.....	186

Table 6.15	Life prediction summary, residual stresses included.....	188
Table 7.1	Load distribution, circular vs. elliptical trunnion ($e_t = 1.003$).....	193
Table 7.2	Life comparison, circular vs. elliptical trunnion at 816Nm and 7°.....	194
Table 7.3	Load distribution, circular vs. elliptical vs. optimized trunnion.....	198
Table 7.4	Life comparison, different trunnion forms at 816Nm and 7°.....	199
Table B.1	Residual stresses.....	208
Table C.1	Chemical composition.....	209
Table C.2	Hardness.....	210

LIST OF FIGURES

Figure 1.1a	Steering motion (schematic aerial view).....	2
Figure 1.1b	Suspension motion (schematic front view).....	2
Figure 1.2	Universal Joint.....	3
Figure 1.3	Double Hooke Joint.....	4
Figure 1.4	Fixed Center CVJ.....	4
Figure 1.5	CGJ (left) and DOJ (right).....	5
Figure 1.6	Tripode Joint.....	6
Figure 1.7	Axial motion and support in Roller Bearing and Tripode Joint.....	7
Figure 1.8	Outer member support in Roller Bearing and Tripode Joint.....	8
Figure 1.9	Variation of load distribution in a tripod joint.....	8
Figure 1.10	Inner member shape in Roller Bearing and Tripode Joint.....	9
Figure 2.1	Exploded view of tripod joint.....	12
Figure 2.2	Housing Reference Frame.....	16
Figure 2.3	Spider Reference Frame.....	16
Figure 2.4	Fixed and mobile coordinate frames.....	17
Figure 2.5	Coordinates and orientation of spider shaft.....	21
Figure 2.6	Fluctuation of joint angle in a revolution.....	24
Figure 2.7	Deviation from nominal angle in a revolution.....	25
Figure 2.8	Orbiting path of spider on spider plane.....	26
Figure 2.9	Fluctuation of eccentricity within a revolution.....	27
Figure 2.10	Difference between input and output angular displacements.....	27

Figure 2.11	Orbiting path of spider on housing plane.....	28
Figure 2.12	Variations of the axial displacement of the spider center.....	29
Figure 2.13	Displacement of the spherical roller center along ball bore axis.....	30
Figure 2.14	Radial position of the spherical roller center, from spider center.....	30
Figure 2.15	Radial displacement of the spherical roller center, along trunnion axis.....	31
Figure 2.16	Trunnion, local cylindrical coordinate system.....	32
Figure 2.17	Secondary-rotating coordinate systems.....	33
Figure 2.18	Angle δ , per Eq. (2.30).....	36
Figure 2.19	Angle δ , per Eq. (2.31).....	36
Figure 2.20	Partial rolling of ball due to tilting.....	37
Figure 2.21	Actual arch displaced at ball outer diameter.....	40
Figure 2.22	Difference in arch displacement without and with ball tilting effect.....	40
Figure 2.23	Graphical representation of angle ϵ	41
Figure 2.24	Angle ϵ , per expression (2.39).....	42
Figure 2.25	Angle ϵ' , per expression (2.40).....	43
Figure 2.26	Angle η , per expression (2.41).....	44
Figure 2.27	Angular displacements and positions in trunnion-rollers set.....	45
Figure 2.28	Angular position of needle $j = 1$, per expression (2.44).....	46
Figure 2.29	Deviation from nominal angle in a revolution at $\theta_o = 23^\circ, 6^\circ$	48
Figure 2.30	Maximum proportional deviation from nominal angle vs. θ_o	49
Figure 2.31	Difference in arch displacement without and with ball tilting, at 6°	51
Figure 2.32	Relative error of ignoring ball tilting, at 6°	51

Figure 2.33	Relative error of arch-length displacement, ignoring tilting, vs. θ_o	52
Figure 2.34	Needle roller displacement, complete vs. simplified solution.....	54
Figure 3.1	Forces on spider plane.....	60
Figure 3.2	Rotating coordinate systems and joint orientation when $\psi_j = 0$	62
Figure 3.3	Graphical representation of angle ε and forces q_j and p_j	62
Figure 3.4	Magnitude of p_1 with (solid line) and without joint angle variation.....	64
Figure 3.5	Magnitude of q_1 with (solid line) and without joint angle variation.....	66
Figure 3.6	Tangential force w_1 , at 600Nm, 7.5°, grease A.....	68
Figure 3.7	Generated axial force, at 600Nm, 7.5°, grease A.....	68
Figure 3.8	Generated axial force, at 300N, experimental vs. theoretical values....	69
Figure 3.9	Generated axial force, at 600N, experimental vs. theoretical values....	70
Figure 4.1	Case 1: Spherical roller fully supported, no offset.....	73
Figure 4.2a	Case 2: Positive offset (Λ).....	74
Figure 4.2b	Case 3: Negative offset ($-\Lambda$).....	74
Figure 4.3	Clearance between needle, roller-retainer and spacer ring.....	76
Figure 4.4a	Needle axial displacement at 6° joint angle.....	77
Figure 4.4b	Needle axial displacement at 23° joint angle.....	78
Figure 4.5	Offset between ball equator and needles symmetry plane.....	79
Figure 4.6	Effective contact length between needle roller and ball, at 23°.....	81
Figure 4.7	Load per unit length at upper end of needle, at 19.5°.....	90
Figure 4.8	Load per unit length at lower end of needle, at 19.5°.....	91
Figure 4.9	Spider Geometry.....	92

Figure 4.10	Cross section of spherical roller.....	95
Figure 4.11	Schematic view of loads.....	96
Figure 4.12	Load distribution at 25% and 50% of yield torque.....	101
Figure 4.13	Load distribution at 50% of yield torque, perfect vs. lobed trunnion...	102
Figure 4.14	Load distribution at 50% of yield torque, circular vs. elliptical trunnion.....	104
Figure 4.15	Example of initial wear in a trunnion.....	105
Figure 4.16	Position of roller within load profile.....	106
Figure 4.17	Roller position with respect to symmetry plane of loading profile.....	107
Figure 4.18	Load profile at joint angle of 6°.....	108
Figure 5.1	Ideal cylindrical contact.....	111
Figure 5.2	Subsurface stresses along the plane of symmetry of the contact.....	113
Figure 5.3	Two bodies in contact.....	115
Figure 5.4	Pressure distribution in a sphere-plane contact.....	119
Figure 5.5	Pressure distribution in a cylinder contact.....	122
Figure 5.6	Needle roller dimensions.....	123
Figure 5.7	Crowning of 10.81mm needle roller.....	124
Figure 5.8a	Pressure distribution of needle roller with crowning.....	125
Figure 5.8b	Lateral view of pressure distribution of needle roller with crowning....	125
Figure 5.9	View of needle skewing.....	126
Figure 5.10a	Pressure distribution of needle roller with crowning and skewing.....	127
Figure 5.10b	Lateral view of pressure distribution of needle roller with crowning and skewing.....	128
Figure 5.11	Undercut on trunnion surface.....	129

Figure 5.12a	Pressure distribution of skewed needle roller with undercut on trunnion.....	130
Figure 5.12b	Lateral view of pressure distribution of skewed needle roller with undercut on trunnion.....	130
Figure 5.13	Case of asymmetrical load, positive offset.....	131
Figure 5.14a	Pressure distribution of needle roller with crowning and a load offset Δ_j of -1mm , no skewing.....	133
Figure 5.14b	Lateral view of pressure distribution of needle roller with crowning and a load offset Δ_j of -1mm , no skewing.....	134
Figure 5.15a	Pressure distribution of needle roller with crowning and a load offset Δ_j of -1mm , skewing of 4°	134
Figure 5.15b	Lateral view of pressure distribution of needle roller with crowning and a load offset Δ_j of -1mm , skewing of 4°	135
Figure 5.16a	Stress distribution along the depth of the contact, σ_x component.....	141
Figure 5.16b	Stress distribution along the depth of the contact, σ_y component.....	141
Figure 5.16c	Stress distribution along the depth of the contact, σ_z component.....	142
Figure 5.16d	Stress distribution along the depth of the contact, τ_{\max}	142
Figure 5.17a	Stress distribution along the depth of the contact, σ_x component represented with a solid line, σ_y component represented by a dashed line.....	144
Figure 5.17b	Stress distribution along the depth of the contact, σ_z component.....	144
Figure 5.17c	Stress distribution along the depth of the contact, τ_{\max}	145
Figure 6.1	CVJ wear test bench.....	154
Figure 6.2	Example of roundness check.....	156
Figure 6.3	Needle displacement.....	158
Figure 6.4	Load offset.....	159

Figure 6.5a	Variation of load on ball bore, housing plane at 272Nm.....	160
Figure 6.5b	Loads on ball bore, housing plane.....	161
Figure 6.6	Plane formed by housing axis and spider axis, zero plane for rotation.....	161
Figure 6.7a	Virtual load of needle to trunnion at spider plane, at 272Nm.....	162
Figure 6.7b	Virtual load of needle to trunnion at spider plane.....	162
Figure 6.8	Pressure distribution, input torque of 272Nm.....	166
Figure 6.9	Pressure distribution, input torque of 466Nm.....	166
Figure 6.10	Pressure distribution, input torque of 816Nm.....	166
Figure 6.11	Max Shear and Octahedral shear at center of contact.....	168
Figure 6.12	Max Shear and Octahedral shear at point of maximum pressure.....	169
Figure 6.13	Max Shear and Octahedral shear at point of maximum pressure.....	174
Figure 6.14	Shear stress τ_{zxr} at a depth of 0.047mm.....	178
Figure 6.15	Parts A-1 and A-2.....	181
Figure 6.16	Parts B-3 and B-1.....	182
Figure 6.17	Part C-2.....	182
Figure 6.18a	Part B-2 (units are microns).....	183
Figure 6.18b	Part B-2 (units are microns).....	184
Figure 6.19	Actual versus theoretical life.....	186
Figure 6.20	Residual stresses in Spider C-4.....	187
Figure 6.21	Actual versus theoretical life after superposing residual stresses.....	188
Figure 6.22	Hardness gradient in trunnion.....	190
Figure 7.1	Load distribution on a trunnion.....	195
Figure 7.2	Pareto Front.....	197

Figure A.1	Surface texture before testing.....	206
Figure A.2	Surface texture after testing.....	206
Figure D.1	Roundness with filter 0-15UPR.....	209
Figure D.2	Roundness with filter 0-50UPR.....	210
Figure D.3	Roundness with filter 0-150UPR.....	211
Figure D.4	Roundness with filter 0-500UPR.....	212

LIST OF SYMBOLS

BCD	=	ball circle diameter
a	=	$bcd / 2$, radial distance between housing axis and ball bore axis
${}^i \mathbf{A}$	=	Orientation matrix of spider reference frame $X_i^S - Y_i^S - Z_i^S$, with respect to housing reference frame $X_i^H - Y_i^H - Z_i^H$
b	=	spider shaft length, from spider center to spherical joint center
c_o	=	initial stroke position of spider center with respect to housing plane
d	=	needle roller diameter
h, g, k	=	coordinates of spherical joint center (end of spider axle bar)
e	=	eccentricity of spider center to housing axis
e_x, e_y	=	coordinates of spider center on the frame $X^* - Y^* - Z^*$
f_j	=	radial displacements of ball center, measured along trunnions
m_j	=	spherical roller (ball) inner diameter
m_o	=	spherical roller (ball) outer diameter
n	=	number of needle rollers per trunnion
r_j	=	radial distance between spider axis and ball bore centerlines, measured along trunnions
s_j	=	arch length displaced on ball outer diameter due to ball travel along ball bore
t	=	trunnion diameter
$X-Y-Z$	=	fixed reference frame
$X' - Y' - Z'$	=	mobile spider reference frame

- $X^* - Y^* - Z^* =$ mobile spider offset reference frame
- $x, y, z =$ coordinates of spider center with respect to housing reference frame
- $X_i - Y_i - Z_i =$ coordinates of spherical roller centers with respect to fixed reference frame $X - Y - Z$
- $X_i' - Y_i' - Z_i' =$ coordinates of spherical roller centers with respect to spider reference frame, $X' - Y' - Z'$
- $X_i^* - Y_i^* - Z_i^* =$ coordinates of spherical roller centers with respect to spider offset reference frame, $X^* - Y^* - Z^*$
- $X^* = X' + e_x$
- $Y^* = Y' + e_y$
- $X_i^H - Y_i^H - Z_i^H =$ Housing, secondary mobile reference frame
- $X_i^S - Y_i^S - Z_i^S =$ Spider, secondary mobile reference frame
- $\mathbf{X}_i^S, \mathbf{X}_i^H =$ Vectors that define orientation of spider and housing rays
- $\alpha, \beta, \theta =$ direction angles of spider axis, with respect to fixed reference frame
- $\kappa_i, \lambda_i, \mu_i =$ direction angles of spider rays, with respect to housing mobile reference frame, $X_i^H - Y_i^H - Z_i^H$
- $U_i - \Phi_i - V_i =$ trunnion local reference frame, cylindrical coordinate system
- $\theta =$ joint angle, angle between spider and housing axes
- $\theta_0 =$ joint angle, angle between spider and housing axes, when $\varphi = 0$
- $\theta_{cr} =$ critical joint angle
- $\theta_{cr\Delta} =$ critical joint angle to assumption of linear load distribution

- ϕ_{ij} = Needle roller angular position, with respect to trunnion local reference frame $U_i - \Phi_i - V_i$
- δ_i = angle between spider ray and housing plane $X_i^H - Y_i^H$, measured on plane formed by vectors \mathbf{X}_i^S and \mathbf{Z}_i^H
- ε_i = angle between vectors \mathbf{Y}_i^S and \mathbf{Y}_i^H
- η_i = angular displacement of contact point between spherical roller and ball bore, with respect to trunnion local reference frame
- φ = angular displacement of housing shaft (input angle)
- ψ = angular displacement of spider (output angle)
- $\psi_1 = \psi_2 - 2\pi/3 = \psi_3 + 2\pi/3$
- $\varphi_1 = \varphi_2 - 2\pi/3 = \varphi_3 + 2\pi/3$
- i = Trunnion index, 1, 2, 3
- j = Needle roller index, 1, 2, 3, ... , n
- ξ = Angular displacement of O^*O' with respect to X^*
- p_{ij} = concentrated normal force from needle j to trunnion i
- p_i = force normal to trunnion axis, on spider plane
- q_i = force normal to ball bore axis, on housing plane
- w_j = tangential force at ball bore, parallel to ball bore axis
- t_φ = input torque
- t_ψ = output torque
- GAF = generated axial force, measured on the housing axis
- μ_b = sliding friction coefficient between ball and ball bore

μ_r	=	rolling friction coefficient between ball and ball bore
c_t	=	effective contact length of needle on trunnion
c_b	=	effective contact length of needle on ball
c_{bu}	=	effective upper contact length of needle on ball
c_{bd}	=	effective lower contact length of needle on ball
Λ_i	=	distance between plane passing thru equator of spherical roller and transversal symmetry plane of needle rollers, offset
Λ_o	=	initial offset, when joint angle is zero
θ_i	=	axial displacement of needle along trunnion
θ_o	=	clearance between needle, roller retainer and ring spacer
c_{buo}	=	initial effective upper contact length of needle on ball
c_{bdo}	=	initial effective lower contact length of needle on ball
p_{tmij}	=	mean load per unit of length on trunnion
p_{bmij}	=	mean load per unit of length on ball
p_{tuij}	=	load per unit of length on trunnion at point TU
p_{tdij}	=	load per unit of length on trunnion at point TD
p_{buij}	=	load per unit of length on ball at point BU
p_{bdij}	=	load per unit of length on ball at point BD
e_{spider}	=	height of spider shoulder from spider axis
c_{spacer}	=	thickness of spacer

- b_{needle} = total needle length
- R_b = radius to the centroid of the radial cross section of the ball
- h_b = distance from the centroid of the cross section of the ball to the extreme fiber on the concave side
- c_{bw} = ball height (lateral face to lateral face distance)
- α_b = semi-arch of ball width
- y_{bA} = radius to intersection point of circular and rectangular segments of the radial cross section of the ball
- y_{b1} = radius to centroid of circular segment
- y_{b2} = radius to centroid of rectangular segment
- a_{b1} = area of circular segment of ball cross section
- a_{b2} = area of rectangular segment of ball cross section
- a_b = area of ball radial cross section
- I_{b1x} = second moment of area of circular segment of ball cross section
- I_{b2x} = second moment of area of rectangular segment of ball cross section
- I_{bxx} = second moment of area of ball radial cross section
- ϕ_u = angular position on inner diameter of ball when $\phi_{i1} = 0$
- ϕ_v = angular position of needle roller v when $\phi_{i1} = 0$
- u = auxiliary needle spacing index, 2, 3, 4, ... , n
- v = auxiliary needle roller index, 2, 3, 4, ... , n
- pC_{uv} = influence coefficient for ring (ball) deflection due to a roller load
- qC_u = influence coefficient for ring (ball) deflection due applied load q_j

- δ_b = radial displacement of ball center with respect to trunnion center
- δ_u = relative radial approach of ball to trunnion at angle ϕ_u
- v_u = combined radial deformation of ball, for needle roller at angle ϕ_u
- Ω_u = radial deviation of actual trunnion surface with respect to trunnion basic circle at angle ϕ_u
- r_u = radial distance to trunnion surface at angle ϕ_u
- E_Y = modulus of elasticity of steel = 207GPa
- k_{pt} = material constant for contact between needle and trunnion
- k_{pb} = material constant for contact between needle and ball
- k_p = combined material constant for needle contacts
- p_v = radial load transmitted by needle roller v , when $\phi_{i1} = 0$
- h_w = order of dominant harmonica causing distortion on trunnion
- Ω_o = profile or roundness tolerance of trunnion
- n_r = constant for elastic properties roller bearings = 10 / 9
- $p_v \Delta_u$ = radial deflection of ball at angle ϕ_u due to a load p_v
- $q \Delta_u$ = radial deflection of ball at angle ϕ_u due to a load q_j
- Γ_o = constant that takes its value based on position of first roller
- Γ = upper limit to index v
- Γ_v = 0.5 for $\phi_v = 0$. Otherwise, $\Gamma_v = 1$
- χ_{ij} = angle between the plane passing thru the center of trunnion i and the center of roller j , and plane $X' - Y'$

Ψ	=	roller to trunnion continuous load profile function
a	=	semi-width of rectangular contact element (<i>for section 5 only</i>)
b	=	semi-length of rectangular contact element (<i>for section 5 only</i>)
b_h	=	semi-width of line contact area, perpendicular to contact line
l_h	=	length of line contact area, parallel to contact line, Hertz
σ_h	=	surface pressure in a cylindrical contact, Hertz
σ_{hmax}	=	maximum surface pressure in a cylindrical contact, Hertz
σ_{hx}	=	stress component in the x-direction in the region of contact, Hertz
σ_{hy}	=	stress component in the y-direction in the region of contact, Hertz
σ_{hz}	=	stress component in the z-direction in the region of contact, Hertz
τ_h	=	maximum principal shear stress in the region of contact, Hertz
τ_{hmax}	=	peak value of the maximum principal shear stress, Hertz
$\sigma_x, \sigma_y, \sigma_z$	=	normal stress components in the region of contact, numeric
$\tau_{xy}, \tau_{yz}, \tau_{xz}$	=	shear stress components in the region of contact, numeric
$\sigma_I, \sigma_{II}, \sigma_{III}$	=	stress invariants
$\sigma_{p1}, \sigma_{p2}, \sigma_{p3}$	=	principal stresses in the region of contact, numeric
$\sigma_{p1} = \sigma_{pmax}$	=	max principal stress in the region of contact, numeric
$\sigma_{p3} = \sigma_{pmin}$	=	min principal stress in the region of contact, numeric
τ_{max}	=	maximum principal shear stress in the region of contact, numeric
E_Y	=	modulus of elasticity, for steel = 207GPa
ν_s	=	Poisson's ratio, for steel = 0.3

κ	=	material constant
$X-Y-Z$	=	reference frame at the contact region (<i>for section 5 only</i>)
x, y, z	=	coordinates of a point in the contact region (<i>for section 5 only</i>)
α_{ij}	=	displacement of roller j with respect to trunnion i , caused by deformation
v_1, v_2	=	displacements of points in or near the contact area, parallel to the direction of the applied force to the contact
z_1, z_2	=	initial separation of points in or near the contact area, parallel to the direction of the applied force to the contact
z_{cw}	=	crowning, deviation from nominal cylinder along its axis
z_{sk}	=	equivalent crowning cause by needle skewing
z_{ξ}	=	equivalent crowning due to asymmetrical load distribution
z_t	=	total equivalent crowning
r_{sk}	=	radial clearance caused by needle skewing
s_n	=	uniform pressure on element n
n, m	=	dummy variables, 1, 2, 3, ... , r
r	=	number of rectangles in the mesh used to calculate contact area
f_{mn}	=	influence coefficients
ζ	=	skewing angle of needle roller with respect to trunnion
ξ_{ij}	=	slope of equivalent contact deformation on needle j of trunnion i due to slope of asymmetric load distribution
ε	=	Weibull slope or Weibull modulus
ϑ	=	Exponent, experimentally obtained
c	=	critical shear-stress life exponent

σ_w	=	fracture strength of a specimen
$\sigma_{w\beta}$	=	characteristic fracture strength of a specimen
S	=	specimen survival to fracture strength σ_w
V	=	stressed volume in a specimen
N	=	number of cycles to fracture
L	=	life of a component, in cycles
τ_{cr}	=	critical shear stress
τ_o	=	maximum octahedral shear stress
τ_U	=	Fatigue limit
C_i	=	constants, for $i = 1, 2, 3, \dots$
z_{cr}	=	depth of critical shear stress
n_h	=	life exponent for Hertzian contacts
l_{eff}	=	effective, non-Hertzian contact length
ϕ_{eff}	=	effective angular displacement of a needle roller within a revolution at a given joint angle
τ_{eff}	=	effective shear stress (varies depending on the static failure theory used)
YS	=	uni-axial yield strength
TS	=	uni-axial tensile strength
Hv	=	Vickers Hardness
HRc	=	Rockwell-C Hardness
SF	=	Ratio of shear yield strength to critical shear stress

1. INTRODUCTION

1.1 Background

This work focuses on the wear life prediction of the Tripode (TP) type Constant Velocity Joint (CVJ). Internally, the TP CVJ is composed of rolling elements which function similar to those of roller bearings. Rolling bearing technology, as we know it today, began to develop in the nineteenth century. In 1881, H. Hertz published his contact stress analysis beginning the analytical study of bearings. The first paper discussing life bearing prediction was published in 1924 by A. Palmgren [1]. Bearing technology, contact stress and life prediction theories continued to develop in the second half of the twentieth century and are still developing.

A Constant Velocity Joint (CVJ) is a mechanical device capable of transmitting torque and motion between two rotating shafts that are not aligned. One of the first applications of constant velocity joints in the U.S. auto industry was in the 1960's, in the halfshafts of front wheel drive vehicles [2]. A halfshaft is an assembly of two constant velocity joints and an axle bar. Its purpose is to transmit motion and torque from the transmission to the powered wheels of a vehicle. One of the most common halfshaft configurations includes a fixed center constant velocity joint and a stroking constant velocity joint. Such configuration allows the halfshaft to articulate and change its length as a result of steering and suspension motions in a vehicle, as shown schematically in Figures 1.1a and 1.1b

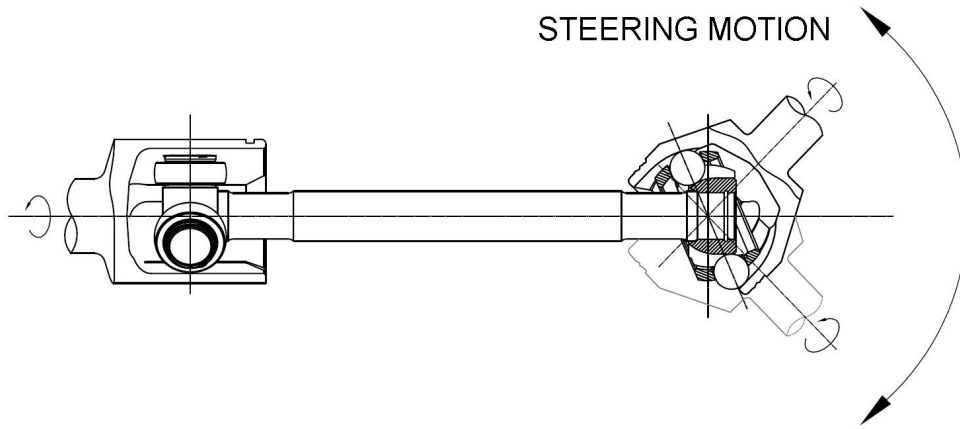


Figure 1.1a. Steering motion (schematic aerial view)

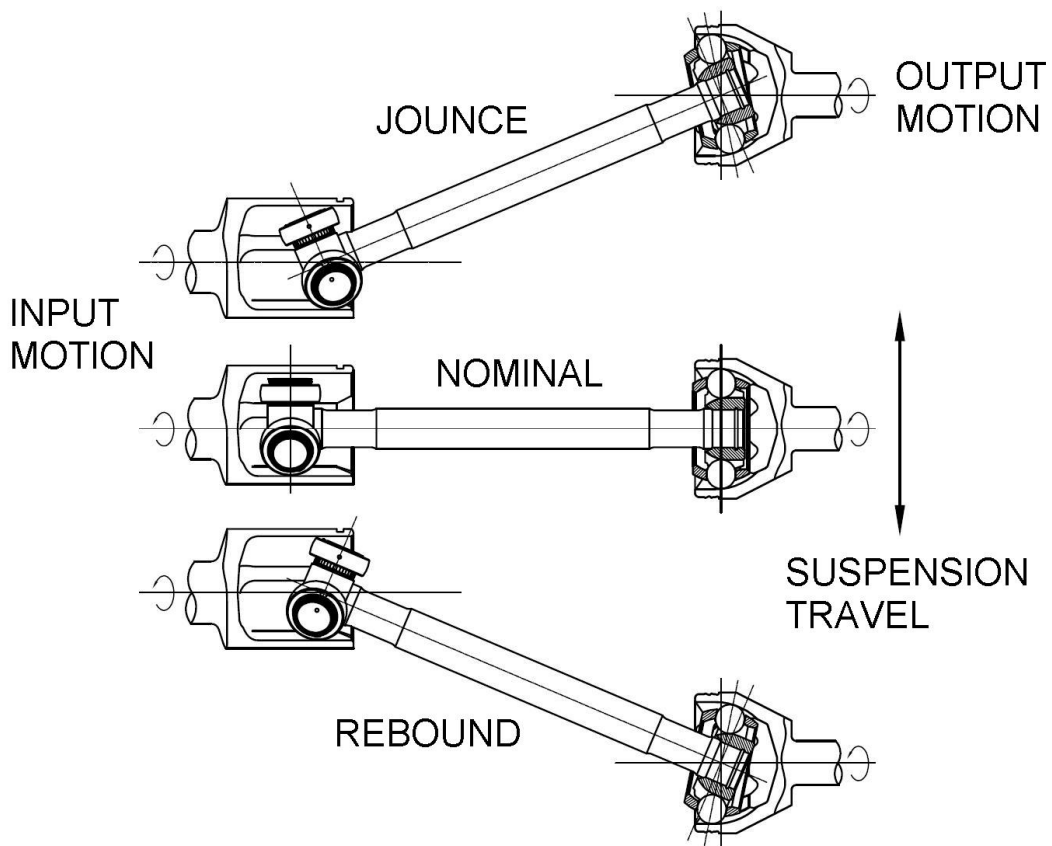


Figure 1.1b. Suspension motion (schematic front view)

Even though constant velocity joints have been around for almost one hundred years little has been done to develop specific analytical models to predict its wear life. *It's the purpose of this work to develop a wear life model for a specific type of constant velocity joint, the Tripode joint.*

1.2 Fixed center constant velocity joints

The first predecessor of the constant velocity joint was the Universal Joint or Cardan Joint, named after Geronimo Cardano who was the first to describe it in the mid sixteenth century [3]. The Universal joint allows transmission of torque and motion between two shafts that are not aligned but with variation of torque and speed. A schematic view of the Universal Joint is shown in Figure 1.2.

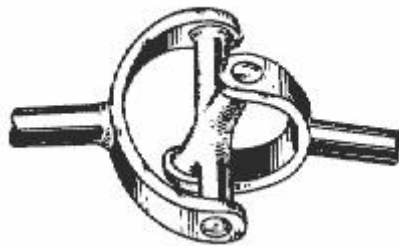


Figure 1.2. Universal Joint

Almost 100 years later Robert Hooke had the idea of combining two universal joints to eliminate the non-uniformity, which was the first mechanism with true constant velocity properties [3].



Figure 1.3. Double Hooke Joint

One of the first ball-type constant velocity joints, as we know it today, was patented by Alfred Rzeppa in 1934 [4]. This joint is composed of an inner race member, an outer race member, balls connecting the two races and a cage to keep the balls in the constant velocity plane. The constant velocity transmission is achieved by keeping the balls on a bisecting plane, which is the same principle that is used to transmit constant velocity using bevel gears.

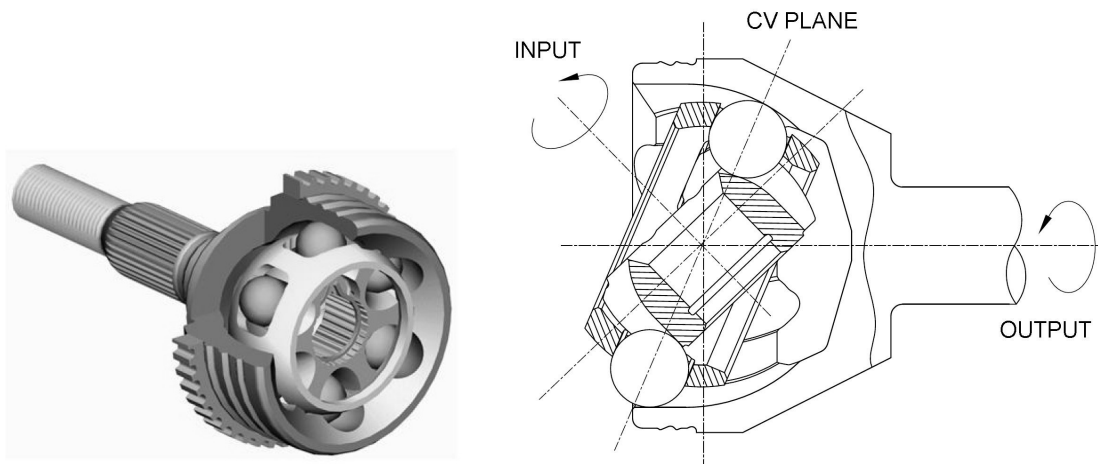


Figure 1.4. Fixed Center CVJ

1.3 Stroking constant velocity joints

There are several types of stroking or plunging constant velocity joints. They can be classified in ball-type joints and tripod-type joints. The first type uses the same principle of the bisecting plane to transmit constant velocity. The two most common types of ball-type stroking joints are the cross groove joint (CGJ) and the double offset joint (DOJ) [2].

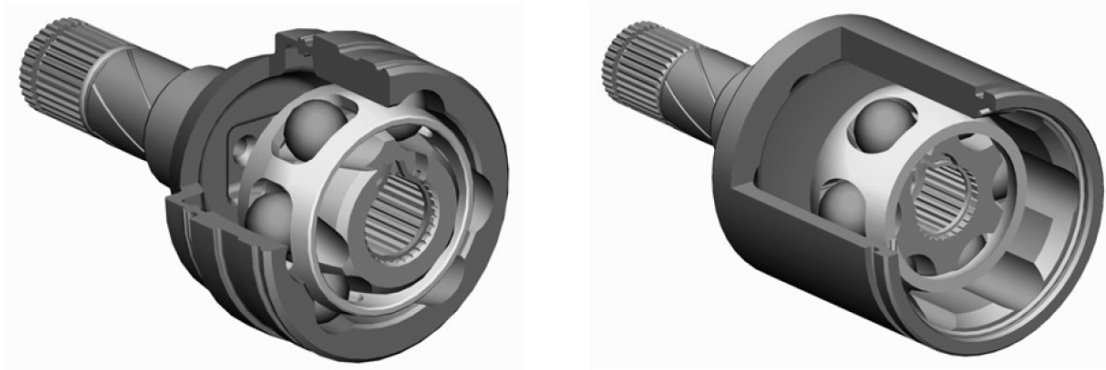


Figure 1.5. CGJ (left) and DOJ (right)

The tripod-type joints are not perfect constant velocity joints but they approximate constant velocity at the typical operating angles in a vehicle, and can be considered a constant velocity joint for practical purposes. Section 2 of this work explains in detail the kinematics of the tripod joint and explains why it is a quasi-constant velocity joint.



Figure 1.6. Tripode Joint

1.4 Rolling Bearings and Tripode Joints

A tripod joint is composed of a spider assembly and a housing. The spider assembly is composed of a spider and three sets of rollers that rotate and slide along the trunnions of the spider. Some of the characteristics that make the roller sets in a tripod joint different from a typical roller bearing are the following:

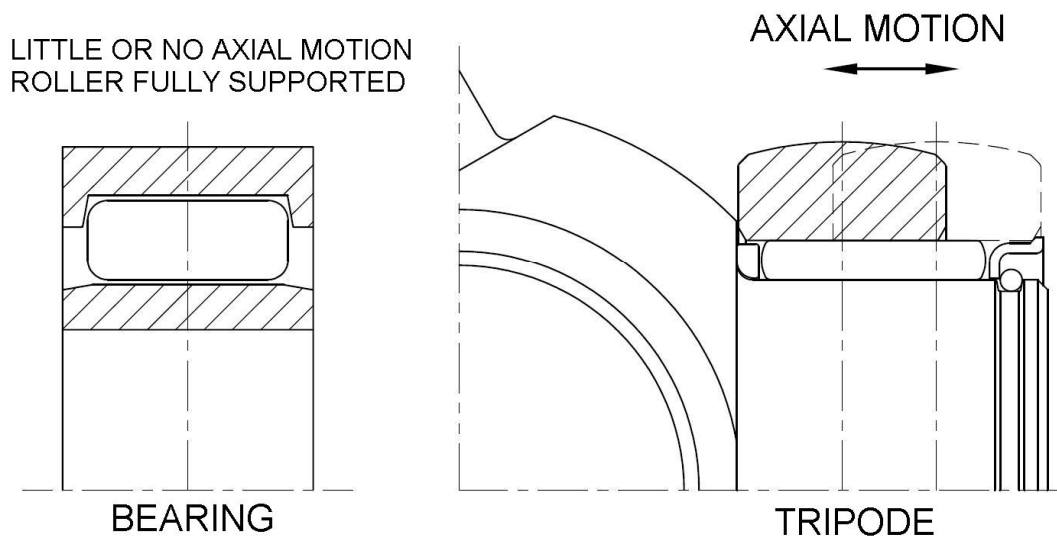


Figure 1.7. Axial motion and support in Roller Bearing and Tripode Joint

1. In most roller bearing applications the race members remain axially static or quasi-static with respect to themselves. In a tripod joint the outer member of the roller set, named roller or ball, moves axially with respect to the inner member, named trunnion. This is shown schematically in Figure 1.7.
2. In most roller bearing applications the needle rollers connecting the races are fully supported. In a tripod joint the needle rollers are not fully supported all the time. As shown in Figure 1.7.
3. In most roller bearing applications the outer race is fully supported. In a tripod joint the outer member of the roller set is supported at only one point. This is shown schematically in Figure 1.8.

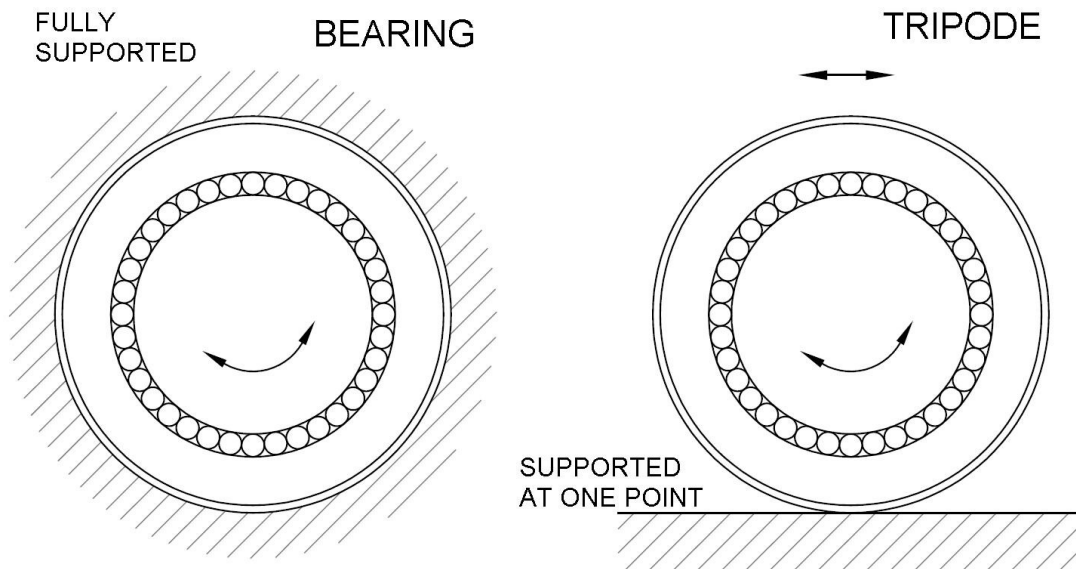


Figure 1.8. Outer member support in Roller Bearing and Tripode Joint

4. In most roller bearing applications possible misalignment is constant, making easier to predict load distributions. In a tripod, equivalent misalignment in the roller set continuously changes within a revolution and is a function of the joint angle, making it necessary to predict instantaneous load distributions. This is shown schematically in Figure 1.9 and will be covered in detail in Section 4.

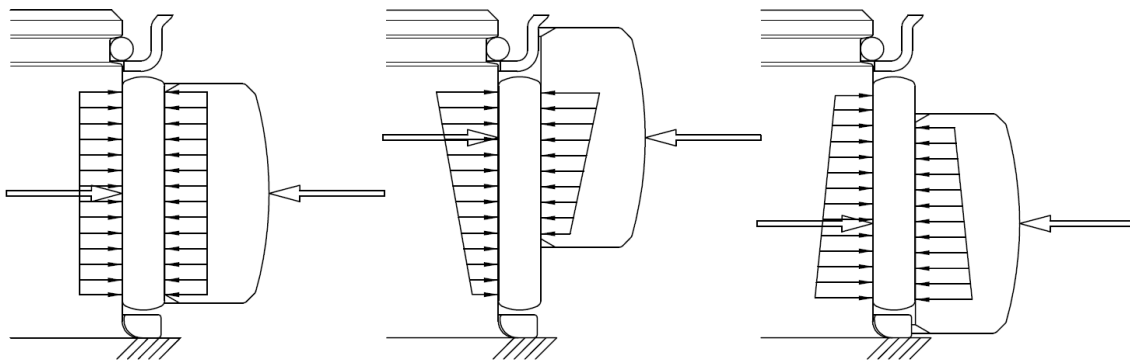


Figure 1.9. Variation of load distribution in a tripod joint

5. In most roller bearing applications the race members are round. In a tripod joint the trunnion may have non-round shapes, which changes the load distribution in the needle rollers. A circular and a non-circular shape are shown schematically in Figure 1.10. The non-circular shape has been exaggerated for visualization purposes.

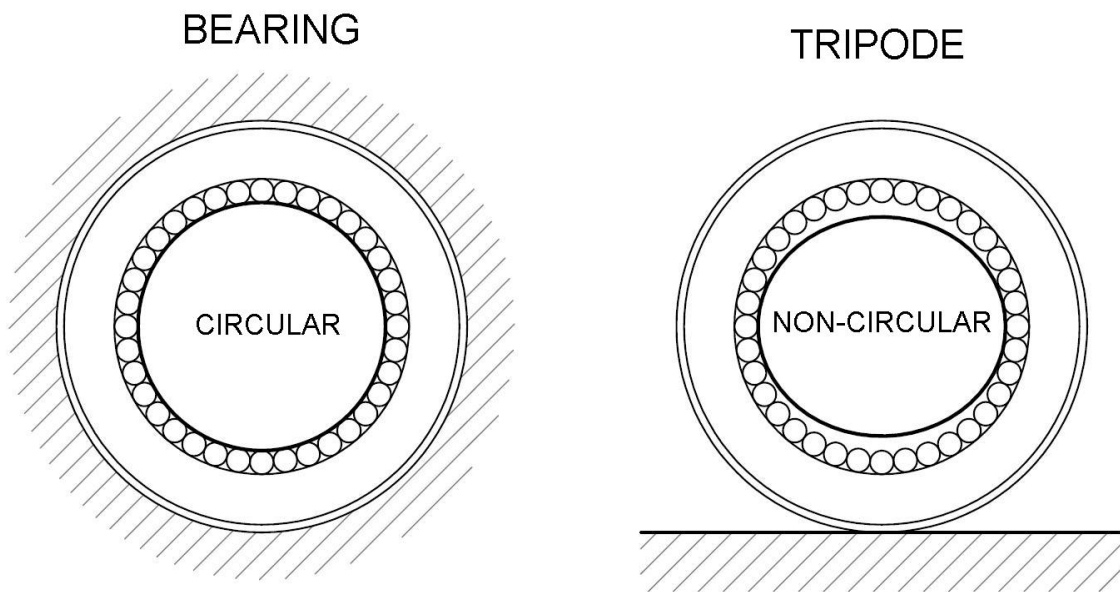


Figure 1.10. Inner member shape in Roller Bearing and Tripode Joint

For the reasons formerly mentioned, traditional approaches to estimate the life of the roller set in a tripod joint, such as the ISO-ANSI/AFBMA standards, can not be employed. A new specific analytical model, with experimental verification, to predict the life of tripod joints is necessary.

1.5 Benefits of a life model

Traditionally, a semi-empiric approach has been used by some CVJ manufacturers to estimate the life of a tripod joint, resulting in joints that may be over-designed or under-designed. By knowing the kinematics of the joint, the internal load conditions, the generated stress fields in the contacts and its relationship to wear life, optimized joints can be developed, resulting in packaging, mass and cost reductions.

Another benefit of developing a valid analytic model is that in a family of products only one size needs to be tested and validated. Larger and smaller sizes can be developed with a bigger level of confidence, reducing the development time and cost of the project.

1.6 Joint Size and Packaging

The size of a tripod joint is typically defined by the torque capacity of the largest axle bar that can be plugged into the spider. “Yield Torque” is a common term used by CVJ manufacturers and refers to the maximum torque an axle bar or splined interface can transmit before having plastic deformation. The joint used for the experimental portion of this work is a “21-size” joint. The yield torque of the largest axle bar that can be used in combination with the joint is around 2100Nm.

The “packaging” of the joint is another common term used by CVJ manufacturers and is used to refer to the maximum swing diameter of the joint.

1.7 Project description

The sequence of steps taken in this project is as follows:

1. Description of the architecture of the tripod joint
2. Study of the kinematics of the tripod joint
3. Study of the forces at the internal contacts of the tripod joint
4. Calculation of the stress field resulting from the forces at the contacts
5. Use of the state of stress to predict wear life using fatigue theories
6. Experimentation, analysis and correlation of results
7. Optimization of the roller assemblies to maximize life and/or minimize packaging.

The experimental portion of this work was conducted at an industrial facility that has specialized test machines for halfshafts, proprietary to the CVJ manufacturer sponsoring this work. Details of the testing performed such as speed, torque, angle and test time, and inspection results of tested parts will be discussed in Section 7.

2. KINEMATIC ANALYSIS OF A STROKING TRIPODE JOINT

2.1 Introduction

The tripod joint has been around for almost a hundred years [2]. However, many investigations have not been published. Most of them are related to motion analysis, kinematic structure and properties [5-10], dynamic effects such as Generated Axial Force (GAF) [11-14] and general design guidelines [2, 3, 15-16]. The purpose of this section is not to propose a totally new kinematic approach to analyze the tripod joint but to use, improve and expand what is currently available, knowing its limitations and related assumptions, in order to define internal displacements, which will be subsequently used to predict internal forces and the state of stress at the contacts within the joint.

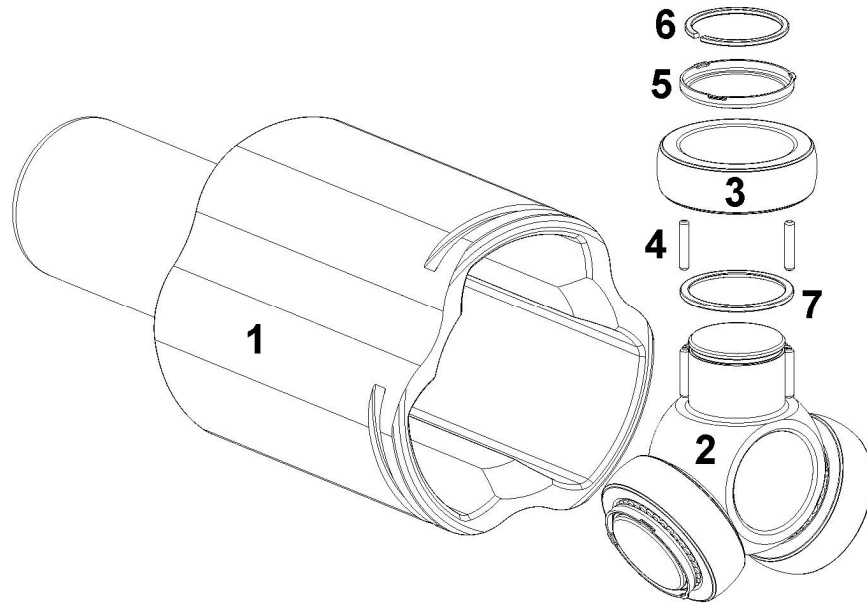


Figure 2.1. Exploded view of tripod joint

This work treats the tripod joint as a single universal joint. Therefore, the joint angle and the respective positions of the input and output shafts are chosen arbitrarily.

As shown in Figure 2.1, the joint is composed of:

- A **housing (1)** with three straight parallel and equally spaced ball bores (grooves or slots).
- A **spider (2)** whose three trunnions (legs) lie on the same plane, are equally spaced and converge to the same point.
- Three **spherical rollers (3)** which can rotate and slide on the trunnions thanks to the interaction with the **needle rollers (4)**. This interaction can be simplified to a cylindrical pair for purposes of kinematic analysis. The interaction between spherical balls and housing ball bores can be simplified to a sphere-groove kinematic pair.
- A set of **rings (6)** and **roller retainers (5)** whose main function is to keep all components in place. Their kinematic and dynamic effects can be neglected since they are not mobile parts and its mass is very small compared to the mass of other components formerly mentioned.
- Optional **spacer rings (7)** which can be used to eliminate edge contact on the needle rollers at the base of the trunnion. Its kinematic and dynamic effects can also be neglected.

2.2 Assumptions

Individual components are considered as rigid bodies. Geometrical errors (i.e. spacing errors) and clearances are neglected during the kinematic and quasi-static analysis since they are very small compared to the displacements and joint dimensions.

2.3 Definitions

The reference frames used in this section are shown in Figure 2.2, Figure 2.3 and Figure 2.4. The housing is typically connected to the transmission output in a vehicle and its only motion is rotational about its axis. Thus, a fixed reference frame X - Y - Z is chosen on the housing side, where plane X - Y is the housing plane and Z is the housing axis. The spider rotates together with the housing and at the same time it can displace and change its orientation with respect to the housing due to suspension and steering motion in a vehicle. Thus, two moving frames are chosen on the spider side. The first one, denoted by X' - Y' - Z' has its origin at the spider center O' and Z' is the spider axis. Plane X' - Y' is the spider plane. Y' is oriented parallel to the common perpendicular of the Z and Z' axes. The second moving frame, X^* - Y^* - Z^* , has its axes, X^* , Y^* and Z^* parallel to axes X' , Y' and Z' , respectively. Origin O^* is the intersection of the spider plane and the housing axis. X^* and Y^* lie on the spider plane. The following terms are defined:

Housing plane: An arbitrary plane normal to the housing axis, Z (Figure 2.2).

BCD: Ball Circle Diameter, the diameter of the circle on the housing plane passing through the intersections of ball bore centerlines and housing plane (Figure 2.2). This is a main joint parameter and will be constantly referenced.

BCR: Ball Circle Radius, defined in this work as variable a . It is half of the BCD

Ball bore plane: A plane that passes through the housing axis and a ball bore centerline or ball bore axis (Figure 2.2).

Housing rays: Equally spaced (each 120° apart), represent the intersection between housing plane and ball bore planes. The three rays intersect at the housing axis (Figure 2.2).

Spider rays: The centerline or axis of each trunnion (leg) of the spider, equally spaced (each 120° apart) (Figure 2.3).

Spider center: The common intersection of the three spider rays (Figure 2.3).

Spider plane: The plane that passes through the three spider rays (Figure 2.3).

Spider axis: Axis perpendicular to the spider plane passing through the spider center (Figure 2.3).

Spherical roller (ball) center: The center point of each of the three spherical rollers (Figure 2.3).

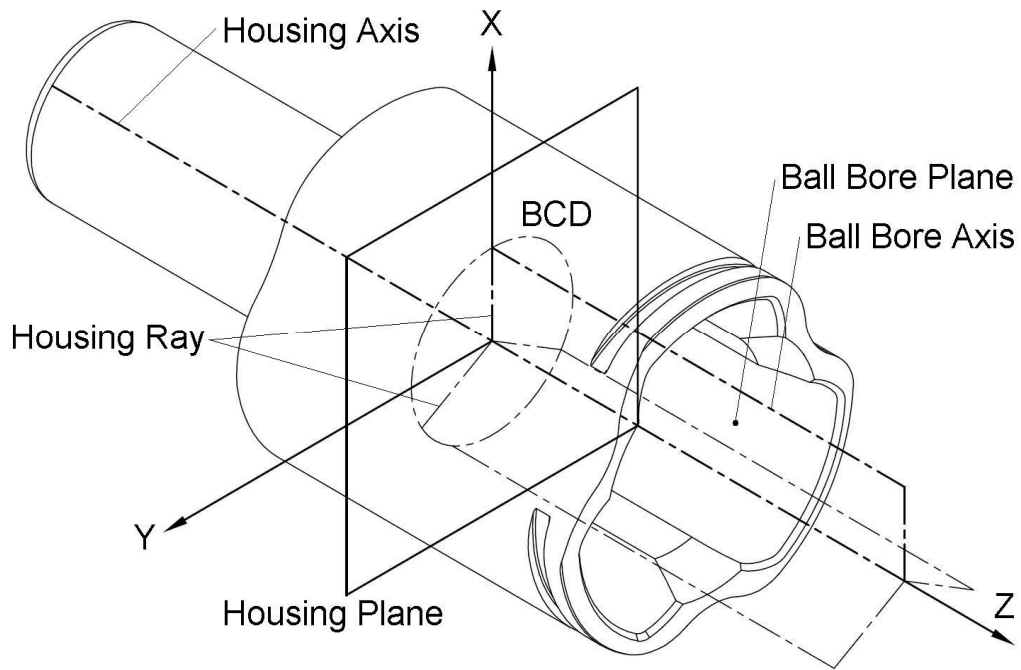


Figure 2.2. Housing Reference Frame

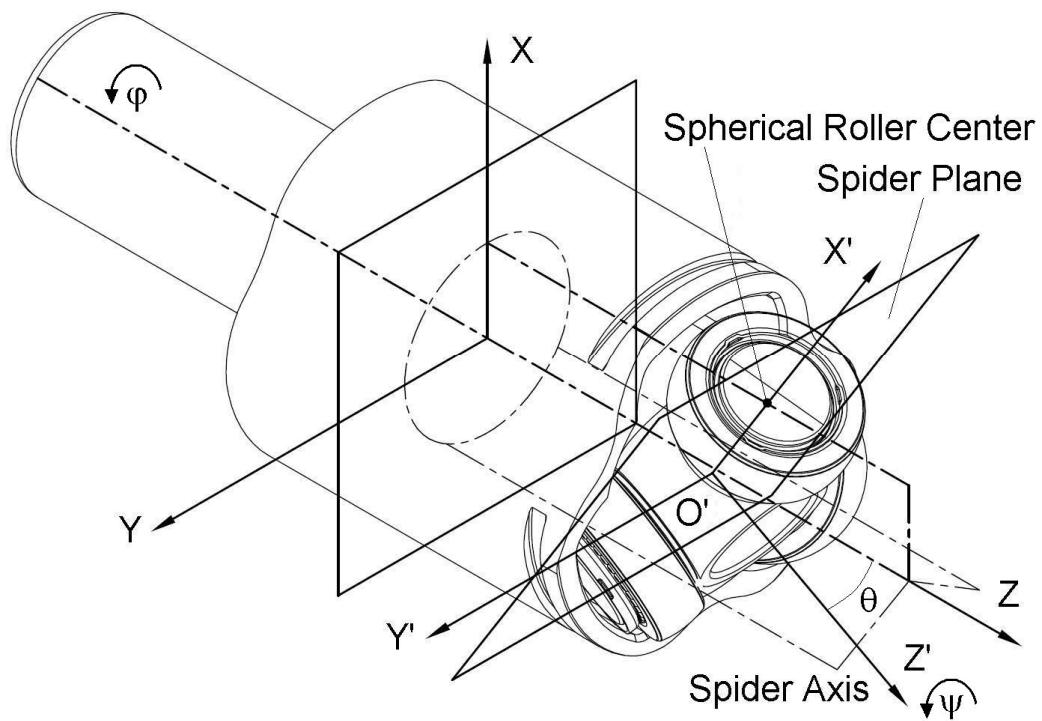


Figure 2.3. Spider Reference Frame

The eccentricity e shown in Figure 2.4 is defined as the distance from O^* to O' . The rotation of the spider shaft (output) is defined as ψ and the rotation of the housing shaft (input) is defined as φ . The joint angle θ is defined as the angle between the spider and housing axes. Due to the small variations between input and output angular displacements, which are inherent to the kinematic structure of the joint, the tripod joint is in fact a non-constant velocity joint.

$$|\varphi - \psi| \neq 0 \quad (2.1)$$

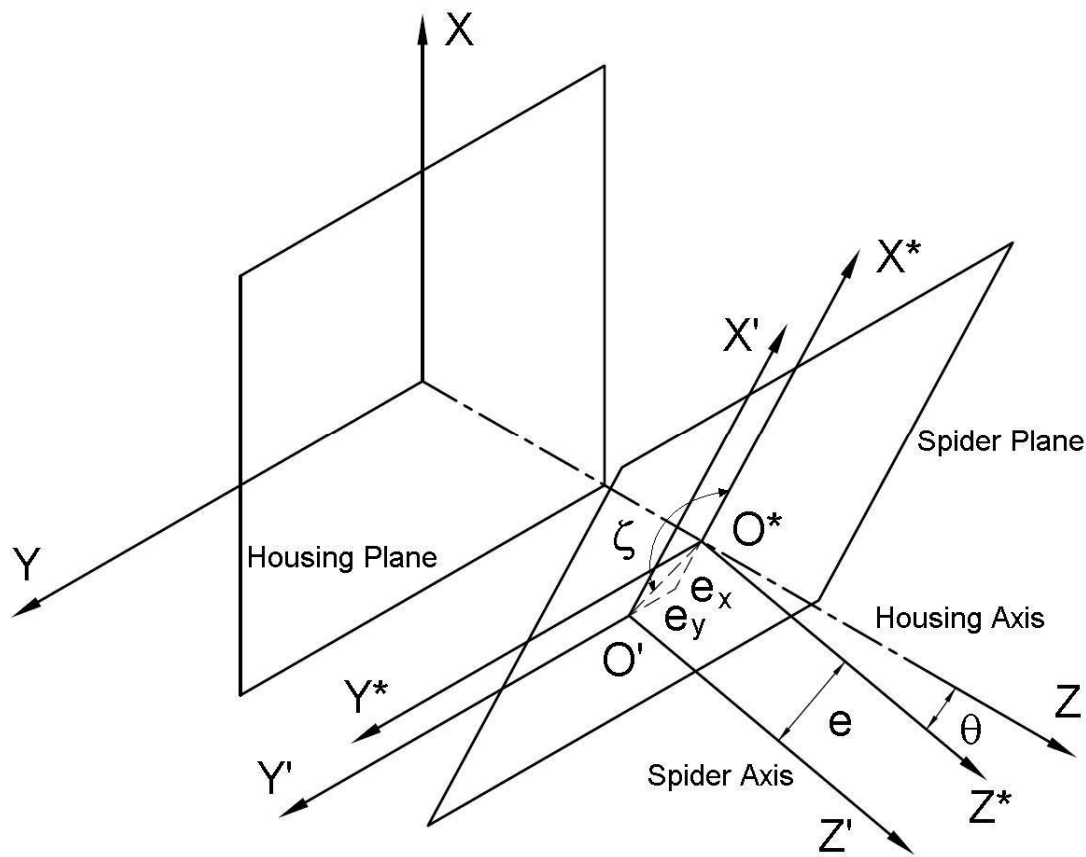


Figure 2.4. Fixed and mobile coordinate frames

Neither φ nor ψ are constants, the derivatives of Eq. (2.1) with respect to time clearly indicate that the variations between input and output displacements translate into the variations between input and output angular velocities. Such variation has little influence in the displacements of the spherical rollers during normal operation conditions in most commercial applications (typically, joint angle is below 25deg). This problem has been treated in detail by Akbil and Lee [7-8] and by Mariot and K'Nevez [9] and will be discussed in the following subsections. Both investigations lead to the same equations of motion.

2.4 Spherical roller positions

When the tripod joint is angulated an eccentricity e of the spider center with respect to the housing axis is generated since the pivoting point is not the center of the spider (Figure 2.3 and Figure 2.4). The magnitude of such eccentricity, O^*O' , is [2, 5, 7, 9].

$$e = \frac{a(1 - \cos \theta)}{2 \cos \theta} \quad (2.2)$$

This eccentricity when projected on the X^* and Y^* axes has the components

$$e_x = e \cos(\pi - \xi) \quad (2.3)$$

$$e_y = e \sin(\pi - \xi) \quad (2.4)$$

where ξ is the angular displacement of O^*O' with respect to X^* . Because of the symmetry of the tripod joint, the orientation of O^*O' with respect to X^* will repeat three times per revolution. The expression relating rotation of the spider and angular displacement of the eccentricity vector O^*O' is [4],

$$\xi = 3\psi - \pi \quad (2.5)$$

Then, Eqs. (2.3) and (2.4) can be rewritten as a function of spider rotation

$$e_x = -\frac{a(1 - \cos \theta)}{2 \cos \theta} \cos 3\psi \quad (2.6)$$

$$e_y = -\frac{a(1 - \cos \theta)}{2 \cos \theta} \sin 3\psi \quad (2.7)$$

When the joint rotates, the eccentricity previously described causes an orbiting motion of the spider. Position of the spider center with respect to the fixed reference frame is [7],

$$x = e(\sin 3\psi \sin(\varphi - \psi) - \cos \theta \cos 3\psi \cos(\varphi - \psi)) \quad (2.8)$$

$$y = e(-\sin 3\psi \cos(\varphi - \psi) - \cos \theta \cos 3\psi \sin(\varphi - \psi)) \quad (2.9)$$

and the position of the center of the spherical rollers with respect to the fixed reference frame is given by [7]

$$Z_i = (a/2)(2\cos\psi_i + (1 - \cos\theta)\cos 3\psi)\tan\theta + z \quad (2.10)$$

$$z = b(\cos\theta_o - \cos\theta) + c_o \quad (2.11)$$

for $i = 1, 2, 3$, where “ z ” is the position of O' with respect to the fixed reference frame in the Z -direction, c_o is the initial stroke position of the spider (axial position) and θ_o is the joint angle when $\varphi = 0$. These initial conditions correspond to the stroke-angle position of the joint, a function of the suspension and steering motions in an automobile. It is assumed in this work that the tripod joint will be coupled to a fixed-center type constant velocity (C/V) joint, through the spider shaft. A fixed-center C/V joint can be simplified as a spherical joint. The case when two tripod joints are coupled has been studied by Mariot and K'Nevez [9] and will not be considered here.

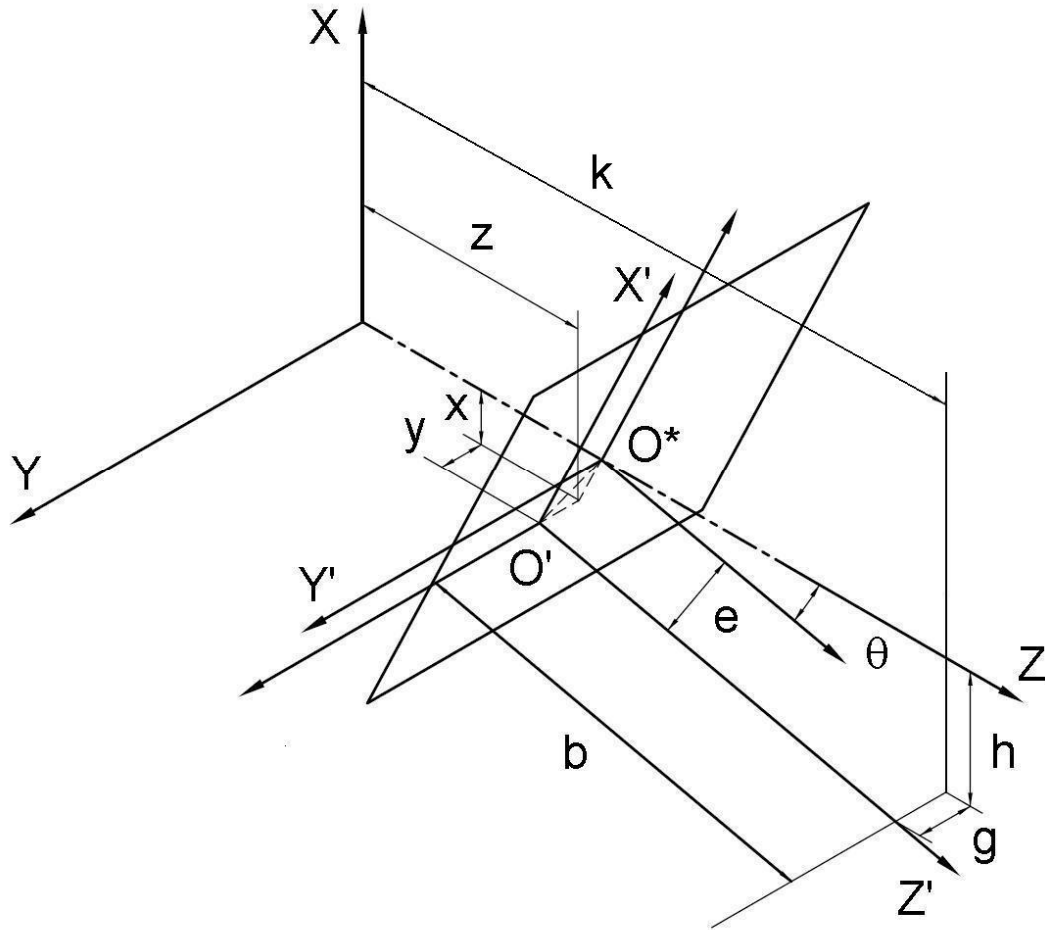


Figure 2.5. Coordinates and orientation of spider shaft

The position of the end of the shaft that is coupled to the spherical joint can be identified as point $P(h,g,k)$. The length of spider shaft or distance from the spider center to the spherical joint center is defined as distance b . At the same time the orientation of the shaft can be defined by three direction angles, α , β , θ , with respect to the fixed coordinate system X - Y - Z (Figure 2.5). Then, the direction cosines of Z' (spider axis) are

$$\cos \alpha = (h - x) / b \tag{2.12}$$

$$\cos \beta = (g - y) / b \quad (2.13)$$

$$\cos \theta = (k - z) / b \quad (2.14)$$

If g , h and b are treated as independent variables, k may be obtained by simple trigonometry. Eqs. (2.12), (2.13) and (2.14) can be combined with Eqs. (2.8) and (2.9), which is simplified to get

$$h^2 + g^2 = (b \sin \theta + e \cos \theta \cos 3\psi)^2 + (e \sin 3\psi)^2 \quad (2.15)$$

Then, Eq. (2.2) can be substituted into Eq. (2.15) and solved numerically for θ . An important expression that relates the input and output angular displacements, derived by Akbil and Lee [7-8], is

$$\tan(\varphi - \psi) = \cos \beta / \cos \alpha \quad (2.16)$$

Eq. (2.16) can be solved for φ , numerically, by substituting Eqs. (2.12), (2.13), (2.8) and (2.9) and using the value of θ obtained from solving Eq. (2.15). The radial position of the ball centers, with respect to the spider center is given by [4, 6]

$$r_i = \frac{a}{2} \left(\frac{(1 + \cos \theta)}{\cos \theta} + \frac{2(1 - \cos \theta)}{\cos \theta} \cos 2\psi_i \right) = a + e(1 + 2 \cos 2\psi_i) \quad (2.17)$$

for $i = 1, 2, 3$

Therefore, the displacement of the spherical roller center is

$$f_i = e(1 + 2\cos 2\psi_i) \quad (2.18)$$

for $i = 1, 2, 3$

2.5 Numerical examples of spherical roller positions and displacements

It is interesting to note that Eqs. (2.17) and (2.18) indicate that spherical roller positions depend only on joint angle (orientation of spider shaft), BCD and rotational displacement of the joint. The reader is reminded that variable a is defined as half of the BCD . A computer program was written to perform calculations. The code was debugged by verifying the outputs with the numerical results of the examples published by Akbil and Lee [8]. Graphics and numerical values in this and subsequent sections were obtained using the characteristics of the actual tripod joint design that will be used to do the experimental portion of this work, unless otherwise indicated. The joint characteristics are:

Nominal BCD	=	40.8mm
Shaft length	=	300mm
Maximum functional angle	=	23°
Trunnion diameter	=	20.97mm
Needle roller diameter	=	1.9975mm
Number of needles (n)	=	36

Spherical roller outer diameter = 34.942mm

Figure 2.6 describes the fluctuation of joint angle in a revolution, when the joint is operating at a nominal joint angle θ_o of 23° , and was obtained solving Eq. (2.15). The coordinates of the center of the spherical joint were obtained using Eqs. (2.19) and (2.20).

$$h = -b \sin \theta_o - \frac{a}{2} (1 - \cos \theta_o) \quad (2.19)$$

$$k = \sqrt{b^2 - g^2 - h^2} \quad (2.20)$$

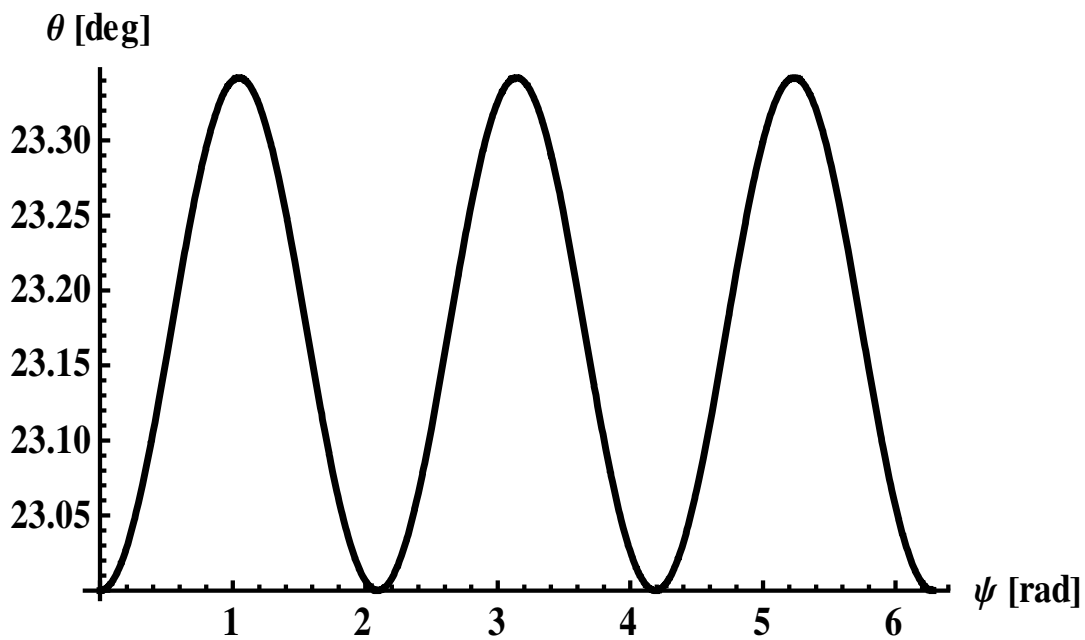


Figure 2.6. Fluctuation of joint angle in a revolution

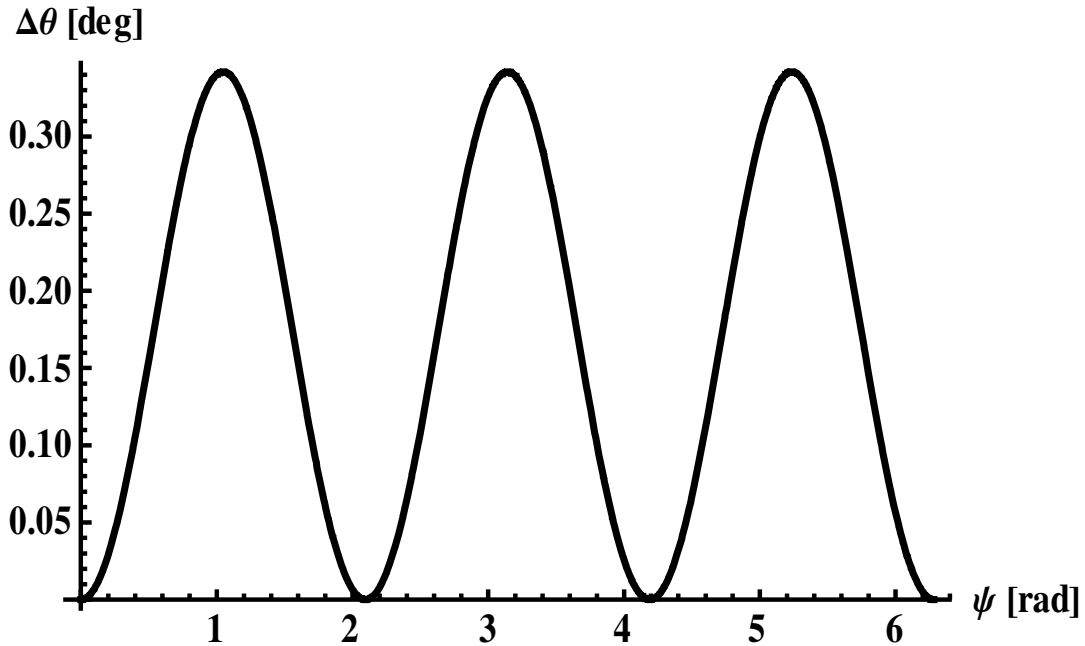


Figure 2.7. Deviation from nominal angle in a revolution

Figure 2.7 was obtained from Eq. (2.21), which represents the angle variation with respect to the nominal joint angle.

$$\Delta\theta = \theta - \theta_0 \quad (2.21)$$

Figure 2.8 represents the spider orbiting path and was obtained by generating a parametric plot of e_x versus e_y where ψ is the parameter. The dashed line represents the orbiting path neglecting joint angle fluctuation ($\psi = \varphi$), while the solid line represents the orbiting path including joint angle fluctuation $\Delta\theta$. Orbiting path on spider plane is a circle.

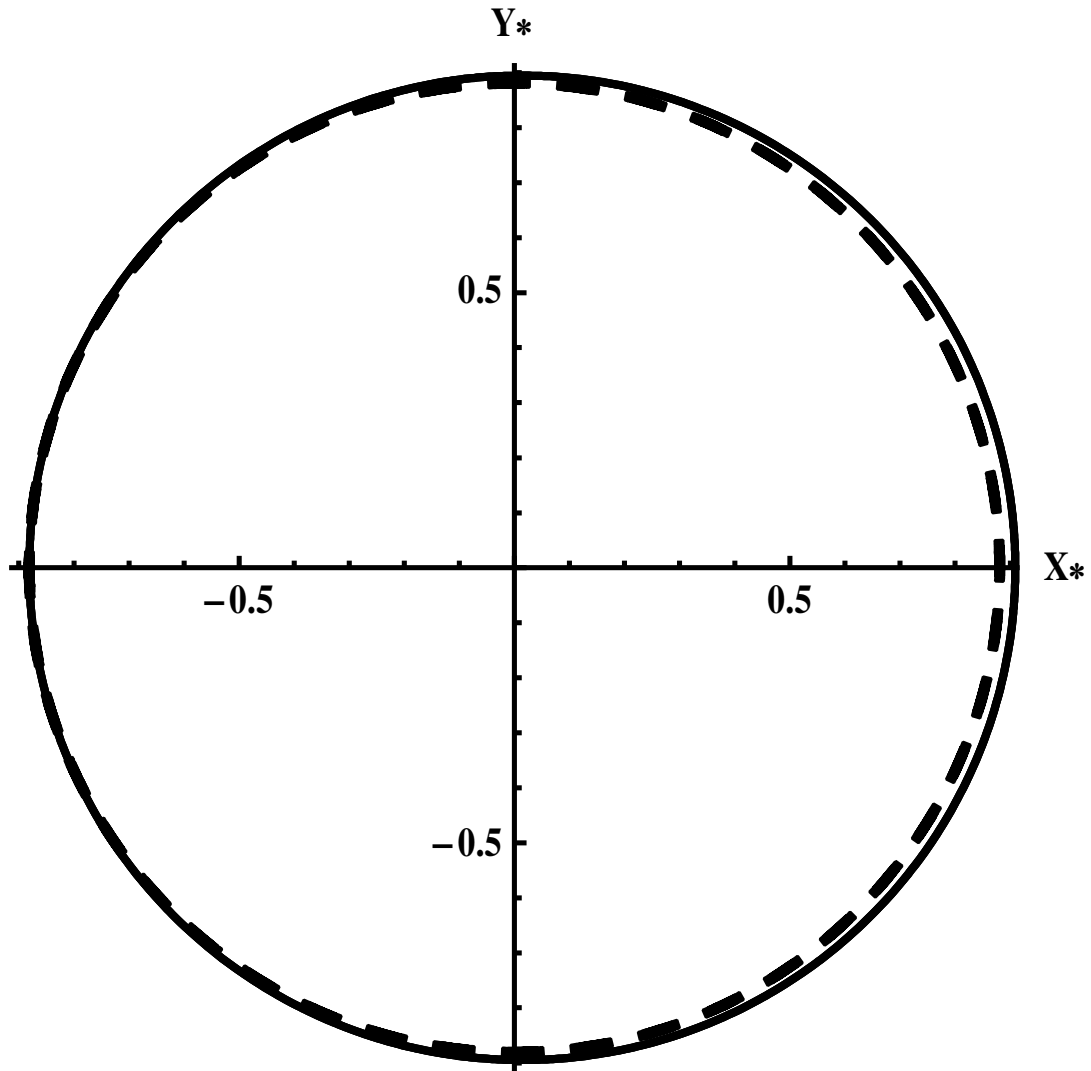


Figure 2.8. Orbiting path of spider on spider plane

Figure 2.9 was obtained from solving simultaneously Eqs. (2.2) and (2.15). If joint angle fluctuation $\Delta\theta$ was ignored the function plotted in Figure 2.9 would be a straight horizontal line.

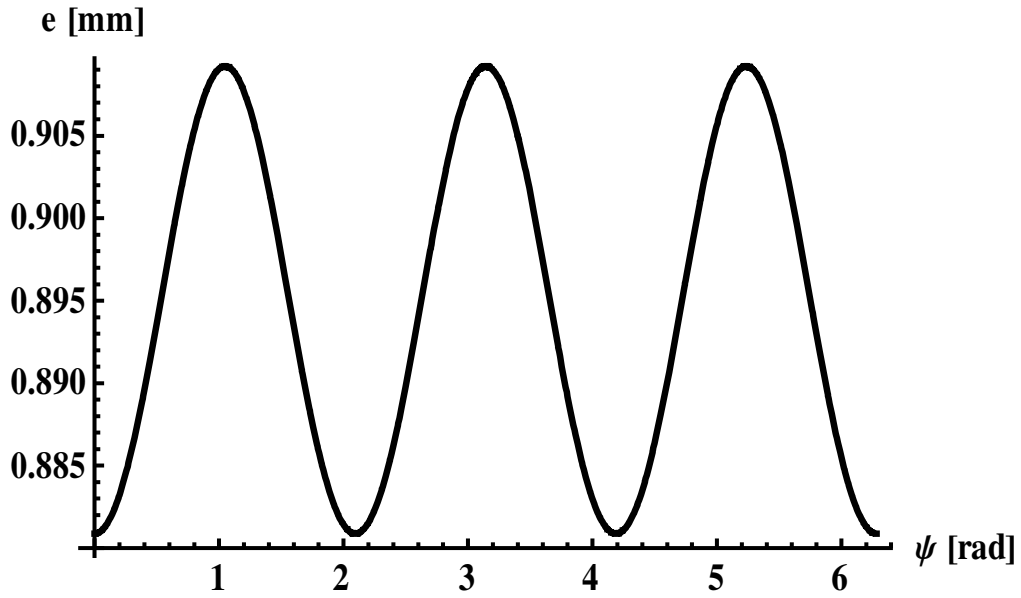


Figure 2.9. Fluctuation of eccentricity within a revolution

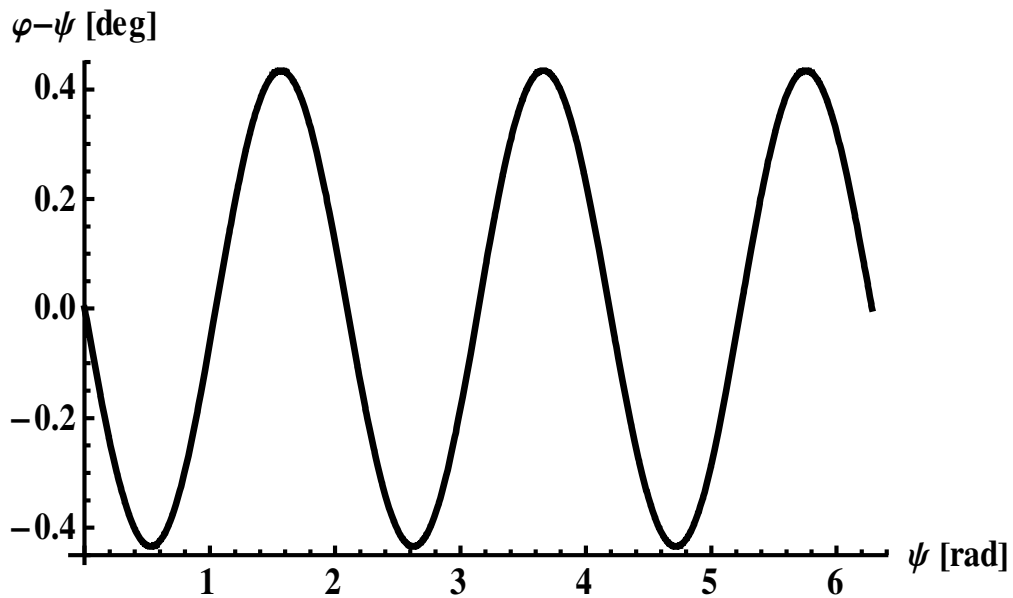


Figure 2.10. Difference between input and output angular displacements

Figure 2.10 is obtained solving Eq. (2.16). It shows the difference between input and output angular displacements caused by joint angle fluctuation $\Delta\theta$. From Figure

2.10 it can be observed that the joint behaves as a true C/V joint at six specific positions within a revolution. Such positions are $\psi = n\pi/3$, where $n = 0, 1, 2, \dots, \infty$.

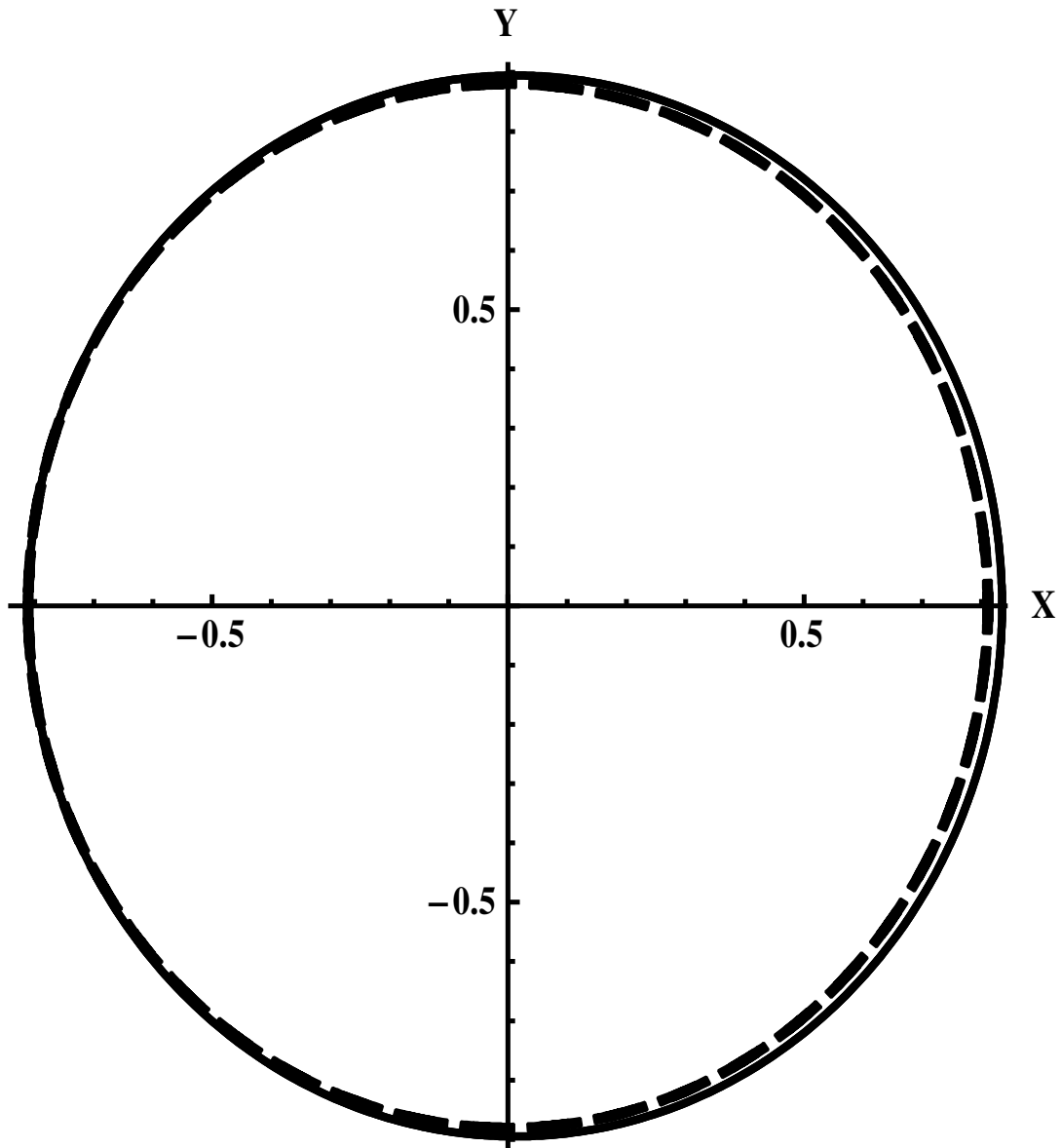


Figure 2.11. Orbiting path of spider on housing plane

Figure 2.11 represents the spider orbiting path on the housing plane. It was obtained generating a parametric plot of x versus y where ψ is the parameter. The

dashed line represents the orbiting path neglecting joint angle fluctuation ($\psi = \phi$), while the solid line represents the orbiting path including joint angle fluctuation $\Delta\theta$. Orbiting path on housing plane is an ellipse.

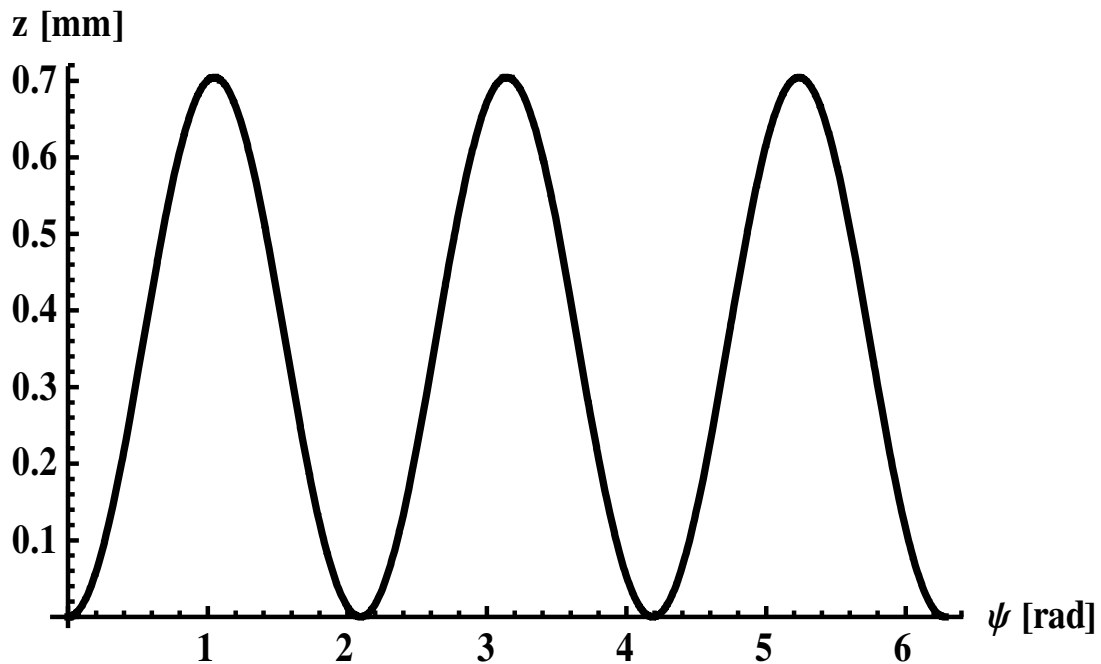


Figure 2.12. Variations of the axial displacement of the spider center

Figure 2.12 describes the movement of the spider center along axis Z, when the joint is operating at a nominal joint angle θ_o of 23° . It was obtained solving Eq. (2.11). Similarly, Figure 2.13 was obtained solving Eq. (2.10).

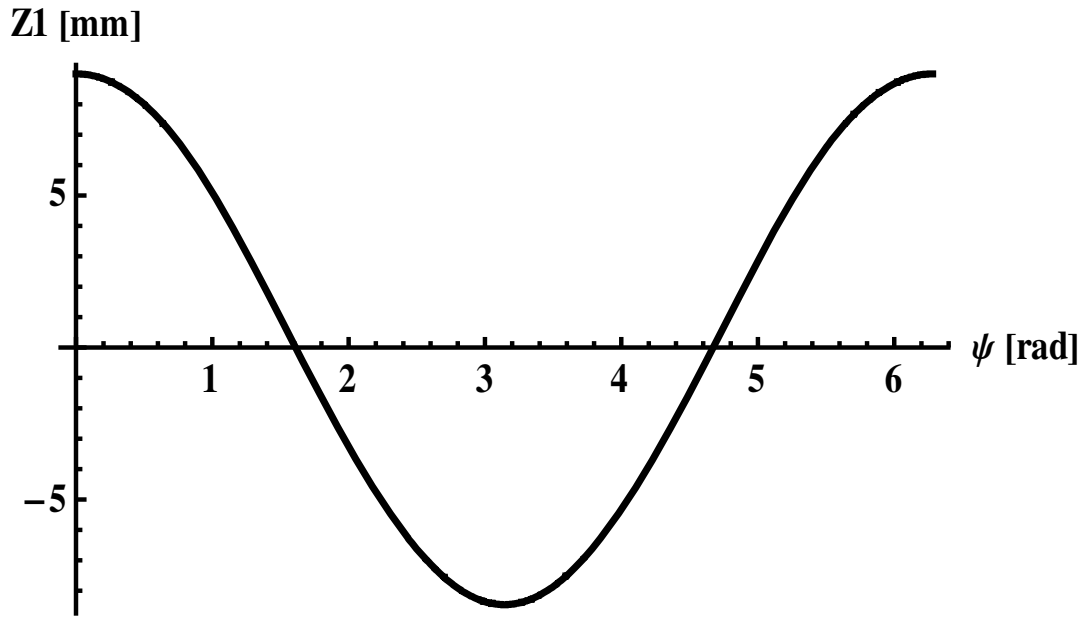


Figure 2.13. Displacement of the spherical roller center along ball bore axis

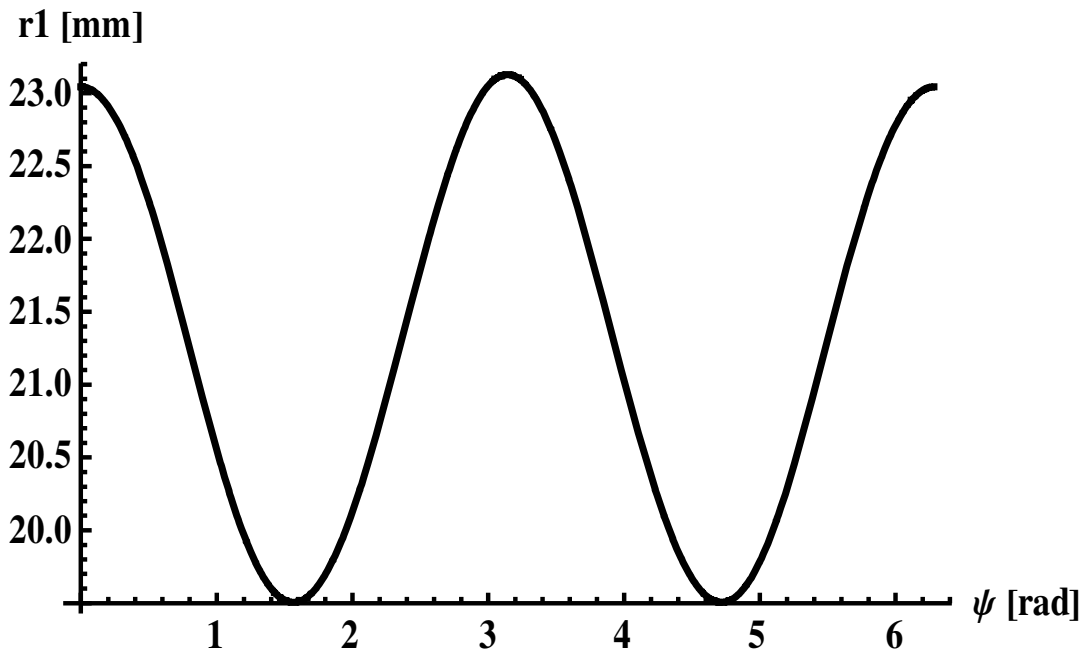


Figure 2.14. Radial position of the spherical roller center, from spider center

Figure 2.14 represents the radial position of ball center with respect to the spider center. It was obtained solving Eq. (2.17). The position at zero joint angle would be half of the BCD , $a = 20.4\text{mm}$.

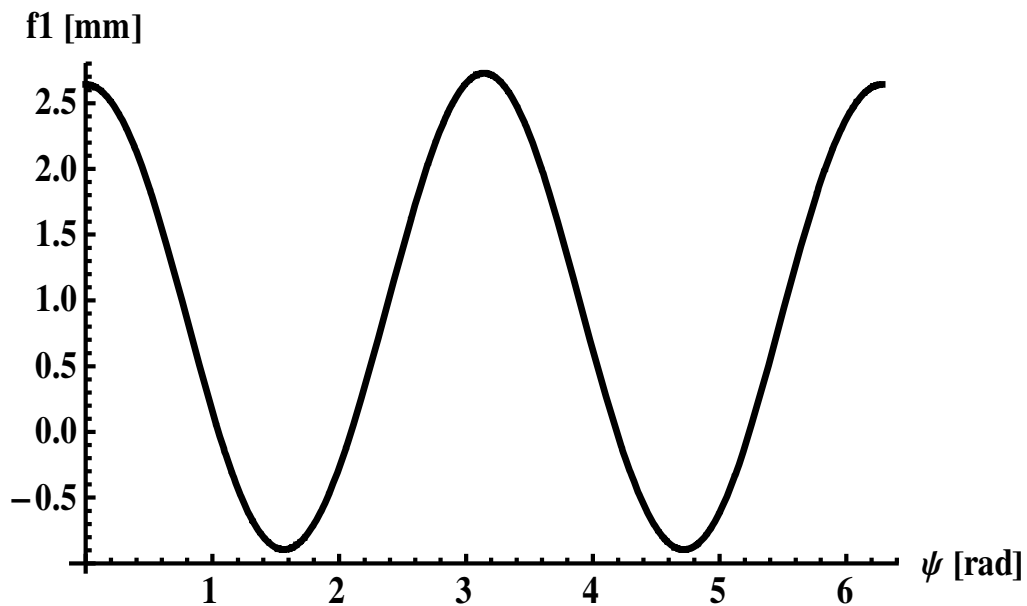


Figure 2.15. Radial displacement of the spherical roller center, along trunnion axis

Figure 2.15 represents the displacement of the ball center along the trunnion with respect to its “zero” position, which is defined then $r_j = a$. It was obtained solving Eq. (2.18).

2.6 Needle roller positions and displacements

There is no published work about needle roller positions and displacements within a tripod joint. Motion of spherical rollers (balls) causes rolling and sliding motion of

needle rollers on contacting trunnions. A cylindrical coordinate system $U_i - \Phi_i - V_i$, whose origin is O' , can be defined for each trunnion, $i = 1, 2, 3$. Axis V_i is a spider ray and Φ_i is measured positive from the spider plane around V_i in a CCW direction, as shown in Figure 2.16. Variable ϕ_{ij} , also shown in Figure 2.16, defines the angular position of each needle roller, labeled $j = 1, 2, 3, \dots, n$. It is assumed that needles are uniformly spaced around the trunnion and clearance between them is neglected. On the other hand, interference is not allowed by design.

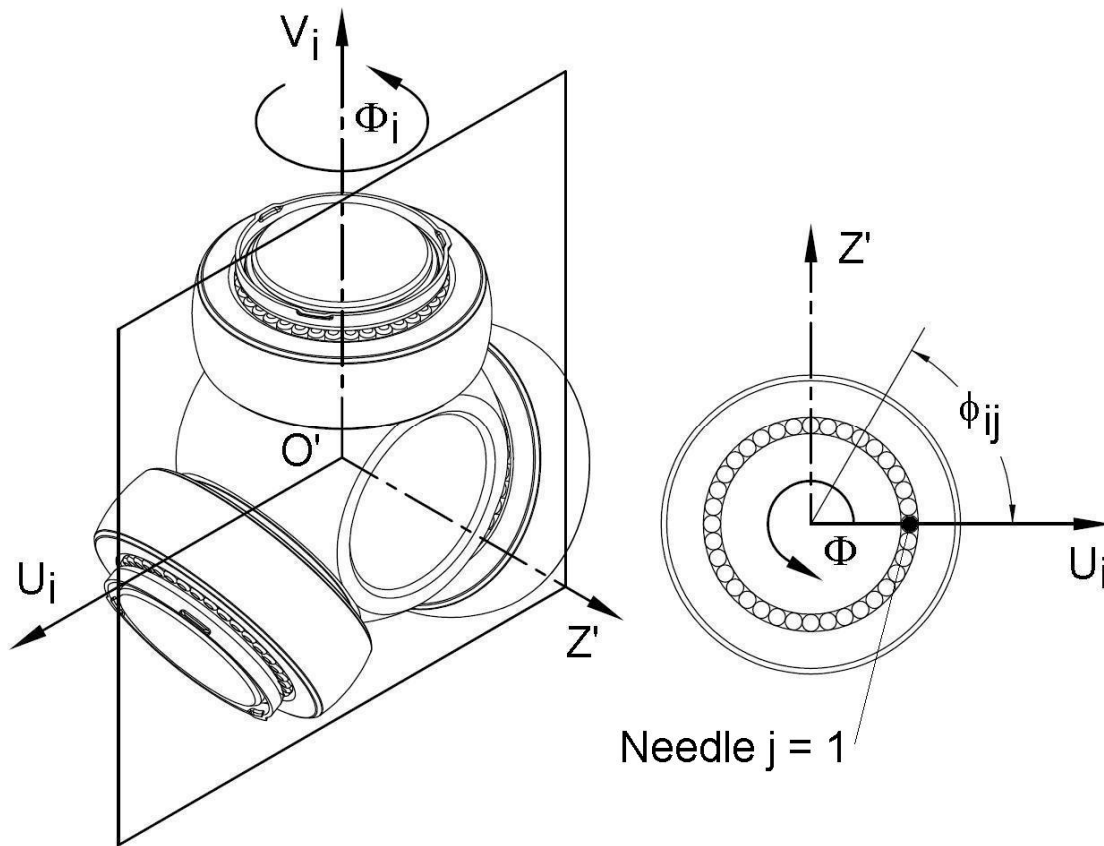


Figure 2.16. Trunnion, local cylindrical coordinate system

A secondary housing reference frame, $X_i^H - Y_i^H - Z_i^H$, and a secondary spider reference frame, $X_i^S - Y_i^S - Z_i^S$, which rotate together with the joint are also defined. Axis Z_i^H is always parallel to axis Z and axis Z_i^S is always parallel to axis Z' (Figure 2.17).

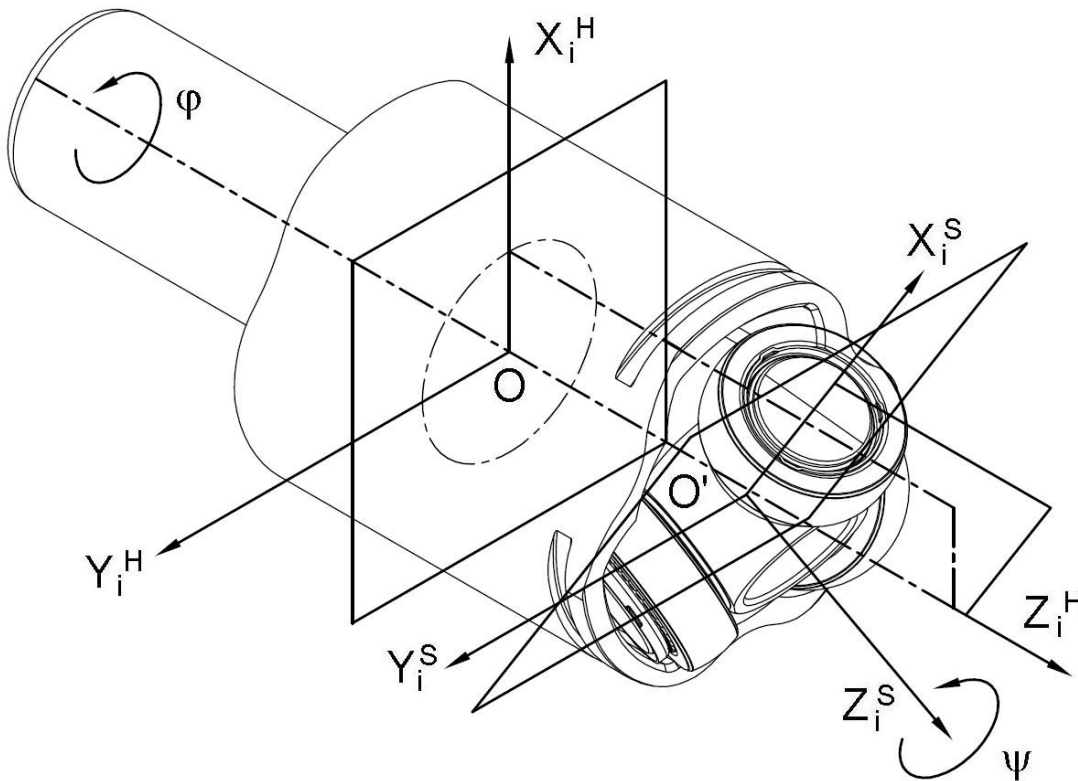


Figure 2.17. Secondary-rotating coordinate systems

To define the angular position of a needle on a trunnion, it is necessary to know the amount of rolling of the spherical roller (ball) due to translation of its center along ball bore axis. If the rolling axes of spherical rollers were parallel to housing rays, there would be pure rolling motion, no sliding. On the other hand, if they were perpendicular there would be pure sliding, no rolling at all. In a tripod joint, spider rays are the rolling axes of spherical rollers and they are neither parallel, with the exception of few specific

positions, nor perpendicular to housing rays. Ball rolling is a function of trunnion axis inclination, relative to the housing plane, measured on an auxiliary plane formed by vectors \mathbf{X}_i^S and \mathbf{Z}_i^H since ball rolling can only occur around axis \mathbf{X}_i^S and ball translation along ball bore can only occur on \mathbf{Z}_i^H direction. The orientation of the trunnion axis \mathbf{X}_i^S is defined by the direction angles $\kappa_i, \lambda_i, \mu_i$, measured from $\mathbf{X}_i^H, \mathbf{Y}_i^H$ and \mathbf{Z}_i^H , respectively. Trunnion axis inclination with respect to plane $X_i^H-Y_i^H$ is identified by angle δ_i and is measured on auxiliary plane $X_i^S-Z_i^H$, as previously indicated.

To calculate the angles formerly mentioned the orientation matrix developed by K'Nevez, Mariot and Diaby [10] (obtained using different reference frames) is modified such that orientation can be described with respect to the reference frames used in this work. Modification consisted of adding a $\pi/2$ phase to the input and output angular displacements. After some algebraic and trigonometric manipulation the matrix that defines orientation of the spider reference frame $X_i^S-Y_i^S-Z_i^S$ with respect to the housing reference frame $X_i^H-Y_i^H-Z_i^H$ can be written as,

$${}^i \mathbf{A} = \begin{pmatrix} \cos \theta \cos \varphi \cos \psi + \sin \varphi \sin \psi & \cos \theta \cos \varphi \sin \psi - \cos \psi \sin \varphi & \cos \varphi \sin \theta \\ \cos \theta \sin \varphi \cos \psi - \cos \varphi \sin \psi & \cos \theta \sin \varphi \sin \psi + \cos \varphi \cos \psi & \sin \theta \sin \varphi \\ -\cos \psi \sin \theta & -\sin \theta \sin \psi & \cos \theta \end{pmatrix}$$

where $\psi = \psi_i$ and $\varphi = \varphi_i$; for $i = 1, 2, 3$ (2.22)

To calculate the direction angles of spider rays the dot products between unit vector \mathbf{X}_i^S and unit vectors \mathbf{X}_i^H , \mathbf{Y}_i^H , \mathbf{Z}_i^H , are obtained

$$\mathbf{X}_i^S = \begin{bmatrix} \cos \theta \cos \varphi_i \cos \psi_i + \sin \varphi_i \sin \psi_i \\ \cos \theta \cos \varphi_i \sin \psi_i - \cos \psi_i \sin \varphi_i \\ \cos \varphi_i \sin \theta \end{bmatrix}^T \quad (2.23)$$

$$\mathbf{X}_i^H = [1 \ 0 \ 0] \quad (2.24)$$

$$\mathbf{Y}_i^H = [0 \ 1 \ 0] \quad (2.25)$$

$$\mathbf{Z}_i^H = [0 \ 0 \ 1] \quad (2.26)$$

$$\cos \kappa_i = \cos \theta \cos \varphi_i \cos \psi_i + \sin \varphi_i \sin \psi_i \quad (2.27)$$

$$\cos \lambda_i = \cos \theta \cos \varphi_i \sin \psi_i - \cos \psi_i \sin \varphi_i \quad (2.28)$$

$$\cos \mu_i = \cos \varphi_i \sin \theta \quad (2.29)$$

Using simple trigonometry, angle δ_i may be related to the complementary angle of μ_i .

$$\cos \delta_i = \sqrt{1 - (\cos \mu_i)^2} \quad (2.30)$$

$$\delta_i = \pi/2 - \mu_i \quad (2.31)$$

Even though Eqs. (2.30) and (2.31) are equivalent, only Eq. (2.31) can indicate on which side of the housing plane (positive or negative Z_i^H) the trunnion is located (Figure 2.18 and Figure 2.19).

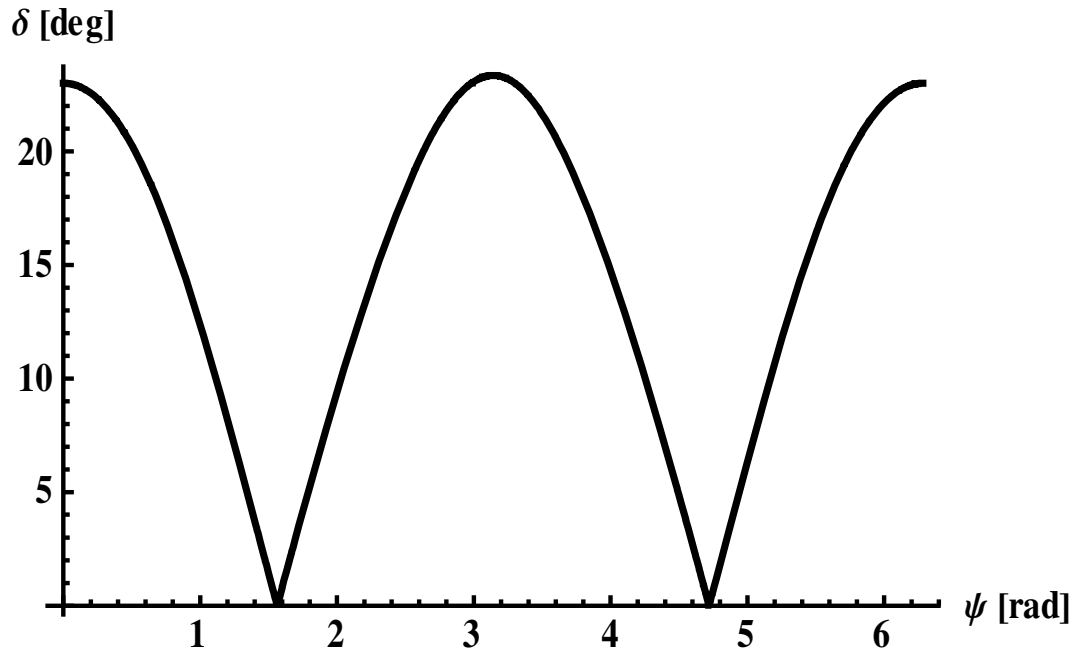


Figure 2.18. Angle δ , per Eq. (2.30)

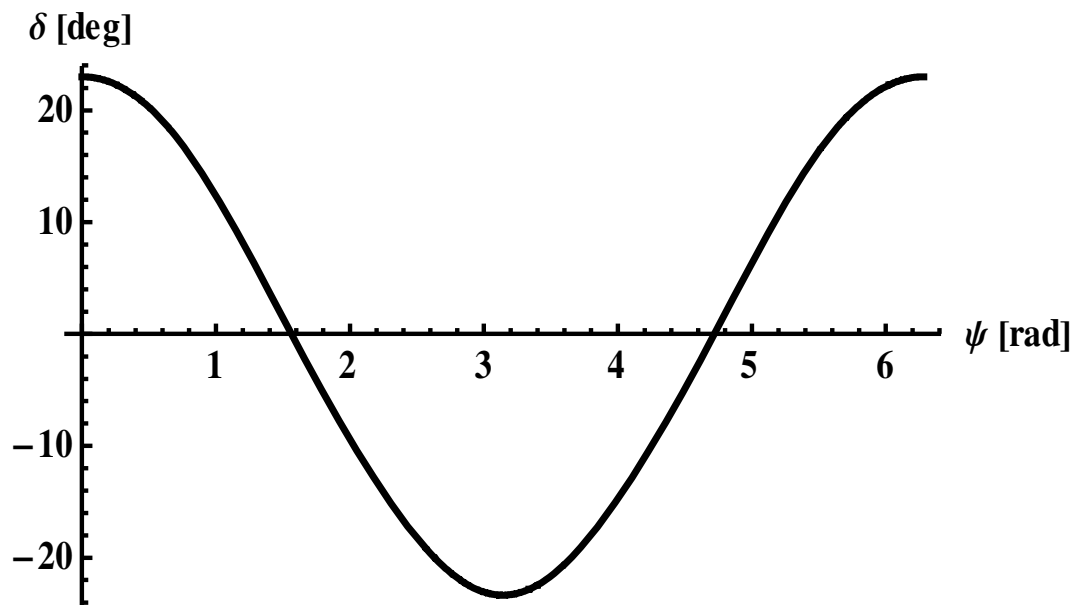


Figure 2.19. Angle δ , per Eq. (2.31)

When the spherical roller is tilted only a fraction of the distance traveled along the housing ball bore will cause rolling (Figure 2.20). More tilting means less rolling. In the case of constant inclination, the arch length displaced at the outer diameter of the spherical roller can be obtained from Eq. (2.32), which is valid only if there is contact, all the time, between spherical roller and housing ball bore.

$$s_i = Z_i \cos \delta_i \quad (2.32)$$

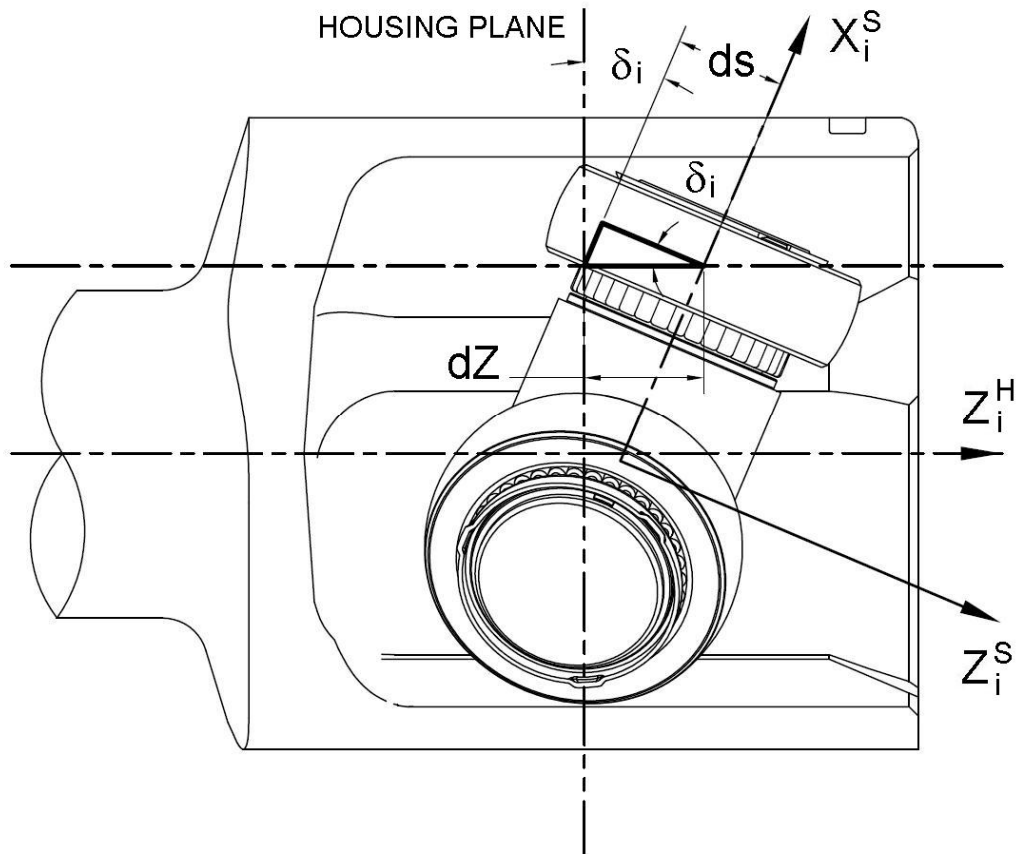


Figure 2.20. Partial rolling of ball due to tilting

However, in a tripod joint, angle δ_j is not constant (Figure 2.19) during the whole Z_j displacement. Therefore, a differential approach has to be followed and Eq. (2.32) can be rewritten as Eq. (2.33). If Eqs. (2.29) and (2.30) are substituted into Eq. (2.33) then Eq. (2.34) is obtained.

$$ds_j = dZ_j \cos \delta_j \quad (2.33)$$

$$ds_j = dZ_j \sqrt{1 - (\cos \varphi_j \cos \theta)^2} \quad (2.34)$$

Variable Z_j is a function of angular displacement ψ_j and joint angle θ . Let's consider a simple case for the sake of clarity. Assume that the initial position of the spider in Figure 2.20 is the position where the origin of the spider reference frame coincides with the origin of the housing reference frame. This can only happen when joint angle θ is zero. Then, without rotating the joint ($\psi_j = \varphi_j = 0$) change joint angle θ from 0 to θ_o (if $\varphi_j = 0$, then $\delta_j = \theta_o$). When the spherical roller starts to displace, tilting angle will be very small and its effect in ball rolling could be discarded but as joint angle gets closer to θ_o tilting will impact ball rolling. If the actual ball rolling wants to be known Eq. (2.34) has to be integrated from zero joint angle to actual joint angle, for a given rotational (angular) displacement ψ_j of the spider. Differential dZ_j can be obtained from Eqs. (2.10) and (2.11).

$$dZ_j = \frac{\partial Z_j}{\partial \theta} d\theta + \frac{\partial Z_j}{\partial \psi_j} d\psi_j + \frac{\partial Z_j}{\partial \theta_o} d\theta_o \quad (2.35)$$

Where $d\psi_i = 0$, since dZ_i will be evaluated for a specific displacement ψ_i . Thus, Eq. (2.34) becomes

$$\int_0^{s_i} ds_i = \int_0^{\theta(\psi_i, \theta_o\text{-max})} \left(\frac{\partial Z_i}{\partial \theta} \sqrt{1 - (\cos \varphi_i \cos \theta)^2} \right) d\theta \quad (2.36)$$

$$+ \int_0^{\theta_o\text{-max}} \left(\frac{\partial Z_i}{\partial \theta_o} \sqrt{1 - (\cos \varphi_i \cos \theta(\psi_i, \theta_o))^2} \right) d\theta_o$$

and the partial differentials contained in Eq. (2.36) are,

$$\frac{\partial Z_i}{\partial \theta} = \frac{1}{2} a(2 \cos \psi_i + (1 - \cos \theta) \cos 3\psi_i) \sec^2 \theta \quad (2.37)$$

$$+ b \sin \theta + \frac{1}{2} a \cos 3\psi_i \sin \theta \tan \theta$$

$$\frac{\partial Z_i}{\partial \theta_o} = -b \sin \theta_o \quad (2.38)$$

Eq. (2.36) can be evaluated numerically to calculate s_i . Displacement s_i follows the same trend that Z_i , as expected (Figure 2.13 and Figure 2.21). On the other hand, the difference between Z_i and s_i is maximum at the points where angle δ_i is maximum, and zero (Figure 2.22) where δ_i is zero, which is the condition when the spherical roller doesn't displace along the ball bore.

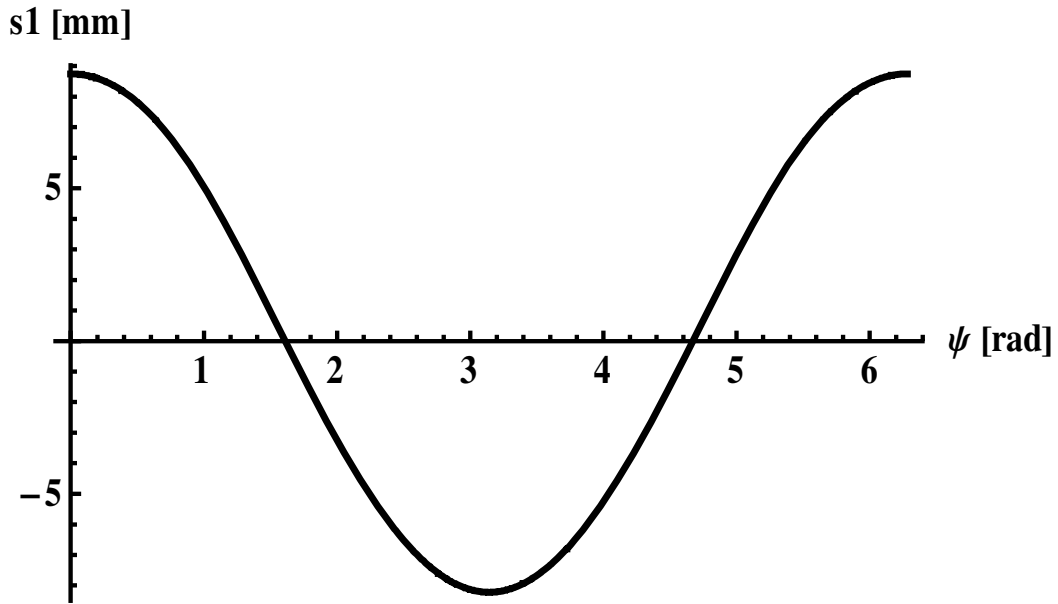


Figure 2.21. Actual arch displaced at ball outer diameter

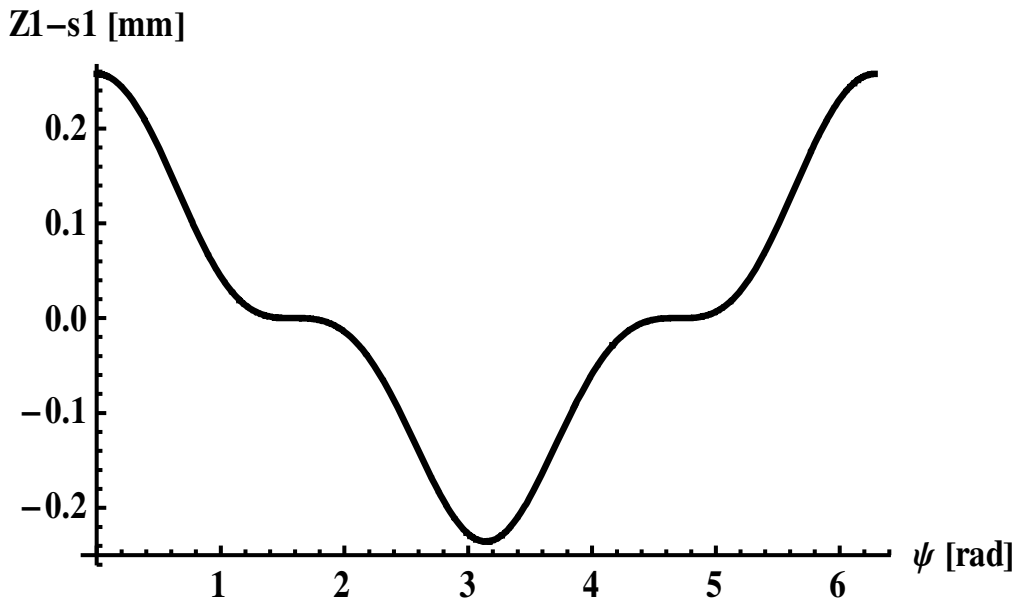


Figure 2.22. Difference in arch displacement without and with ball tilting effect

Before proceeding to calculate angles ϕ_{ij} , there is an additional component that must be taken into account due to the change of orientation of the spider axis within a

revolution. Let's consider another simple case. When angular displacement $\psi_j = \pi/2$ the spherical roller will not move along the ball bore. However, there will be an angle between the plane that passes through $\phi_{i1} = 0$ and a plane parallel to the housing plane that passes through the point of contact between ball and ball bore (Figure 2.23). Needle $j = 1$ is the needle that is located at ϕ_{i1} when joint angle $\theta = 0$ (Figure 2.16).

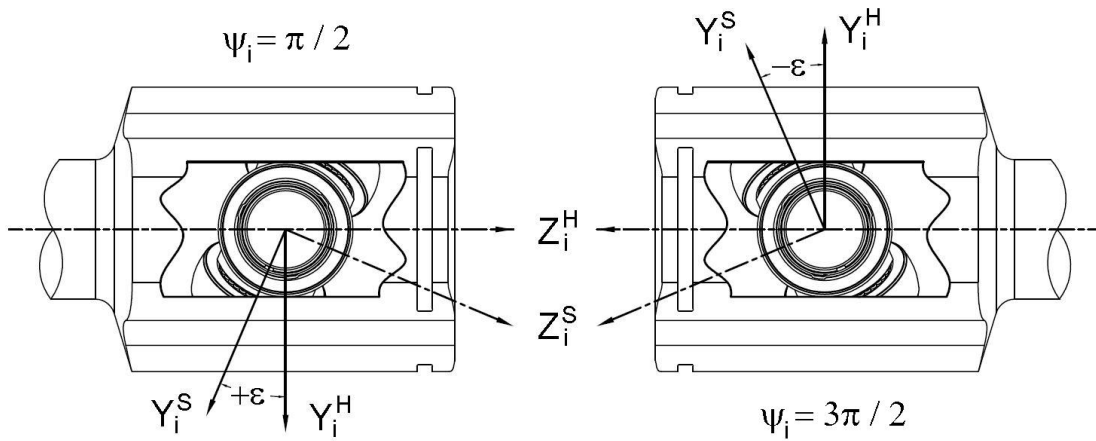


Figure 2.23. Graphical representation of angle ε

The angle formerly mentioned will be named ε_i and can be obtained from calculating the angle between vectors \mathbf{Y}_i^S and \mathbf{Y}_i^H . Thus, the dot product of such vectors is

$$\cos \varepsilon_i = \cos \theta \sin \phi_i \sin \psi_i + \cos \psi_i \cos \phi_i \quad (2.39)$$

Evaluating ε_j numerically, through one revolution, can be observed that only positive angles are obtained (Figure 2.24). Even though this is mathematically correct, it represents a disadvantage. Position of needles on the trunnion depends not only on the magnitude of angle ε_j . Let's consider needle $j=1$. Position ϕ_{i1} of this needle on the trunnion will be a positive number when $\psi_j = \pi/2$ and negative number when $\psi_j = 3\pi/2$, even though magnitude of ε_j is the same at both ψ_j positions (Figure 2.23).

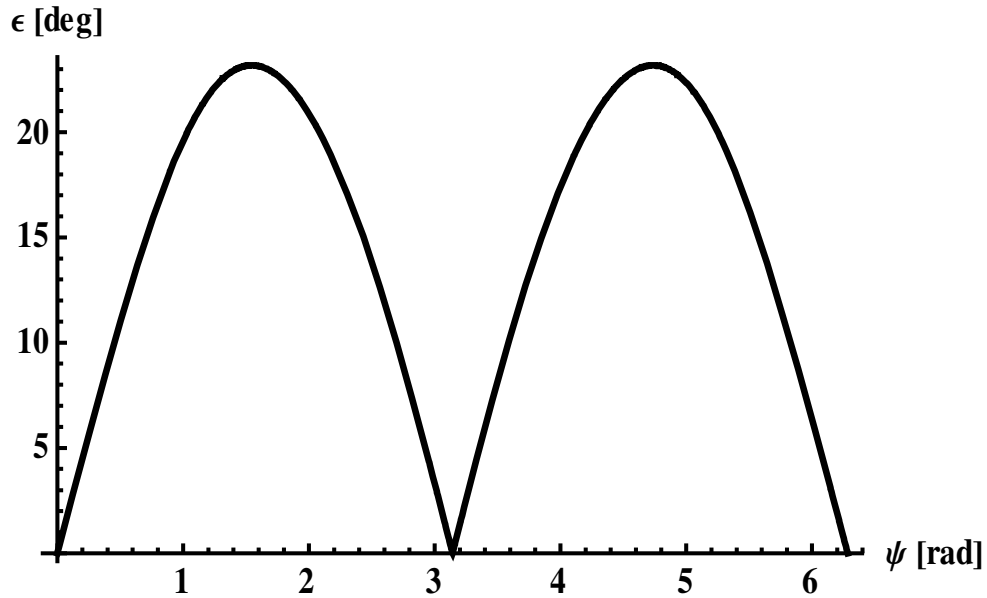


Figure 2.24. Angle ε , per expression (2.39)

To overcome such problem a SIGN function, which depends on ψ_j , can be used. Angle ε_j is redefined as angle ε'_j , which is phase corrected (Figure 2.25).

$$\varepsilon'_j = \text{sign}(\sin \psi_j) \cdot \arccos(\cos \theta \sin \varphi_j \sin \psi_j + \cos \psi_j \cos \varphi_j) \quad (2.40)$$

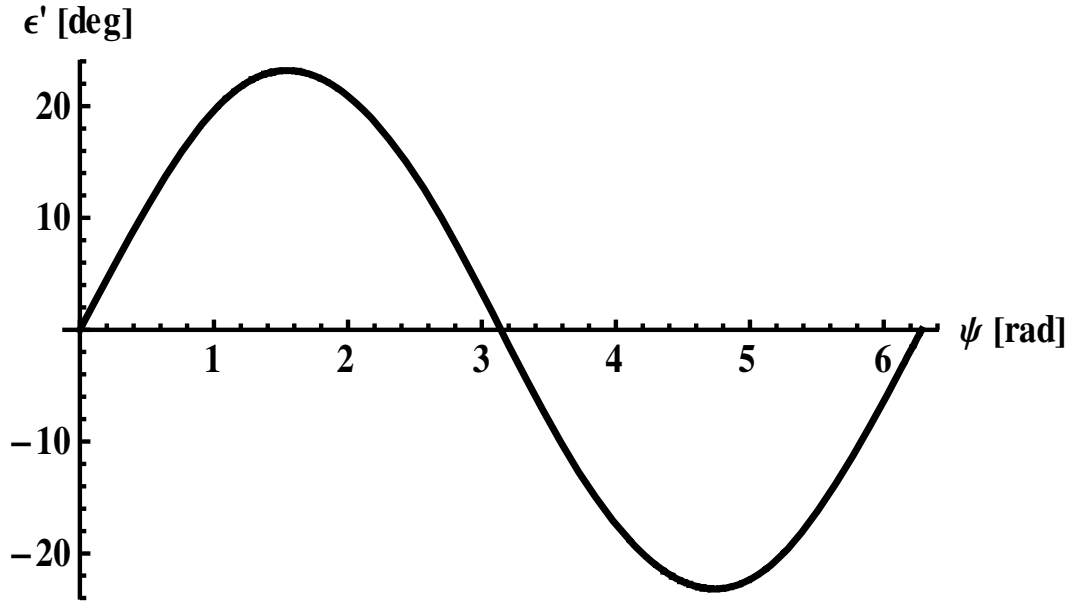


Figure 2.25. Angle ϵ' , per expression (2.40)

Then, after considering the effects of ball tilting and the change in spider orientation, the angular displacement of the contact point between spherical roller (ball) and ball bore, with respect to the local trunnion reference frame, is defined as η_i .

$$\eta_i = \epsilon'_i - \frac{2}{m_o} s_i \quad (2.41)$$

The second term of Eq. (2.41) comes from dividing the arch length displaced, s_i , calculated from Eq. (2.36), by the outer radius of the spherical roller. Eq. (2.41) can also be evaluated numerically and plotted (Figure 2.26).

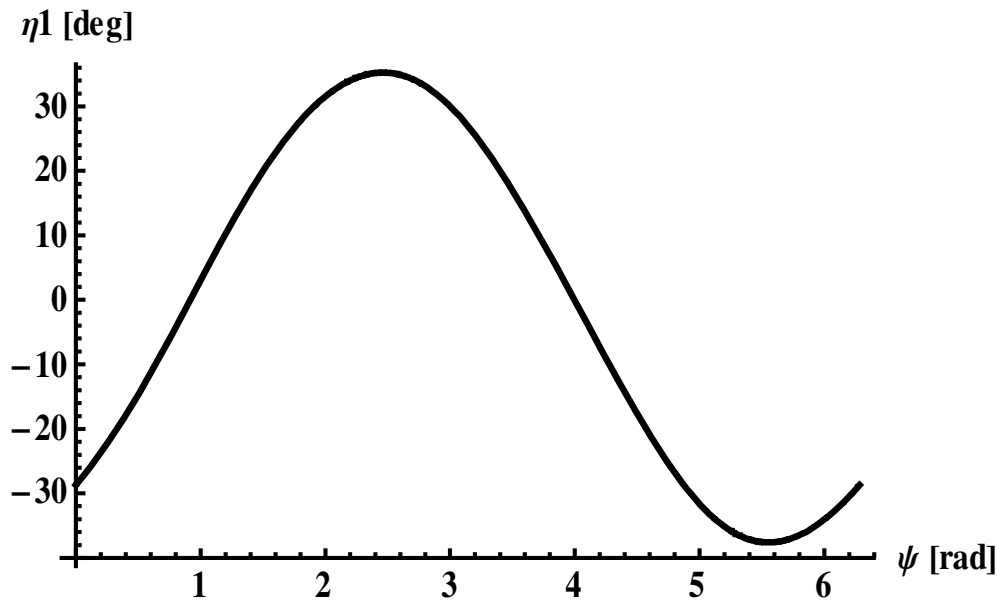


Figure 2.26. Angle η , per expression (2.41)

Relative angular motion between spherical rollers and trunnions will result in needle angular displacements. It is convenient to establish a relationship between the angular displacement of the ball and the angular displacement of the needles, with respect to the local trunnion cylindrical coordinate system $U_i - \Phi_i - V_i$ (Figure 2.16). Assuming contact and no sliding between trunnion, needle rollers and spherical roller (ball), consider the case where a needle roller displaces from position $(B-C)$ to position $(B'-C')$ as a result of an angular displacement η_i of the ball, from point (A) to point (A') . Since no needle sliding around the trunnion was assumed, it can be said (based on kinematic principles of relative motion) that the arch-length of segment $(C-C')$ equals arch-length of segment $(B'-D)$ (Figure 2.27).

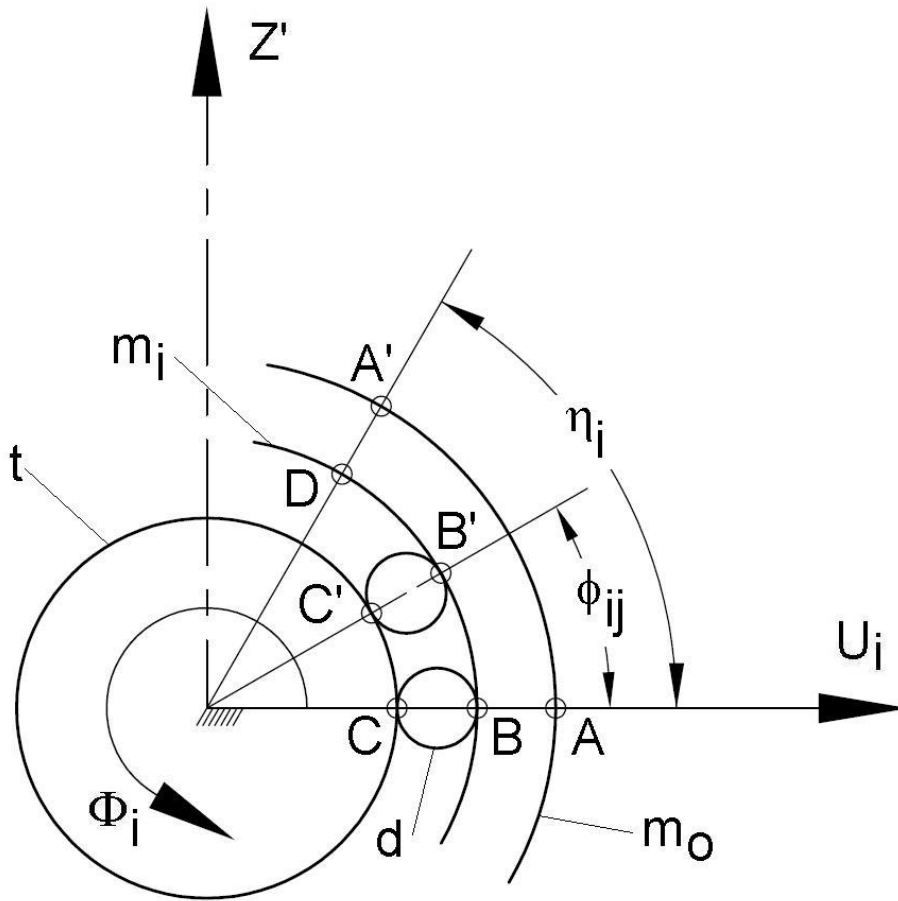


Figure 2.27. Angular displacements and positions in trunnion-rollers set

Diametrical clearance in the trunnion-rollers set can be neglected (as stated in the beginning of this section) for kinematic analysis purposes. Clearance is three to four orders of magnitude smaller than the trunnion diameter. This makes the inner diameter of the ball similar to the trunnion diameter plus two times the needle roller diameter. Thus, the following identities can be generated when initial needle position is zero,

$$m_i \approx t + 2d \quad (2.42)$$

$$\frac{t}{2}\phi_{ij} = \left(\frac{t}{2} + d\right)(\eta_i - \phi_{ij}) \quad (2.43)$$

Isolating position ϕ_{ij} from Eq. (2.43) and adding a term to take into account the initial conditions of needles that are not in a zero position it is obtained,

$$\phi_{ij} = \left(\frac{\frac{t}{2} + d}{t + d}\right) \eta_i + (j-1) \frac{2\pi}{n} \quad (2.44)$$

for $j = 1, 2, 3, \dots, n$

Evaluating Eq. (2.44), numerically, and plotting for the case $i=1$ and $j=1$,

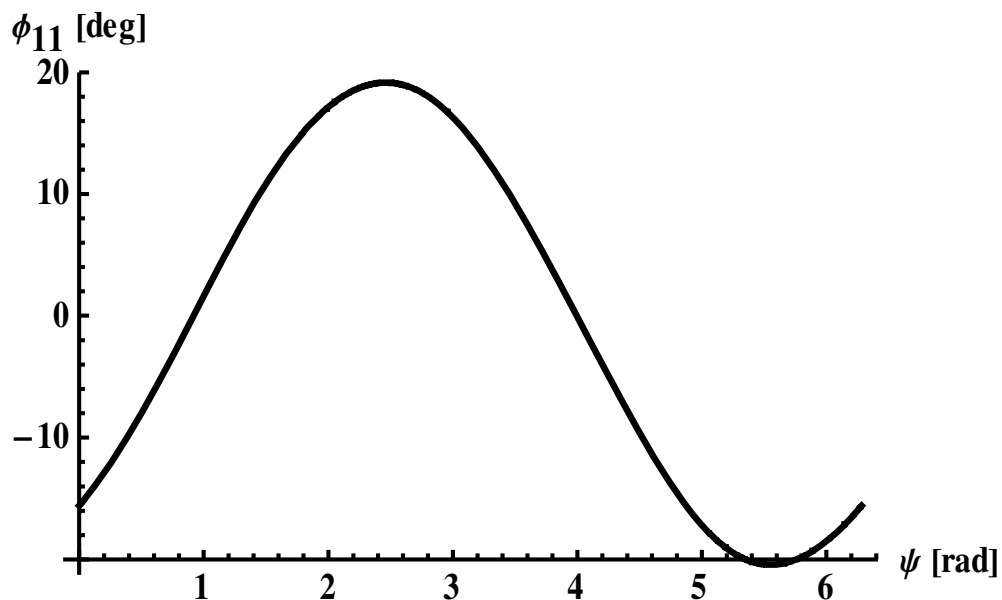


Figure 2.28. Angular position of needle $j = 1$, per expression (2.44)

It must be noted that when $j = 1$, position and displacement are equal in magnitude. Therefore, ϕ_{i1} will be used to refer to needle displacement as well.

2.7 Critical joint angle

Critical joint angle is an important design parameter. In a tripod joint, it is defined as the joint angle that causes a total needle displacement equal to the angular spacing between needles. In other words, critical joint angle is when fatigue cycles duplicate due to more than one needle passing over the same trunnion area in a joint revolution. Given the complexity of the equations derived in previous sub-sections, it is difficult to obtain a closed form solution for critical angle. Such problem can be tackled numerically, using a numeric method that iterates joint angle until total needle displacement equals needle spacing.

$$2\pi/n - |\phi_{i1}(\theta_o, \psi_i)_{\max}| - |\phi_{i1}(\theta_o, \psi_i)_{\min}| = 0 \quad (2.45)$$

A computer program was developed to solve Eq. (2.45) for θ_o . The calculated critical angle of the joint used for the experimental portion of this work, whose main characteristics were previously described, is $\theta_{cr} = 5.965^\circ$

2.8 Critical joint angle, when ball tilting is neglected and $\psi = \varphi$

In most commercial applications, joints will spend most of its life running between 3° and 5° . In some applications, continuous running angles may be as high as 11° but that is uncommon. Tripode joints are designed to have a critical angle in the range of 5° to 9° , typically. It was discussed in previous sub-sections the joint angle variation due to the small variations in input and output displacements. Such joint angle variation reduces as the nominal joint angle decreases. Figure 2.29 compares the deviation from nominal angle, in a revolution, at two different nominal angles. The solid line represents a nominal angle of 23° , maximum deviation is 0.342° or 1.49%. The dashed line represents a nominal angle of 6° , maximum deviation is 0.022° or 0.37%.

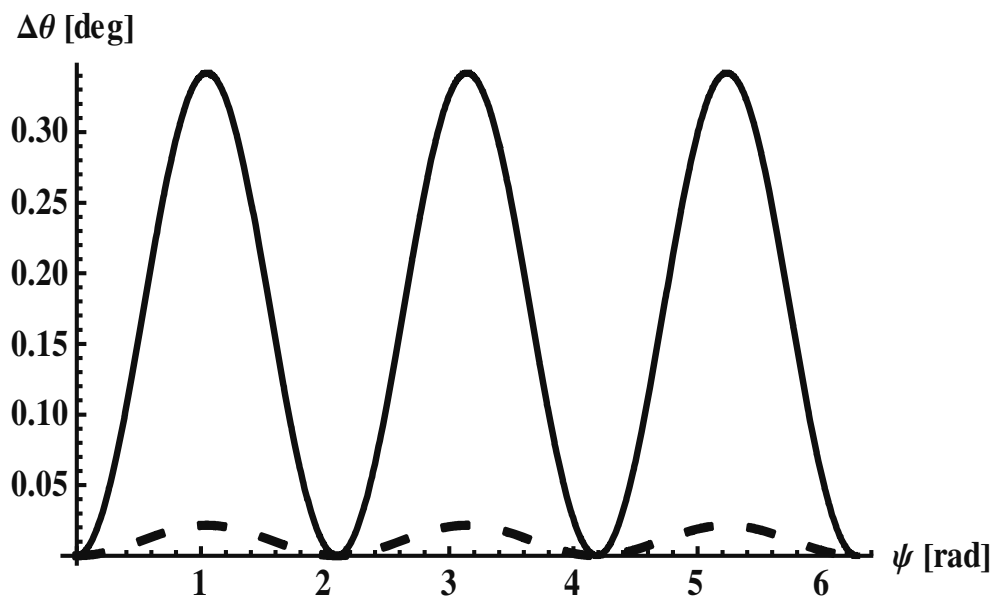


Figure 2.29. Deviation from nominal angle in a revolution at $\theta_o = 23^\circ, 6^\circ$

Figure 2.30 shows the maximum proportional deviation from nominal angle as a function of nominal angle. It can be observed that the behavior is almost linear and that even at angles as high as 15° the relative error is still less than 1%. Of course the maximum deviation will be different for different joint dimensions but magnitude will be of the same order. In this work a relative error of joint angle variation of less than 1% will be considered acceptable when predicting critical angle. Therefore, it can be assumed that $\psi_i = \varphi_i$, and consequently $\theta = \theta_o$, for the purpose of calculating critical joint angle.

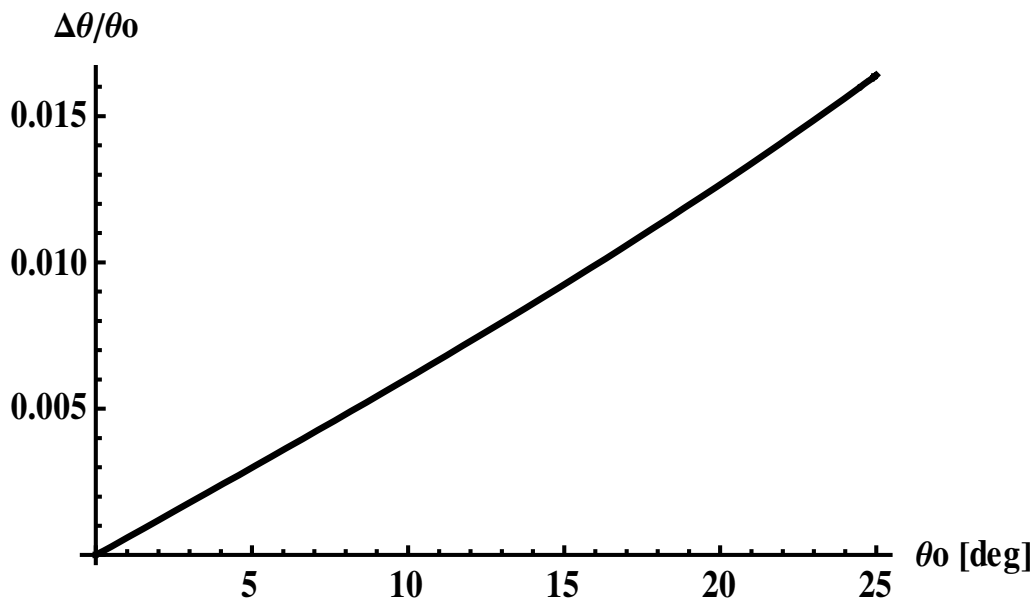


Figure 2.30. Maximum proportional deviation from nominal angle vs. θ_o

Given the assumption of equal input and output displacements, many of the equations used to calculate needle roller displacement can be simplified. Let's start by defining ϕ_{i1}^* as needle displacement and η_i^* as angular ball displacement, when $\psi_i = \varphi_i$.

$$\phi_{i1}^* = \left(\frac{\frac{t}{2} + d}{t + d} \right) \eta_i^* \quad (2.46)$$

Similarly, ε'_{i^*} and s_{i^*} are defined when $\psi_j = \varphi_j$,

$$\eta_i^* = \varepsilon'_{i^*} - \frac{2}{m_o} s_{i^*} \quad (2.47)$$

It was mentioned in the previous section that the effect of ball tilting at low joint angles could be neglected.

Figure 2.31 shows the difference between Z_j and s_j , in a revolution, for a joint angle of 6° , while Figure 2.32 shows the relative error, with respect to s_j , of assuming $s_j = Z_j$. The absolute error in arch length displaced is in the order of microns, while the relative error is less than 0.2%, including joint angle variation ($\psi_j \neq \varphi_j$). If joint angle variation is ignored, the relative error becomes 0.37%, at 6° (Figure 2.33).

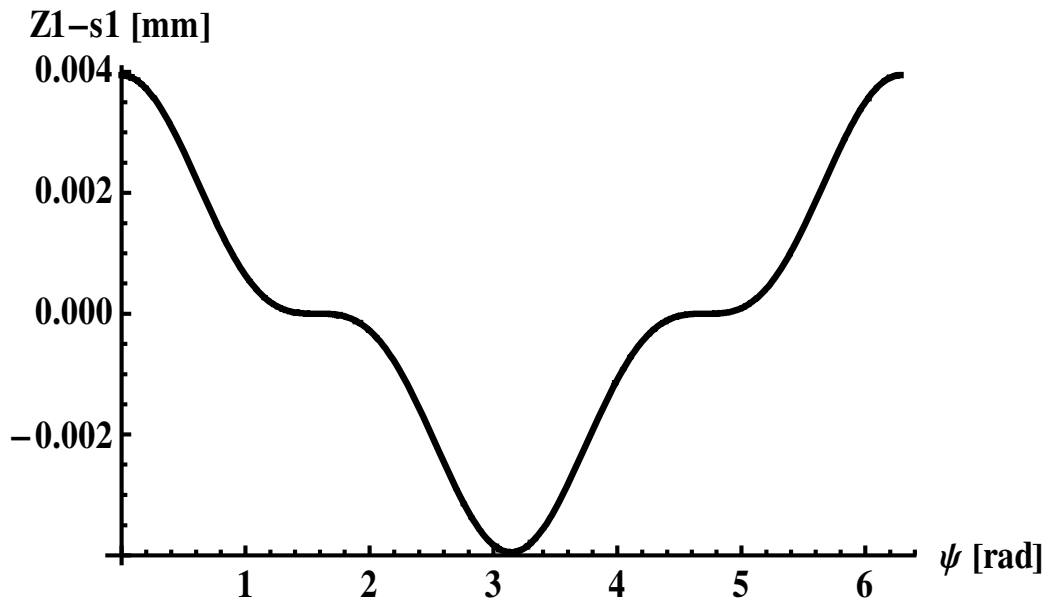


Figure 2.31. Difference in arch displacement without and with ball tilting, at 6°

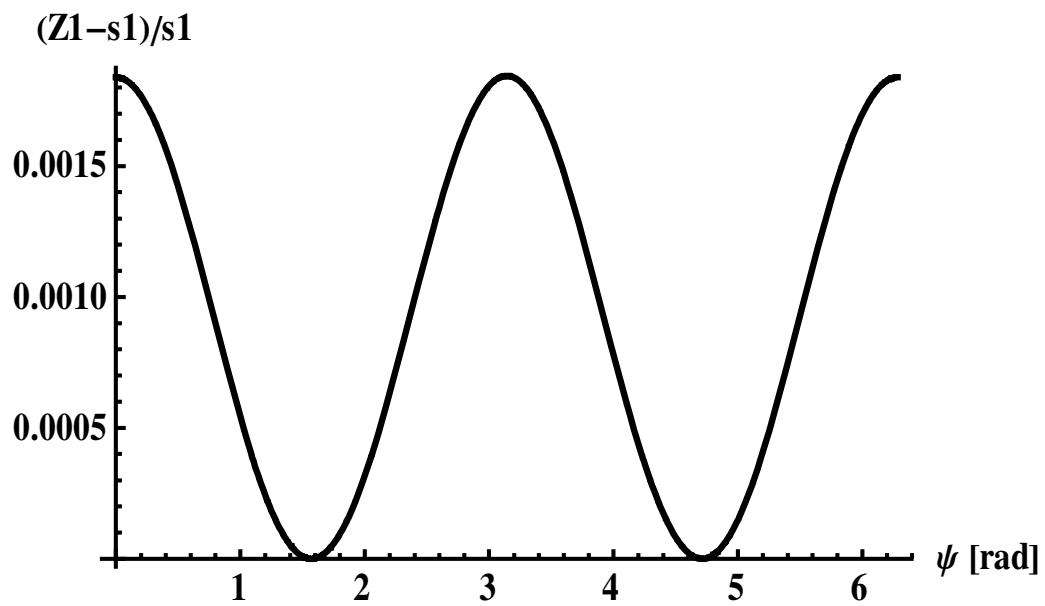


Figure 2.32. Relative error of ignoring ball tilting, at 6°

Figure 2.33 shows the maximum relative error caused by ignoring ball tilting and ignoring joint angle fluctuation. It can be observed that the behavior is highly non-linear

at large angles. However, at low angles the error is in the order of 1% or lower. Such error will be considered acceptable in this work and it will be assumed that $Z_i \approx s_i$ for the purpose of calculating critical joint angle.

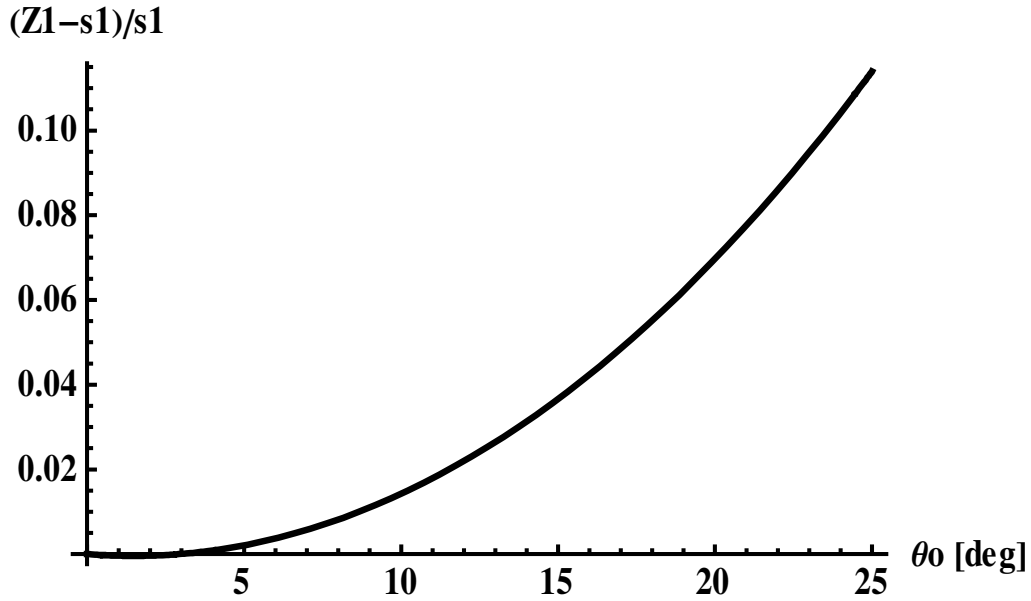


Figure 2.33. Relative error of arch-length displacement, ignoring tilting, vs. θ_0

Once the two main assumptions for a simplified formulation of critical angle have been established, Eqs. (2.10), (2.40), (2.46) and (2.47) can be reduced and reformulated. Another secondary assumption, nevertheless important, is that initial stroke $c_0 = 0$. Therefore,

$$s_i^* \approx Z_i^* = \left(\frac{a}{2}\right)(2\cos\psi_i + (1 - \cos\theta)\cos 3\psi_i)\tan\theta_0 \quad (2.48)$$

$$\varepsilon_i^* = \text{sign}(\sin\psi_i) \cdot \arccos\left(\sqrt{1 - \sin^2\theta_0 \cdot \sin^2\psi_i}\right) \quad (2.49)$$

$$\eta_i^* = \text{sign}(\sin \psi_i) \cdot \arccos\left(\sqrt{1 - \sin^2 \theta_o \cdot \sin^2 \psi_i}\right) - \frac{2}{m_o} \left(\frac{a}{2}\right) (2 \cos \psi_i + (1 - \cos \theta_o) \cos(3\psi_i)) \tan \theta_o \quad (2.50)$$

$$\phi_{i1}^* = \left(\frac{\frac{t}{2} + d}{t + d}\right) \left(\text{sign}(\sin \psi_i) \cdot \arccos\left(\sqrt{1 - \sin^2 \theta_o \cdot \sin^2 \psi_i}\right) - \frac{a}{m_o} (2 \cos \psi_i + (1 - \cos \theta_o) \cos(3\psi_i)) \tan \theta_o\right) \quad (2.51)$$

Eq. (2.45) represents the simplified formulation for needle roller displacement, which is valid only at low joint angles, as previously described. Figure 2.34 shows a comparison between ϕ_{i1} and ϕ_{i1}^* at 23° joint angle. The solid line represents the needle roller displacement including joint angle fluctuation and ball tilting effect. The dashed line represents the simplified version.

Eq. (2.45) can be rewritten as Eq. (2.52) and solved numerically for θ_o , using the same joint parameters.

$$2\pi/n - |\phi_{i1}^*(\theta_o, \psi_i)_{\max}| - |\phi_{i1}^*(\theta_o, \psi_i)_{\min}| = 0 \quad (2.52)$$

Then, the resulting critical angle is $\theta_{cr}^* = 5.981^\circ$

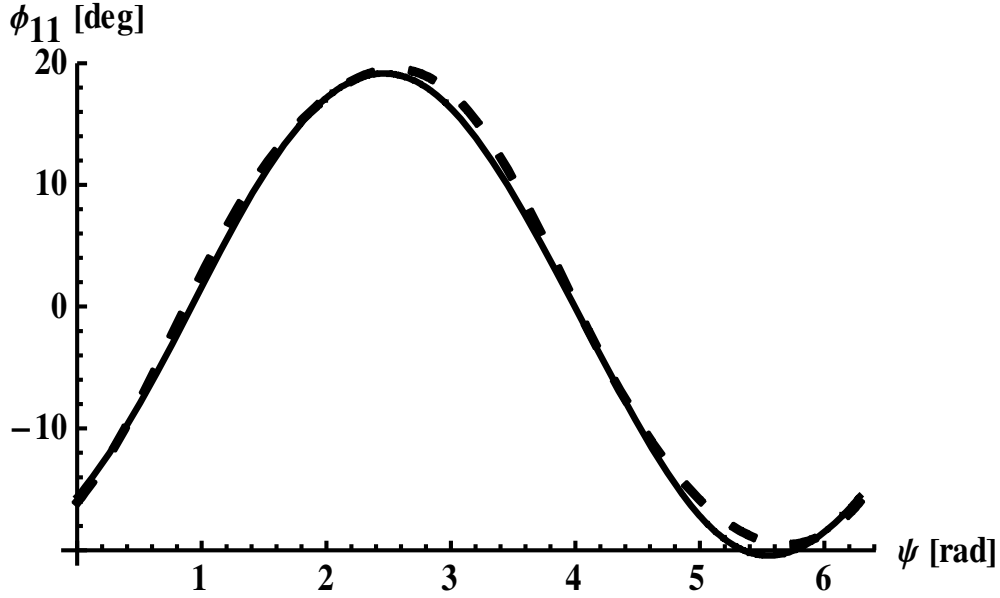


Figure 2.34. Needle roller displacement, complete vs. simplified solution

Relative error of θ_{cr}^* , with respect to θ_{cr} , is calculated and is found to be equal to 0.27%. It was mentioned before that this difference will change from joint to joint but the order of magnitude will be the same. Therefore, Eqs. (2.51) and (2.52) will be considered as fairly good approximations to calculate critical angle. To finalize this section, it will be made reference to an expression, formerly used by a C/V joint manufacturer [14], to calculate critical angle in tripod joints. Such expression was developed considering only one position of ψ , which was $\psi = 0$.

$$\theta_{cr}' = \arctan\left(\frac{2\pi}{n} \cdot \frac{m_o(t+d)}{bcd \cdot m_i}\right) \quad (2.53)$$

Evaluating Eq. (2.53) with previously used joint parameters, it is found that the critical angle predicted by this expression is $\theta_{cr}' = 7.83^\circ$. This represents a considerable difference with respect to the exact and the approximate solutions derived in this work. The source of this difference, as previously explained, is the fact that Eq. (2.53) was derived without considering full joint rotation, which makes it incomplete.

3. QUASI-STATIC ANALYSIS OF A STROKING TRIPODE JOINT

3.1 Introduction

This section deals with the way internal forces are distributed in a tripod joint. Forces can be dynamic or static and be influenced by the friction in the system. Many authors [2-3, 11-15] have dealt with this problem from different perspectives. Small variations between input and output angular displacements may cause non constant velocity (CV) behavior in a tripod joint. Such variations were discussed in Section 2. The reader may refer back to Eq. (2.1) and Figure 2.10. The first major assumption in this section will be to neglect the small variations between input and output angular displacements, as well as the joint angle fluctuation caused by them (Figures 2.6 and 2.7), and consider the tripod joint as a true constant velocity (CV) joint. Urbinati and Pennestri [11] performed a complete dynamic analysis of the tripod joint. They concluded that in steady state or constant input velocity the effect of joint angle fluctuation (source of the deviation from constant velocity) on reaction forces inside the joint can be neglected.

The second major assumption made in this section is relative to inertial forces. In most commercial applications tripod joints operate at relatively low speeds. Mariot, K'Nevez and Barbedette [12] verified in their work that for a constant input velocity, dynamical effects are negligible versus static effects.

The third major assumption is relative to rolling and sliding friction between spherical roller and needle rollers on the trunnion. Sliding between spherical roller and needle rollers occurs when the spherical roller displaces along the trunnion. Serveto, Mariot and Diaby [13] modeled analytically and numerically (ADAMS model) the Generated Axial Force (GAF) in tripod joints. GAF is the main generator of shudder and vibrations in the joint and is a function of internal forces. They concluded that friction between spherical roller and needle rollers on the trunnion, when the joint is lubricated, has little influence in GAF and its effect can be neglected. Lee [14] in his doctoral dissertation measured the sliding friction force between spherical rollers and needles and found the average to be very close to zero, within a joint revolution, under quasi-static conditions.

Published studies on GAF [12-14] identify the friction between spherical roller and ball track as the dominant element in the disturbances generated by the joint. Friction forces at this contact are also larger than friction forces between spherical roller, needle rollers and trunnion, by one order of magnitude, even in the absence of lubricant.

3.2 Normal forces at spider trunnions

Input torque is applied to the tripod at the housing axis. This torque is transmitted through three loads to the spider. Loads on the spider generate torque at the spider axis, equal in magnitude to the input torque. If sliding and rolling friction

between spherical rollers and trunnions are ignored, it can be assumed that the forces that generate torque in the spider axis are all located on the spider plane $X'-Y'$, pass through the center of the spherical roller and are perpendicular to the trunnion axes (Figure 3.1).

Neglecting inertial effects the analysis can be simplified to a simple static analysis. Thus, the three equations that define the sum of forces and moments in the spider plane are:

$$p_1 \cos \psi + p_2 \cos(\psi + 2\pi/3) + p_3 \cos(\psi + 4\pi/3) = 0 \quad (3.1)$$

$$p_1 \sin \psi + p_2 \sin(\psi + 2\pi/3) + p_3 \sin(\psi + 4\pi/3) = 0 \quad (3.2)$$

$$p_1 r_1 + p_2 r_2 + p_3 r_3 = t_\psi \quad (3.3)$$

Solving Eqs. (3.1), (3.2) and (3.3) simultaneously,

$$p_1 = p_2 = p_3 = p = \frac{t_\psi}{r_1 + r_2 + r_3} \quad (3.4)$$

Let's remember that r_i can be obtained from Eqs. (2.2) and (2.14),

$$e = \frac{a(1 - \cos \theta)}{2 \cos \theta} \quad (2.2)$$

$$r_i = \frac{a}{2} \left(\frac{(1 + \cos \theta)}{\cos \theta} + \frac{2(1 - \cos \theta)}{\cos \theta} \cos 2\psi_i \right) = a + e(1 + 2\cos 2\psi_i) \quad (2.14)$$

for $i = 1, 2, 3$

Then, the sum of r_1 , r_2 , and r_3 can be expressed as,

$$r_1 + r_2 + r_3 = 3(a + e) = \frac{3}{2}a \left(1 + \frac{1}{\cos \theta} \right) \quad (3.5)$$

Therefore,

$$\rho_1 = \rho_2 = \rho_3 = \rho = \frac{2}{3} \frac{t_\psi}{a \left(1 + \frac{1}{\cos \theta} \right)} \quad (3.6)$$

3.3 Normal forces at ball bores

Forces q_i are defined to be perpendicular to ball bore axes. Forces p_i are components of forces q_i when projected on the spider plane. Wagner [2] derived expressions to estimate forces q_i as a function of torque through graphical methods, for only two phase angles of the joint ($\psi = 0$ and $\psi = \pi / 2$). Orain [15] derived expressions for a full revolution of the joint, which yield numerical values similar to those obtained from Wagner's expressions at $\psi = 0$, $\psi = \pi / 2$ and mirror positions. Lee [14] measured values of q_i and p_i in a joint lubricated with grease under quasi-static conditions and

found them to be very close, where p_i behaves like a constant within a revolution and q_i has little fluctuation, following a trend similar to that predicted by Orain [15].

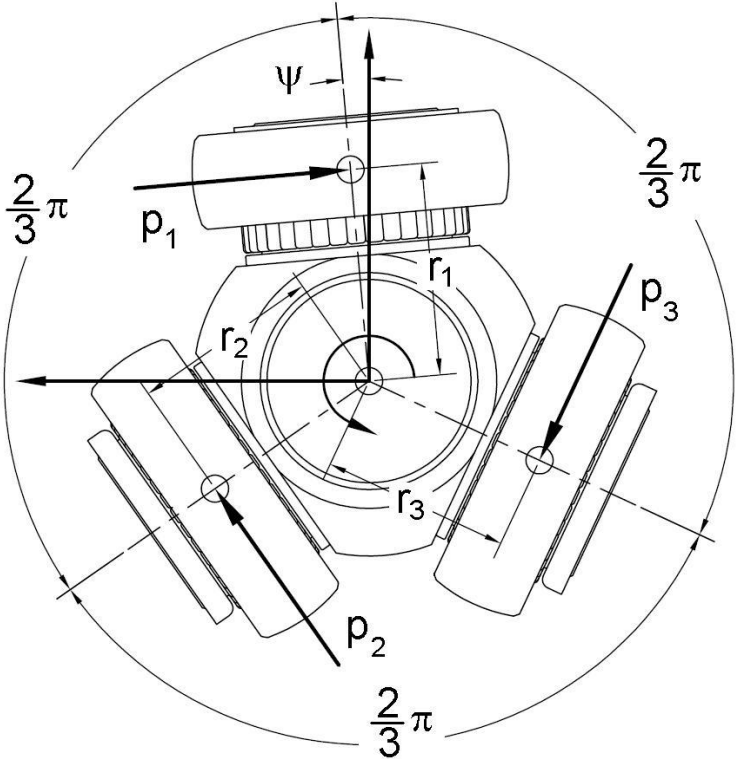


Figure 3.1. Forces on spider plane

Experimental data, computer simulations (ADAMS) and analytical formulations presented by Mariot, Serveto and Diaby [13] for GAF show that the influence of rotational speed in GAF can be neglected, within the normal operation range in most commercial applications. GAF is a function of friction and internal loads. The formerly mentioned authors simplified the analysis at low joint angles by making $q_i \approx p_i$ to develop GAF expressions. The equations used in this work to calculate GAF are

equivalent to expressions derived by Lee [14], Wagner [2] and Mariot, Serveto and Diaby [13].

$$GAF = \sum_{i=1}^3 w_i \quad (3.7)$$

$$w_i = \mu_b q_i \sin \delta_i \text{sign}(\sin \delta_i \sin \psi_i) + \mu_r q_i \text{sign}(\sin \psi_i) \quad (3.8)$$

where angle δ_i can be obtained from Eqs. (2.31) and (2.29), derived in the previous section,

$$\delta_i = \pi/2 - \mu_i \quad (2.31)$$

$$\cos \mu_i = \cos \varphi_i \sin \theta \quad (2.29)$$

After a break-in period, friction in the joint is assumed to be constant. Therefore, peak GAF will be proportional to the normal load applied on the ball bore, where the constants of proportionality are the friction coefficients.

This being said, equations for q_i can be developed making sure quasi-static equilibrium of forces is maintained.

$$(q_1 + q_2 + q_3)a = t_\psi = t_\varphi \quad (3.9)$$

The input torque and the distance between housing axis and ball bore axes are constants. Therefore, the sum of normal forces acting on housing ball bores is an invariant. In the position shown in Figure 3.2 the normal force on the ball bore has the same direction of the normal force on the trunnion. In other words, $q_i = p_i$ at $\psi_i = 0$.

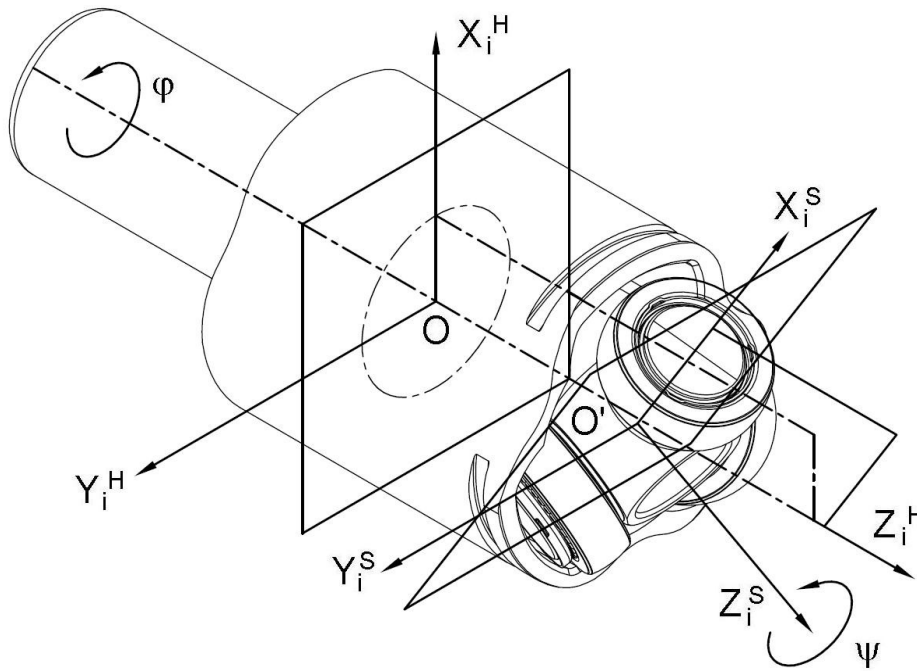


Figure 3.2. Rotating coordinate systems and joint orientation when $\psi_i = 0$

When the joint has rotated 90° and 270° , the relationship between q_i and p_i can be represented graphically as shown in Figure 3.3.

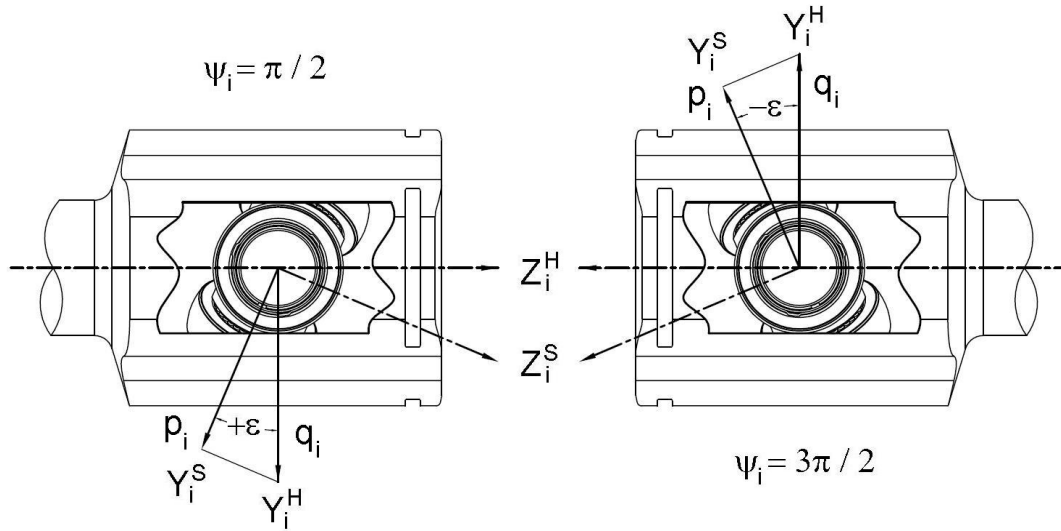


Figure 3.3. Graphical representation of angle ε and forces q_i and p_i

It will be noticed that p_i has the same direction that Y_i^S and q_i has the same direction that Y_i^H . Therefore, the angle ε between p_i and q_i is equivalent to angle ε_i , from Eq. (2.39), for $i = 1$.

$$\cos \varepsilon_i = \cos \theta_i \sin \varphi_i \sin \psi_i + \cos \psi_i \cos \varphi_i \quad (2.33)$$

Since p_i is a projection of q_i its relationship can be expressed as

$$q_i = p_i / \cos \varepsilon_i \quad (3.10)$$

3.4 Numerical examples and GAF experimental results

Following the process developed in the previous section, a computer program was written to perform calculations. The code was debugged verifying the outputs with the numerical results of examples published by Wagner [2] and Orain [15]. Graphics and numerical values in this section were obtained using the characteristics the tripod joint used to do the experimental portion of this work. The joint characteristics and torque applied are:

Nominal BCD	=	40.8mm
Shaft length	=	300mm
Maximum functional angle	=	23° (design limit)
Trunnion diameter	=	20.97mm
Needle roller diameter	=	1.9975mm
Number of needles (n)	=	36
Spherical roller outer diameter	=	34.942mm
Input torque	=	2118Nm (design limit)

Figure 3.4 compares the magnitude of force p_1 assuming a constant joint angle (dashed line) and including joint angle variation (solid line). It can be observed that the frequency is the same as joint angle variation calculated in section two. The maximum and minimum values in a revolution, at the design limits of the joint, are: $p_{1\max} = 33,175.3N$ and $p_{1\min} = 33,131.2N$. The magnitude of the variation, with respect to the maximum value of p_1 is 0.13%. This small variation justifies the assumption of neglecting joint angle fluctuation, as indicated at the beginning of the section.

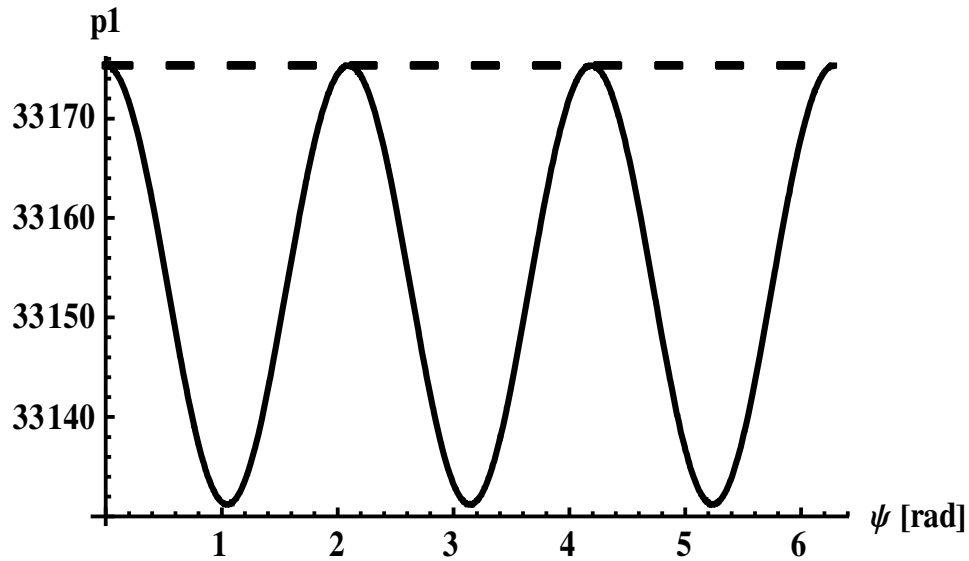


Figure 3.4. Magnitude of p_1 with (solid line) and without joint angle variation

Similarly, q_1 is calculated and plotted in Figure 3.4 with and without joint angle variation effects. The maximum and minimum values for each case are,

$$q_{1\max} (\text{constant joint angle}) = 36,040.4N$$

$$q_{1\min} (\text{constant joint angle}) = 33,175.3N$$

$$q_{1\max} (\text{joint angle variation}) = 36,062.9N$$

$$q_{1\min} (\text{joint angle variation}) = 33,175.3N$$

The relative error associated with ignoring joint angle variation to calculate the maximum value of q_1 is 0.06%, at extreme joint conditions. This verifies the assumption of neglecting joint angle variation and considering the tripod joint as a CV joint through

the rest of this work. The reader will also notice that the amplitude of q_1 is small with respect to its medium value, even at maximum joint angle of 23° (Figure 3.5). It must be considered that at lower joint angles the amplitude to mean value ratio will reduce.

$$\frac{\text{amplitude}}{\text{mean_value}} = \frac{(36,062 - 33,175)N/2}{(36,062 + 33,175)N/2} = 0.0417$$

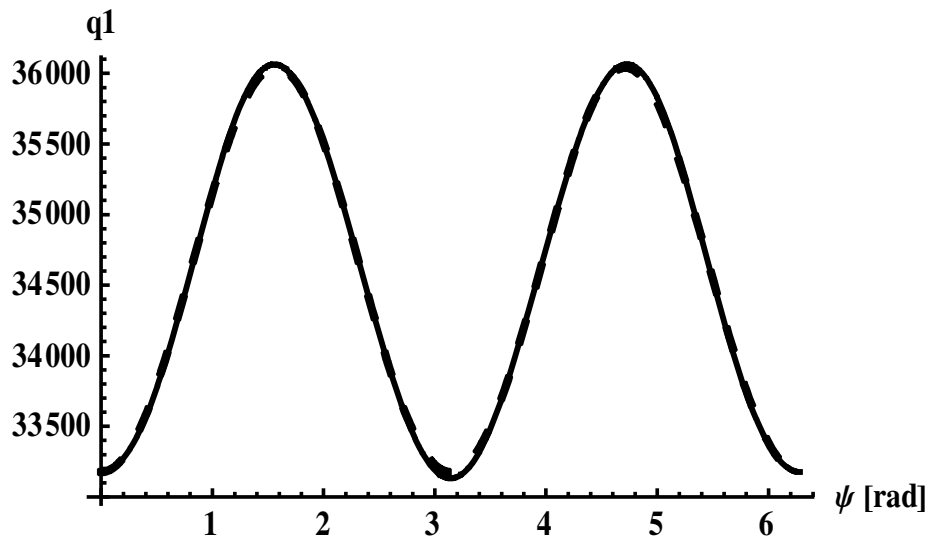


Figure 3.5. Magnitude of q_1 with (solid line) and without joint angle variation

GAF was measured in joints that have the geometric characteristics of the joint simulated in this section. The same greases that Lee [5] used in his experiments are used in this work. Table 3.1 summarizes the main characteristics of the greases.

A total of sixteen tripod joints were tested. Only the average of peak GAF values (third order components) are reported in this work and compared against the theoretical calculations using Eqs. (3.7) and (3.8). The full set of measurements can be found in

referenced Nexteer Automotive Test Activities [17]. Such experiments were performed in a machine specifically designed and created to measure GAF in CV joints. Details of the machine are not disclosed in this work since they are proprietary to Nexteer Automotive.

Figures 3.6 and 3.7 show the graphs corresponding to Eqs. (3.8) and (3.7). Load used to generate such figures was 600Nm, at 7.5°, using grease A, with $\mu_b = 0.04$ and $\mu_r = 0.001$. For grease B $\mu_b = 0.08$ and $\mu_r = 0.001$. The coefficients of friction used in this work are slightly lower than coefficients of friction reported by Lee [14]. Hardware used by Lee to do his experiments was made by manufacturing processes less accurate than the processes used to make the hardware used for the experimental portion of this work.

Properties	Grease A	Grease B
Type	PU (polyurea)	PU (polyurea)
Performance	Low Friction	High Durability
NLGI grade	2	2
Base oil	Mineral / synthetic	Mineral
Viscosity @ 100°C η (mPa-s)	12	12
Representative additives	Organo-molybdenum	Solid EP*
Color	Green	Blue

Table 3.1. Properties of CVJ greases. () stands for "Extreme Pressure"*

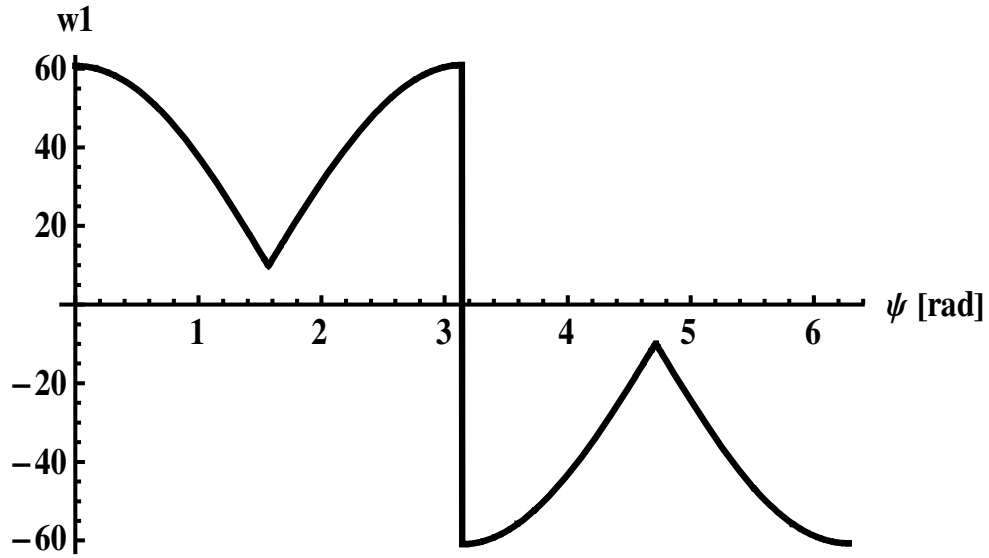


Figure 3.6. Tangential force w_1 , at 600Nm, 7.5°, grease A

Figures 3.8 and 3.9 compare theoretical calculations against experimental values, for two levels of torque, two different greases and a set of joint angles that range from 2.5° to 17°.

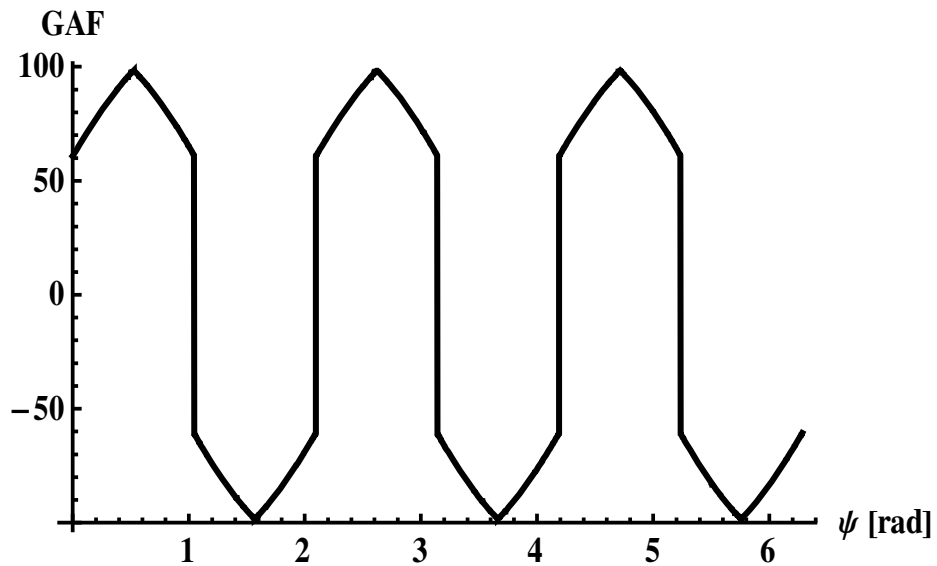


Figure 3.7. Generated axial force, at 600Nm, 7.5°, grease A

It can be observed that theoretical calculations do not match experimental data perfectly but clearly follow the same trend. The purpose of this work is not to develop an accurate GAF model, which could be achieved by defining coefficients of friction as functions of torque and joint angle instead of constants. Such approach was already used by Lee [5] and is outside of the scope of this work.

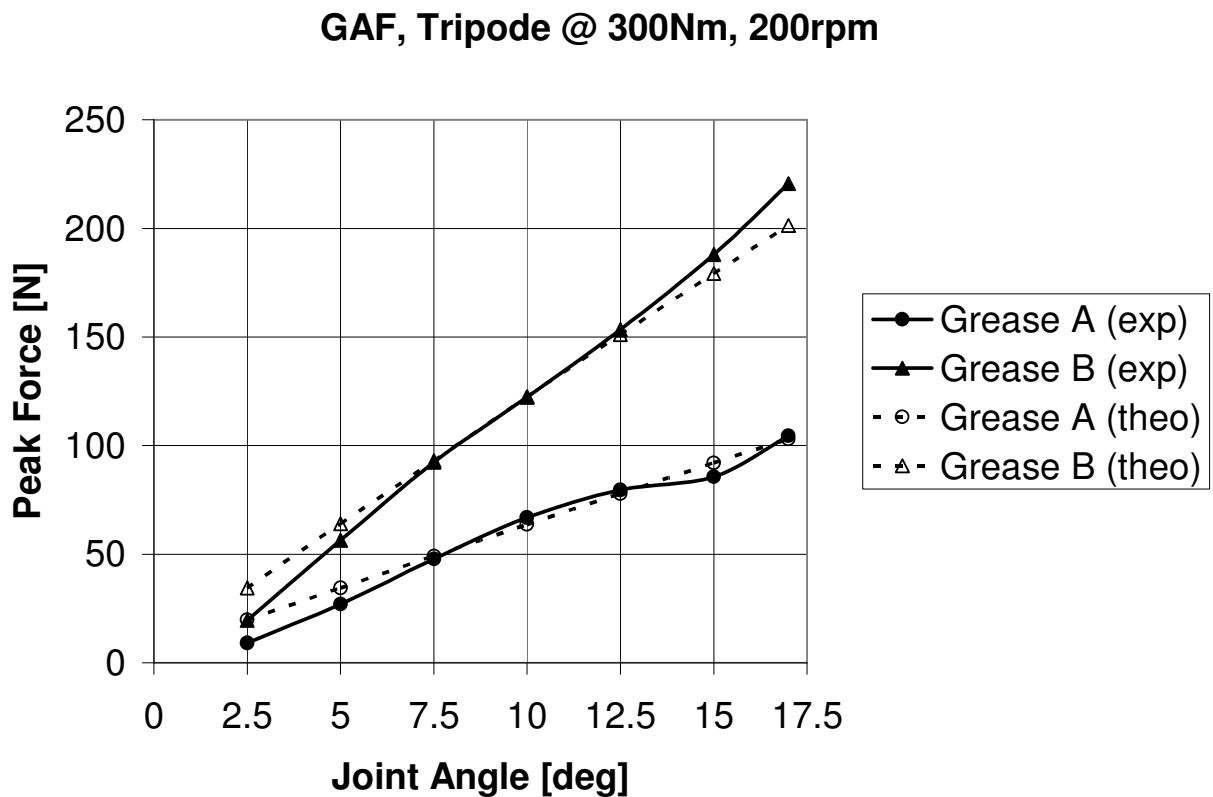


Figure 3.8. Generated axial force, at 300N, experimental vs. theoretical values

The purpose of comparing theoretical GAF calculations against real experimental data is to justify the validity of the assumptions described at the beginning of this section

to calculate normal loads on trunnions. Such loads will be the basis to estimate load distribution at the contacts between needle rollers and trunnion and determine the state of stress, in the next sections.

GAF, Tripode @ 600Nm, 200rpm

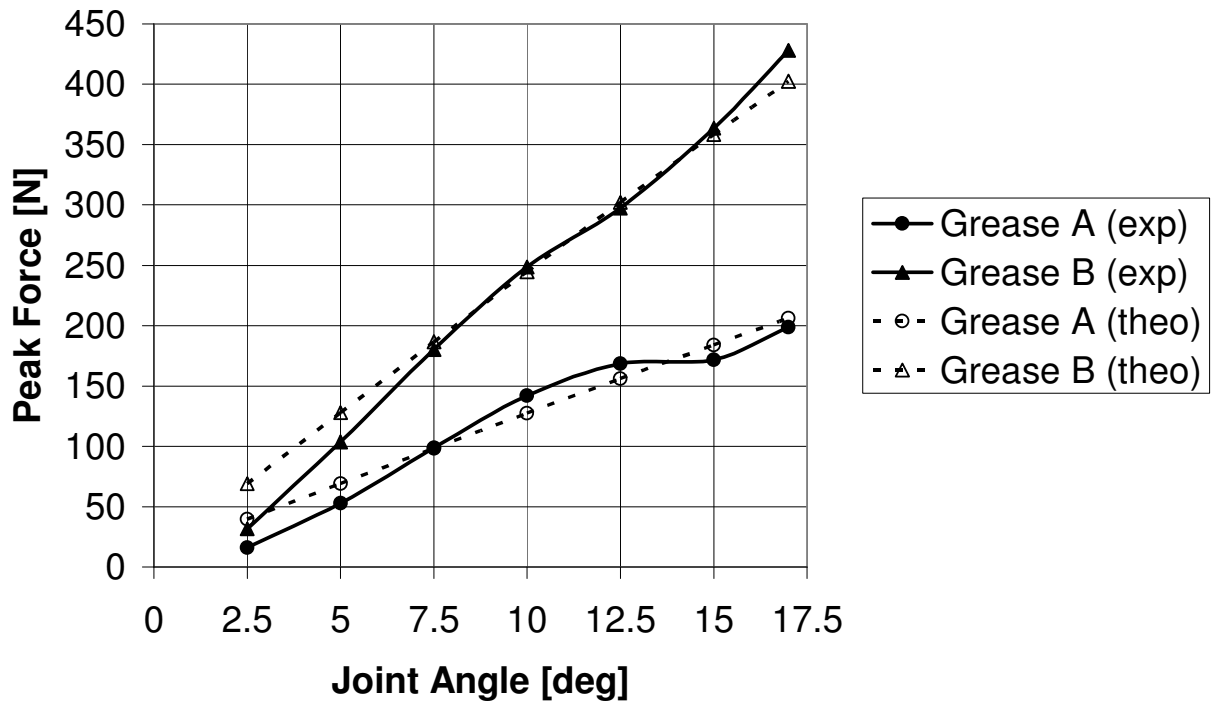


Figure 3.9. Generated axial force, at 600N, experimental vs. theoretical values

4. LOAD DISTRIBUTION ON A TRUNNION

4.1 Introduction

This section deals with the way contact forces are distributed on trunnions of a tripod joint. Three areas in the joint where mating surfaces are subjected to contact forces are:

- a) Contact between spherical roller and ball bore in the housing
- b) Contact between needle rollers and spherical roller (ball)
- c) Contact between needle rollers and trunnion

Typically, the contact region to present the first signs of wear is the contact area between trunnion and needle rollers. Countless validation tests of different sizes of joints throughout the past 30 years at Nexteer Automotive support the statement. This is the reason to consider that the wear life of a tripod joint will be defined by the wear performance of trunnion surface. It is possible for needles to wear first. However, this condition occurs rarely in tripod joints.

Methods used to analyze roller bearings will be employed to study load distribution in spider trunnions. The following assumptions are made:

- a) Needle rollers and trunnions are made of steel, similar elastic properties and homogeneous material.

- b) Unless otherwise indicated, it is assumed in this section that plastic deformation doesn't occur at the contacts.
- c) Unless otherwise indicated, residual stresses are assumed to be zero in this section.

4.2 Normal load distribution on needles (axial direction)

The forces transmitted from housing to spider are shown to be normal to the trunnion axis in Section 3. The spherical roller rotates and slides with respect to the trunnion. The spider assembly can be treated as a set of three roller bearings, where the trunnions function as inner races, the needles are equivalent to simple cylindrical rollers and the spherical rollers or balls function as outer races, one per roller bearing.

In traditional roller bearings the rollers are fully supported in both inner and outer races. This is not the case in a tripod joint, where needles are not fully supported on the spherical roller with axial relative motion between them. Three main load cases are identified, as shown schematically in Figures 4.1, 4.2a and 4.2b. It must be noted that, for the sake of clarity, the sketches represent only one needle and the concentrated force p_{ij} is the equivalent concentrated force acting on that particular needle and not the total force acting between spherical roller and ball bore.

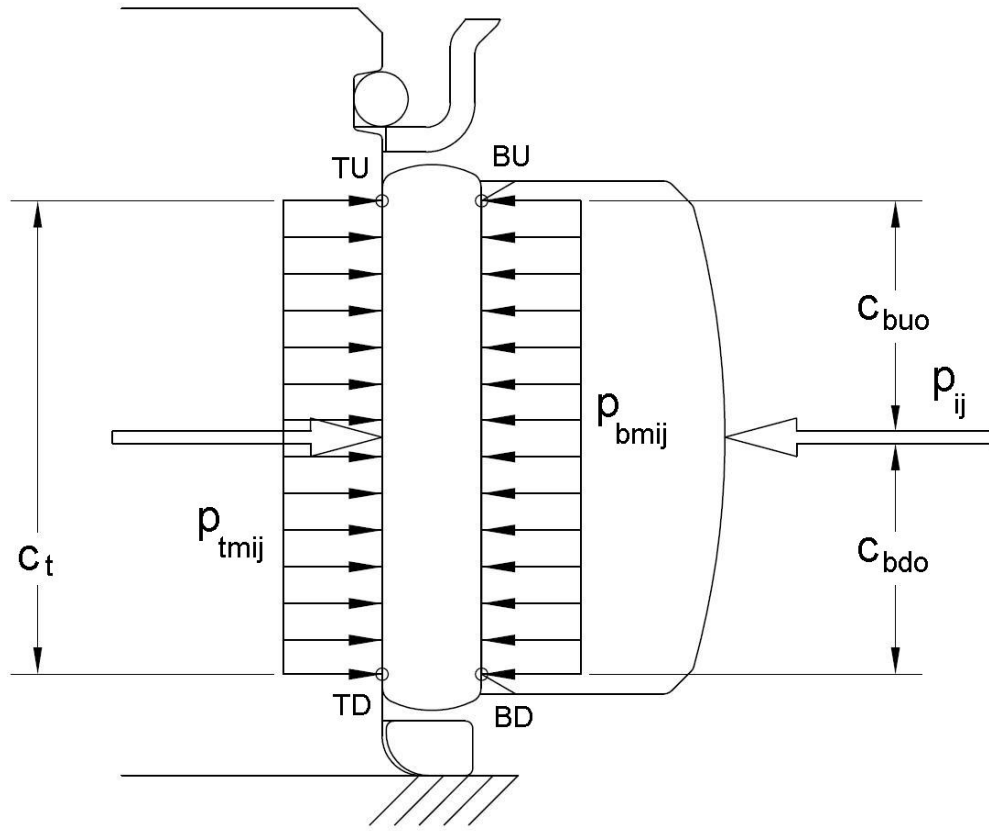


Figure 4.1. Case 1: Spherical roller fully supported, no offset

Figure 4.1 depicts Case 1, which is the ideal case. The equator of the spherical roller is aligned with the transversal plane of symmetry of the needles. Since there is no offset between such planes, the load transmitted by the needles can be considered uniformly distributed along the effective contact length. Figure 2.14 was presented to show radial position of the spherical roller center from the spider center, measured along the trunnion axis. Case 1 will occur at one radial position. Typically, this position will be $r_i \approx a$. The reader is reminded that $a = BCD / 2$. Solving Eq. (2.17) for $r_i \approx a$, it is found that Case 1 will occur four times per joint revolution.

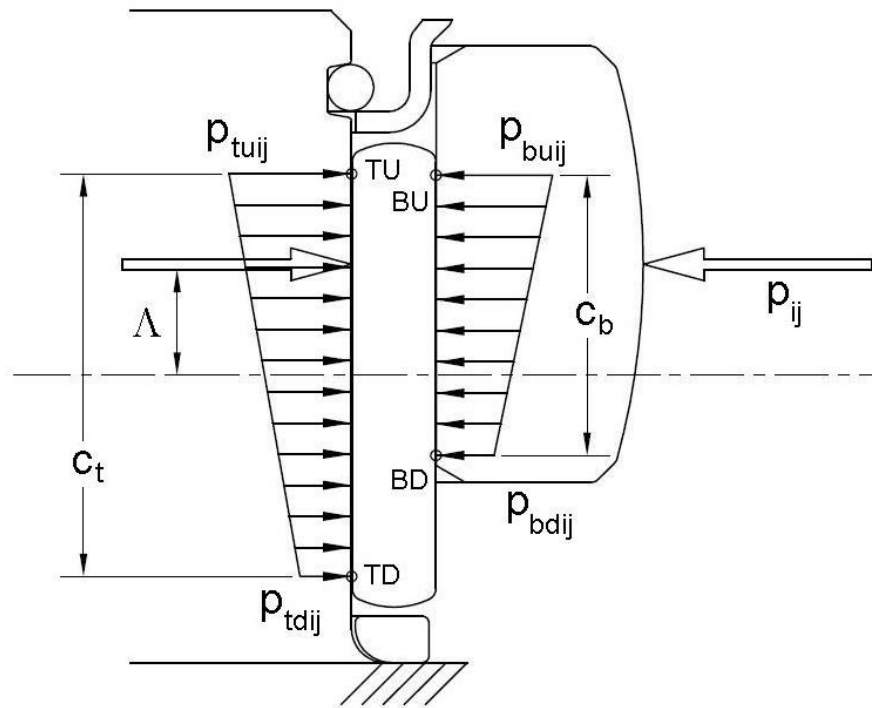


Figure 4.2a. Case 2: Positive offset (Λ)

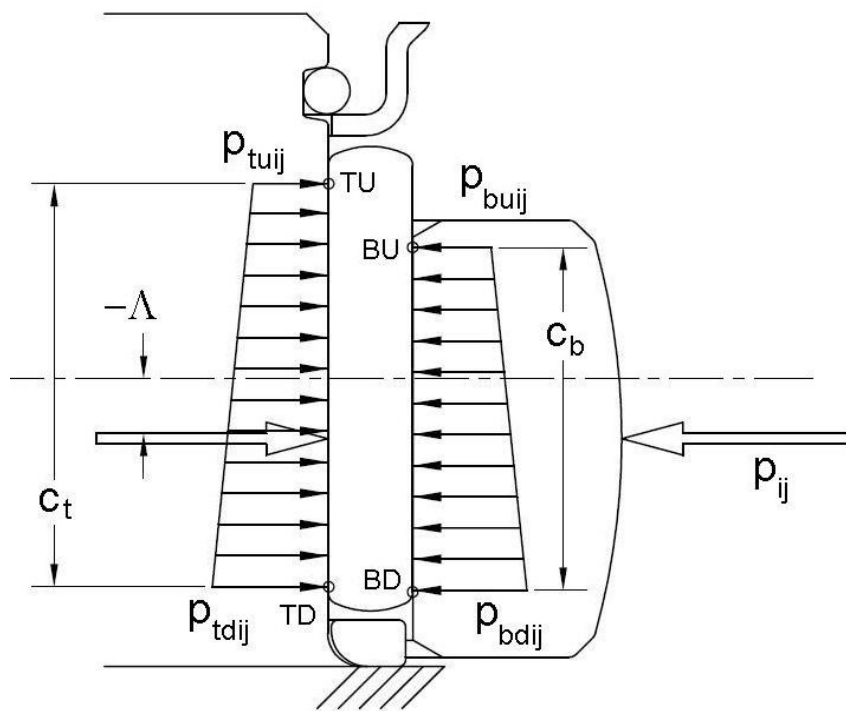


Figure 4.2b. Case 3: Negative offset ($-\Lambda$)

Figure 4.2a and Figure 4.2b depict Case 2 and Case 3, respectively, which occur twice per revolution. Case 2 represents the condition where the ball spends more time in a joint revolution. Offset Λ_i is a direct function of ball axial displacement. Therefore, it can be expressed as,

$$\Lambda_i = \Lambda_o + f_i = \Lambda_o + e(1 + 2\cos 2\psi_i) \quad (4.1)$$

for $i = 1, 2, 3$

where Λ_o is the offset at zero degree joint angle. In other words, Λ_o is an initial condition. The ends of the needle rollers have the clearance θ_o , with respect to roller retainer and ring spacer, which allows some additional axial motion of the needles with respect to the trunnion. This motion is very small if compared to the length of the needle but not very small if compared to the ball displacement at low angles. It will be assumed that the coefficient of friction between needle and ball is larger than the coefficient of friction between needle and trunnion. Therefore, the needle will displace together with the ball while there is clearance between the top end of the needle and the roller retainer in one direction, and the low end of the needle and the ring spacer in the opposite direction. Once the clearance becomes zero, the needle will stop displacing and the ball will continue its motion. This is shown graphically in Figure 4.3.

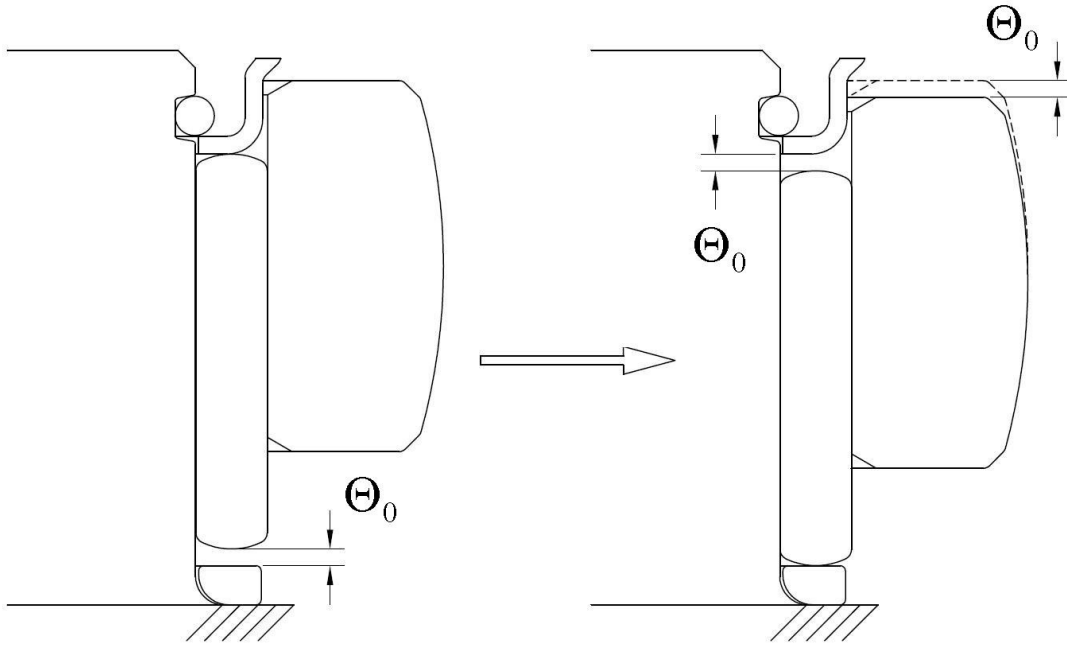


Figure 4.3. Clearance between needle, roller-retainer and spacer ring

Such displacement can be considered as a lash that allows the needles to oscillate to the same frequency of the ball axial displacement, twice per revolution. Thus, the following piecewise function is defined to take into account needle axial displacement,

$$3e > \frac{\Theta_0}{2}; 0 \leq \psi_i < \frac{\pi}{2}; \pi \leq \psi_i < \frac{3\pi}{2}$$

$$\Theta_i = -\frac{\Theta_0}{2};$$

$$f_i - 3e + \frac{\Theta_0}{2} < -\frac{\Theta_0}{2}$$

$$\Theta_i = f_i - 3e + \frac{\Theta_0}{2};$$

$$f_i - 3e + \frac{\Theta_0}{2} \geq -\frac{\Theta_0}{2}$$

$$3e > \frac{\Theta_0}{2}; \frac{\pi}{2} \leq \psi_i < \pi; \frac{3\pi}{2} \leq \psi_i < 2\pi$$

$$\begin{aligned}
\theta_i &= \frac{\theta_o}{2} + \zeta; & f_i + e - \frac{\theta_o}{2} &> \frac{\theta_o}{2} \\
\theta_i &= f_i + e - \frac{\theta_o}{2} + \zeta; & f_i + e - \frac{\theta_o}{2} &\leq \frac{\theta_o}{2} \\
\zeta &= \theta_o - 4e; & 4e &< \theta_o < 6e \\
\zeta &= 0; & \theta_o &< 4e; \theta_o > 6e \\
3e &\leq \frac{\theta_o}{2}; 0 \leq \psi_i < 2\pi \\
\theta_i &= f_i \\
\text{for } i &= 1, 2, 3
\end{aligned} \tag{4.2}$$

Using the same joint characteristics employed in Section 2 and Section 3, Expression (4.2) is plotted for two different joint angles, 6° and 23°, for a nominal value $\theta_o = 0.452\text{mm}$.

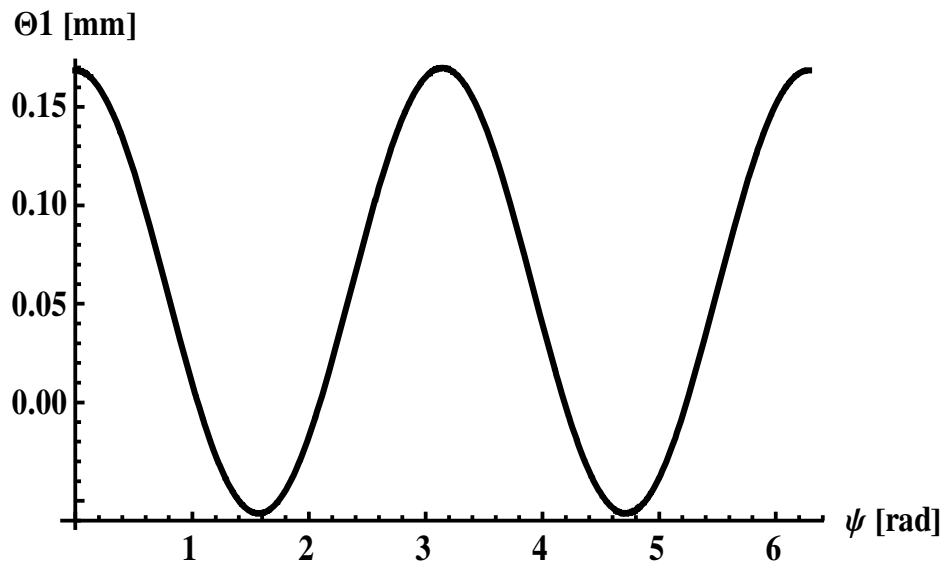


Figure 4.4a. Needle axial displacement at 6° joint angle

Figure 4.4a shows that the loaded needles follow the same axial motion of the ball. Amplitude of the motion is less than the clearance ϑ_0 . Therefore, it is expected that the motion of the needles will not be limited by lack of the clearance. On the other hand, Figure 4.4b shows the truncation of the amplitude of axial motion of needles beyond the clearance ϑ_0 . This clearly indicates that the needle displacement will be limited by the contact between roller retainer and spacer ring during a revolution.

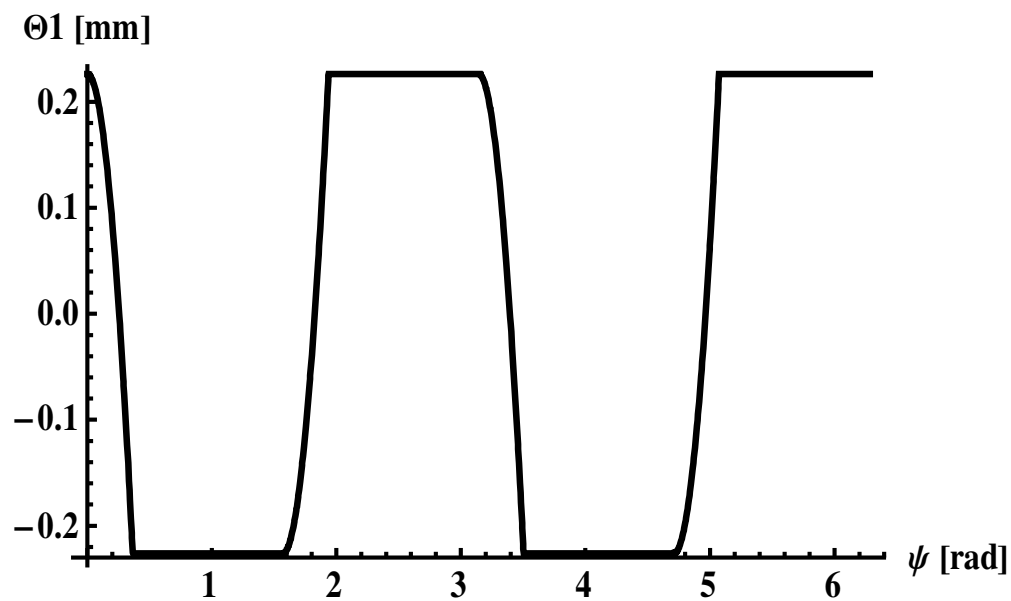


Figure 4.4b. Needle axial displacement at 23° joint angle

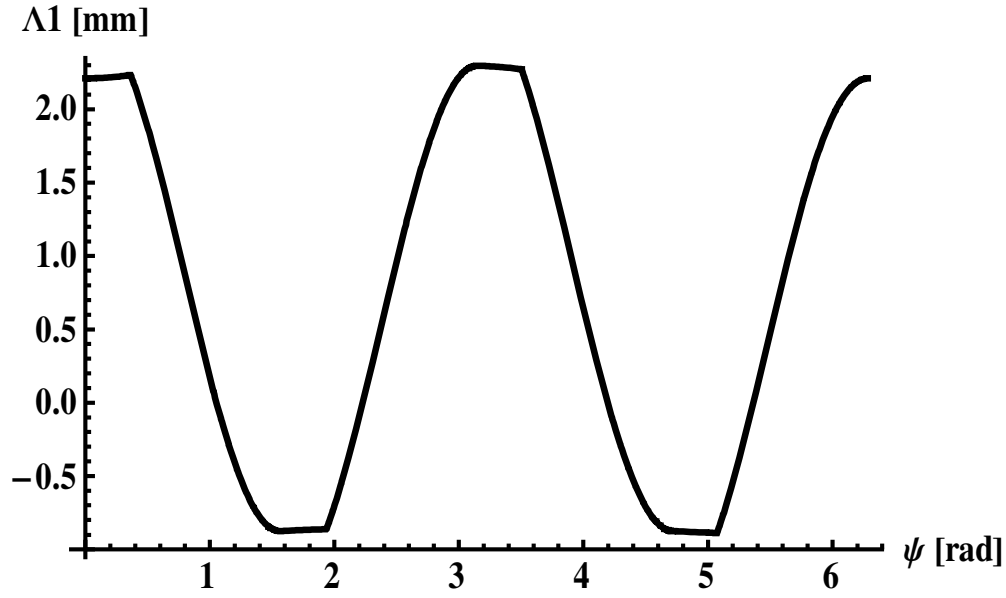


Figure 4.5. Offset between ball equator and needles symmetry plane

Then, Eq. (4.1) can be re-written by adding a term for needle motion, resulting in Eq. (4.3). It is plotted in Figure 4.5, for $\Delta_0 = -0.206\text{mm}$.

$$\Delta_i = \Delta_0 + f_i - \Theta_i = \Delta_0 + e(1 + 2\cos 2\psi_i) - \Theta_i \quad (4.3)$$

for $i = 1, 2, 3$

Once the offset between ball and needles has been defined, the analysis can continue to estimate load distribution on needles. Average loads per unit of length in ball and trunnion, are respectively,

$$p_{bmij} = \frac{p_{ij}}{c_b} \quad (4.4)$$

$$\rho_{tmij} = \frac{\rho_{ij}}{c_t} \quad (4.5)$$

Crowning of needle rollers used in tripod joints is very small and its effect will be neglected in this section. Effective contact length between needle and trunnion c_t is a constant, while the effective contact length between needle and ball c_b is a function of offset Λ_i and is defined by Eq. (4.6) through Eq. (4.8). The relationship is plotted in Figure 4.6,

$$c_b = c_{bu} + c_{bd} \quad (4.6)$$

$$c_{bu} = c_{buo} \quad \frac{c_t}{2} - (c_{buo} + \Lambda_i) \geq 0$$

$$c_{bu} = \frac{c_t}{2} - \Lambda_i \quad \frac{c_t}{2} - (c_{buo} + \Lambda_i) < 0 \quad (4.7)$$

$$c_{bd} = c_{bdo} \quad \frac{c_t}{2} - (c_{bdo} - \Lambda_i) \geq 0$$

$$c_{bd} = \frac{c_t}{2} + \Lambda_i \quad \frac{c_t}{2} - (c_{bdo} - \Lambda_i) < 0 \quad (4.8)$$

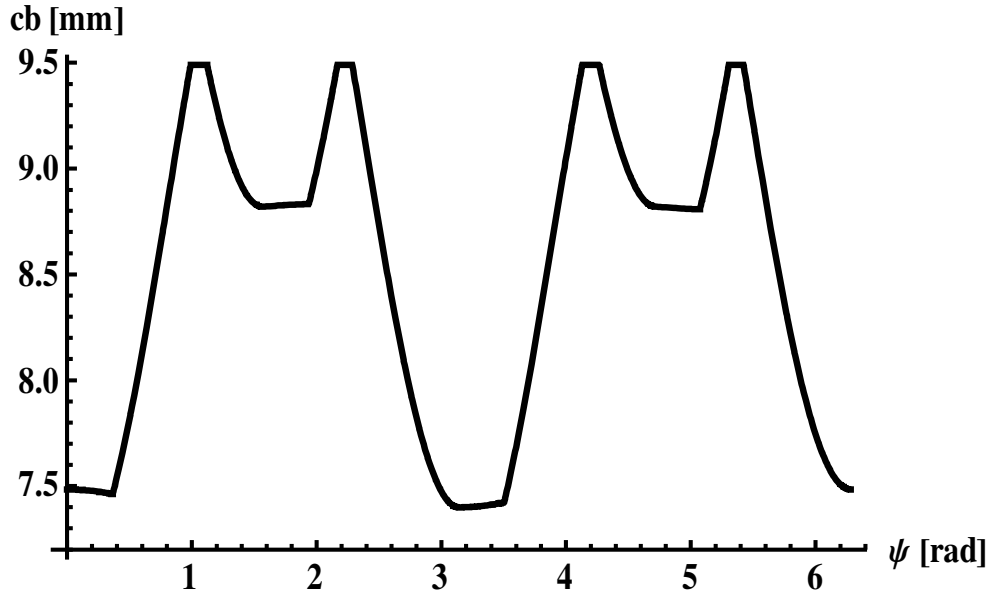


Figure 4.6. Effective contact length between needle roller and ball, at 23°

Orain's [15] assumption of linear load distribution will be considered in this section and moments trying to rotate the ball in any direction perpendicular to trunnion axis will be neglected. Therefore, the equivalent concentrated force applied on the ball will be collinear with the equivalent concentrated reacting force on the trunnion. Under these conditions, the following relationship can be established for the load distribution between needle and ball,

$$c_b \left(\frac{p_{buij} + p_{bdij}}{2} \right) = p_{bmij} c_b = p_{ij} \quad (4.9)$$

Simplifying,

$$p_{bdij} = 2p_{bmij} - p_{buij} \quad (4.10)$$

The following paragraphs will describe the load distribution at the contact between needle roller and ball for the three cases previously identified.

Case 1 occurs when $p_{buij} = p_{bdij}$. If the ball is symmetric, $c_b = c_{buo} + c_{bdo}$.

Case 2 occurs when offset Δ_i is positive. Then, summing the moments with respect to point BD,

$$p_{ij}c_{bdo} - p_{bdij}c_b\left(\frac{c_b}{2}\right) - (p_{buij} - p_{bdij})\frac{c_b}{2}\left(\frac{2}{3}c_b\right) = 0 \quad (4.11)$$

Simplifying,

$$p_{ij}c_{bdo} - \frac{p_{buij}c_b^2}{3} - \frac{p_{bdij}c_b^2}{6} = 0 \quad (4.12)$$

Case 3 occurs when offset Δ_i is negative. Then, doing sum of moments with respect to point BU,

$$-p_{ij}c_{buo} + p_{buij}c_b\left(\frac{c_b}{2}\right) + (p_{bdij} - p_{buij})\frac{c_b}{2}\left(\frac{2}{3}c_b\right) = 0 \quad (4.13)$$

Simplifying,

$$-p_{ij}c_{buo} + \frac{\rho_{buij}c_b^2}{6} + \frac{\rho_{bdij}c_b^2}{3} = 0 \quad (4.14)$$

Equations (4.10) and (4.12) can be solved simultaneously to obtain ρ_{buij} and ρ_{bdij} for Case 2,

$$\rho_{buij} = \frac{6\rho_{ij}c_{bdo}}{c_b^2} - 2\rho_{bmij} \quad (4.15)$$

$$\rho_{bdij} = 4\rho_{bmij} - \frac{6\rho_{ij}c_{bdo}}{c_b^2} \quad (4.16)$$

When $\rho_{bdij} \leq 0$, the above solution is no longer valid since ρ_{bdij} can not be negative. Additionally, such condition is not desired during the operation of the joint since the load would be concentrated on a very small area. Thus, making $\rho_{bdij} = 0$ in Eq. (4.16) and solving for c_b it can be found the minimum contact length required for ball support when Case 2 is present.

$$c_{b\min} = \sqrt{\frac{3\rho_{ij}c_{bdo}}{2\rho_{bmij}}} = \frac{3}{2}c_{bdo} \quad (4.17)$$

Using Eqs. (4.6), (4.7) and (4.8), the effective contact length between needle and ball for Case 2 can be expressed as,

$$c_b = \frac{c_t}{2} - \Delta_j + c_{bdo} \quad (4.18)$$

From Eqs. (4.1), (2.2) and (2.18), it is known that Δ_j is a function of joint angle and reaches its maximum value when phase angle ψ_j equals zero or π . The formerly mentioned equations are combined with Eqs. (4.17) and (4.18), where $c_b = c_{b\min}$ and $\theta_j \approx 0$. Such conditions are equivalent to assume the needle does not displace axially (which is the worst possible condition). Then, it can be solved for the maximum joint angle where the full contact between needle and spherical roller exists, when offset Δ_j is positive,

$$\cos \theta_{bcr \Delta+} = \frac{3a}{3a - 2\Delta_o - c_{bdo} + c_t} \quad (4.19)$$

The dimensions of the joint used for the experimental portion of this work are used to evaluate Eq. (4.19) and $\theta_{bcr \Delta+} = 23.56^\circ$.

Similarly, Eqs. (4.10) and (4.14) can be solved simultaneously to obtain ρ_{buij} and ρ_{bdij} for Case 3,

$$\rho_{buij} = \frac{6}{c_b^2} \left(-\rho_{ij} c_{buo} + \frac{2}{3} c_b^2 \rho_{bmij} \right) \quad (4.20)$$

$$p_{bdij} = 2p_{bmij} - \frac{6}{c_b^2} \left(-p_{ij}c_{buo} + \frac{2}{3}c_b^2 p_{bmij} \right) \quad (4.21)$$

When $p_{buij} \leq 0$, the above solution is no longer valid since p_{buij} cannot be negative. Additionally, similar to Case 2, such condition is not desired during the operation of the joint since load would be concentrated on a very small area. Thus, making $p_{buij} = 0$ in Eq. (4.20) and solving for c_b it can be found the minimum contact length required for ball support when Case 3 is present.

$$c_{bmin} = \sqrt{\frac{3p_{ij}c_{buo}}{2p_{bmij}}} = \frac{3}{2}c_{buo} \quad (4.22)$$

If the ball is symmetrical, $c_{buo} = c_{bdo}$, and Eq. (4.17) equals Eq. (4.22). Using Eqs. (4.6), (4.7) and (4.8), the effective contact length between needle and ball for Case 3, can be expressed as,

$$c_b = \frac{c_t}{2} + \mathcal{A}_i + c_{buo} \quad (4.23)$$

Similar to Case 2, Eqs. (4.22), (4.23), (4.1), (2.2) and (2.18) are combined for $\psi_i = \pi/2$, $c_b = c_{bmin}$ and $\theta_i \approx 0$. Then, it can be solved for the maximum joint angle, where full contact between needle and spherical roller exists, when offset \mathcal{A}_i is negative,

$$\cos \theta_{bcr} \Lambda_i = \frac{a}{a + 2\Lambda_o - c_{buo} + c_t} \quad (4.24)$$

Evaluating Eq. (4.24) numerically, $\theta_{bcr} \Lambda_i = 35.77^\circ$.

Load distribution at the contact between needle and ball has been obtained, as well as the joint angles where the assumption of linear load distribution stops being valid. Now the analysis will be done for the load distribution between needle and trunnion, following the same assumptions.

$$c_t \left(\frac{p_{tuij} + p_{tdij}}{2} \right) = p_{tmij} c_t = p_{ij} \quad (4.25)$$

Simplifying,

$$p_{tdij} = 2p_{tmij} - p_{tuij} \quad (4.26)$$

Case 1 occurs when $p_{tuij} = p_{tdij}$ and $\Lambda_i = 0$

Case 2 occurs when offset Λ_i is positive. Then, doing sum of moments with respect to point TD,

$$p_{ij} \left(\frac{c_t}{2} + \Lambda_i \right) - p_{tdij} c_t \left(\frac{c_t}{2} \right) - (p_{tuij} - p_{tdij}) \frac{c_t}{2} \left(\frac{2}{3} c_t \right) = 0 \quad (4.27)$$

Simplifying,

$$p_{ij} \left(\frac{c_t}{2} + \Lambda_i \right) - \frac{p_{t_{uij}} c_t^2}{3} - \frac{p_{t_{dij}} c_t^2}{6} = 0 \quad (4.28)$$

Case 3 occurs when offset Λ_i is negative. Then, doing sum of moments with respect to point TU,

$$-p_{ij} \left(\frac{c_t}{2} - \Lambda_i \right) + p_{t_{uij}} c_t \left(\frac{c_t}{2} \right) + (p_{t_{dij}} - p_{t_{uij}}) \frac{c_t}{2} \left(\frac{2}{3} c_t \right) = 0 \quad (4.29)$$

Simplifying,

$$-p_{ij} \left(\frac{c_t}{2} - \Lambda_i \right) + \frac{p_{t_{uij}} c_t^2}{6} + \frac{p_{t_{dij}} c_t^2}{3} = 0 \quad (4.30)$$

Equations (4.26) and (4.28) can be solved simultaneously to obtain $p_{t_{uij}}$ and $p_{t_{dij}}$ for Case 2,

$$p_{t_{uij}} = \frac{6p_{ij}}{c_t^2} \left(\frac{c_t}{2} + \Lambda_i \right) - 2p_{t_{mij}} \quad (4.31)$$

$$p_{tdij} = 4p_{tmij} - \frac{6p_{ij}}{c_t^2} \left(\frac{c_t}{2} + \Lambda_i \right) \quad (4.32)$$

When $p_{tdij} \leq 0$, the above solution is no longer valid since p_{tdij} cannot be negative. Additionally, such condition is not desired during the operation of the joint since load would be concentrated on a very small area. Thus, making $p_{tdij} = 0$ in Eq. (4.32) and solving for Λ_i it can be found the maximum offset allowed to have full needle support when Case 2 is present.

$$\Lambda_{cr\Lambda+} = \frac{2p_{tmij}c_t^2}{3p_{ij}} - \frac{c_t}{2} = \frac{c_t}{6} \quad (4.33)$$

Combining Eqs. (4.1), (2.2) and (2.18) with Eq. (4.33), when $\psi_i = 0$, $\Lambda_i = \Lambda_{cr\Lambda+}$ and $\theta_i \approx 0$ and solving for joint angle,

$$\cos \theta_{tcr\Lambda+} = \frac{3a}{3a - 2\Lambda_o + \frac{c_t}{3}} \quad (4.34)$$

The dimensions of the joint used for the experimental portion of this work are used to evaluate Eq. (4.34) and $\theta_{tcr\Lambda+} = 19.47^\circ$.

Similarly, Eqs. (4.26) and (4.30) can be solved simultaneously to obtain p_{tuj} and p_{tdij} for Case 3,

$$p_{tuj} = \frac{6}{c_t^2} \left(-p_{ij} \left(\frac{c_t}{2} - \Lambda_i \right) + \frac{2}{3} c_t^2 p_{tmij} \right) \quad (4.35)$$

$$p_{tdij} = 2p_{tmij} - \frac{6}{c_t^2} \left(-p_{ij} \left(\frac{c_t}{2} - \Lambda_i \right) + \frac{2}{3} c_t^2 p_{tmij} \right) \quad (4.36)$$

When $p_{tuj} \leq 0$ the above solution is no longer valid since p_{tuj} cannot be negative. Additionally, similar to Case 2, such condition is not desired during the operation of the joint since the load would be concentrated on a very small area. Thus, making $p_{tuj} = 0$ in Eq. (4.35) and solving for Λ_i , it can be found that the maximum offset is allowed to have full needle support when Case 3 is present.

$$\Lambda_{cr\Lambda-} = -\frac{2p_{tmij}c_t^2}{3p_{ij}} + \frac{c_t}{2} = -\frac{c_t}{6} \quad (4.37)$$

Similar to Case 2, Eqs. (4.37), (4.1), (2.2) and (2.18), are combined for $\psi_j = \pi/2$, $\Lambda_i = \Lambda_{cr\Lambda+}$ and $\theta_j \approx 0$. Then, it can be solved for the maximum joint angle with the full contact between needle and trunnion when the offset Λ_i is negative,

$$\cos \theta_{tcr \Lambda -} = \frac{a}{a + 2\Lambda_o + \frac{c_t}{3}} \quad (4.38)$$

and

$$\theta_{cr \Lambda} = \min(\theta_{bcr \Lambda +}, \theta_{bcr \Lambda -}, \theta_{tcr \Lambda +}, \theta_{bcr \Lambda -}) \quad (4.39)$$

Evaluating Eq. (4.38) numerically, $\theta_{tcr \Lambda -} = 28.84^\circ$. The lowest critical angle for the joint used in this work is $\theta_{tcr \Lambda +} = 19.47^\circ = \theta_{cr \Lambda}$. To illustrate this, loads per unit length p_{tuij} and p_{tuij} are plotted for p_{ij} , which is assumed to be 1000N, $\theta_o = 0$ and $\theta_o = 19.5^\circ$, as shown in Figure 4.7 and Figure 4.8.

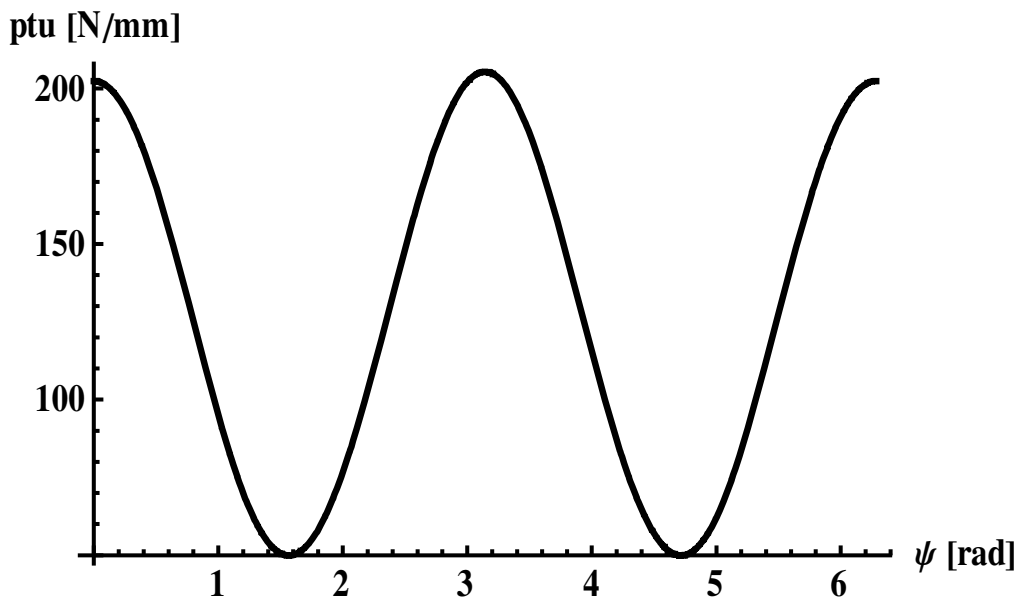


Figure 4.7. Load per unit length at upper end of needle, at 19.5°

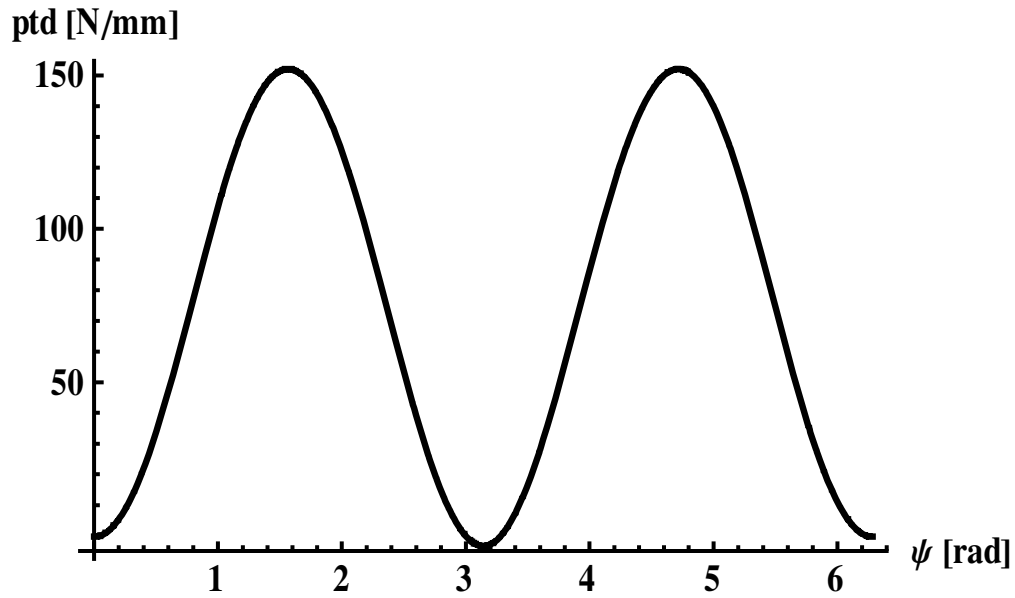


Figure 4.8. Load per unit length at lower end of needle, at 19.5°

Figure 4.8 shows that the load at the lower end of the needle gets slightly below zero, verifying the formulation of the critical angles. Initial joint offset Δ_o may be obtained from the geometry of the joint,

$$\Delta_o = a - \left(e_{spider} + c_{spacer} + \frac{\theta_o}{2} + \frac{b_{needle}}{2} \right) \quad (4.40)$$

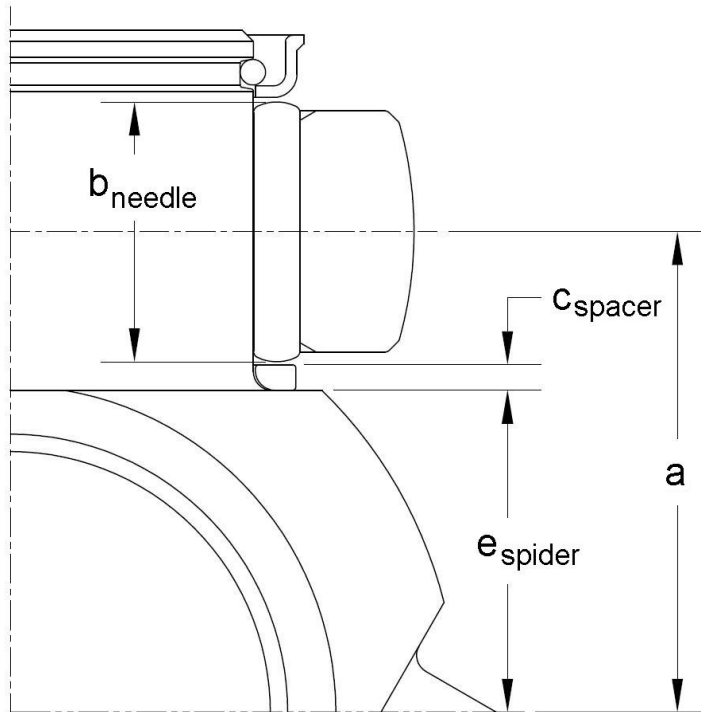


Figure 4.9. Spider Geometry

4.3 Normal load distribution on needles (radial direction)

In most roller bearings, the outer race is fully supported along its perimeter. In a tripod joint the outer perimeter of the spherical rollers is supported at only one contact point in its matching ball bore. This difference in boundary conditions changes the load distribution among needles due to the flexibility of the spherical roller (outer race). Harris [18] studied load distributions in bearings loaded at two points, used in planetary gears, Filleti and Rumbarger [19] also studied the case of a bearing supported at two points, collecting experimental data to verify their theoretical results, Papadopoulos [20] studied the load distribution in a roller bearing by experimental methods and Zhao [21] by finite element methods.

This work will apply the method developed by Harris [18] to estimate the radial load distribution on a trunnion. The main advantage of this method is its compactness and the ability to be easily incorporated into the program written to calculate kinematic and quasi-static variables in previous sections. The main disadvantage of the method is the assumption of considering outer races (balls in our case) as “thin rings” to calculate deflections. This assumption makes the method inaccurate when dealing with balls that are “thick rings”. Ugural and Fenster [22] consider that for curved beams in which the depth of the member is small relative to the radius of curvature, strain energy due to the bending can be approximated by that of a straight beam. Then, the deflections in a “thin ring” can be calculated under this assumption. The ratio used by Ugural and Fenster is given by,

$$\frac{R_b}{h_b} > 4 \tag{4.41}$$

and the formulation in this section will apply only to joints with the balls that meet this condition. Before proceeding to describe the method used to calculate the load distribution on the trunnion, the properties of the area defined by the radial cross section of the ball will be determined (Figure 4.10). The small chamfers cut in the ball to avoid sharp corners will be neglected for the purposes of calculating areas and second moments of area. The specifications of the geometry in Figure 4.10 are the following,

$$y_{bA} = \frac{1}{2} \sqrt{m_o^2 - c_{bw}^2} \quad (4.42)$$

$$\alpha_b = \arcsin\left(\frac{c_{bw}}{m_o}\right) \quad (4.43)$$

$$a_{b1} = \frac{2}{3} \left(\frac{m_o}{2}\right)^2 \alpha_b^3 (1 - 0.2\alpha_b^2 + 0.019\alpha_b^4) \quad (4.44)$$

$$a_{b2} = c_{bw} \left(y_{bA} - \frac{m_i}{2}\right) \quad (4.45)$$

$$a_b = a_{b1} + a_{b2} \quad (4.46)$$

$$y_{b1} = \frac{m_o}{2} \left(1 - 0.3\alpha_b^2 (1 - 0.0976\alpha_b^2 + 0.0028\alpha_b^4)\right) \quad (4.47)$$

$$y_{b2} = \frac{y_{bA}}{2} + \frac{m_i}{4} \quad (4.48)$$

$$R_b = \frac{y_{b1}a_{b1} + y_{b2}a_{b2}}{a_b} \quad (4.49)$$

$$I_{b1x} = 0.01143 \left(\frac{m_o}{2}\right)^4 \alpha_b^7 (1 - 0.3491\alpha_b^2 + 0.0450\alpha_b^4) \quad (4.50)$$

$$I_{b2x} = \frac{1}{12} c_{bw} \left(y_{bA} - \frac{m_i}{2}\right)^3 \quad (4.51)$$

$$I_{bxx} = I_{b1x} + I_{b2x} + (R_b - y_{b1})^2 a_{b1} + (R_b - y_{b2})^2 a_{b2} \quad (4.52)$$

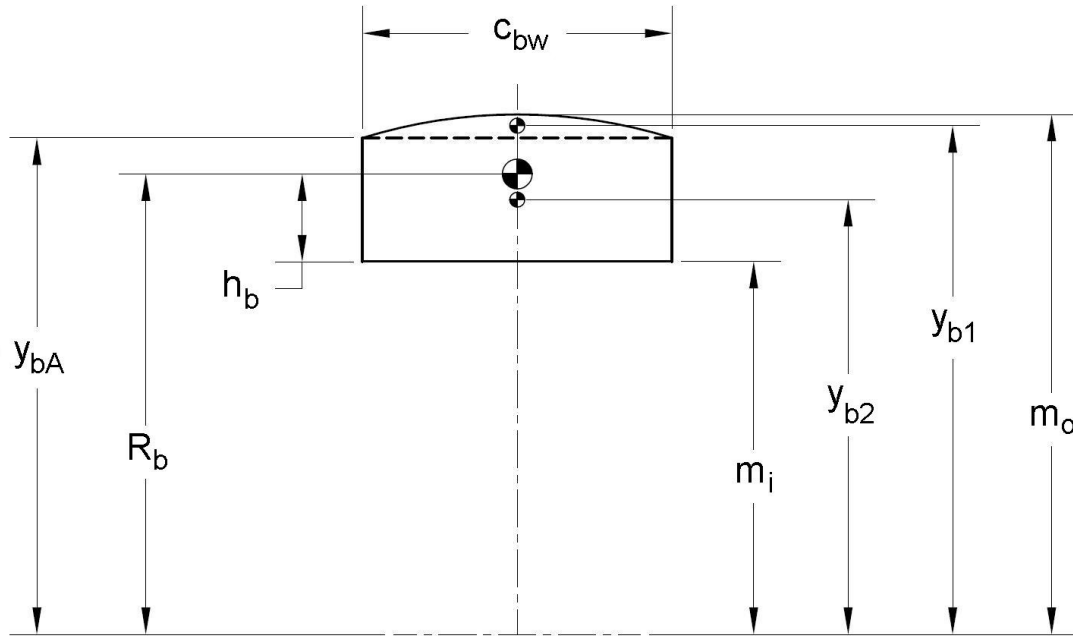


Figure 4.10. Cross section of spherical roller

Figure 4.11 shows schematically the loading on the spherical roller. Following the Harris' approach, only one half of the ball is analyzed due to the symmetry condition. Superposition is used in conjunction with the method of influence coefficients to calculate the radial deflections of the ball. The influence coefficient method implies,

$$p_v \Delta_u = \rho C_{uv} p_v \quad (4.53)$$

where, $p_v \Delta_u$ is the deflection at angle (position) ϕ_u due to the load p_v and ρC_{uv} is the influence coefficient. Similarly, the deflections $q \Delta_u$ experienced by the ring at angle ϕ_u due to the external load q_i applied to the ball can be obtained from Eq. (4.54).

$$q\Delta_u = q C_u q_i \quad (4.54)$$

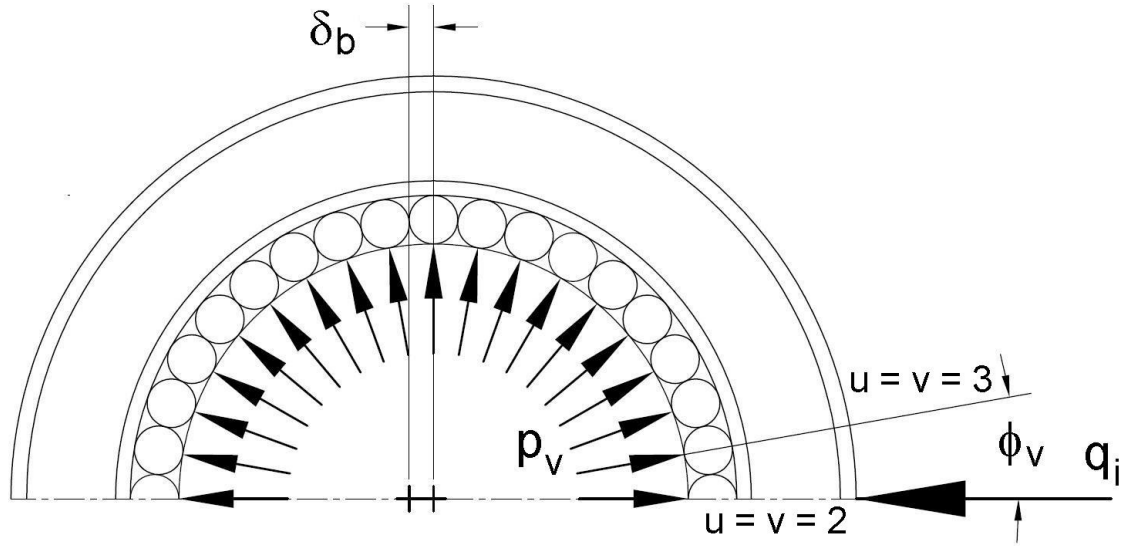


Figure 4.11. Schematic view of loads

The influence coefficients published by Harris [18] that can be applied to the tripod problem are given by Eqs. (4.55) and (4.56).

$$p C_{uv} = -\frac{2R_b^3}{\pi E_Y I_{bxx}} \sum_{m=2}^{\infty} \left(\frac{\cos(m\phi_v)}{(m^2 - 1)^2} \cos(m\phi_u) \right) \quad (4.55)$$

$$q C_u = \frac{2R_b^3}{\pi E_Y I_{bxx}} \sum_{m=2}^{\infty} \left(\frac{1}{(m^2 - 1)^2} \cos(m\phi_u) \right) \quad (4.56)$$

Using the principle of superposition, the radial deflection of the ring at angle ϕ_u can be obtained from Eq. (4.57),

$$\Delta_{u=q} = \Delta_u + \sum_v \rho_v \Delta_{u=q} C_{Uq} q_i + \sum_v \rho C_{UV} \rho_v \quad (4.57)$$

It is assumed that the center of the trunnion will remain in its original position after applying the load to the ball. Therefore, due to the contact deformations and clearance in the trunnion-needle-ball assembly, the center of the ball will displace a distance δ_b as shown in Figure 4.11. Thus, the relative radial approach δ_v between ball and trunnion at angle ϕ_v can be obtained from Eq. (4.58),

$$\delta_u = \delta_b \cos(\phi_u) + \Delta_{u=q} + \sum_v \rho_v \Delta_{u=q} C_{Uq} q_i + \sum_v \rho C_{UV} \rho_v \quad (4.58)$$

For the roller compressed between raceways Palmgren [18] gives the following equation,

$$\rho_v = k_p v_v^{n_r} \quad (4.59)$$

where k_p is a material constant defined for this work, based on Palmgren's approach, using effective contact lengths at trunnion and ball, as,

$$k_p = \left(\frac{1}{(1/k_{pt})^{1/n_r} + (1/k_{pb})^{1/n_r}} \right)^{n_r} \quad (4.60)$$

$$k_{pt} = 7.86 \times 10^4 c_t^{8/9} \quad (4.61)$$

$$k_{pb} = 7.86 \times 10^4 c_b^{8/9} \quad (4.62)$$

Deformation v_v is the difference between the relative radial approach δ_u and actual clearance between the trunnion and ball at angle ϕ_u . Therefore, the load at the needle roller with index v can be expressed as,

$$\begin{aligned} p_v &= k_p \left(\delta_u - \frac{1}{2}(m_i - 2d - t) - \Omega_v \right)^{n_r}; & \left(\delta_u - \frac{1}{2}(m_i - 2d - t) - \Omega_v \right) > 0 \\ p_v &= 0; & \left(\delta_u - \frac{1}{2}(m_i - 2d - t) - \Omega_v \right) \leq 0 \end{aligned} \quad (4.63)$$

The assumption is that the first roller position of the n needle rollers is right at the plane of symmetry of the trunnion. This needle roller is assigned the index $v = 2$. Thus, angle ϕ_v is defined as,

$$\phi_v = \frac{2\pi}{n}(v - 2 + \Gamma_o) \quad (4.64)$$

where $\Gamma_o = 0$ if the first roller is at the plane of symmetry. Otherwise, $\Gamma_o = 0.5$.

Similarly,

$$\phi_u = \frac{2\pi}{n}(v-2 + \Gamma_o) \quad (4.65)$$

The upper limit for both u and v is,

$$\Gamma = \text{Floor}\left(\frac{n}{2} + 2 - \Gamma_o\right) \quad (4.66)$$

So far only the displacements and deformations have been defined. Equilibrium of forces must be satisfied in the problem. Therefore, sum of forces on the trunnion must equal zero.

$$q_i - \sum_{v=2}^{\Gamma} (\Gamma_v p_v \cos \phi_v) = 0 \quad (4.67)$$

where $\Gamma_v = 0.5$ for $\phi_v = 0$. Otherwise, $\Gamma_v = 1$. Then, we have a set of Γ equations that is obtained combining and simplifying Eqs. (4.53) through (4.67). This set of equations can be solved simultaneously for δ_t and δ_2 through δ_{Γ} using a numerical method. Once the relative radial approaches have been determined the load at each trunnion can be obtained from Eq. (4.63).

4.4 Numerical examples of load distribution on trunnions

The equations to calculate load distribution on the trunnion were programmed and incorporated to the computer program developed and presented in Sections 2 and 3. The dimensions of the tripod used to generate numerical values in the previous sections (2 and 3) are used in this section as well. The computer program developed allows the calculation of load distribution at any joint angle. To show the effect of applied torque on load distribution and number of loaded needles, the tripod joint is analyzed at a joint angle of 2° and at a rotational position of 0° . A perfect round trunnion is assumed and the load distribution is calculated for different levels of applied torque. Table 4.1 summarizes the loads, reported in Newtons, on each needle roller versus percentage of yield torque (first row).

ϕ_V	100%	75%	50%	25%	10%
0°	7211	5302	3591	1810	763
10°	6233	4673	3124	1586	673
20°	4222	3189	2153	1112	471
30°	2479	1890	1287	665	251
40°	1298	990	658	303	35
50°	571	408	215	8	0
60°	168	51	0	0	0
70°	0	0	0	0	0

Table 4.1. Load distribution (N) at different proportions of yield torque

Figure 4.12 shows a graphical representation of the load distribution at 50% (solid line) and 25% (dashed line) of the nominal yield torque in the joint. The reader will notice that when a higher torque is applied more needles will be loaded. Ideally, a round trunnion is “round” but in reality most trunnions have some type of lobing or waviness occurred during the manufacturing processes. In center-less grinding processes the trunnions tend to be tri-lobal or penta-lobal. The small deviations from the basic circle that generate the lobes in the trunnion are in the order of microns and can only be checked with specialized equipment. In later sections actual measurements of parts will be shown. The lobing in the trunnion will cause needles that roll at the peaks of the undulations to be more heavily loaded than those that roll at the valleys.

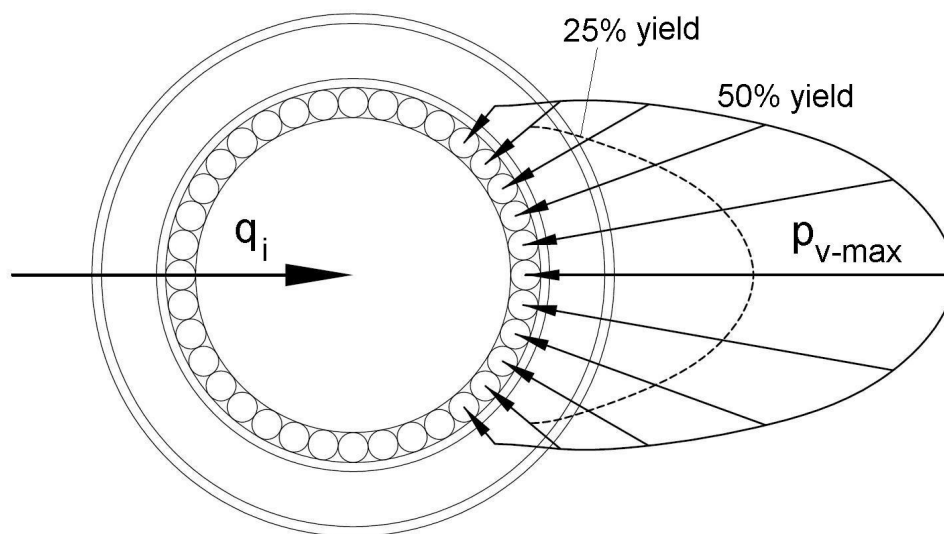


Figure 4.12. Load distribution at 25% and 50% of yield torque

For a single harmonic causing lobing in the trunnion the function that defines the deviation from the basic circle can be written as,

$$\Omega_V = \Omega_O \cos(h_W \phi_V) \quad (4.68)$$

With more than one frequency, amplitude and phase that need to be considered to estimate the undulations in the trunnion, Eq. (4.68) can be expanded to Eq. (4.69) and be substituted in Eq. (4.63).

$$\Omega_V = \sum_{w=2}^{\infty} (\Omega_W \cos(h_W \phi_V)) + \sum_{w=2}^{\infty} (\Omega_W \sin(h_W \phi_V)) \quad (4.69)$$

Figure 4.13 shows a comparison of load distribution at 50% of yield torque between a perfect circular trunnion (solid line) and a penta-lobed trunnion (dashed line), roundness error is in the order of 0.010mm. The shape of the penta-lobed trunnion (phantom line) has been exaggerated for clarity purposes.

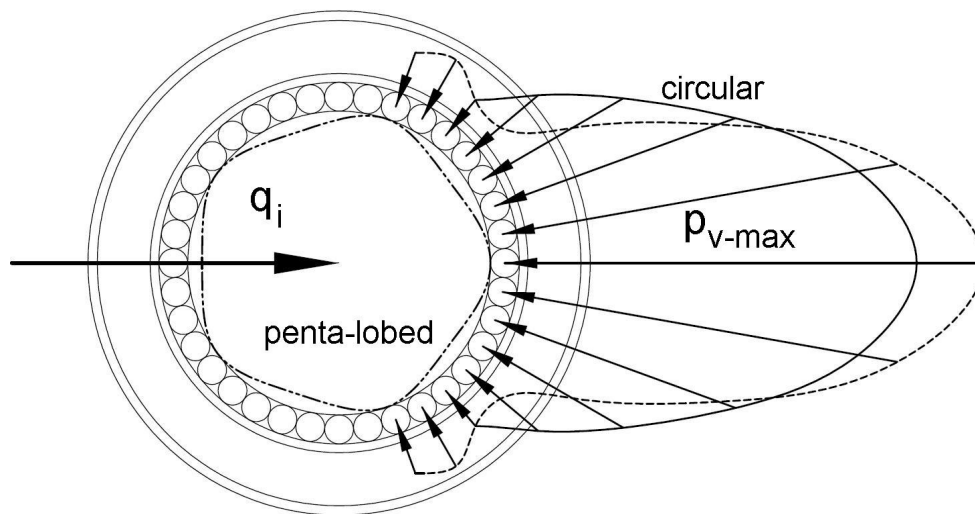


Figure 4.13. Load distribution at 50% of yield torque, perfect vs. lobed trunnion

It can be observed that even though the load in some of the needles is lower due to the pentagon shape the central needle will be more heavily loaded than those in the circular case. This difference in the load magnitude will increase the contact stresses and reduce the wear life of the part. The contact stresses and estimated fatigue life will be studied in subsequent sections of this work.

The shape of the trunnion can also be made different from a perfect circle to have a better load distribution and/or to reduce the highest load in the distribution. “Elliptical-like” shapes have been used by Harris [18] in roller bearings and Orain in tripod joints [15]. Such “elliptical” shapes may not match the mathematical definition of an ellipse but “elliptical” is a generic name that has been used in industry.

Figure 4.14 shows a comparison at 50% of yield torque between a perfect circular trunnion (solid line) and a perfect elliptical trunnion (dashed line), where the difference between the semi-major axis and the semi-minor axis is 0.031mm. The minor axis is parallel to the spider axis. The radial deviations of the ellipse with respect to its minimum circumscribed circle are given by Eq. (4.70). It can be combined with Eq. (4.69) to form Eq. (4.71) and take into account the shape of the ellipse and its waviness due to manufacturing. Then, Eq. (4.71) can be substituted in Eq. (4.63) to calculate the load distribution on the trunnion.

$$\Omega_V = -\frac{t}{2} \left(1 - \sqrt{\cos\left(\phi_V + \frac{\pi}{2}\right)^2 + \frac{1}{e_t^2} \sin\left(\phi_V + \frac{\pi}{2}\right)^2} \right) \quad (4.70)$$

$$\Omega_V = -\frac{t}{2} \left(1 - \sqrt{\cos\left(\phi_V + \frac{\pi}{2}\right)^2 + \frac{1}{e_t^2} \sin\left(\phi_V + \frac{\pi}{2}\right)^2} \right) \quad (4.71)$$

$$+ \sum_{w=2}^{\infty} (\Omega_w \cos(h_w \phi_V)) + \sum_{w=2}^{\infty} (\Omega_w \sin(h_w \phi_V))$$

Variable e_t is the elliptical ratio of the trunnion, defined as the ratio of the major to the minor axis. More terms could be added to Eq. (4.71) and virtually any possible trunnion shape could be analyzed.

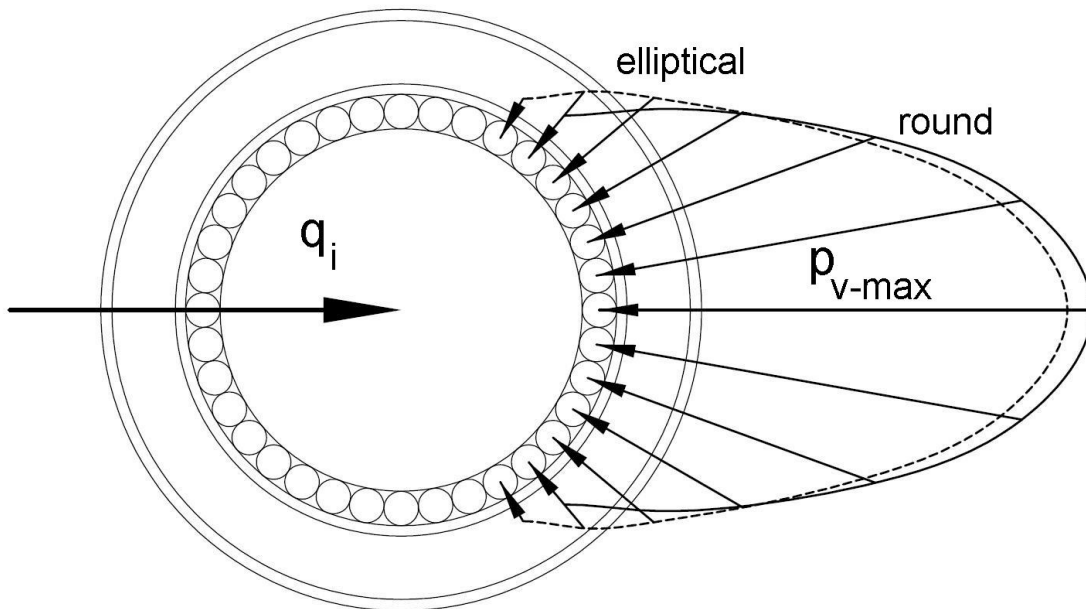


Figure 4.14. Load distribution at 50% of yield torque, circular vs. elliptical trunnion

4.5 Making trunnion load distribution a function of joint angle

After finding out how loads are distributed in a tripod joint it is necessary to relate them to the displacements of the internal components, caused by the rotation of the joint at angle, in order to estimate the fatigue cycles. It is assumed that the load profile on a trunnion, such as that shown in Figure 4.12, will change as a function of the normal load between ball and ball bore. The instantaneous position of the rollers may also affect the load distribution when they are not symmetrically positioned. However, the variation in load distribution profile due to non-symmetrical conditions is assumed to be small and will be neglected. The loads when the rollers are located at non-symmetrical positions will be obtained interpolating within the load distribution profile obtained from the symmetrical case. Observation of tripod joints tested in the Nexteer Automotive validation labs suggests wear tends to start at the intersection of the trunnion surface and spider plane, which is the region where a roller will see the highest possible loads and more fatigue cycles. The reader may refer to Figure 4.15 which shows an example of initial wear in a spider trunnion [23].



Figure 4.15. Example of initial wear in a trunnion

It is necessary to define the position of a roller with respect to the plane of symmetry of the load distribution. This position is defined by angle χ_{ij} , which can be obtained from Eq. 4.72 and is shown in Figure 4.16.

$$\chi_{ij} = \phi_{ij} - \varepsilon_i \tag{4.72}$$

where i is the trunnion index and j is the needle index

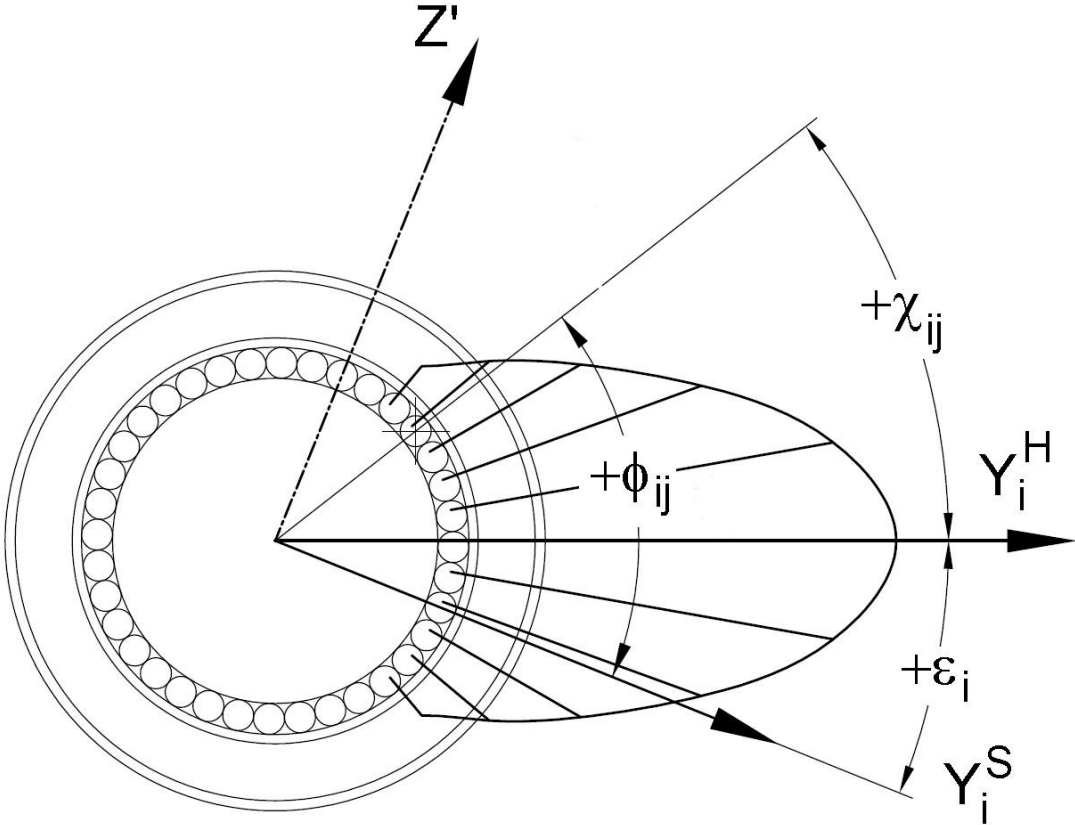


Figure 4.16. Position of roller within load profile

Once χ_{ij} is known, the load acting on a roller at any position within the load profile may be calculated from Eqs. (4.73) and (4.74). Eq. (4.73) is an interpolation function that uses positions ϕ_v and loads p_v , calculated from Eqs. (4.63) and (4.64), as data points.

$$\Psi = \text{Interpolation}[\{\{\phi_v, p_v\}, \dots, \{\phi_\Gamma, p_\Gamma\}\}] \quad (4.73)$$

where $v = 2, 3, \dots, \Gamma$

$$p_{ij} = \Psi[\chi_{ij}] \quad (4.74)$$

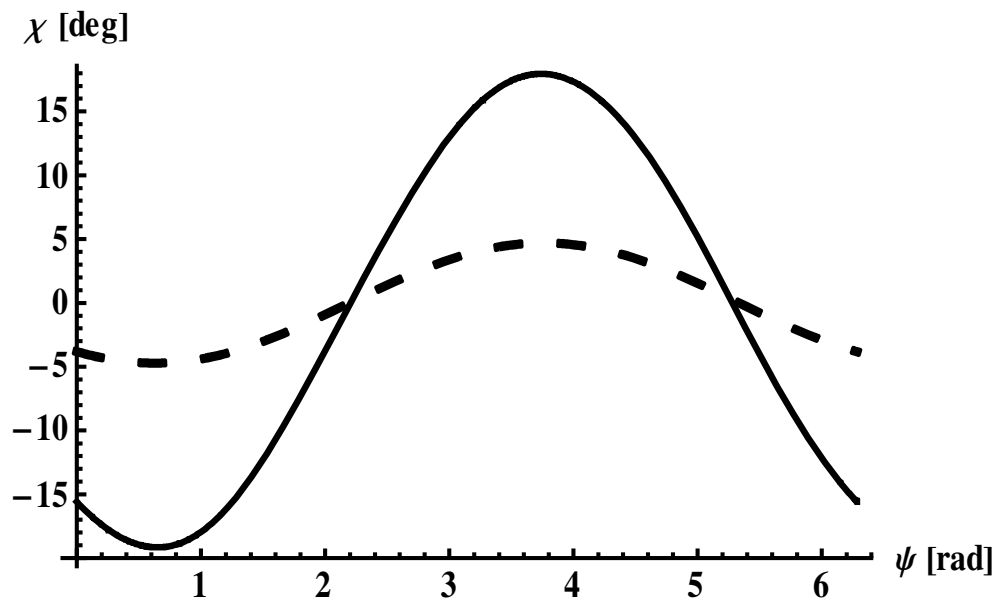


Figure 4.17. Roller position with respect to symmetry plane of loading profile

The angle χ_{11} , obtained using Eq. (4.72), is plotted in Figure 4.17 at 23° (continuous line) and 6° (dashed line). The reader is asked to remember that the calculated critical angle in Section 2 was very close to 6° . That is why the peak-valley amplitude of χ_{11} at 6° is very similar to the needle spacing $360^\circ / n$, where $n = 36$.

Figure 4.18 shows the load profile at a joint angle of 6° and zero angular displacement ψ , when an input torque of 1059Nm is applied. Eqs. (4.73) and (4.74) were used to obtain the load profile. The type of interpolation chosen is a third order type.

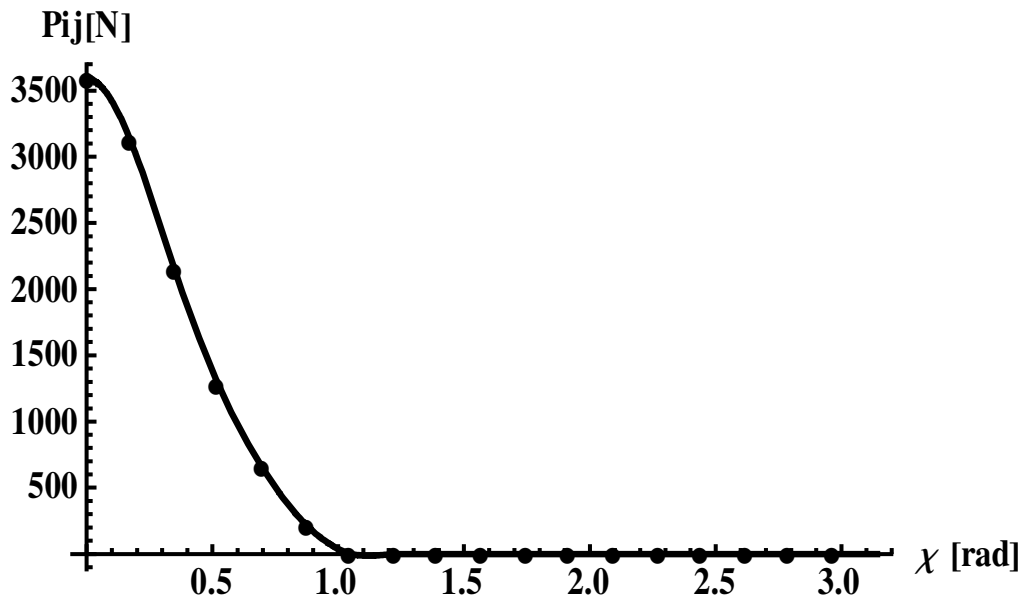


Figure 4.18. Load profile at joint angle of 6°

5. STATE OF STRESS AT THE ROLLER-TRUNNION CONTACT

5.1 Introduction

This section deals with the state of stress at the roller-trunnion contact. The first introductory part of this section explains the state of stress using a Hertzian formulation for line contacts. In the second part, the contact stress problem is solved using a numerical technique based on the Boussinesq solution for point loads. The following assumptions are made:

- a) The yield limit of the material is not exceeded. In other words, all deformation occurs in the elastic range.
- b) Loading is perpendicular to the surface.

The contact area dimensions are small compared to the radii of curvature of the roller and trunnion. In the third part of this section it is studied the effects of needle roller crowning and the stress distribution when the applied load is non-symmetrical. In the fourth part sub-surface stress calculations are described.

In Section 4 it was stated that the contact region to show the first signs of wear is the contact between trunnion and needle rollers. Contact stresses between balls and needle rollers and pressure distribution between balls and housing ball bores are not studied in this work.

5.2 Hertzian formulation for line (cylindrical) contacts

The Hertz solution to a general contact problem is not discussed here. The reader is referred to contact stress and elasticity books such as those written by Ugural [22] and Johnson [24].

A line contact exists, as its name clearly states, when the contact between two bodies is along a line and not at a single point. Line contact is an ideal condition where two bodies of cylindrical shape are in contact and have the same length. A schematic representation of a line contact is shown in Figure 5.1. The area of contact is a narrow rectangle of width $2b_h$ and length l_h . Pressure distribution is elliptical. The half width b_h is given by Eq. (5.1), the elliptical pressure distribution σ_h is given by Eq. (5.2) and the maximum pressure σ_{hmax} is given by Eq. (5.3) [18].

$$b_h = \sqrt{\frac{4p_{ij} \left(\frac{1-\nu_s^2}{E_Y} + \frac{1-\nu_s^2}{E_Y} \right)}{l_h \pi \left(\frac{1}{d} + \frac{1}{t} \right)}} \quad (5.1)$$

$$\sigma_h = \frac{2p_{ij}}{b_h l_h \pi} \sqrt{1 + \left(\frac{x}{b_h} \right)^2} \quad (5.2)$$

$$\sigma_{hmax} = \frac{2p_{ij}}{b_h l_h \pi} \quad (5.3)$$

In this work it is assumed that the Poisson's ratio of steel is 0.3. Both needle roller and spider are made of steel. Therefore, Eq. (5.1) can be simplified to,

$$b_h = 1.522267 \sqrt{\frac{p_{ij}}{l_h E_Y} \frac{d \cdot t}{d+t}} \quad (5.4)$$

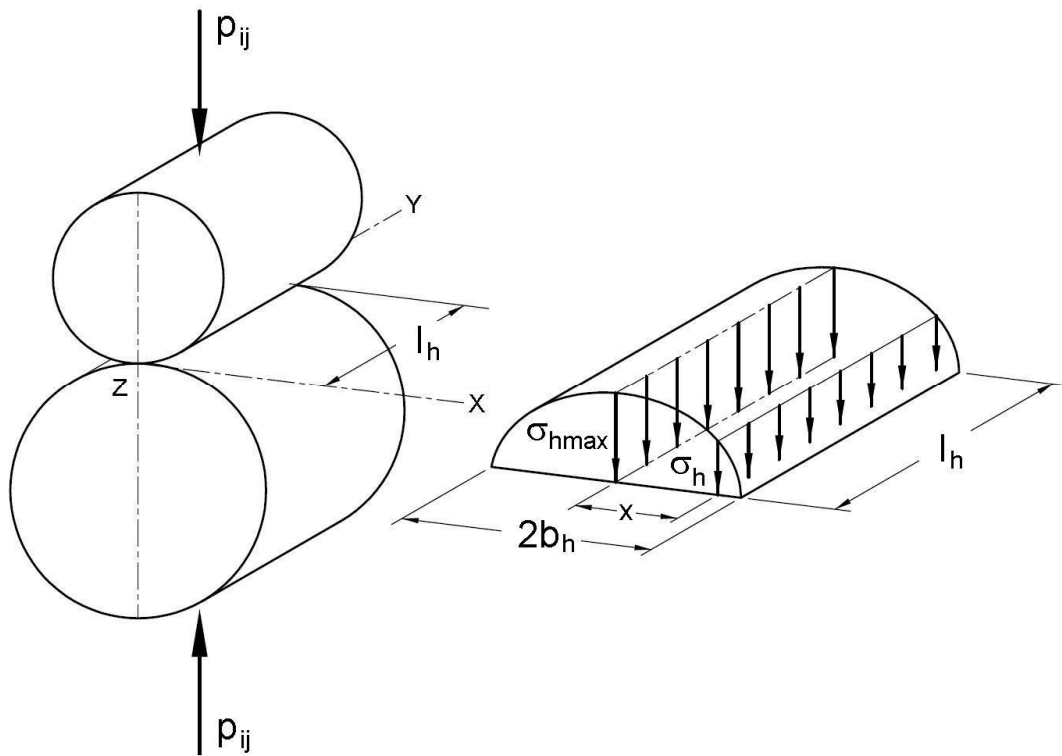


Figure 5.1. Ideal cylindrical contact

Experimental evidence in roller bearings [18] suggests that surface fatigue is originated at points below the stressed surface. Experimental evidence shows that CV joints operating under normal conditions will fail due to sub-surface fatigue (also named “spalling”) [25]. Therefore, it is of interest in this work to know the state of stress in the contact region below the surface. Eqs. (5.5) through (5.11) define the sub-surface stress components [24], along the Z-axis, shown in Figure 5.1.

$$\sigma_{hx} = -\sigma_{hmax} \left(\frac{1 + 2\left(\frac{z}{b_h}\right)^2}{\sqrt{1 + \left(\frac{z}{b_h}\right)^2}} - 2\left|\frac{z}{b_h}\right| \right) \quad (5.5)$$

$$\sigma_{hy} = -2\nu_s \sigma_{hmax} \left(\sqrt{1 + \left(\frac{z}{b_h}\right)^2} - \left|\frac{z}{b_h}\right| \right) \quad (5.6)$$

$$\sigma_{hz} = -\frac{\sigma_{hmax}}{\sqrt{1 + \left(\frac{z}{b_h}\right)^2}} \quad (5.7)$$

$$\sigma_{h1} = \sigma_{hy} \quad 0 \leq z \leq 0.436b_h \quad (5.8)$$

$$\sigma_{h1} = \sigma_{hx} \quad z > 0.436b_h \quad (5.9)$$

$$\sigma_{h3} = \sigma_{hz} \quad (5.10)$$

$$\tau_h = \frac{\sigma_{h1} - \sigma_{h3}}{2} \quad (5.11)$$

The stress components and the maximum principal shear are plotted and shown in Figure 5.2, where the continuous line represents principal shear, the small-dashed line represents σ_{hy} , the medium-dashed line represents σ_{hx} and the large-dashed line represents σ_{hz} . It is noted that the principal stress $\sigma_{h1} = \sigma_{hy}$ changes to $\sigma_{h1} = \sigma_{hx}$ at $z = 0.436b_h$. The peak value of the maximum shear occurs at $z = 0.786b_h$, with a value of $0.3\sigma_{hmax}$.

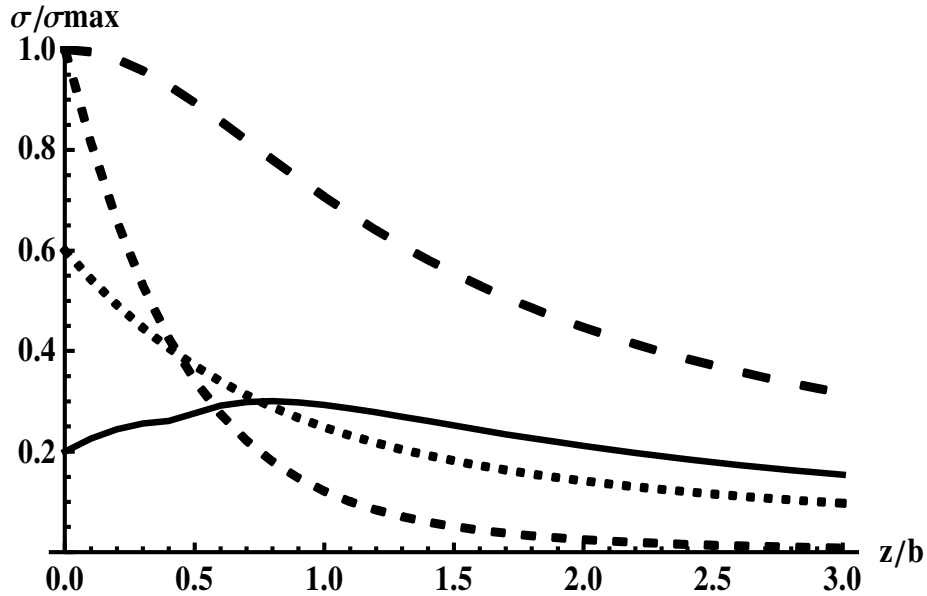


Figure 5.2. Subsurface stresses along the plane of symmetry of the contact

Hertz provided an analytical solution for the load-deflection relationship of a point contact but not for a line contact. Others have established load-deflection relationships based on some experiments. Teutsch and Sauer [26] compiled and compared most of the published load-deflection relationships for rollers in contact. The contact roller to trunnion in this work is equivalent to the contact between a roller and an inner race. Teutsch found that Palmgren's relationship for a roller to inner race contact has deviated somewhat with respect to more modern and sophisticated relationships. The main advantage of Palmgren's load-deflection relationship is its closed form and simplicity. It is described as Eq. (5.12).

$$\alpha_{ij} = 3.84 \times 10^{-5} \frac{p_{ij}^{0.9}}{c_t^{0.8}} \quad (5.12)$$

5.3 Non-Hertzian formulation for line (cylindrical) contacts

Several authors, Conry and Seireg [27], Singh and Paul [28], Oh and Trachman [29] and Hartnett [30], have tried to solve Non-Hertzian contact problems using numerical techniques based on the Boussinesq solution for a concentrated load, applied normally to a homogeneous elastic space. Other authors, Harris [18] and Teutsch and Sauer [26], have tried to solve the pressure and force distribution in line contacts using slicing techniques.

The numerical solution published by Hartnett [30] has the advantage of being three dimensional. This solution divides the contact regions in rectangles and superposition can be used to calculate sub-surface stresses. Hartnett's method was programmed and its convergence was verified in this work with a relatively simple problem: Contact of a sphere on a plane. The validity of Hartnett's numerical solution to line contact problems has been verified experimentally by Hartnett and Kannel [31].

The contact of two elastic bodies is shown in Figure 5.3. The origin of the coordinate system is located at the first point of contact. If two arbitrary points are brought into contact by the displacement α of body 1 to body 2, the displacements v_1 and v_2 , and the initial separations z_1 and z_2 of the points inside the contact region, can be described by Eq. (5.13), and by Eq. (5.14) outside of the contact region.

$$v_1 + v_2 + z_1 + z_2 = \alpha \tag{5.13}$$

$$v_1 + v_2 + z_1 + z_2 \geq \alpha \quad (5.14)$$

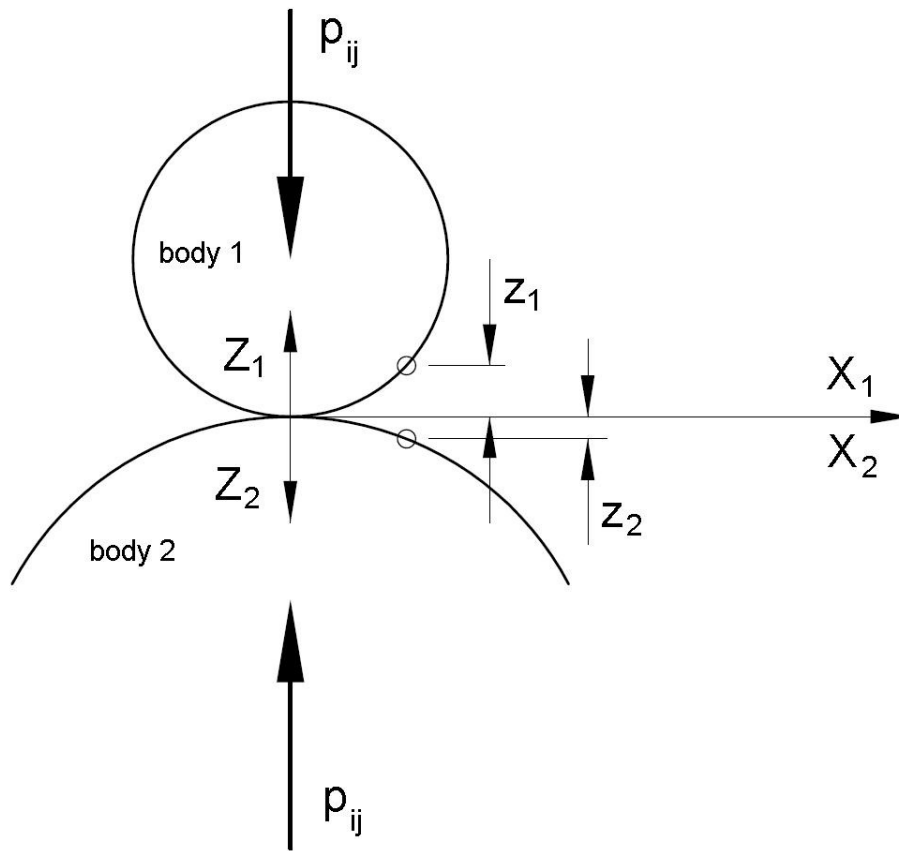


Figure 5.3. Two bodies in contact

If the area of contact is divided in r rectangles and it is assumed that each rectangle has a uniform pressure s_n , then, the sum of pressures times the area of the rectangular element equals the applied load p_{ij} . This is expressed as Eq. (5.15), where the product $4ab$ is the area of a single rectangular element.

$$4ab \sum_{n=1}^r s_n = p_{ij} \quad (5.15)$$

It is assumed that negative pressures may not occur on the contact surface.

Therefore,

$$s_n \geq 0 \quad (5.16)$$

The pressure s_n on an element n will cause a deflection at the element n and a deflection at an element m in the contact region and vice versa. Then, using superposition, the total displacement at an element m is given by Eq. (5.17).

$$\sum_{n=1}^r s_n f_{mn} = \alpha - z_{1m} - z_{2m} \quad (5.17)$$

and the influence coefficients f_{mn} are given by Eq. (5.18), which comes from integrating the Boussinesq solution for a normal point load.

$$\begin{aligned}
f_{mn} = \kappa & \left[(x+b) \ln \left(\frac{(y+a) + \sqrt{(y+a)^2 + (x+b)^2}}{(y-a) + \sqrt{(y-a)^2 + (x+b)^2}} \right) + \right. \\
& (y+a) \ln \left(\frac{(x+b) + \sqrt{(y+a)^2 + (x+b)^2}}{(x-b) + \sqrt{(y+a)^2 + (x-b)^2}} \right) + \\
& (x-b) \ln \left(\frac{(y-a) + \sqrt{(y-a)^2 + (x-b)^2}}{(y+a) + \sqrt{(y+a)^2 + (x-b)^2}} \right) + \\
& \left. (y-a) \ln \left(\frac{(x-b) + \sqrt{(y-a)^2 + (x-b)^2}}{(x+b) + \sqrt{(y-a)^2 + (x+b)^2}} \right) \right]
\end{aligned} \tag{5.18}$$

where κ is a material constant, given by Eq. (5.19), when the contacting bodies are made of the same material.

$$\kappa = 2 \frac{(1-\nu_s^2)}{E_s \pi} \tag{5.19}$$

Thus, the problem consists of solving the set of linear equations, given by Eq. (5.15) and Eq. (5.17), constrained by Eq. (5.16), for α and s_n . A combination of the Newton-Raphson and the Gauss-Seidel methods is used in this work to solve the set of equations.

A sphere-plane contact was evaluated and compared to the exact solution to debug the code. The radius of the sphere is 10mm and the applied load is 100N. It was

assumed both contacting bodies are made of steel. The exact solutions for contact patch radius, maximum stress and displacement are [32]:

$$a_{ball} = 0.881 \left(\frac{2r_{ball}w}{E_Y} \right)^{\frac{1}{3}} \quad (5.20)$$

$$\sigma_{ball\ max} = 0.616 \left(\frac{E_Y^2 w}{4r_{ball}} \right)^{\frac{1}{3}} \quad (5.21)$$

$$\alpha_{ball} = 1.55 \left(\frac{w^2}{2E_Y^2 r_{ball}} \right)^{\frac{1}{3}} \quad (5.22)$$

where, w is the applied load at the contact. Using Eq. (5.20) it is found that the radius of the contact patch is 0.1873mm. Therefore, a rectangular mesh of 0.4mm x 0.4mm was used. When it is not possible to obtain an initial approximation of the size of the contact patch, a coarse mesh can be used to get a rough estimate of the size of the contact area. Then, the mesh can be refined. Table 5.1 shows the convergence of the approximate solution as the number of elements is increased and compares to the exact solution.

Mesh	$\sigma_{ball\ max}$ [MPa]	α_{ball} [mm]
3 x 3	1443.7	0.003431
5 x 5	1367.4	0.003463
7 x 7	1366.3	0.003486
9 x 9	1366.5	0.003499
11 x 11	1364.7	0.003500
15 x 15	1364.4	0.003505
41 x 41	1362.4	0.003505
Exact	1362.3	0.003504

Table 5.1. Convergence of maximum pressure and deflection

The reader may observe that with a relatively small number of elements a good approximation may be obtained.

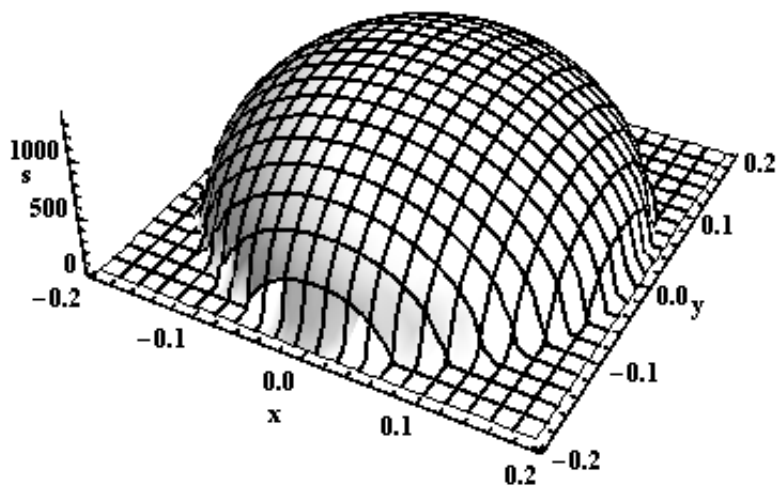


Figure 5.4. Pressure distribution in a sphere-plane contact

Figure 5.4 shows the pressure distribution in the contact, calculated using a 41 x 41 mesh. Once the program has been verified it can be proceeded to analyze the roller to trunnion contact.

In Section 4 it was found that the load on a needle roller varies within one revolution of the tripod joint. It was also found that the applied load is not always symmetrical. This section deals with the contact problem only. Therefore, an arbitrary load and an arbitrary position of the load will be used to exemplify the pressure distribution in the contact. In a later section of this work, the stress distributions will be calculated for different positions of the tripod joint to estimate fatigue life.

The peak load on the trunnion at 25% of the yield torque of the joint, from Table 4.1 is selected arbitrarily. It is assumed an initial effective contact length c_t of 9.9mm, based on the geometry of the needle. The semi-width of the contact area, maximum contact pressure and deflection, per Hertz solution, may be obtained from Eq. (5.4), Eq. (5.3) and Eq. (5.12), respectively. Such values are,

$$b_h = 0.0432mm$$

$$\sigma_{hmax} = 2694.1MPa$$

$$\alpha_j = 0.00524mm$$

For the first numerical solution it was assumed no crowning on the needle and a sharp transition at the end of the contact length. The discontinuity caused by the sharp edge generates a stress concentration, which is captured by the numeric model. The reader will observe in Table 5.2 that the more refined the mesh the higher the stress at the edge of the contact. This makes sense since the stress at a discontinuity, assuming the material doesn't yield, tends to infinite. The size of the grid was 0.1mm x 9.9mm.

Mesh	σ_{hmax} [MPa]	$\sigma_{hcenter}$ [MPa]	α [mm]
9 x 11	2910.3	2623.1	0.006477
13 x 13	2942.0	2605.9	0.006464
21 x 21	3058.2	2604.5	0.006448
41 x 41	3296.9	2597.7	0.006430

Table 5.2. Convergence of maximum pressure and deflection

The difference in the stress value with respect to the Hertzian formulation can be explained due to the stress concentrations at the edge. The difference in deflection can be explained due to the lack of crowning since Palgrem's equation was experimentally developed for rollers with a specific type of crowning on a flat surface. Figure 5.5 shows the pressure distribution in the line contact for the 41 x 41 mesh.

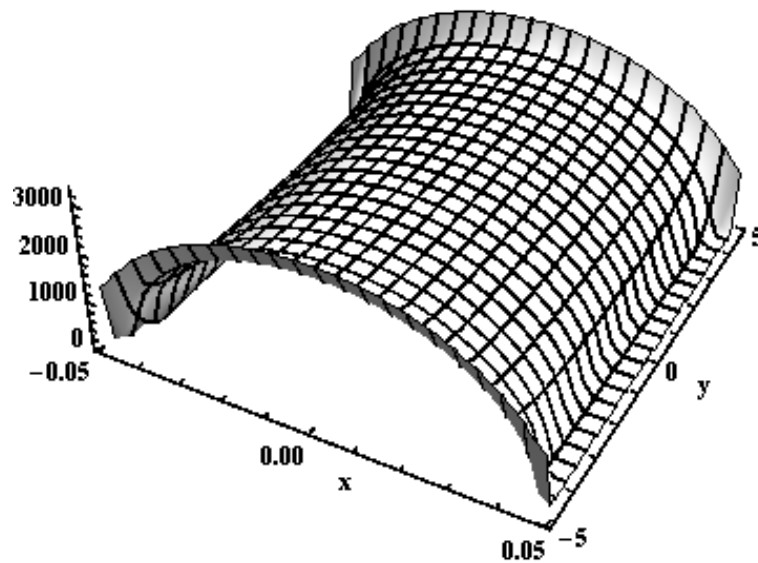


Figure 5.5. Pressure distribution in a cylinder contact

5.4 Non-Hertzian formulation for contact of rollers with crowning

Needle rollers are typically made by grinding its diameter to a given size. Subsequently, a tumble polishing process is used to remove sharp edges. The polishing process causes crowning at the end of the needle rollers. Crowning is defined in this work as a convex deviation from a perfect cylindrical form. Figure 5.6 shows the dimensions of the needle roller considered and used in this work. Eq. (5.23) and Eq (5.24) are the mathematical representation of the crowning in such roller.

Crowning starts at a distance of 2mm from the end of the needle. This distance will vary depending on the length and diameter of the needle roller.

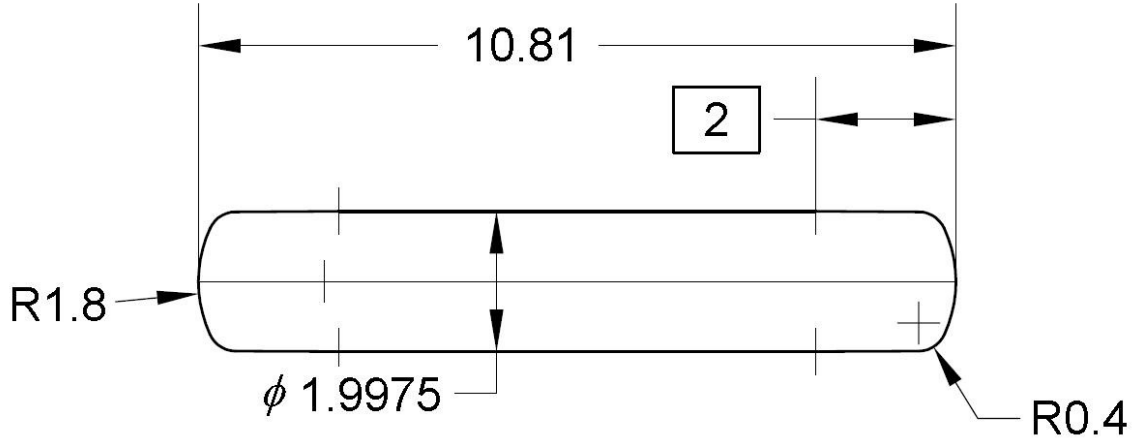


Figure 5.6. Needle roller dimensions

$$z_{CW} = 0.002(\exp(y) - 1) \quad \text{for } y \leq 1.47237 \quad (5.23)$$

$$z_{CW} = 0.4067033 - \sqrt{0.4^2 - (y - 1.46881)^2} \quad \text{for } y > 1.47237 \quad (5.24)$$

where the origin of the reference frame is at the gage height of 2mm, as shown in Figure 5.6. It must be noted that crowning is symmetrical. The portion of the roller between the 2mm gage heights is assumed to be a perfect cylinder. Thus, if Eq. (5.23) and Eq. (5.24) are rewritten with respect to roller's transversal plane of symmetry, crowning can be expressed as,

$$z_{CW} = 0 \quad \text{for } |y| \leq 3.405 \quad (5.25)$$

$$z_{CW} = 0.002(\exp(|y| - 3.405) - 1) \quad \text{for } 3.405 < |y| \leq 4.87737 \quad (5.26)$$

$$z_{CW} = 0.4067033 - \sqrt{0.4^2 - (|y| - 4.87381)^2} \quad \text{for } |y| > 4.87737 \quad (5.27)$$

Figure 5.7 shows a graphical representation of crowning, based on Eqs. (5.25) through (5.27), for the needle roller used in this work.

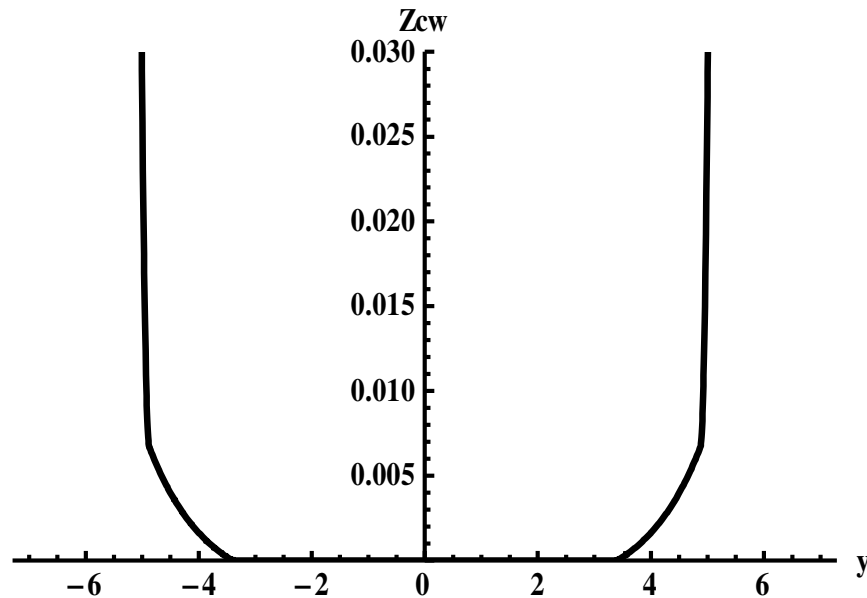


Figure 5.7. Crowning of 10.81mm needle roller

The formerly mentioned equations are incorporated into the contact model and the pressure distribution is recalculated. Such distribution is shown in Figure 5.8a and Figure 5.8b. The reader will notice that there is still a slight “edge contact” effect. Such effect could be reduced or eliminated by introducing more crowning. Table 5.3 shows the convergence of the solution as the mesh was refined.

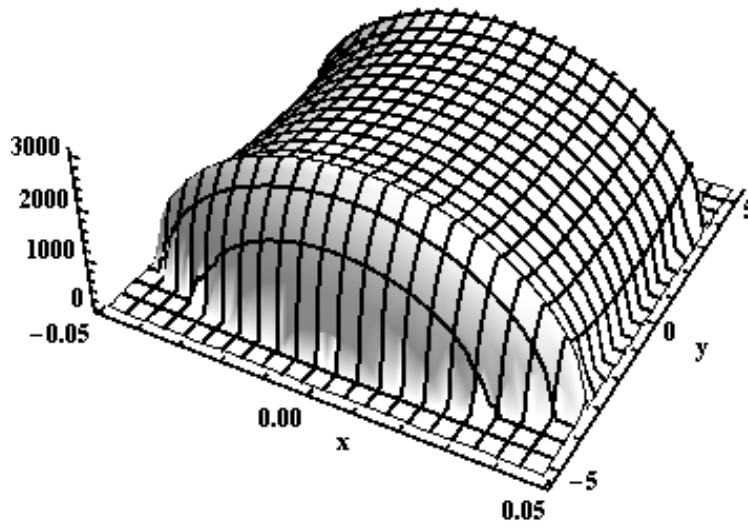


Figure 5.8a. Pressure distribution of needle roller with crowning

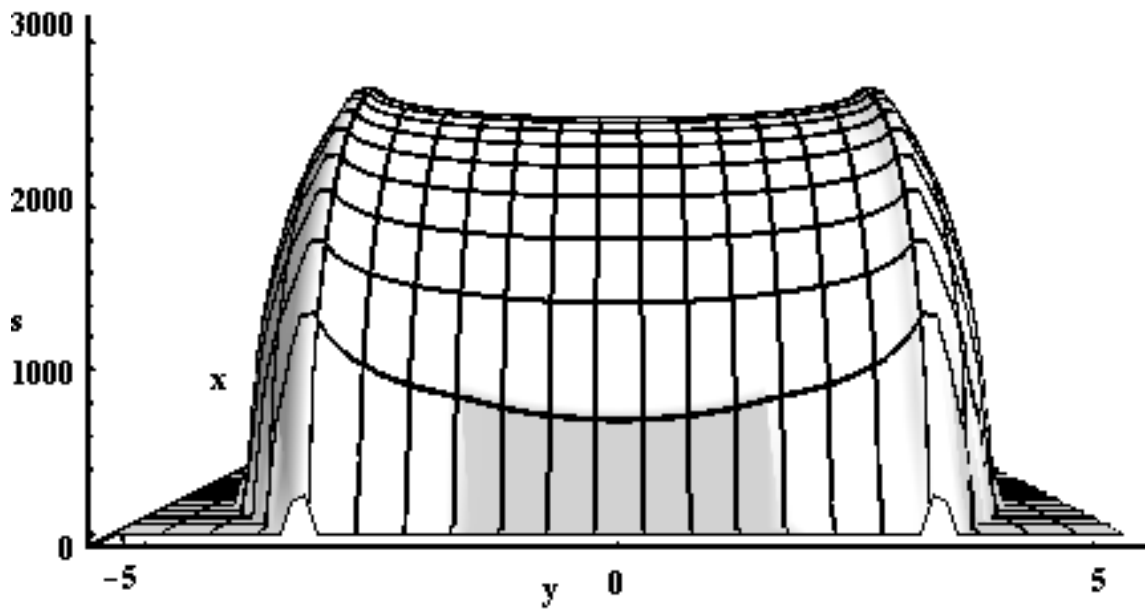


Figure 5.8b. Lateral view of pressure distribution of needle roller with crowning

Mesh	σ_{hmax} [MPa]	$\sigma_{hcenter}$ [MPa]	α [mm]
9 x 9	2980.5	2869.9	0.007492
13 x 13	3035.2	2837.2	0.007346
21 x 21	2993.7	2841.7	0.007384
41 x 41	3083.9	2840.3	0.007379
41 x 81	3066.1	2840.2	0.007379

Table 5.3. Convergence of maximum pressure and deflection

So far the assumption has been that the needle roller axis is parallel to the trunnion axis. This occurs only when there is no clearance in the trunnion-roller-ball assembly. Manufacturing processes have variation and interference is not desired in the design. Therefore, the trunnion-roller-ball assembly is designed with clearance. Such clearance allows “skewing” of the needle roller. When the roller skews the “edge contact” effect is eliminated since the ends of the needle are not in direct contact with the trunnion. Figure 5.9 shows a needle skewed with respect to the trunnion.

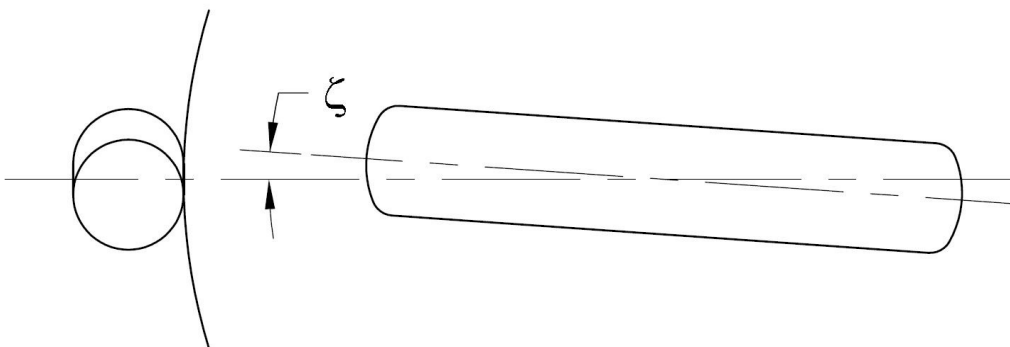


Figure 5.9. View of needle skewing

The clearance at the ends of the needle due to the skewing can be modeled as additional crowning. Such equivalent crowning is given by Eq. (5.28) and Eq. (5.29).

$$r_{sk} = \sqrt{\left(\frac{t}{2} + \frac{d}{2}\right)^2 - (y \tan(\zeta))^2} - \left(\frac{t}{2} + \frac{d}{2}\right) \quad (5.28)$$

$$z_{sk} = \cos\left(\arctan\left(\frac{y \tan(\zeta)}{\frac{t}{2} + \frac{d}{2}}\right)\right) r_{sk} \quad (5.29)$$

where y is the distance from the initial contact point. It may be noticed that the sign of y does not influence the value of the equivalent crowning. Skew angles of needle rollers in tripod joints are typically around 4° . Eq. (5.28) and Eq. (5.29) were added to the contact model and the pressure distribution was recalculated considering a skew angle of 4° . A mesh of 41×41 elements was used. Figure 5.10a and Figure 5.10b show the pressure distribution including skewing effect.

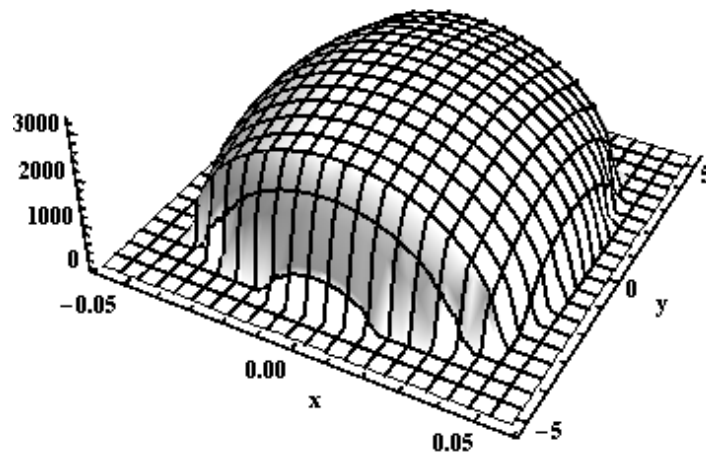


Figure 5.10a. Pressure distribution of needle roller with crowning and skewing

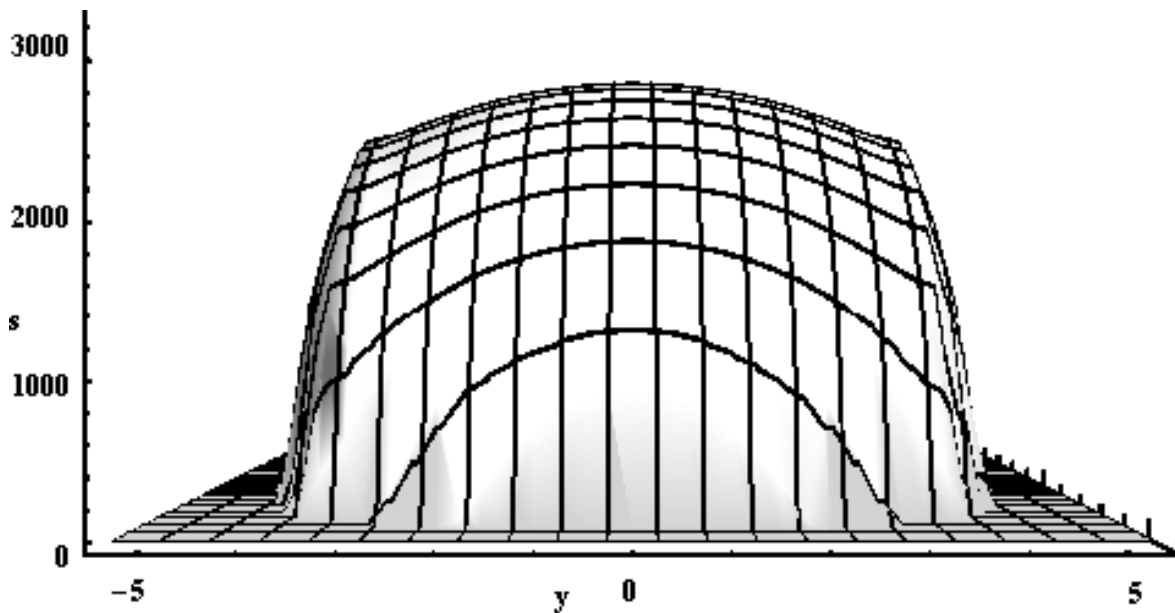


Figure 5.10b. Lateral view of pressure distribution of needle roller with crowning and skewing

It is clear that the “edge contact” effect is not present and pressure has a “barrel” type pressure distribution. On the other hand, given the symmetry conditions, the pressure at the center of the contact equals the maximum pressure. In practice the needle roller will see perfect alignment with the trunnion only twice per joint revolution (the reader may refer to Section 2 for details). Therefore, analysis of pressure distribution in subsequent portions of this work will assume a skew angle of 4° , unless otherwise indicated.

Sometimes “undercuts” on the cylindrical surface of the trunnion are required due to the manufacturing constraints. An example of an undercut is shown in Figure 5.11. When this type of discontinuity is present in the cylindrical surface of the trunnion an

edge contact effect will take place. The edge contact may be minimized by having extra crowning in the needle. However, the additional crowning will concentrate the load more at the center, thus, causing a higher maximum stress. To run experiments, parts without undercut will be used to avoid adding an extra variable.

Mesh	σ_{hmax} [MPa]	$\sigma_{hcenter}$ [MPa]	α [mm]
13 x 13	3233.8	3233.8	0.008857
21 x 21	3233.3	3233.3	0.008863
41 x 41	3233.3	3233.3	0.008868

Table 5.4. Convergence of maximum pressure and deflection

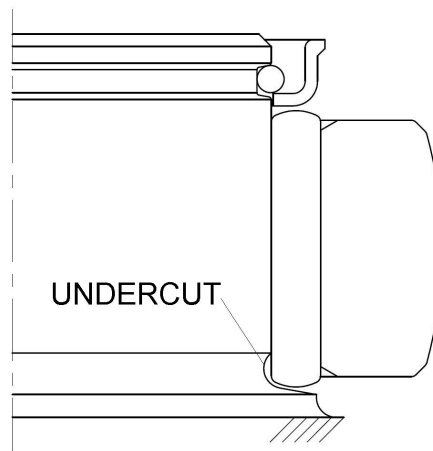


Figure 5.11. Undercut on trunnion surface

Figure 5.12a and Figure 5.12b show the pressure distribution when a 2mm undercut is present and the needle has been skewed 4°. The maximum stress in the distribution is 3324MPa. The edge effect will be more pronounced in the absence of needle skewing.

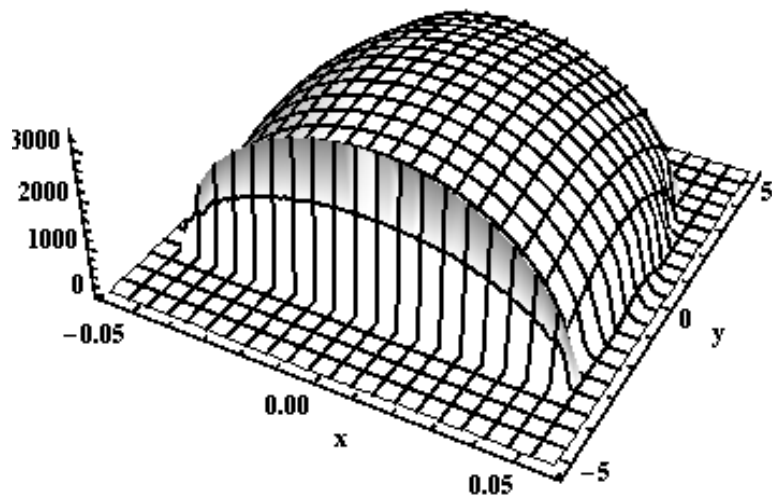


Figure 5.12a. Pressure distribution of skewed needle roller with undercut on trunnion

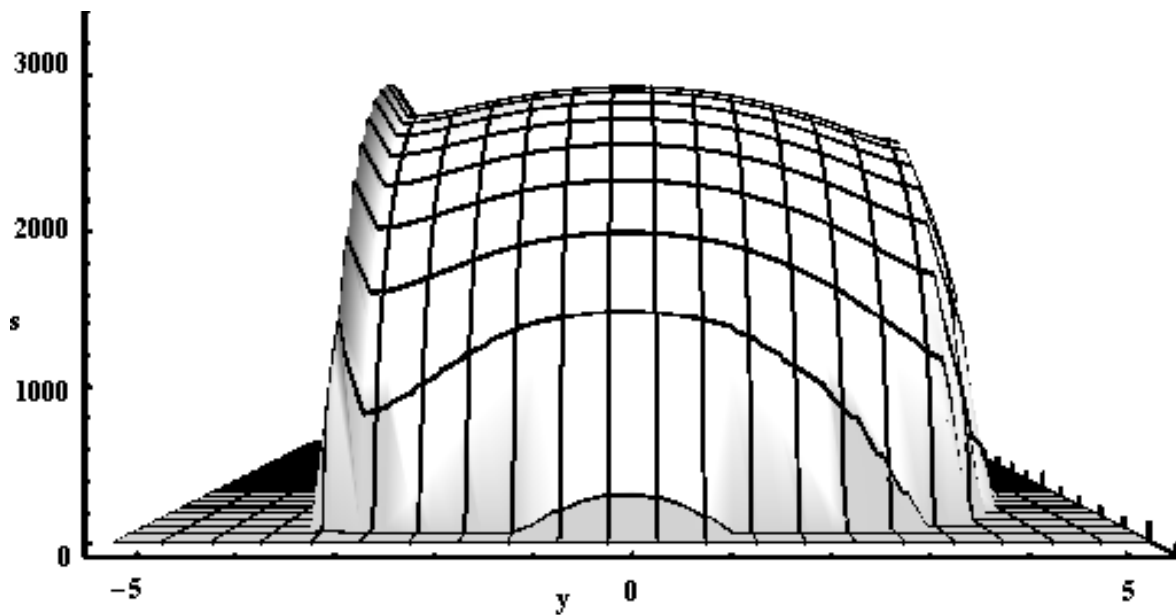


Figure 5.12b. Lateral view of pressure distribution of skewed needle roller with undercut on trunnion

So far perfect symmetry has been assumed at the contact. When a equivalent concentrated load on the needle roller is not centered, the pressure distribution will

change. An example of an asymmetrical load distribution is shown in Figure 5.13. Other cases can be reviewed in Section 4.2. Rotation of the contact elements is not part of the model. Thus, the slope of the load distribution must be transformed into an equivalent slope of misalignment to model the asymmetry.

The variables p_{tuij} and p_{tdij} represent the load per unit of length at the ends of the load distribution. If a unit length is assumed and the formerly mentioned variables substitute p_{ij} in Eq. (5.12) then Eq. (5.30) and Eq. (5.31) are obtained.

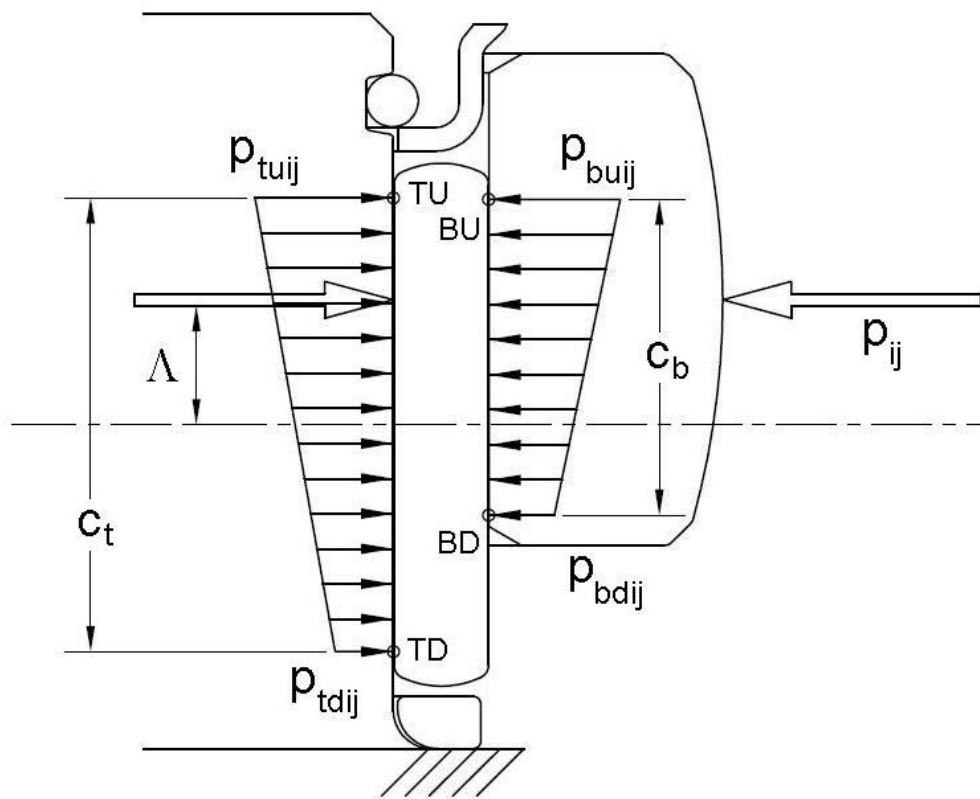


Figure 5.13. Case of asymmetrical load, positive offset

$$\alpha_{uij} = 3.84 \times 10^{-5} p_{tuij}^{0.9} \quad (5.30)$$

$$\alpha_{dij} = 3.84 \times 10^{-5} p_{duij}^{0.9} \quad (5.31)$$

Now, the slope of the equivalent misalignment caused by the asymmetrical load distribution can be calculated along the effective contact length c_t , yielding Eq. (5.32).

$$\xi_{ij} = \frac{\alpha_{uij} - \alpha_{dij}}{c_t} = 3.84 \times 10^{-5} \left(\frac{p_{tuij}^{0.9} - p_{duij}^{0.9}}{c_t} \right) \quad (5.32)$$

The slope is defined as positive when the equivalent concentrated load is above the plane of symmetry of the needle or there is a positive offset A_j , as shown in Figure 5.13. The additional equivalent crowning due the asymmetrical load can be estimated from Eq. (5.33)

$$z_\xi = y \xi_{ij} \quad (5.33)$$

The previous expression, combined with the expressions for crowning and equivalent crowning due to skewing can be combined and used to accurately describe the pressure distribution at the contact between needle and trunnion, at any position of the tripod joint. Thus,

$$z_t = z_{cw} + z_{sk} + z_\xi \quad (5.34)$$

Some numeric examples, to illustrate the effect of an asymmetrical load distribution, are carried out for an arbitrary offset Δ_i of -1mm . The same concentrated load magnitude used for previous numeric examples is applied and the calculated pressure distribution assuming no skewing is shown in Figure 5.14a and Figure 5.14b. The maximum pressure in the distribution is 3420MPa .

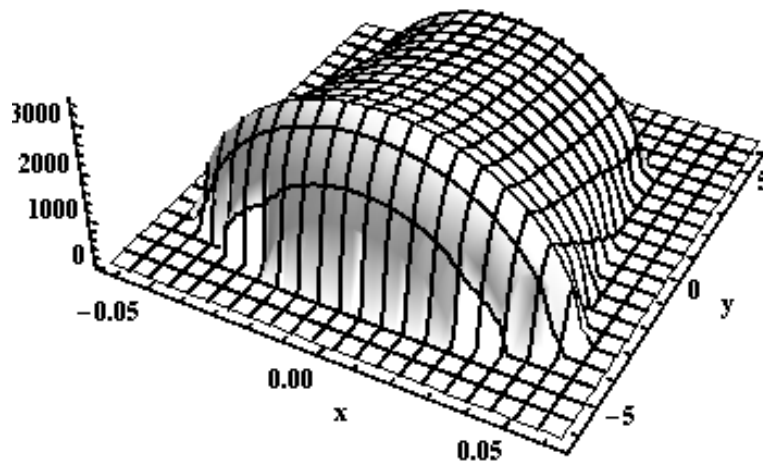


Figure 5.14a. Pressure distribution of needle roller with crowning and a load offset Δ_i of -1mm , no skewing

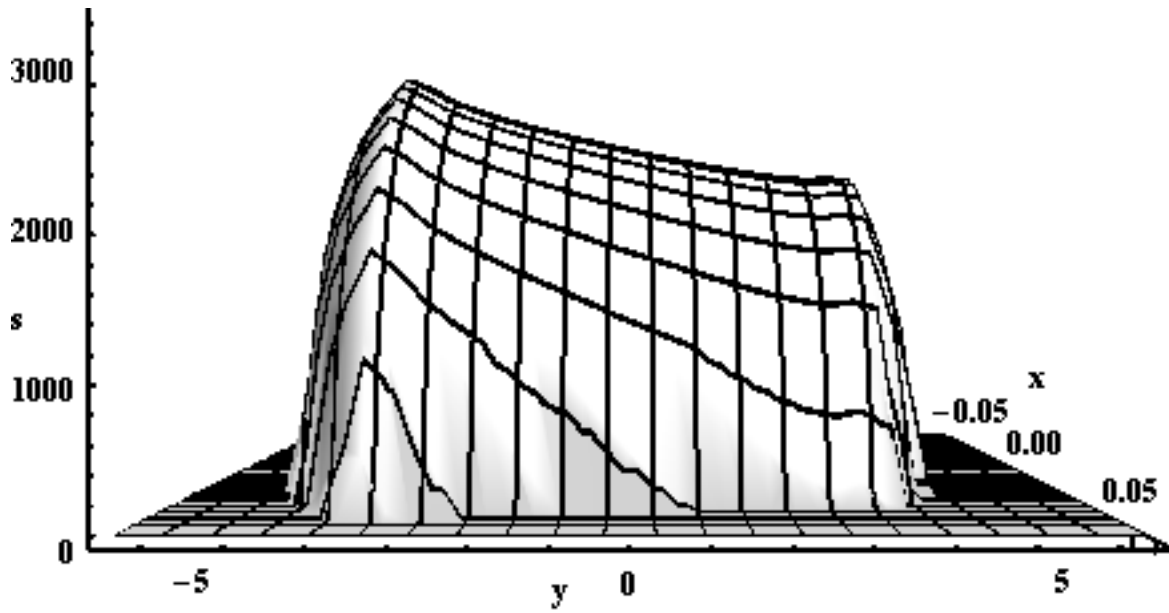


Figure 5.14b. Lateral view of pressure distribution of needle roller with crowning and a load offset Δ_i of -1mm , no skewing

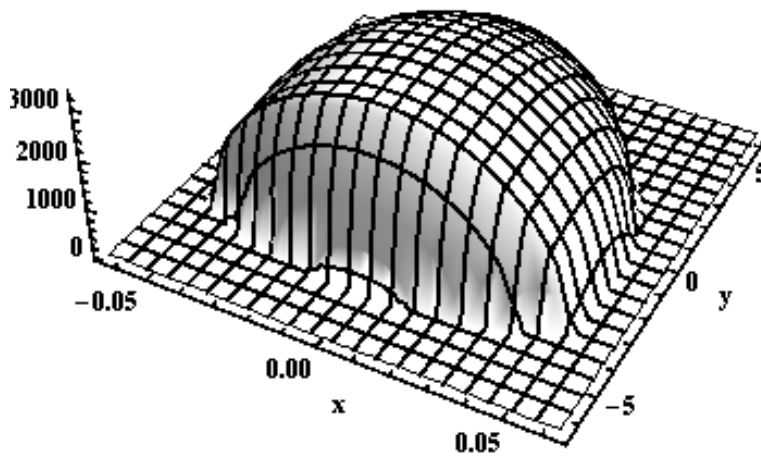


Figure 5.15a. Pressure distribution of needle roller with crowning and a load offset Δ_i of -1mm , skewing of 4°

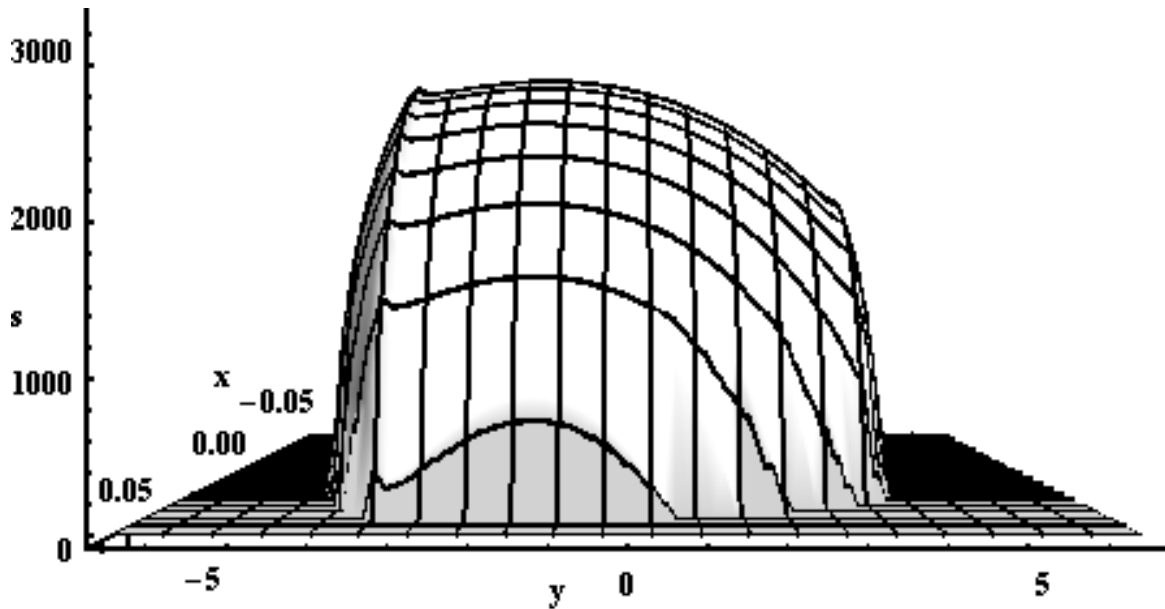


Figure 5.15b. Lateral view of pressure distribution of needle roller with crowning and a load offset Δ_i of -1mm , skewing of 4°

If a skewing of 4° is added, while keeping the same offset, a maximum pressure of 3286MPa is calculated. The corresponding pressure distribution is shown in Figure 5.15a and 5.15b.

5.5 Sub-surface stress distribution

Once the surface pressure in each one of the rectangular elements that compose the contact area is known, it can be proceeded to calculate the sub-surface stress distribution. The approach to calculate the stress distribution under the surface is superposition. The solution for stress components in a semi-infinite solid due to the uniform pressure over a rectangle is published as the appendix in Trachman's [29]

work. They were originally published by Love [33] and are shown in this work for reference purposes. Consider the potential functions V and X for each element n . Then,

$$V = \int_A \int \frac{s_n d\xi d\eta}{r} \quad (5.35)$$

$$X = \int_A \int s_n \log(z+r) d\xi d\eta \quad (5.36)$$

where,

$$r = \sqrt{(x-\xi)^2 + (y-\eta)^2 + z^2} \quad (5.37)$$

Then, the stress components are given by,

$$\sigma_x = \frac{1}{2\pi} \left(2\nu \frac{\partial V}{\partial z} - (1-2\nu) \frac{\partial^2 X}{\partial x^2} - z \frac{\partial^2 V}{\partial x^2} \right) \quad (5.38)$$

$$\sigma_y = \frac{1}{2\pi} \left(2\nu \frac{\partial V}{\partial z} - (1-2\nu) \frac{\partial^2 X}{\partial y^2} - z \frac{\partial^2 V}{\partial y^2} \right) \quad (5.39)$$

$$\sigma_z = \frac{1}{2\pi} \left(\frac{\partial V}{\partial z} - z \frac{\partial^2 V}{\partial z^2} \right) \quad (5.40)$$

$$\tau_{yz} = -\frac{1}{2\pi} z \frac{\partial^2 V}{\partial y \partial z} \quad (5.41)$$

$$\tau_{xz} = -\frac{1}{2\pi} z \frac{\partial^2 V}{\partial x \partial z} \quad (5.42)$$

$$\tau_{xy} = -\frac{1}{2\pi} \left((1-2\nu) \frac{\partial^2 X}{\partial x \partial y} + z \frac{\partial^2 V}{\partial x \partial y} \right) \quad (5.43)$$

where,

$$\begin{aligned}
\frac{\partial V}{\partial z} = & -s_n \left[2\pi - \arccos \left(\frac{(b-x)(a-y)}{\sqrt{(b-x)^2 + z^2} \sqrt{(a-y)^2 + z^2}} \right) \right. \\
& - \arccos \left(\frac{(b-x)(a+y)}{\sqrt{(b-x)^2 + z^2} \sqrt{(a+y)^2 + z^2}} \right) \\
& - \arccos \left(\frac{(b+x)(a-y)}{\sqrt{(b+x)^2 + z^2} \sqrt{(a-y)^2 + z^2}} \right) \\
& \left. - \arccos \left(\frac{(b+x)(a+y)}{\sqrt{(b+x)^2 + z^2} \sqrt{(a+y)^2 + z^2}} \right) \right]
\end{aligned} \tag{5.44}$$

$$\begin{aligned}
\frac{\partial^2 X}{\partial x^2} = & s_n \left[\arctan \left(\frac{a-y}{b-x} \right) + \arctan \left(\frac{a+y}{b-x} \right) - \arctan \left(\frac{z(a-y)}{\alpha_1(b-x)} \right) \right. \\
& - \arctan \left(\frac{z(a+y)}{\alpha_4(b-x)} \right) + \arctan \left(\frac{a-y}{b+x} \right) + \arctan \left(\frac{a+y}{b+x} \right) \\
& \left. - \arctan \left(\frac{z(a-y)}{\alpha_2(b+x)} \right) - \arctan \left(\frac{z(a+y)}{\alpha_3(b+x)} \right) \right]
\end{aligned} \tag{5.45}$$

$$\begin{aligned}
\frac{\partial^2 X}{\partial y^2} = & s_n \left[\arctan \left(\frac{b-x}{a-y} \right) + \arctan \left(\frac{b-x}{a+y} \right) - \arctan \left(\frac{z(b-x)}{\alpha_1(a-y)} \right) \right. \\
& - \arctan \left(\frac{z(b-x)}{\alpha_4(a+y)} \right) + \arctan \left(\frac{b+x}{a-y} \right) + \arctan \left(\frac{b+x}{a+y} \right) \\
& \left. - \arctan \left(\frac{z(b+x)}{\alpha_2(a-y)} \right) - \arctan \left(\frac{z(b+x)}{\alpha_3(a+y)} \right) \right]
\end{aligned} \tag{5.46}$$

$$\frac{\partial^2 X}{\partial x \partial y} = s_n \log \left[\frac{(z + \alpha_1)(z + \alpha_3)}{(z + \alpha_2)(z + \alpha_4)} \right] \tag{5.47}$$

$$\begin{aligned} \frac{\partial^2 V}{\partial x^2} = & -s_n \left[\frac{b-x}{(b-x)^2 + z^2} \left(\frac{a-y}{\alpha_1} + \frac{a+y}{\alpha_4} \right) \right. \\ & \left. + \frac{b+x}{(b+x)^2 + z^2} \left(\frac{a-y}{\alpha_2} + \frac{a+y}{\alpha_3} \right) \right] \end{aligned} \quad (5.48)$$

$$\begin{aligned} \frac{\partial^2 V}{\partial y^2} = & -s_n \left[\frac{a-y}{(a-y)^2 + z^2} \left(\frac{b-x}{\alpha_1} + \frac{b+x}{\alpha_2} \right) \right. \\ & \left. + \frac{a+y}{(a+y)^2 + z^2} \left(\frac{b-x}{\alpha_4} + \frac{b+x}{\alpha_3} \right) \right] \end{aligned} \quad (5.49)$$

$$\begin{aligned} \frac{\partial^2 V}{\partial z^2} = & s_n \left[\frac{b-x}{(b-x)^2 + z^2} \left(\frac{a-y}{\alpha_1} + \frac{a+y}{\alpha_4} \right) \right. \\ & + \frac{b+x}{(b+x)^2 + z^2} \left(\frac{a-y}{\alpha_2} + \frac{a+y}{\alpha_3} \right) + \frac{a-y}{(a-y)^2 + z^2} \left(\frac{b-x}{\alpha_1} + \frac{b+x}{\alpha_2} \right) \\ & \left. + \frac{a+y}{(a+y)^2 + z^2} \left(\frac{b-x}{\alpha_4} + \frac{b+x}{\alpha_3} \right) \right] \end{aligned} \quad (5.50)$$

$$\begin{aligned} \frac{\partial^2 V}{\partial x \partial z} = & s_n \left[\frac{z}{(b-x)^2 + z^2} \left(\frac{a-y}{\alpha_1} + \frac{a+y}{\alpha_4} \right) \right. \\ & \left. - \frac{z}{(b+x)^2 + z^2} \left(\frac{a-y}{\alpha_2} + \frac{a+y}{\alpha_3} \right) \right] \end{aligned} \quad (5.51)$$

$$\frac{\partial^2 V}{\partial x \partial y} = s_n \left[\frac{1}{\alpha_1} - \frac{1}{\alpha_2} + \frac{1}{\alpha_3} - \frac{1}{\alpha_4} \right] \quad (5.52)$$

$$\begin{aligned} \frac{\partial^2 V}{\partial y \partial z} = & s_n \left[\frac{z}{(a-y)^2 + z^2} \left(\frac{b-x}{\alpha_1} + \frac{b+x}{\alpha_2} \right) \right. \\ & \left. - \frac{z}{(a+y)^2 + z^2} \left(\frac{b-x}{\alpha_4} + \frac{b+x}{\alpha_3} \right) \right] \end{aligned} \quad (5.53)$$

and

$$\alpha_1 = \sqrt{(x-b)^2 + (y-a)^2 + z^2} \quad (5.54)$$

$$\alpha_2 = \sqrt{(x+b)^2 + (y-a)^2 + z^2} \quad (5.55)$$

$$\alpha_3 = \sqrt{(x+b)^2 + (y+a)^2 + z^2} \quad (5.56)$$

$$\alpha_4 = \sqrt{(x-b)^2 + (y+a)^2 + z^2} \quad (5.57)$$

$$-\frac{\pi}{2} \leq \arctan \xi \leq \frac{\pi}{2} \quad \text{and} \quad 0 \leq \arccos \xi \leq \pi \quad (5.58)$$

Once the stress components are known, it is possible to calculate the principal stresses, which are the roots σ_p of the cubic equation,

$$\sigma_p^3 + \sigma_I \sigma_p^2 + \sigma_{II} \sigma_p + \sigma_{III} = 0 \quad (5.59)$$

where, the stress invariants are,

$$\sigma_I = \sigma_x + \sigma_y + \sigma_z \quad (5.60)$$

$$\sigma_{II} = \sigma_x \sigma_y + \sigma_y \sigma_z + \sigma_x \sigma_z - \tau_{xy}^2 - \tau_{yz}^2 - \tau_{xz}^2 \quad (5.61)$$

$$\sigma_{III} = -\sigma_x \sigma_y \sigma_z - 2\tau_{xy} \tau_{yz} \tau_{xz} + \sigma_z \tau_{xy}^2 + \sigma_x \tau_{yz}^2 + \sigma_y \tau_{xz}^2 \quad (5.62)$$

and the maximum principal shear stress is,

$$\tau_{\max} = \frac{\sigma_{p1} - \sigma_{p3}}{2} \quad (5.63)$$

Eqs. (5.38) through (5.63) were programmed in addition to the computer program that calculates pressure distribution in a contact. Similar to the pressure distribution calculation, the code was debugged comparing the numeric solution to the exact solution of a sphere-plane contact. The radius of the sphere is 10mm and the applied load is 100N. It was assumed both contacting bodies are made of steel.

From Eq. (5.20) is known that the radius a_{ball} of the contact patch is 0.1873mm and from Eq. (5.21) is known that the maximum pressure in the contact is 1362.3MPa. According to the expressions published by Johnson [24], the maximum principal shear stress has a value of approximately $0.31\sigma_{ball\max}$ at a depth of $0.48a_{ball}$. Thus, maximum shear in the sphere-plane contact problem is 422.31MPa at a depth of 0.89904mm.

Figures 5.16a through 5.16d show the stress components and maximum shear as a function of the depth. Such figures were generated from the numeric solution of the sphere-plane contact problem using a 41x41 mesh. The maximum principal shear, calculated at a depth of 0.9mm using the numeric procedure, is 422.27MPa.

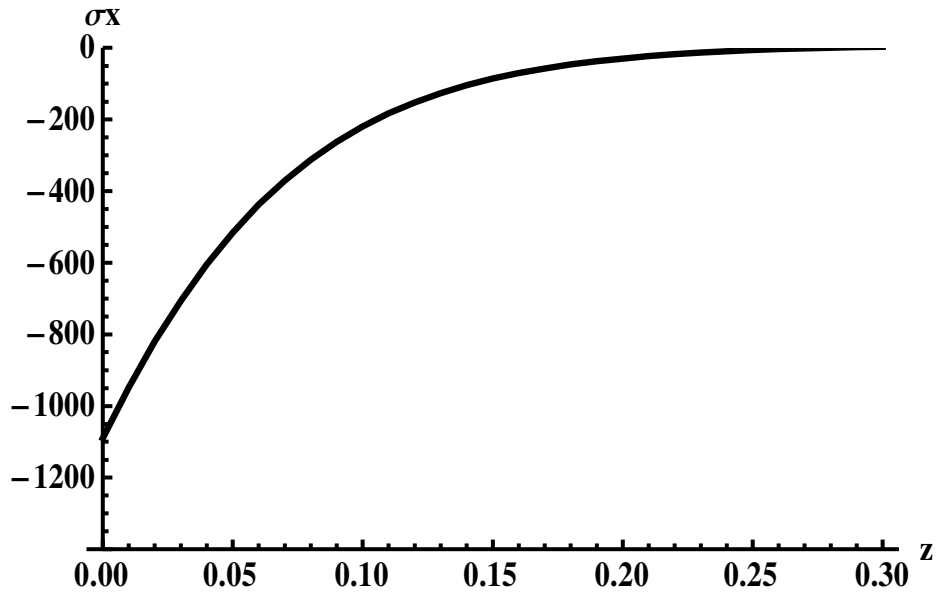


Figure 5.16a. Stress distribution along the depth of the contact, σ_x component

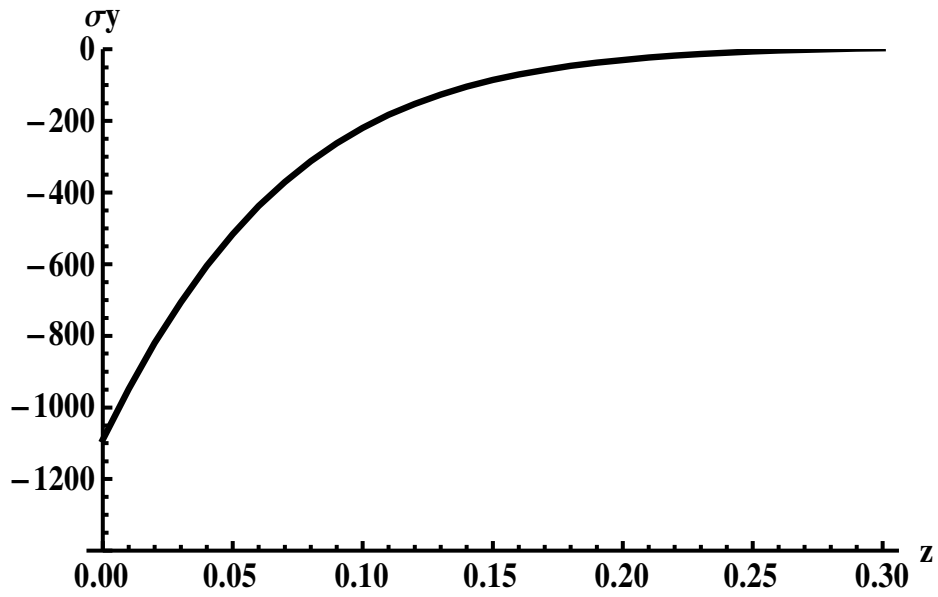


Figure 5.16b. Stress distribution along the depth of the contact, σ_y component

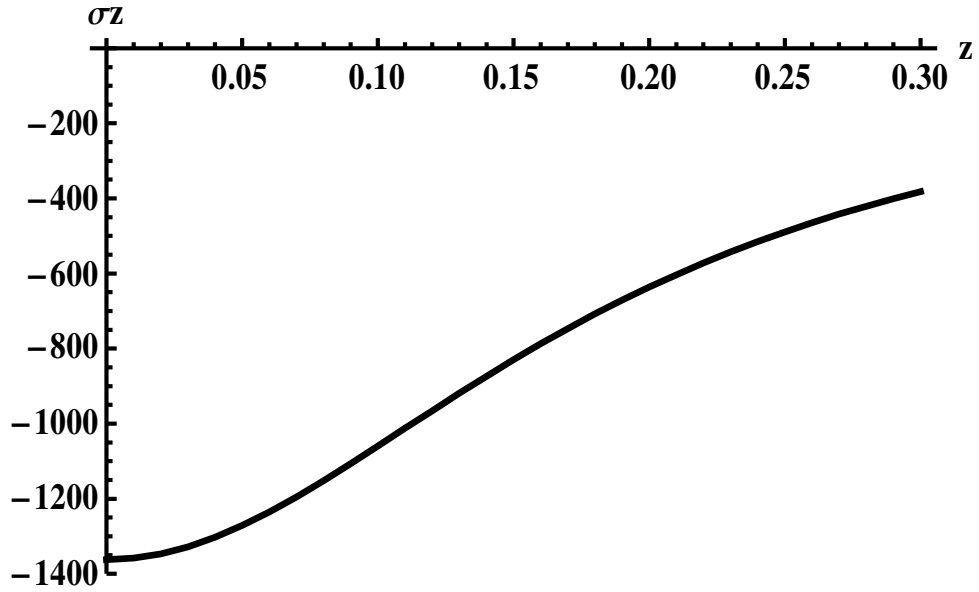


Figure 5.16c. Stress distribution along the depth of the contact, σ_z component

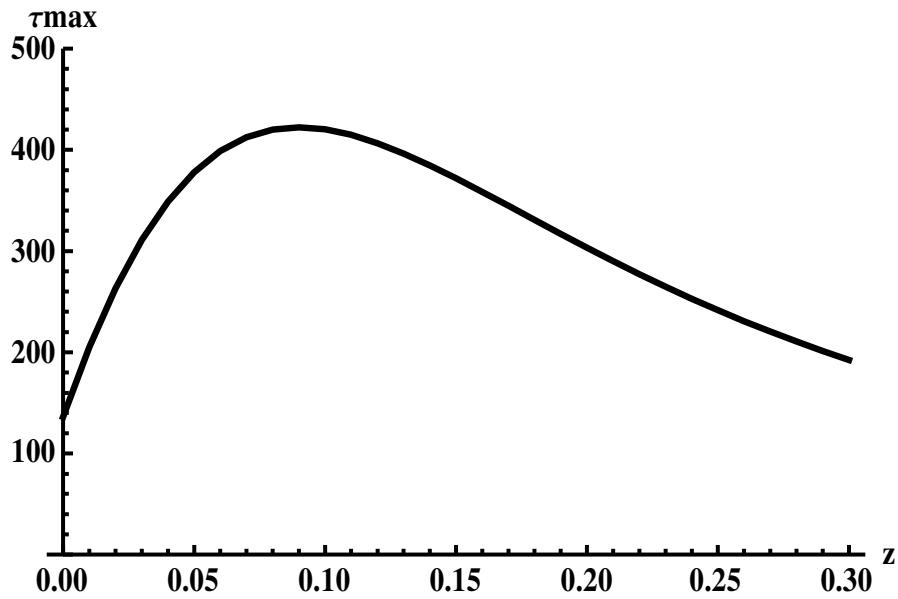


Figure 5.16d. Stress distribution along the depth of the contact, τ_{max}

It must be noted that the previously described state of stress is at the element that matches the position of the applied concentrated load. Shear stress components are

zero at the plane of symmetry. The numeric procedure allows calculation of the state of stress at any element within the mesh. This will prove extremely useful when dealing with needle rollers asymmetrically loaded.

As a second verification of the program, it is calculated the sub-surface stress distribution for the contact problem of a crowned needle (no skewing), described in Table 5.3 and shown in Figure 5.8a and Figure 5.8b. This problem was chosen since it is a very good numerical approximation to a line contact without having the numeric instability caused by an edge contact. It is known that the pressure at the center of the needle roller is 2840MPa and the semi-width of the contact patch, at the plane of symmetry, is approximately 0.048mm. According to the Hertzian subsurface stress distribution shown in Figure 5.2, it is expected that at maximum shear stress of $\tau_{\max} = 0.3s_{\max} = 852\text{MPa}$ will occur at a depth of $z = 0.786b_h = 0.786(0.048) = 0.038\text{mm}$. It is also expected that the stress components σ_x and σ_y will be equal at approximately $z = 0.436b_h = 0.436(0.048) = 0.021\text{mm}$.

Figures 5.17a through 5.17c show the stress components and maximum shear as a function of the depth. Such figures were generated from the numeric solution in Table 5.3 for a 41x41 mesh.

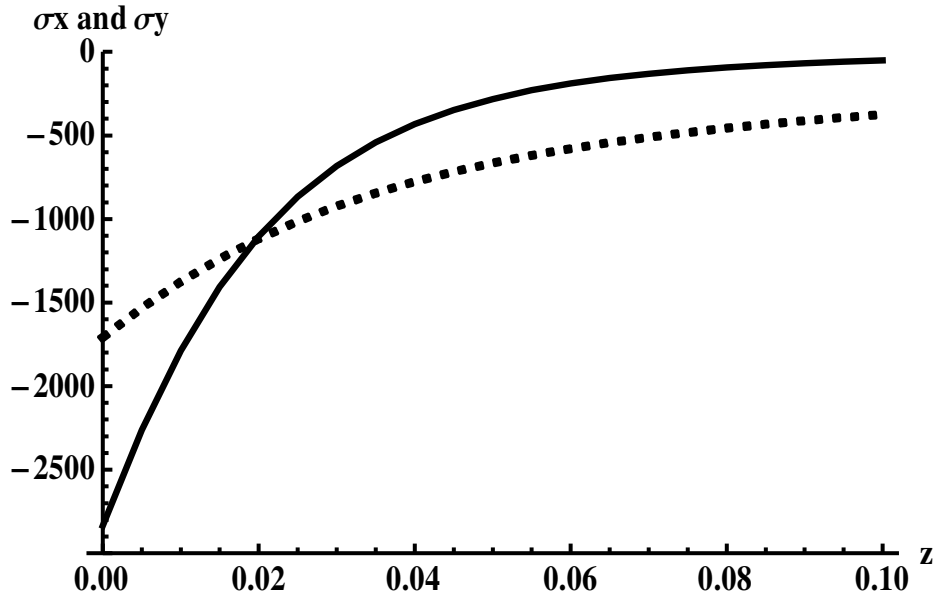


Figure 5.17a. Stress distribution along the depth of the contact, σ_x component represented with a solid line, σ_y component represented by a dashed line

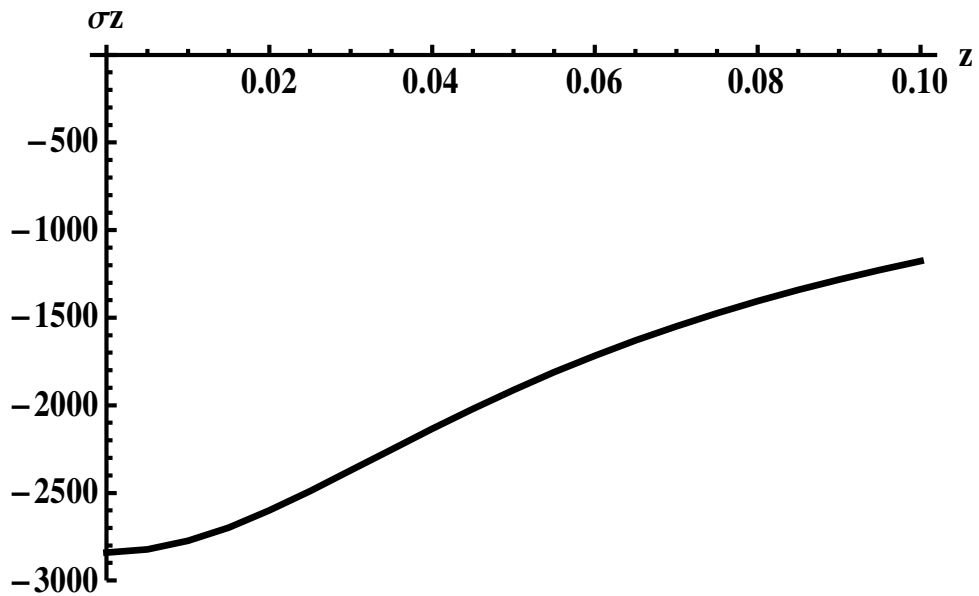


Figure 5.17b. Stress distribution along the depth of the contact, σ_z component

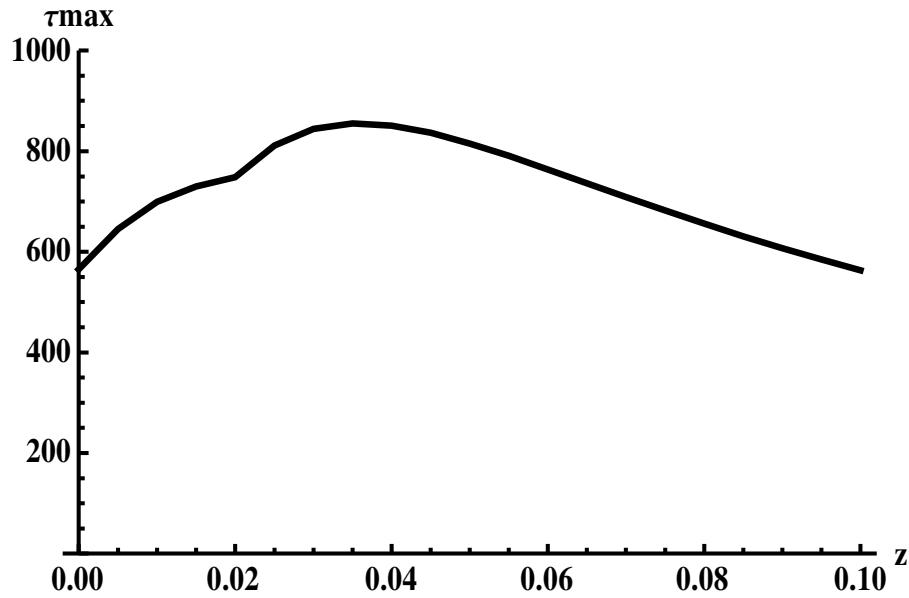


Figure 5.17c. Stress distribution along the depth of the contact, τ_{\max}

From Figure 5.17a it can be verified, graphically, that the point where the stress components σ_x and σ_y are equal happens around 0.02mm, which is very close to the expected value of 0.021mm. From Figure 5.17c it can be obtained that the maximum shear is approximately 850MPa at depth of 0.035mm, not very different from the Hertzian calculation of 852MPa at 0.038mm.

At this point it is possible to calculate the state of stress at any location of the needle-trunnion contact at any position of the joint, under any load conditions. The next section will deal with the different yield and fatigue theories that will be used to predict the wear performance of the tripod joint.

6. FATIGUE-LIFE THEORIES

6.1 Introduction

Studies on bearing life prediction started in the early twentieth century. The dominant model since then has been the Lundberg-Palmgren equation, which is the basis of the current ANSI/ABMA standards [34, 36]. Such standards can be easily applied for traditional bearings under simple load conditions but not to Tripode joints. Other authors such as Zaretsky [34, 35] and Ioannides and Harris [36, 37] have proposed alternative or expanded versions of the Lundberg-Palmgren equation. Such models are discussed in this section and a new model, specific to Tripode joints, will be proposed.

6.2 Weibull Equation

Weibull proposed a statistical approach to determine the strength of solids and observed that the dispersion in material strength for a homogeneous group of test specimens would follow the following relation,

$$\ln\left(\ln\left(\frac{1}{S}\right)\right) = \varepsilon \ln\left(\frac{\sigma_w}{\sigma_w \beta}\right) \quad (6.1)$$

where, S is the survival (i.e. completed load cycles) to the fracture strength σ_w . Eq

(6.1) can be rearranged to have the form of a straight line equation, and if $\ln\left(\ln\left(\frac{1}{S}\right)\right)$ is

used as the ordinate and $\ln(\sigma_w)$ is used as the abscissa the slope of the line ε can be

defined as the Weibull slope, which is a measure of the dispersion of the data in a

statistical distribution. The scatter in the data is inversely proportional to the Weibull

slope, the lower the value of ε the larger the scatter.

$$\ln\left(\ln\left(\frac{1}{S}\right)\right) = \varepsilon \ln(\sigma_w) - \varepsilon \ln(\sigma_w \beta) \quad (6.2)$$

Weibull also proposed the idea of relating the probability of survival of a component to the stressed volume. The larger the stressed volume, the lower the strength or life of the component. This is mathematically expressed in Eq (6.3).

$$\ln\left(\frac{1}{S}\right) = \int_V f(\sigma_w) dV \quad (6.3)$$

According to Zaretsky [34], Weibull proposed the following probability of survival equation to predict bearing life

$$f(\sigma_w) = \tau_{Cr}^c N^\varepsilon \quad (6.4)$$

which if substituted in Eq (6.3) yields,

$$N \propto \left(\frac{1}{\tau_{cr}} \right)^{c/\varepsilon} \left(\frac{1}{V} \right)^{1/\varepsilon} \quad (6.5)$$

From Hertz theory V and τ_{cr} can be expressed as a function of the maximum pressure in the contact σ_{hmax} , and if a proportionality constant is used Eq (6.5) takes the form

$$L = C_1 \left(\frac{1}{\tau_{cr}} \right)^{c/\varepsilon} \left(\frac{1}{V} \right)^{1/\varepsilon} \propto \frac{1}{\sigma_{hmax}^{n_h}} \quad (6.6)$$

where n_h is reported to be 10.2 for a line contact, for $\varepsilon = 1.11$ and $c/\varepsilon = 9.3$ [38].

6.3 Lundberg-Palmgren Equation

Lundberg and Palmgren applied Weibull analysis to the prediction of rolling-element bearing life, including the depth to the maximum critical shear stress in a Hertzian contact. Then Eq (6.4), the probability of survival function, takes the form

$$f(\sigma_w) = \frac{\tau_{cr}^c N^\varepsilon}{Z_{cr}^\beta} \quad (6.7)$$

which, if substituted in Eq (6.3), and assuming a Hertzian contact, can be expressed as,

$$L = C_1 \left(\frac{1}{\tau_{cr}} \right)^{c/\varepsilon} \left(\frac{1}{V} \right)^{1/\varepsilon} z_{cr}^{\vartheta/\varepsilon} \propto \frac{1}{\sigma_{hmax}^{n_h}} \quad (6.8)$$

where n_h is reported to be 8.1 for a line contact, for $\varepsilon = 1.11$, $c/\varepsilon = 9.3$ and $\vartheta = 2.33$ [38].

6.4 Ioannides-Harris Equation

Ioannides and Harris introduced a fatigue-limiting stress to the Lundberg-Palmgren equation, based on reported endurance data of some bearing applications that demonstrated virtually infinite fatigue life. It is reported that such bearings were accurately manufactured from “clean” steel [37]. Then Eq (6.7), takes the form

$$f(\sigma_w) = \frac{(\tau_{cr} - \tau_u)^c N^\varepsilon}{z_{cr}^\vartheta} \quad (6.9)$$

Similarly, if replaced in Eq (6.3),

$$L = C_1 \left(\frac{1}{\tau_{cr} - \tau_u} \right)^{c/\varepsilon} \left(\frac{1}{V} \right)^{1/\varepsilon} z_{cr}^{\vartheta/\varepsilon} \propto \frac{1}{\sigma_{hmax}^{n(\tau_u)}} \quad (6.10)$$

Ioannides and Harris use the same values of Lundberg-Palmgren for ε , c , and ϑ . However, the exponent n is a function of $(\tau_{cr} - \tau_u)$. If τ_u equals 0, the Ioannides-Harris equation is equivalent to the Lundberg-Palmgren equation.

6.5 Zaretsky Equation

In the Weibull and Lundberg-Palmgren equations the critical shear stress exponent c and the Weibull slope ε are related, making c/ε the effective critical shear stress-life exponent, implying that the life of a bearing also depends on the scatter of the life data used to calculate the exponents. Zaretsky states that most stress-life exponents vary from 6 to 12 and appear to be independent of the scatter of the data [34]. Following this observation he modified Weibull's probability of survival function making the exponent c independent of the Weibull slope ε . Such equation has the form,

$$f(\sigma_w) = \tau_{cr}^{c\varepsilon} N^\varepsilon \quad (6.11)$$

Similarly, if replaced in Eq (6.3),

$$L = C_1 \left(\frac{1}{\tau_{cr}} \right)^c \left(\frac{1}{V} \right)^{1/\varepsilon} \propto \frac{1}{\sigma_{h\max}^{n_h}} \quad (6.12)$$

Zaretsky assumes a value for the stress-exponent $c = 9$ and

$$n_h = c + \frac{1}{\varepsilon} \quad (6.13)$$

The proportionality constant C_1 in any of the previous fatigue-life equations accounts for several adjustment factors, which may include: reliability factors, material factors, geometry factors, lubrication factors and temperature factors. These adjustment factors vary depending on the bearing manufacturer and have been refined over time. There have also been efforts to standardize them and both Zaretsky and Harris recognize its importance given all the possible permutations in bearing applications [36, 38].

6.6 Tripode Equation

Lundberg and Palmgren assumed that once initiated, the time a crack takes to propagate to the surface and form a fatigue “spalled” area, similar to the “spalled” area shown in Figure 4.15, is a function of the depth to the critical shear stress [38]. This would imply that fatigue life in a bearing surface is crack propagation time dependent. However, Zaretsky categorizes the life of rolling elements as a “high-cycle fatigue problem” [34]. Zaretsky also supports the idea of crack propagation being an extremely small time fraction of the total running time of the bearing [38].

In the author’s experience, Tripode joints can operate for hundreds, sometimes thousands of hours, depending on the load conditions, without showing any signs of pits or spalling. Once the first pit shows on the surface it takes a few hours to get a large

spalled area, supporting the idea of crack propagation being a very small fraction of the total life of a Tripode joint.

Following Zaretsky's approach for bearings, it is proposed to decouple the life of a Tripode from crack propagation and the relation, Eq (6.14), to the depth of the maximum critical shear stress, used in Lundberg-Palmgren model and Ioannides-Harris models, is dispensed.

$$L \propto Z_{Cr}^{2/\varepsilon} \quad (6.14)$$

Based on the author's observation of the life behavior of Tripode joints, the following empirical model is proposed:

$$L = C_1 C_2 \left(\frac{1}{\tau_{eff}} \right)^c \left(\frac{1}{l_{eff} \phi_{eff} \frac{t}{2}} \right)^{1/\varepsilon} \quad (6.15)$$

Where, τ_{eff} is the effective shear stress, which depends on the static failure theory used. l_{eff} is the effective contact length, which can be obtained from the non-Hertzian contact analysis discussed in Section 5 and is dependent on the crowning of the needle roller and applied load. ϕ_{eff} is the effective trunnion arch traveled by a needle roller during a joint revolution, which times the trunnion radius $t/2$ yields the effective arch-length traveled by the roller. Thus, rather than dealing with a stressed

volume the Tripode model deals with a projected area subject to contact stress. The constant C_1 is an empirical life adjustment factor for different greases and surface textures generated by the manufacturing processes used to make the joint and the constant C_2 accounts for the duplication of load cycles when the critical joint angle, discussed in Section 2, is exceeded.

$$C_2 = \left(\text{Ceiling} \left(\frac{\phi_{eff}}{2\pi / n} \right) \right)^{-1} \quad (6.16)$$

Where the function $\text{Ceiling}[x]$ is defined as the smallest integer greater than or equal to x .

6.7 Testing and prototypes to validate the Tripode model

Once a fatigue-life model has been proposed for the Tripode joint it is necessary to perform actual experiments to verify the validity of the model. The experiments were conducted in an industrial lab at Nexteer Automotive Headquarters. The test benches, an example shown in Figure 6.1, can simulate different speeds, torques and angles that a Constant Velocity Joint can experience in a vehicle.

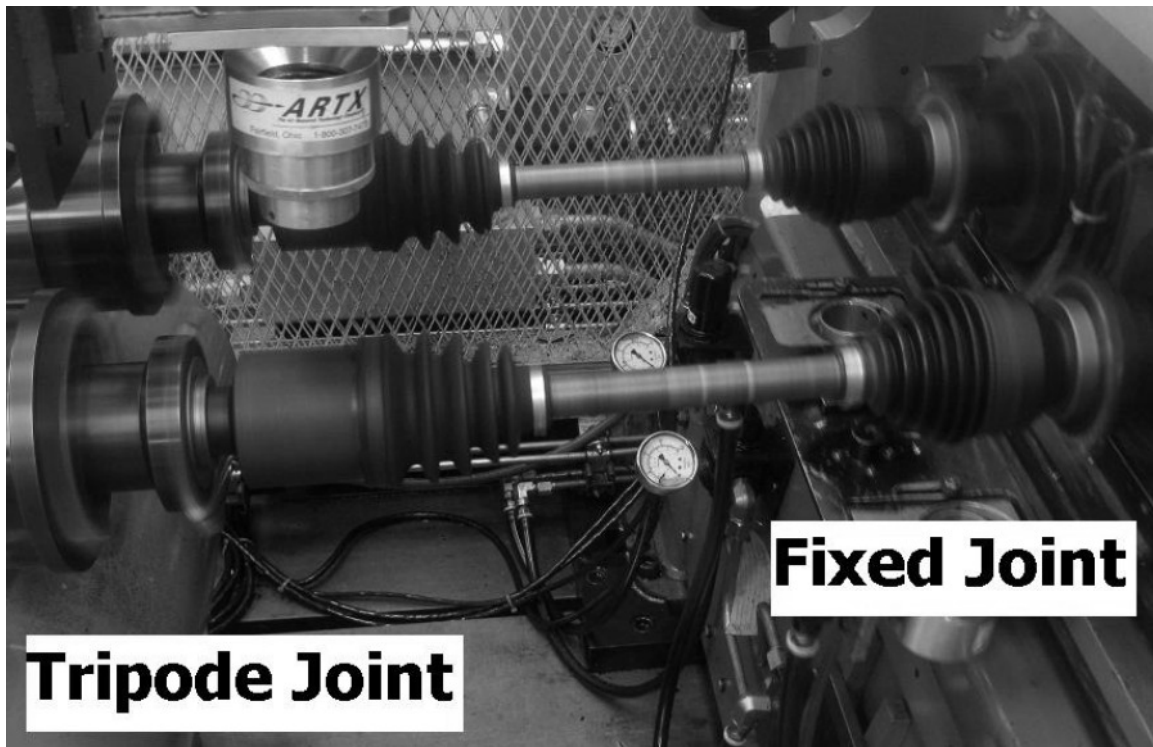


Figure 6.1. CVJ wear test bench

For the purpose of validating the model, considering and subject to time and budget constraints, three tests were performed at a fixed joint angle and constant power. In Section 2 it was found that the critical angle in the Tripode joint used for the experimental portion of this work is 6° . Testing at an angle higher than 6° allows to duplicate load cycles. On the other hand, 7° is an angle commonly used in industry to validate CVJ designs. Thus, a running angle of 7° was chosen. Table 6.1 summarizes the conditions of the three tests.

Test/Schedule 1 (used in parts 1 to 4)				
Step	Torque	Speed	Time	Angle
01	272 Nm	1200 rpm	20 minutes	7deg
02	-80 Nm	300 rpm	1 minutes	0-8deg @ 0.5Hz
Power: 34.18 kW				
Test/Schedule 2 (used in parts 5 to 8)				
Step	Torque	Speed	Time	Angle
01	466 Nm	700 rpm	20 minutes	7deg
02	-80 Nm	300 rpm	1 minutes	0-8deg @ 0.5Hz
Power: 34.16 kW				
Test/Schedule 3 (used in parts 9 to 12)				
Step	Torque	Speed	Time	Angle
01	816 Nm	400 rpm	20 minutes	7deg
02	-80 Nm	300 rpm	1 minutes	0-8deg @ 0.5Hz
Power: 34.18 kW				

Table 6.1. Summary of wear tests conditions

The steps with negative torque were introduced to avoid “grease migration” in the joint and keep functional lubrication conditions during the test. The tests schedules were repeated several times until spalling occurred in at least one trunnion of one spider. Periodic inspections were performed to try to find the spalling in its initial stage. Before discussing the results of the tests it is noted that controlled prototype parts were made to perform the three tests, using production manufacturing processes. The purpose of making controlled prototypes was to try to eliminate possible sources of noise in the test, such as geometric variation from component to component. Some of the key characteristics of the prototype parts are listed:

1. All parts were made from the same batch of material
2. All parts were made using the same machine in a single lot

3. At least four parts of the lot were carefully inspected using a Coordinate Measurement Machine (CMM)
4. At least four parts were carefully inspected in the trunnion area for roundness. Surface finish was also inspected.
5. All parts were visually checked for any possible defects (surface dents) or corrosion that could generate premature spalling.

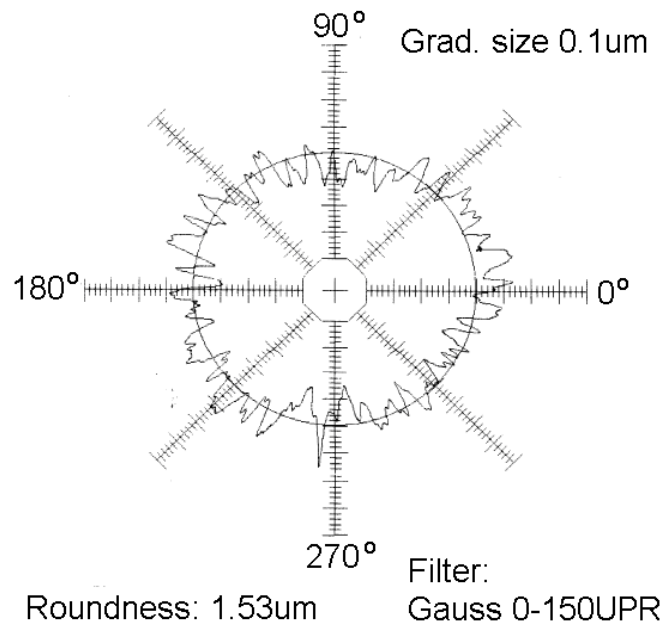


Figure 6.2. Example of roundness check

Roundness in the trunnions, which is the most critical characteristic for fatigue-life in a trunnion, given the changes it produces in load distributions, was found to be in the order of two microns in the inspected parts. Figure 6.2 shows an example of a

roundness check. The reader is asked to refer to the appendices to see surface texture inspection and the effect of filtering in roundness inspection reports.

6.8 Load and stress conditions per test schedule

After knowing the geometrical characteristics of the prototype parts it is possible to calculate the displacements, loads and the state of stress in the contacts between the trunnion and the needle rollers. The following average dimensions were obtained from the prototype inspection.

Housing, BCD	=	40.906mm
Spider shaft length, b	=	300mm
Ball outer diameter, m_o	=	34.992mm
Ball inner diameter, m_i	=	24.994mm
Ball to needle contact length, c_b	=	10.39mm
Number of needles, n	=	36
Needle roller diameter, d	=	1.9975mm
Needle roller length, b_{needle}	=	10.81mm
Trunnion diameter, t	=	20.975mm
Axial clearance of needle, θ_o	=	0.452mm
Height of shoulder, e_{spider}	=	13.921mm
Spacer thickness, c_{spacer}	=	1.05mm
Applied torques, t_φ	=	272Nm, 466Nm, 816Nm

It is reported that there was part to part variation, as expected with any manufacturing process, but the variation was so small, with respect to typical tolerances for Tripode joints, that it can be neglected for the purpose of calculating loads and stresses. Using the dimensions of the components and the computer programs developed in previous sections, the kinematic and quasi-static behavior of the joint at different input torque levels can be known.

From the kinematic analysis of Section 2 it is possible to know the maximum roller displacement on the trunnion within a revolution. Figure 6.3 shows such displacement at a joint angle of 7° . The peak to valley height for the exact solution of roller displacement (considering joint angle fluctuation due to orbiting motion) and the linearized solution are: $\phi_{eff} = 10.76^\circ$ and $\phi_{eff} = 10.75^\circ$, respectively.

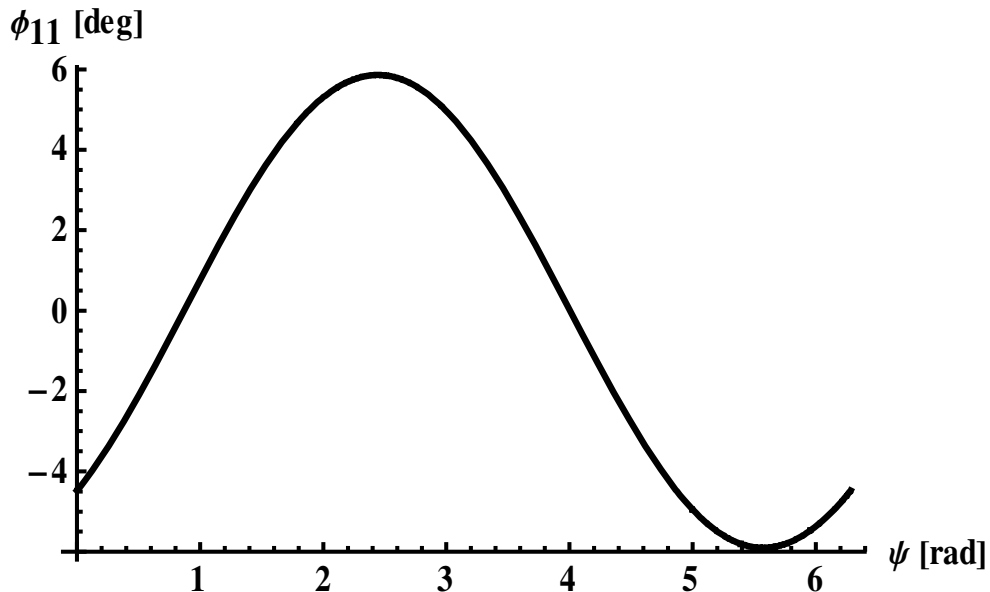


Figure 6.3. Needle displacement

Figure 6.4 shows the offset between the symmetry plane of the ball and the symmetry plane of the needle within a revolution. It can be observed that in this particular set of prototypes the amplitude of the offset variation is about 2% of its mean value.

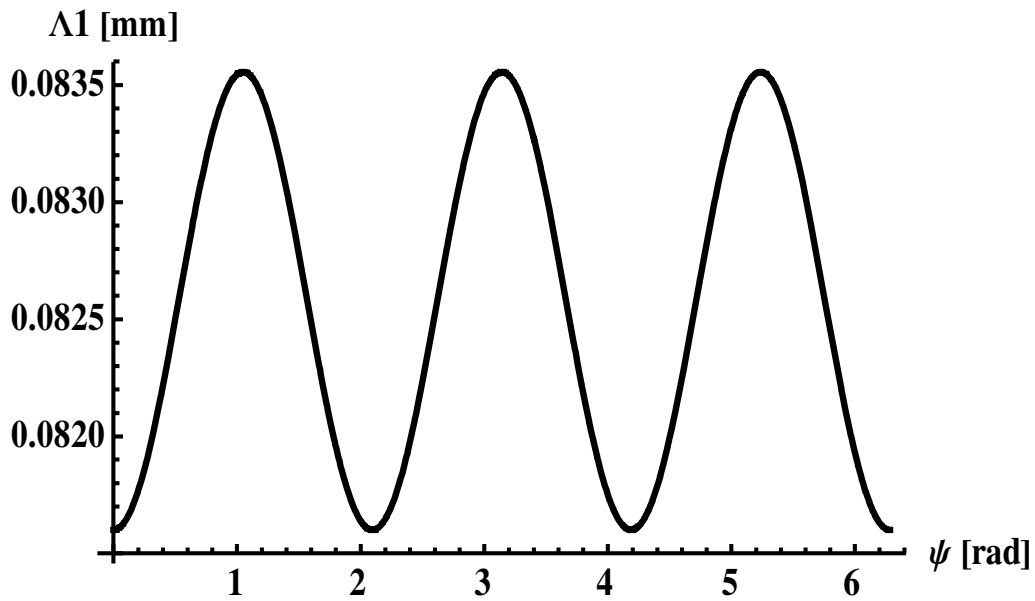
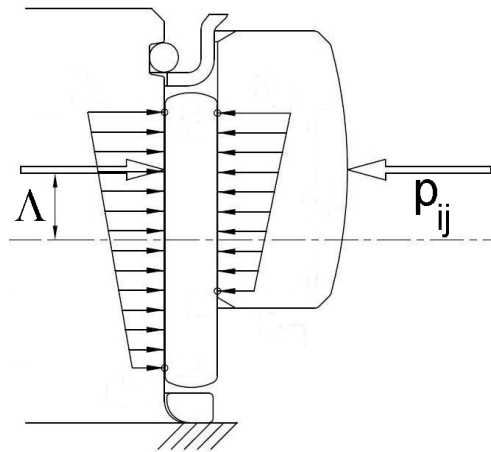


Figure 6.4. Load offset

Figure 6.5a shows the load variation for one of the torque levels corresponding to the test schedules. It can be appreciated that the amplitude of the force variation is

extremely small with respect to the mean force value. Something similar happens with the other two torque levels, which are plotted together in Figure 6.5b, where the solid line corresponds to an input torque of 272Nm, the mid-dashed line to an input torque of 466Nm and the small-dashed line to a torque of 816Nm.

The zero position for rotation is defined at the plane formed by the housing axis and the spider axle axis, as shown in Figure 6.6. The virtual load variation between a needle roller and the trunnion at the spider plane can be modeled within a joint revolution. The load variation is referred as virtual because an actual load at a specific point on the trunnion only exists when the needle roller is located on that specific point. Once the needle roller displaces, because of the joint rotation, the load at that specific point on the trunnion becomes zero until the needle passes through that point again.

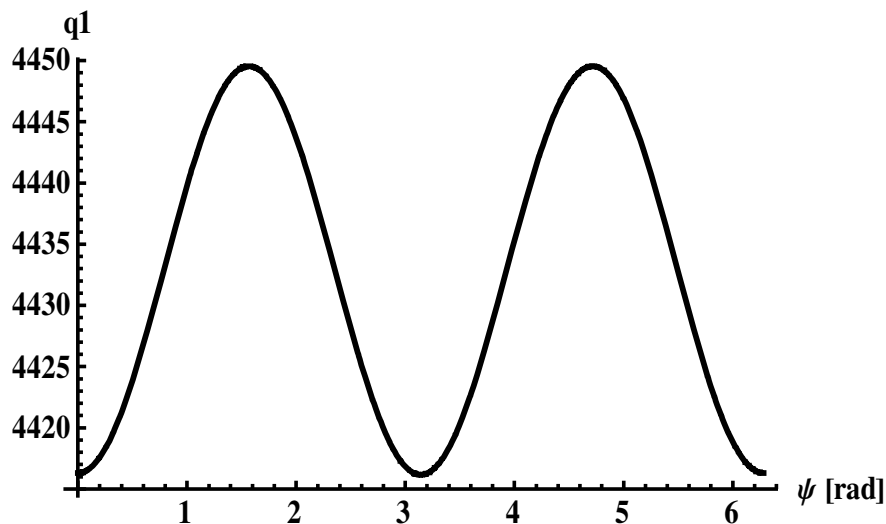


Figure 6.5a. Variation of load on ball bore, housing plane at 272Nm

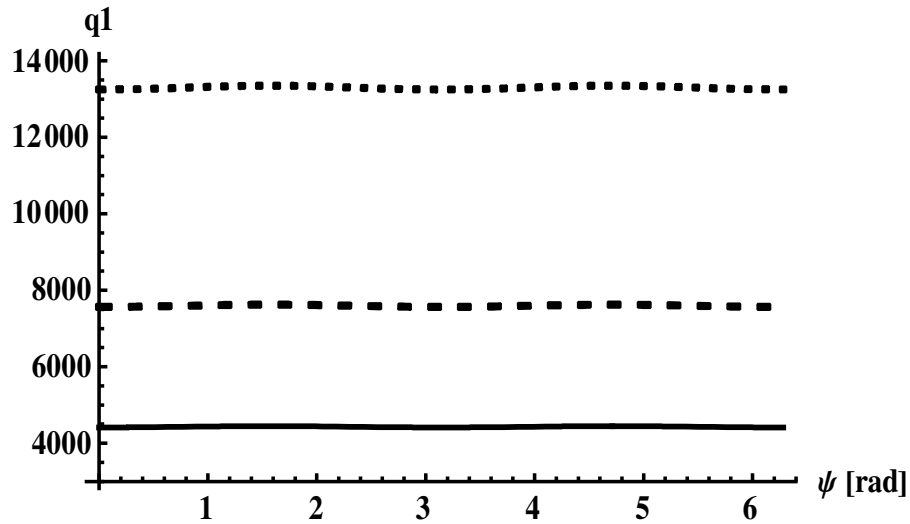


Figure 6.5b. Loads on ball bore, housing plane

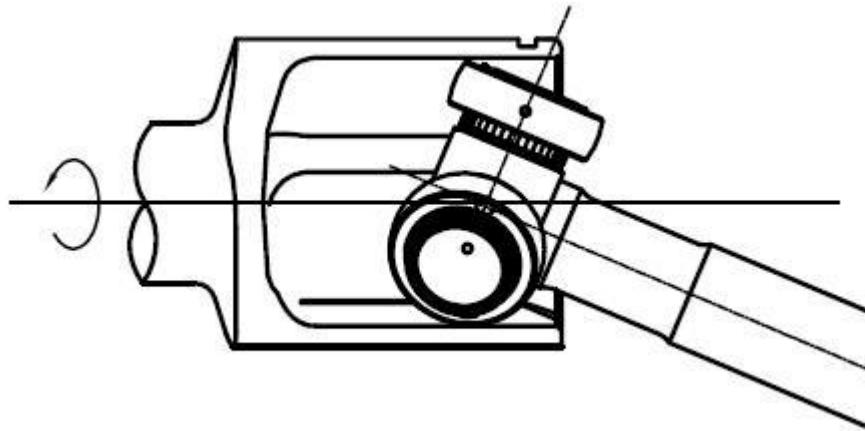


Figure 6.6. Plane formed by housing axis and spider axis, zero plane for rotation

Hence, the plots of Figures 6.7a and 6.7b show load variation on the trunnion at the spider (symmetry) plane and were generated assuming a constant contact between the needle and the trunnion at such plane. The purpose of performing this virtual load evaluation was to identify the possible loads on the area of the trunnion that is most susceptible to fatigue. In Figure 6.7b the solid line corresponds to an input torque of

272Nm, the mid-dashed line to an input torque of 466Nm and the small-dashed line to a torque of 816Nm.

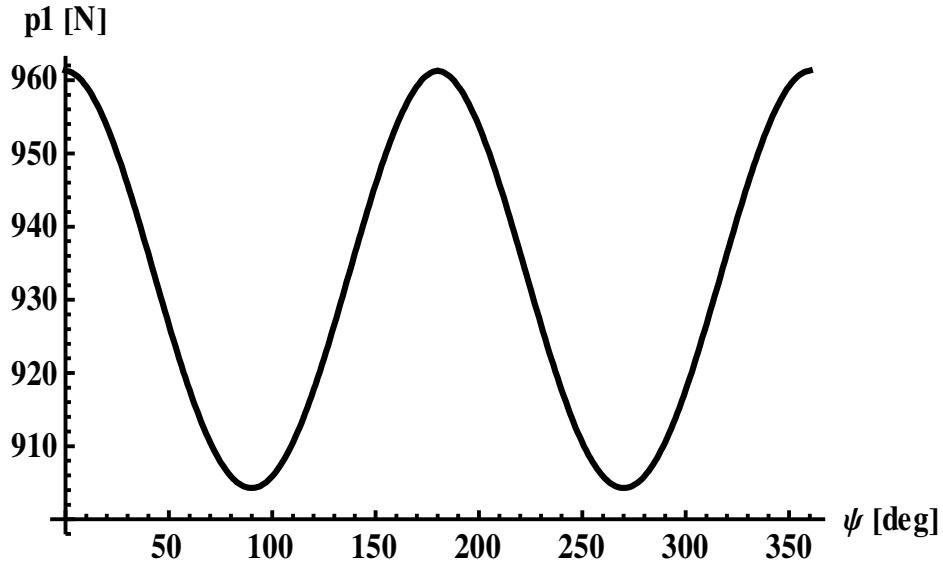


Figure 6.7a. Virtual load of needle to trunnion at spider plane, at 272Nm

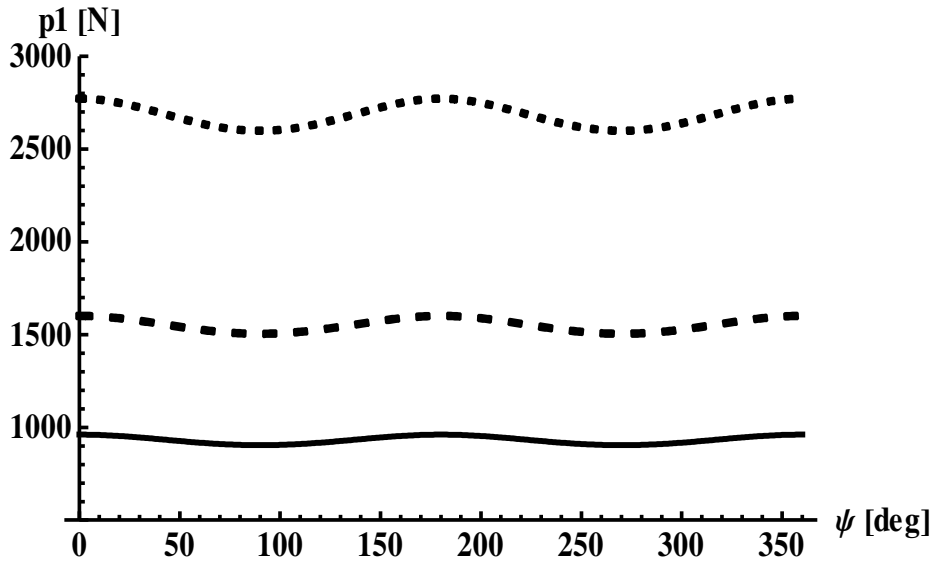


Figure 6.7b. Virtual load of needle to trunnion at spider plane

The virtual needle to trunnion load was also calculated at 4° and 10° joint angle at the loads of 272Nm. The results are summarized in Table 6.2 and the maximum and minimum loads for different torque inputs are summarized in Table 6.3.

θ_o	ϕ_{eff}	P_{1max} [N]	P_{1min} [N]	P_{1mean} [N]	P_{1amp} [N]	P_{1amp}/P_{1mean}
4°	6.70°	963.56	943.45	953.51	20.11	0.0211
7°	10.75°	961.31	904.28	932.80	57.03	0.0611
10°	16.83°	956.85	849.27	903.06	107.58	0.1191

Table 6.2. Needle-trunnion load as a function of joint angle at 272Nm

t_φ [Nm]	ϕ_{eff}	P_{1max} [N]	P_{1min} [N]	P_{1mean} [N]	P_{1amp} [N]	P_{1amp}/P_{1mean}
272	10.75°	961.31	904.28	932.80	57.03	0.0611
466	10.75°	1601.03	1504.38	1552.70	96.65	0.0622
816	10.75°	2771.80	2598.85	2685.33	173.80	0.0647

Table 6.3. Needle-trunnion load as a function of applied torque

The actual load between a needle roller and the trunnion at the spider plane, within a joint revolution, could be any value between P_{1max} and P_{1min} . Data in Table 6.2 suggests that the probability of having actual lower loads at the spider plane is higher as the joint angle increases. Thus, just looking at this data, a higher joint angle would suggest a longer wear life, which is not what happens in reality. In the author's

experience, the higher the joint angle the lower the life of a Tripode Joint. The higher the joint angle, the higher the area over which the needle roller is moving, thus increasing

the probability of a subsurface crack forming. The term $\left(\frac{1}{l_{eff} \phi_{eff} \frac{t}{2}} \right)^{1/\epsilon}$ of the proposed model, Eq (6.15), accounts for this.

On the other hand, significant changes in life occur anytime the critical angle is exceeded because the load cycles are duplicated. If the joint running angle is high enough to exceed two times the needle spacing, the load cycles are triplicated. In the prototype joints used for this work the cycle triplication occurs when $\phi_{eff} = 20^\circ$ at $\theta_o = 11.86^\circ$. The proposed fatigue model characterizes this cycle multiplication in C_2 , Eq (6.16).

It has been explained how the Tripode model captures the effects of joint angle. Now it needs to be described how the model will capture the effects of the applied torque and geometry, such as needle crowning and trunnion roundness, in the term

$$\left(\frac{1}{\tau_{eff}} \right)^c.$$

The reader will observe, from Table 6.2, that the maximum possible load at the spider plane is virtually insensitive to joint angle. P_{1max} occurs at 0° and 180° of rotation. Referring to Figure 6.4 it can be observed that the maximum load offset occurs at 180° .

Thus, this rotational position is what will be used to calculate the state of stress at the contact. Using the equations of Section 4 and Section 5 it is possible to define the state of stress in the contact. Table 6.4 summarizes the inputs to calculate the non-Hertzian pressure distribution.

t_{ϕ} [Nm]	$\Delta \times 10^{-2}$	P_{1max} [N]	P_{tm} [N/mm]	P_{tu} [N/mm]	P_{td} [N/mm]	$\xi \times 10^{-5}$
272	8.3556	961.31	97.10	102.02	92.18	2.173
466	8.3556	1601.03	161.72	169.91	153.53	3.439
816	8.3556	2771.80	279.98	294.16	265.80	5.635

Table 6.4. Inputs to calculate non-Hertzian contacts

The same approach of Section 5 was used to calculate the pressure distribution at the contact region on the trunnion. It was checked for convergence starting with a coarse mesh and making it finer until the maximum pressure and the deformation in the contact converged to five digits. The pressure distributions for the three different torque levels are shown in Figure 6.8, Figure 6.9 and Figure 6.10.

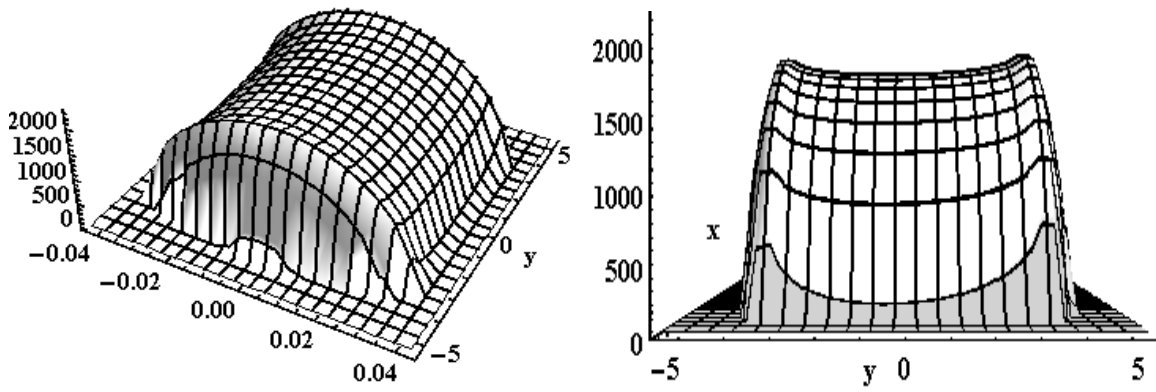


Figure 6.8. Pressure distribution, input torque of 272Nm

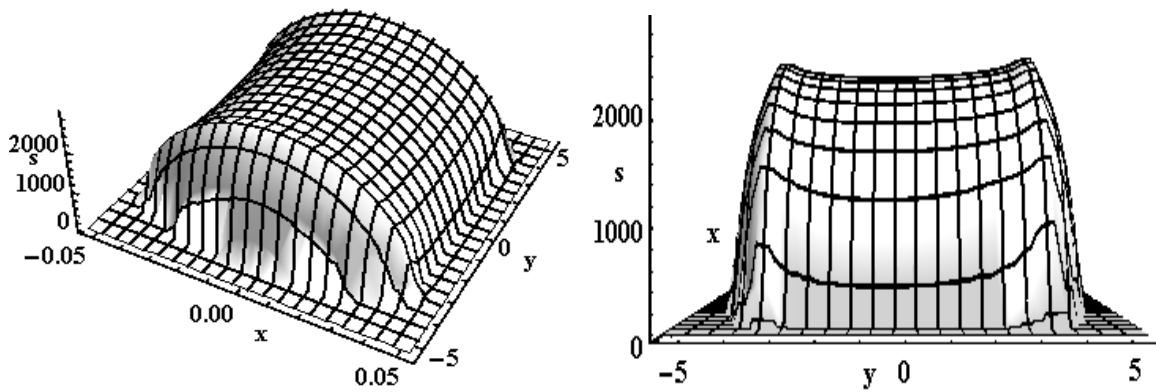


Figure 6.9. Pressure distribution, input torque of 466Nm

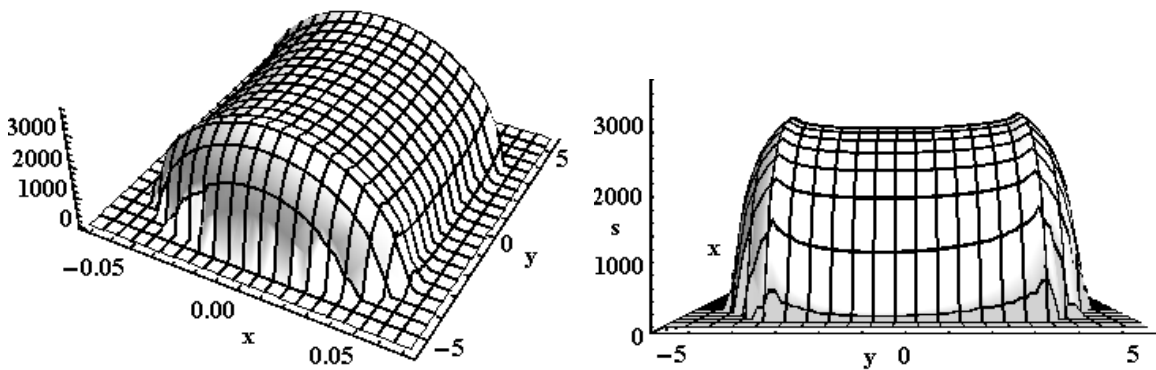


Figure 6.10. Pressure distribution, input torque of 816Nm

Table 6.5 summarizes some characteristics of the non-Hertzian pressure distribution, where s_0 is the pressure at the origin of the local coordinate reference frame, s_{max} is the maximum pressure found in the distribution, α is the relative radial displacement of the roller to the trunnion, $n \times m$ is the mesh and l_{eff} is the length of the area of contact. It is noticed that the point where the maximum pressure occurs is at upper portion of the trunnion, for this specific set of prototypes. Thus, it is expected that spalling will be most likely to start at the upper portion of the contact.

t_φ [Nm]	s_0 [MPa]	s_{max} [MPa]	α [mm]	$n \times m$	l_{eff} [mm]
272	2135.5	2315.9	0.004311	21×41	8.87
466	2688.0	2910.7	0.006652	27×41	9.39
816	3435.0	3729.7	0.010544	27×41	9.82

Table 6.5. Key characteristics of non-Hertzian contacts

For reference purposes, the Hertzian solution is also tabulated, in Table 6.6, where σ_{hmax} is the maximum pressure in the contact, b_h is the semi-width of the contact area, z_{crh} is the depth at which τ_{hmax} is located, which is the maximum principal shear stress. From Section 5 it is known that the maximum principal shear occurs at $0.786 b_h$, with a value of $0.3 \sigma_{hmax}$. The reader may be able to compare the differences in pressure, from both solutions. Once the pressure distribution is known, the effective sub-surface shear stress can be calculated.

t_ϕ [Nm]	σ_{hmax} [MPa]	b_h [mm]	z_{cr} [mm]	τ_{hmax} [MPa]
272	1963.4	0.0315	0.0248	589.0
466	2533.9	0.0406	0.0319	760.2
816	3334.0	0.0535	0.0421	1000.2

Table 6.6. Key characteristics of Hertzian contacts

Two static failure theories for ductile materials will be considered: The Maximum Shear Stress Theory (Tresca), Eq (5.63), and the Maximum Distortion-Energy Theory (Von Mises-Hencky / Octahedral), Eq (6.17).

$$\tau_{oct} = \sqrt{(\sigma_x - \sigma_y)^2 + (\sigma_y - \sigma_z)^2 + (\sigma_x - \sigma_z)^2 + 6(\tau_{xy}^2 + \tau_{yz}^2 + \tau_{xz}^2)} \quad (6.17)$$

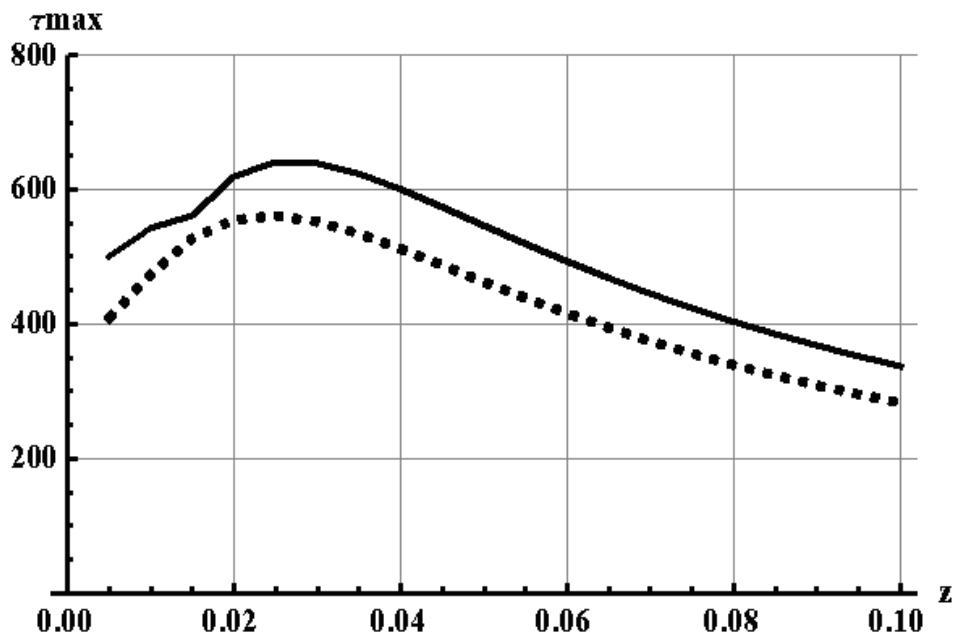


Figure 6.11. Max Shear and Octahedral shear at center of contact

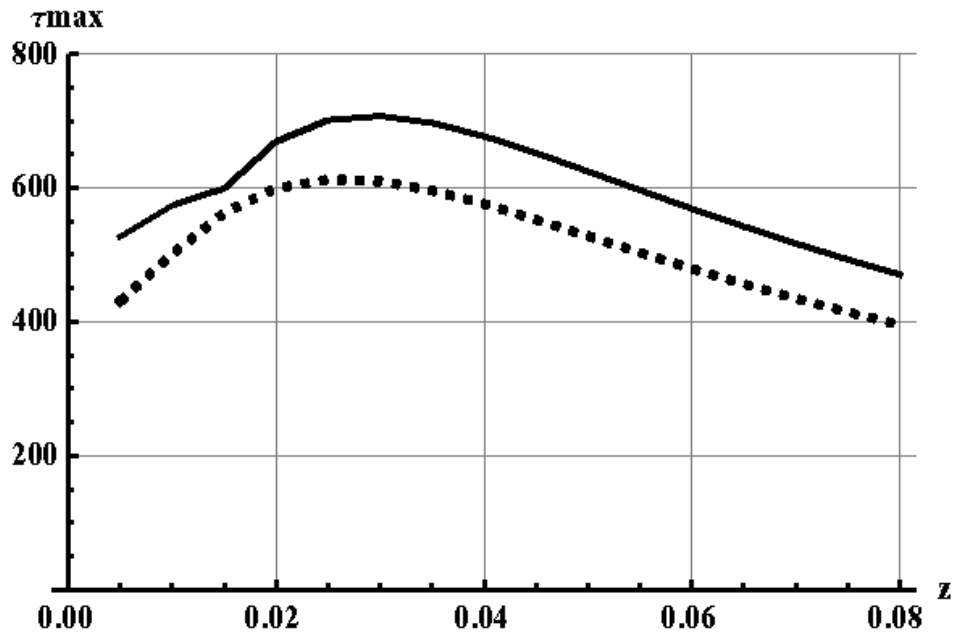


Figure 6.12. Max Shear and Octahedral shear at point of maximum pressure

Figure 6.11 compares the maximum principal shear versus the octahedral shear stress at the center of the contact, while Figure 6.12 does the same thing at the point of maximum pressure, both for an input torque of 272Nm. The analysis is repeated for 466Nm and 816Nm.

t_{φ} [Nm]	z_{max_shear} [mm]	τ_{max} [MPa]	z_{oct} [mm]	τ_{oct} [MPa]
272	0.027	642.4	0.024	561.3
466	0.034	809.1	0.030	706.6
816	0.043	1035.1	0.039	903.6

Table 6.7. Sub-surface Critical shear stresses at the center of the contact

The results for the maximum critical shear stresses τ_{\max} and τ_o , and the depth at which they occur are summarized in Table 6.7 and Table 6.8.

t_{ϕ} [Nm]	z_{\max_shear} [mm]	τ_{\max} [MPa]	z_{oct} [mm]	τ_{oct} [MPa]
272	0.029	707.5	0.026	613.3
466	0.036	888.7	0.033	770.9
816	0.047	1138.3	0.042	988.0

Table 6.8. Sub-surface Critical shear stresses at the point of maximum pressure

Up to this point, the assumption of working in the elastic range of the materials used to make the prototypes has been made. Before continuing the discussion about the proposed tripod fatigue-life model, it needs to be reviewed if plasticity should be considered in this work.

The characteristics of the materials used to make the tripod joints for the experimental portion of this work are listed below.

Spider

Material: SCM-420H (similar to SAE 4118)

Heat treatment: Carburized, quenched and temper

Surface Hardness: 58HRc MIN

Needle Roller

Material: AISI 52100

Surface Hardness: 64HRc MIN

The minimum surface hardness of 58HRc on the trunnions of a tripod spider corresponds to a Vickers hardness of 653Hv, per ASTM E-140, for non-austenitic steels. The depth of the point where the maximum shear stresses occur is very close to the surface and for now it will be assumed that the hardness at the region where the maximum shear stress occur is 653Hv.

Pavlina and Van Tyne [39] recently published linear functions that relate tensile strength and yield strength to hardness, in non-austenitic steels. Such functions are expressed as Eq (6.18) and Eq (6.19), respectively.

$$TS = -99.8 + 3.734Hv \quad (6.18)$$

$$YS = -90.7 + 2.876Hv \quad (6.19)$$

The corresponding strength values to a hardness of 653Hv are $TS = 2338.5MPa$ and $YS = 1787.3MPa$. Applying the Maximum Shear Stress Theory, Eq (6.20), and the Maximum Distortion-Energy Theory, Eq (6.21), the sub-surface critical stresses at the applied torques can be compared to the yield strength of the material.

$$SF_{\max_shear} = \frac{YS}{2\tau_{\max}} \quad (6.20)$$

$$SF_{oct} = \frac{\sqrt{2}YS}{3\tau_{oct}} \quad (6.21)$$

Thus, evaluating Eq (6.20) and Eq (6.21) it can be know if plasticity will occur in the contacts due to the applied loads. Results are summarized in Table 6.9.

t_{ϕ} [Nm]	SF_{\max_shear}	SF_{oct}
272	1.26	1.37
466	1.01	1.09
816	0.79	0.85

Table 6.9. Ratio of yield shear strength to critical shear stress

Pavlina and Van Tyne [39] reported that the standard error for Eq (6.18) and Eq (6.19) were *112MPa* and *102MPa*, respectively. Then, it is clear that plasticity will occur under a load of 816Nm and possibly at a load of 466Nm when the spider is made to its minimum hardness of 58HRc.

The plastic behavior in contacts has been studied by different authors using Finite Element Analysis (FEA) [40] and attempts to solve the problem analytically have also been made [41]. Even though good correlation between FEA and analytical methods

has been reported there is not enough published information on the material constants used in the corresponding plasticity models for a wide range of materials, specifically, carburized steel SCM-420H or SAE 4118.

The problem of elastic-plastic behavior in line contacts has also been studied using simpler approaches, such as that of Johnson, which is described and adopted in this work [24]. The study of elastic-plastic line contacts is based on the idea that in applications where rolling contact occurs and the elastic limit of the material is exceeded the first pass of a roller on a point will induce some plastic deformation and the corresponding residual stresses, when the second pass occurs the state of stress will be defined by the combined action of contact stresses and residual stresses. If the elastic limit is still exceeded more plastic deformation will take place and so on until the residual stresses have build up to the point where the applied load only causes elastic deformation. This process of cyclic deformation until the steady state is purely elastic is known as “shakedown”. Johnson’s approach is based on Melan’s theorem for shakedown (also known as static lower-bound theorem) which states:

Shakedown occurs whenever a system of residual stress, that satisfies equilibrium requirements, acts in conjunction with applied loads in such a manner that the yield criterion is not violated.

If the shakedown limit of a material is exceeded plastic flow will continue until failure occurs. Johnson’s method assumes an elastic cylinder rolling freely on an

elastic-perfectly-plastic half-space [24]. If the elastic limit is not exceeded the contact area and the contact pressure can be obtained by the methods described in Section 5, which assume an elastic cylinder rolling freely on an elastic half-space. The assumption of plane strain (zero strain in the axial direction) is necessary to simplify the problem. Figure 6.13 shows the coordinate reference frame used. The sub-index r is used to denote residual stress components.

Then, the assumption of plane strain eliminates the residual shear stresses τ_{xyr} and τ_{yxr} and makes the remaining components independent of y .

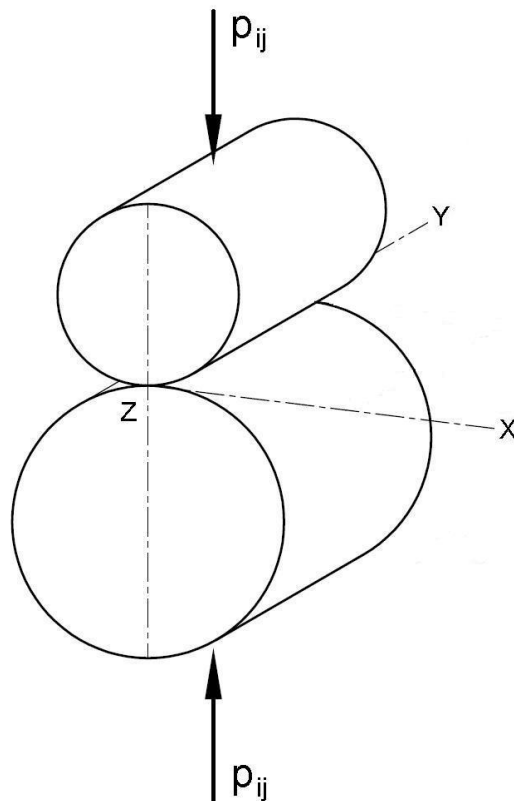


Figure 6.13. Max Shear and Octahedral shear at point of maximum pressure

If it is assumed that the plastic deformation is steady and continuous then the surface of the half-space will remain flat and the residual stresses can be assumed to be independent of x . The surface is traction free, given the assumption of free rolling. Therefore, the residual stresses σ_{zr} and τ_{zxr} are also eliminated and the system of residual stresses reduces to Eq (6.22),

$$\begin{aligned}\sigma_{xr} &= f(z) \\ \sigma_{yr} &= g(z) \\ \sigma_{zr} = \tau_{xyr} = \tau_{yxr} = \tau_{zxr} &= 0\end{aligned}\tag{6.22}$$

Thus, the principal stresses, due to the combination of contact and residual stresses are given by Eq (6.23), Eq (6.24) and Eq (6.25).

$$\sigma_{p1} = \frac{1}{2}(\sigma_x + \sigma_{xr} + \sigma_z) + \frac{1}{2}\sqrt{(\sigma_x + \sigma_{xr} - \sigma_z)^2 + 4\tau_{zx}^2}\tag{6.23}$$

$$\sigma_{p2} = \frac{1}{2}(\sigma_x + \sigma_{xr} + \sigma_z) - \frac{1}{2}\sqrt{(\sigma_x + \sigma_{xr} - \sigma_z)^2 + 4\tau_{zx}^2}\tag{6.24}$$

$$\sigma_{p3} = \nu_s(\sigma_x + \sigma_z) + \sigma_{yr}\tag{6.25}$$

It is also known from Hooke's law and from the plane strain assumption that

$$\varepsilon_y = \frac{1}{E_Y}(\sigma_y - \nu_s(\sigma_x + \sigma_z)) = 0\tag{6.26}$$

When $\sigma_y = \sigma_{yr}$ the steady state residual stress in the axial direction becomes,

$$\sigma_{yr} = \nu_s(\sigma_x + \sigma_z) \quad (6.27)$$

If the Maximum Shear (Tresca) criterion is used and if σ_{yr} is such that σ_{p3} is the intermediate principal stress, the following expression must be satisfied

$$(\sigma_{p1} - \sigma_{p2}) \leq YS \quad (6.28)$$

If Eq (6.28) is expressed in terms of the stress components it takes the form

$$\frac{1}{4}(\sigma_x + \sigma_{xr} - \sigma_z)^2 + \tau_{zx}^2 \leq \frac{YS^2}{4} \quad (6.29)$$

Expression (6.29) can not be satisfied if $\tau_{zxr} > \frac{YS}{2}$. According to Johnson, τ_{zxr} governs the shakedown limit [24]. When $\tau_{zxr} = \frac{YS}{2}$ the residual steady state stress in the tangential direction becomes,

$$\sigma_{xr} = \sigma_z - \sigma_x \quad (6.30)$$

When $\tau_{zxr} < \frac{YS}{2}$ the residual steady state stress is defined by

$$\sigma_{xr} = \sigma_z - \sigma_x + \sqrt{YS^2 - 4\tau_{zx}^2} \quad (6.31)$$

Where the stress components in the tangential (x) and radial (z) directions correspond to the state of stress at the depth of interest and the tangential location where σ_{xr} is maximized, which ensures shakedown. Table 6.10 shows the state of stress at the depth where the maximum principal elastic shear stress occurs, $z = 0.047\text{mm}$. The critical tangential locations are the plane of symmetry of the contact and at the point where τ_{zxr} is maximum. The residual stresses, are calculated using Eq (6.27) and Eq (6.31)

Component	x = 0.000mm	x = 0.056mm
σ_x	-650.0MPa	-821.9MPa
σ_z	-2926.5MPa	-1434.7MPa
τ_{xz}	0MPa	877.8MPa
σ_{xr}	-489.2MPa	-277.7MPa
σ_{yr}	-1073.0MPa	-677.0MPa

Table 6.10. Elastic stress and residual stress components at $z = 0.047\text{mm}$

Figure 6.14 shows the variation of shear stress τ_{zxr} at the depth where the maximum elastic shear stress occurs. Then, superposing the residual stresses to the stress field the principal stresses are computed to $\sigma_{p1} = -1139.2\text{MPa}$,

$\sigma_{p2} = -2926.5 \text{ MPa}$ and $\sigma_{p3} = -2146 \text{ MPa}$. Hence, the assumption of σ_{p3} being the intermediate principal stress is verified and the maximum principal shear stress at a depth of 0.047 mm is $\tau_{\max} = 893.7 \text{ MPa}$.

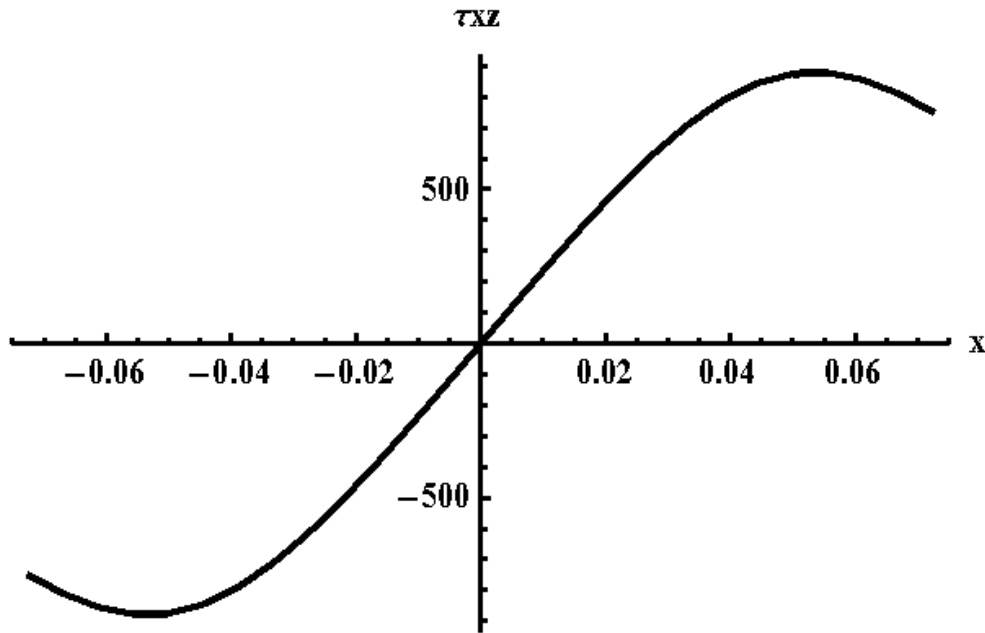


Figure 6.14. Shear stress τ_{zx} at a depth of 0.047 mm

If the Maximum Distortion-Energy (Von Mises-Hencky / Octahedral) criterion is used, the following expression must be satisfied

$$(\sigma_{p1} - \sigma_{p2})^2 + (\sigma_{p2} - \sigma_{p3})^2 + (\sigma_{p3} - \sigma_{p1})^2 \leq 2YS^2 \quad (6.32)$$

Substituting Eq (6.23) through Eq (6.25) and Eq (6.27) into Eq (6.32), simplifying and solving for σ_{xr} it is obtained,

$$\sigma_{xr} = \frac{1}{2}(\sigma_z - 2\sigma_x(1-\nu) + 2\nu\sigma_z) + \frac{1}{2}\sqrt{4YS^2 - 3(\sigma_z^2(1-2\nu)^2 - 4\nu(1-2\nu)\sigma_z\sigma_x + 4(\tau_{zx}^2 + \nu^2\sigma_x^2))} \quad (6.33)$$

Similarly, the state of stress at the plane of symmetry and at the point where τ_{zxr} is maximum is evaluated and summarized in Table 6.11. The depth where the octahedral shear is maximum, $z = 0.042\text{mm}$, is considered. The residual stresses are calculated using Eq (6.27) and Eq (6.33).

Component	x = 0.000mm	x = 0.050mm
σ_x	-780.8MPa	-870.6MPa
σ_z	-3046.9MPa	-1684.4MPa
τ_{xz}	0MPa	899.4MPa
σ_{xr}	-226.0MPa	+128.0MPa
σ_{yr}	-1148.3MPa	-1277.5MPa

Table 6.11. Elastic stress and residual stress components at $z = 0.042\text{mm}$

Finally, superposing the residual stresses to the stress field the principal stresses are computed to $\sigma_{p1} = -1006.8\text{MPa}$, $\sigma_{p2} = -3046.9\text{MPa}$ and $\sigma_{p3} = -2296.6\text{MPa}$. Hence, the octahedral shear stress at depth of 0.042mm is $\tau_{oct} = 842.5\text{MPa}$.

It was indicated at the beginning of this Section that the fatigue life problem in Tripode joints is considered as a “high-cycle fatigue problem”. Therefore, the proposed model applies only when the joint is operating in the elastic region of the material or when shakedown occurs in the studied contacts, which is possible only if the square roots of Eq (6.31) and Eq (6.33) are real, under the assumption of an elastic-perfectly plastic material model.

6.9 Test results

Bearings are characterized by the *L10* life, which is the life or number of cycles that can be completed by 90% of a population of bearings. The same *L10* definition is adopted for tripode joints. Given there are twelve trunnions per test it was expected that one or two trunnions would show pits or spalling before the rest. Therefore, the life of a tripode on the conducted tests is defined as the number of cycles that ten out of twelve or eleven out of twelve trunnions can complete without presenting spalling.

The tests were run per the schedules shown in Table 6.1. A conservative a priori life estimation was done and joints were inspected on regular intervals until pits or spalling were found in at least one trunnion. In two of the tests the spalled parts were replaced by new ones and the evaluation continued to verify the expected dispersion in life data. The test results are summarized in Table 6.12. The naming convention for the tested spiders during the rest of this work will consist of using a letter to indicate the test and the number the part had in the test (i.e. Part B-2).

Test / Torque	Part 1	Part 2	Part 3	Part 4
A – 272Nm	Completed 605hrs: 2mm ² of spalling and 2 pits on one trunnion	Completed 605hrs: 1 pit on one trunnion	Completed 808hrs: Clean surface (test suspended)	Completed 808hrs: Clean surface (test suspended)
B – 466Nm	Completed 246hrs: 5mm ² of spalling and 5 pits on one trunnion	Completed 246hrs: 1 pit on one trunnion	Completed 120hrs: 56mm ² of spalling on one trunnion	Completed 246hrs: Clean surface (test suspended)
C – 816Nm	Completed 96hrs: Clean surface (test suspended)	Completed 96hrs: 26mm ² of spalling on one trunnion	Completed 96hrs: Clean surface (test suspended)	Completed 96hrs: Clean surface (test suspended)

Table 6.12. Test results summary

Pictures of the spalled and/or pitted surfaces are shown in Figures 6.15 through 6.17.

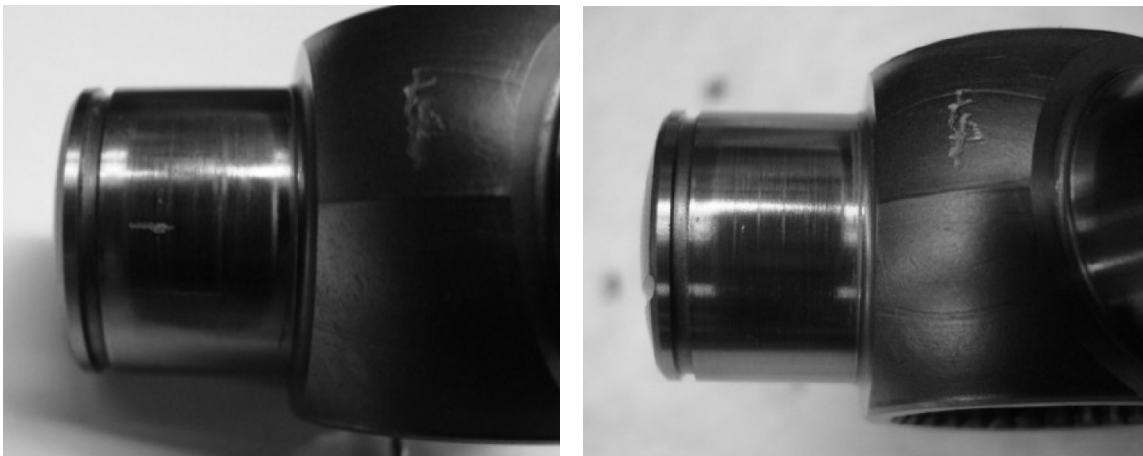


Figure 6.15. Parts A-1 and A-2

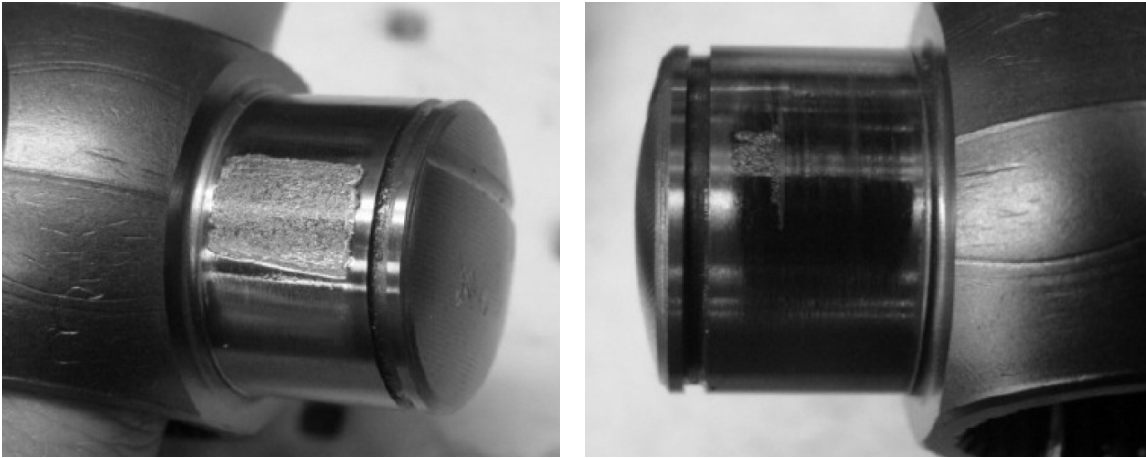


Figure 6.16. Parts B-3 and B-1

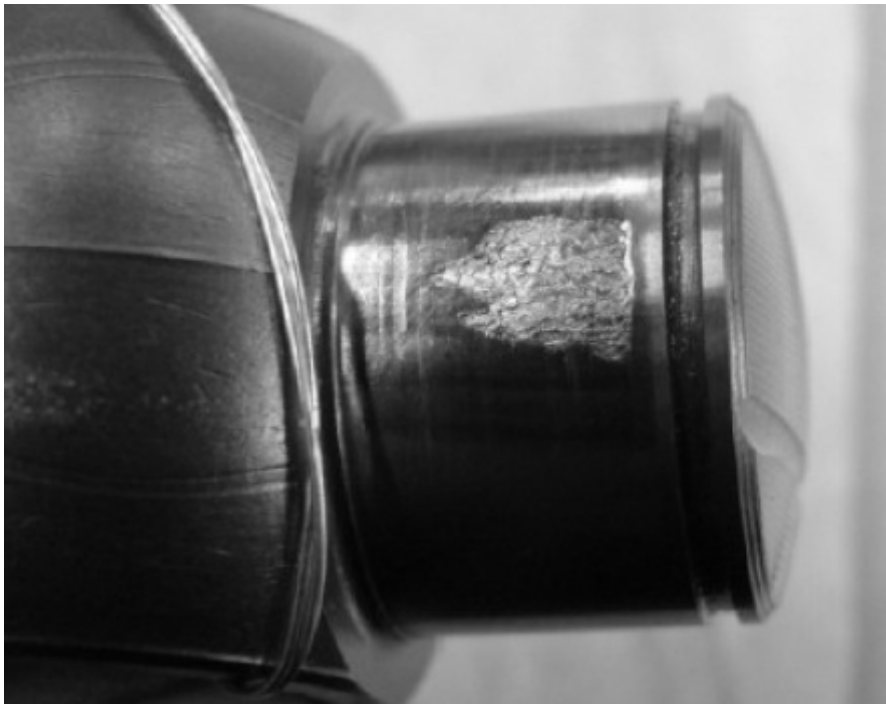


Figure 6.17. Part C-2

It can be observed in the previous pictures that the location of the pits or spalling is in the upper portion of the trunnion. The exception would be Part B-3 where the exact

location of the point of spalling initiation can not be determined given the large area. Analysis using traditional Hertzian line contacts, uniform pressure along the length of contact, would have not been able to predict the region of the trunnion where the spalling was most likely to initiate. The non-Hertzian contact analysis used in this work allows so.

Part B-2 was checked under the confocal microscope. It was removed from test when only a small pit was present, indicating the spalling had just initiated. Figure 6.18a and Figure 6.18b show the scanned surface, which given the curvature of the trunnion was obtained scanning a clean portion of the surface and then scanning and subtracting the collected data from the region with the pit.

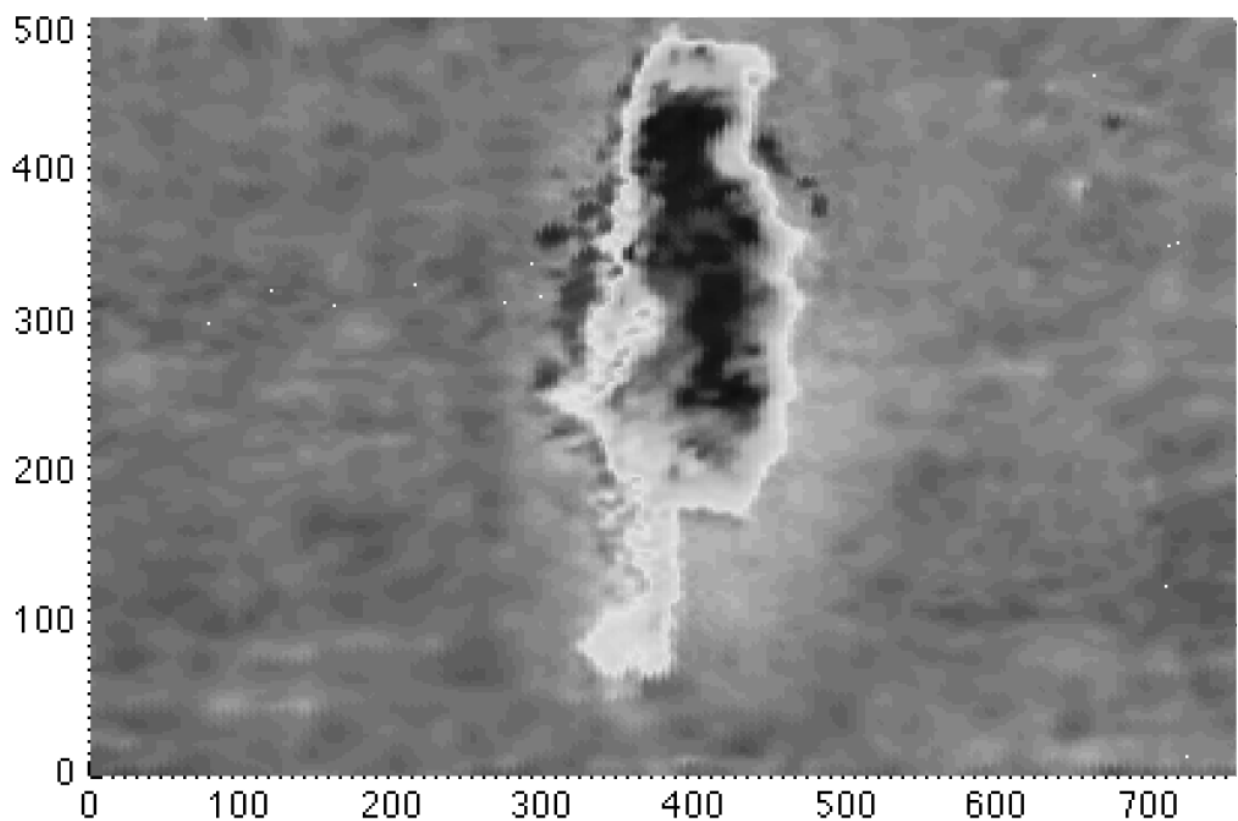


Figure 6.18a. Part B-2 (units are microns)

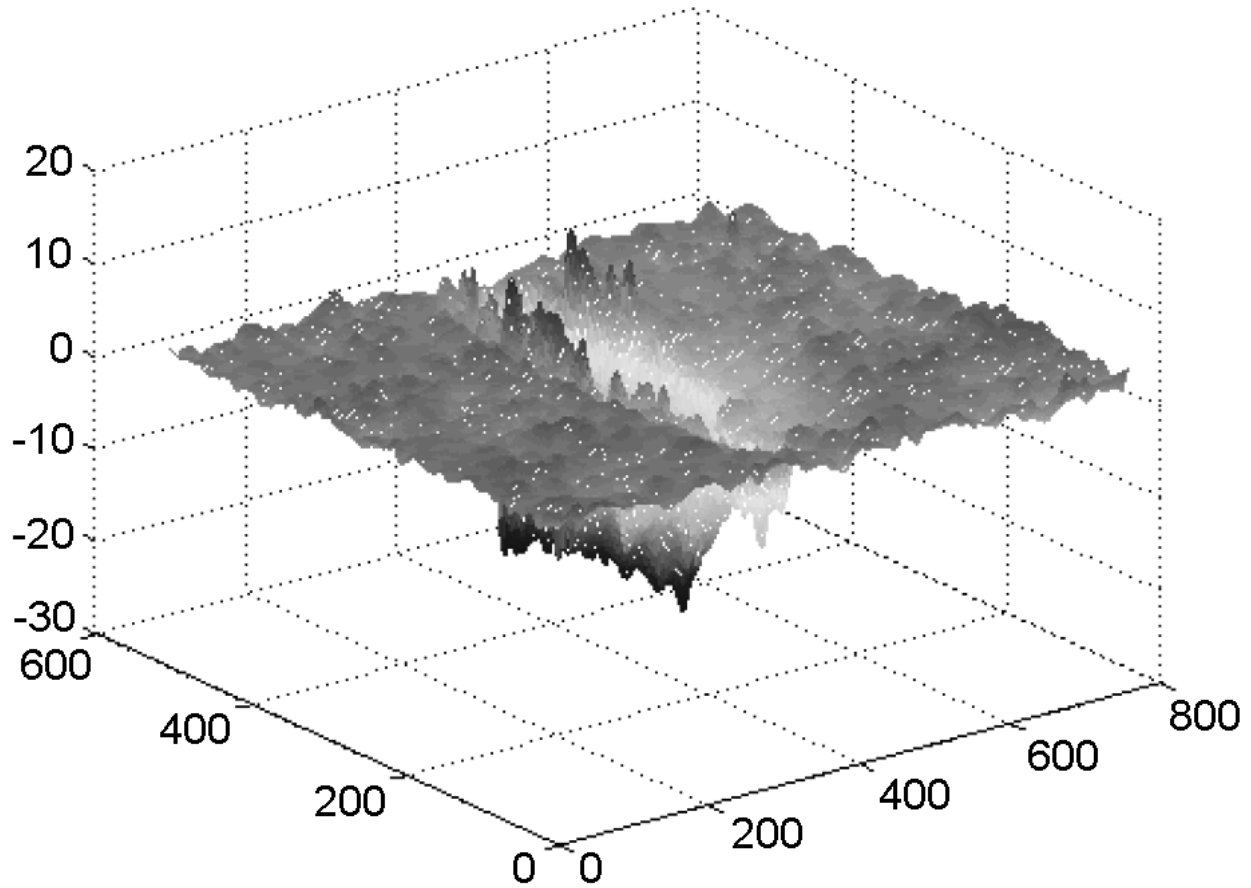


Figure 6.18b. Part B-2 (units are microns)

The depth of the pit has approximately the same value of the calculated depth where the critical shear stress occurs. This fact supports the assumption of the spalling being generated by a crack that starts under the surface at the region where the critical shear stress occurs.

It is assumed in this work that the Weibull slope representing the scatter of the life data for tripod joints is the same Weibull slope present in bearings, which is $\epsilon = 1.11$ [38]. Table 6.13 summarizes the actual life in cycles and the geometric variables that

are input into Eq (6.15) to do curve fitting, using least-squares, for the exponent c and for the constant C_1 .

$$L = C_1 C_2 \left(\frac{1}{\tau_{eff}} \right)^c \left(\frac{1}{l_{eff} \phi_{eff} \frac{t}{2}} \right)^{1/\epsilon} \quad (6.15)$$

The trunnion diameter t and the constant C_2 used in Eq (6.15) are 20.975mm and 0.5, respectively. The time under load in Table 6.13 was obtained by multiplying the time on test by a factor 20/21, which is based on the schedules from Table 6.1. A time of twenty minutes of load and one minute of cooling and grease distribution per every twenty one minutes of testing.

Torque [Nm]	Speed [rpm]	Time on test [Hr]	Time under Load [Hr]	Life $\times 10^6$ [cycles]	ϕ_{eff}	l_{eff} [mm]
272	1200	605	576	41.49	10.75°	8.87
466	700	120	114	4.80	10.75°	9.39
816	400	96	91	2.19	10.75°	9,82

Table 6.13. Inputs to best-fit life equation

Table 6.14 summarizes the effective shear stresses used in Eq (6.15) to do curve-fitting, the fitted values of c and C_1 and the predicted life after the curve fitting.

Torque [Nm]	$c = 9.462$ $C_1 = 1E30$	$c = 9.146$ $C_1 = 3.42E28$	Life $\times 10^6$ [cycles]	Life $\times 10^6$ [cycles]	Life $\times 10^6$ [cycles]
	τ_{max} [MPa]	τ_{oct} [MPa]	Actual	τ_{max}	τ_{oct}
272	707.5	613.3	41.49	41.32	41.49
466	888.7	770.9	4.80	4.54	4.87
816	893.7	842.5	2.19	4.13	2.07

Table 6.14. Life prediction summary

It can be observed from Table 6.14 that the values of the best-fit constant c are within the range of stress-life exponents reported for bearings, which is 8.4 to 12 [38]. The octahedral shear criterion seems to be more appropriate to predict the life of Tripode joints. Figure 6.19 compares the life predictions versus the actual life in a log-log scale, where the circles represent the actual life, the squares represent the maximum principal shear criterion and the triangles represent the octahedral criterion.

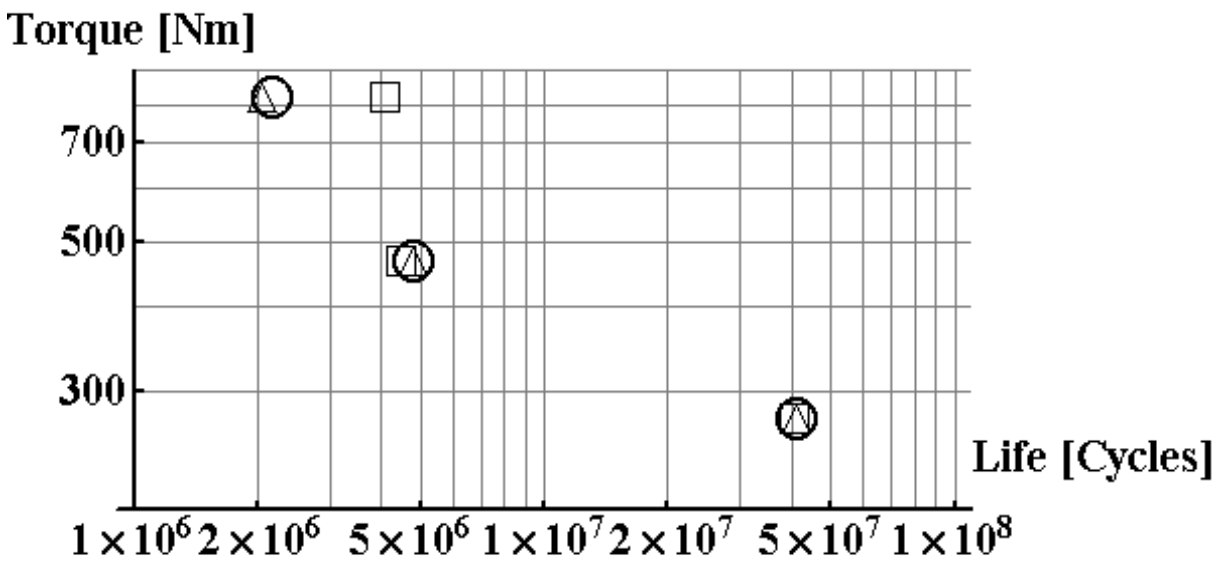


Figure 6.19. Actual versus theoretical life

Residual stresses were checked experimentally by X-Ray diffraction in one of the trunnions of Part C-4. An unloaded area was inspected at various depths to quantify the residual stresses produced by the grinding process used to manufacture the prototypes. Figure 6.20 shows the residual stress gradient, where the circles represent the stresses in the circumferential direction and the triangles represent the stresses in the axial direction. Residual stresses were also checked at the surface and at a depth of 0.042mm in the area where the maximum contact pressure was calculated to occur, after test. Squares in Figure 6.20 represent the steady state circumferential residual stress and diamonds represent the steady state axial residual stress.

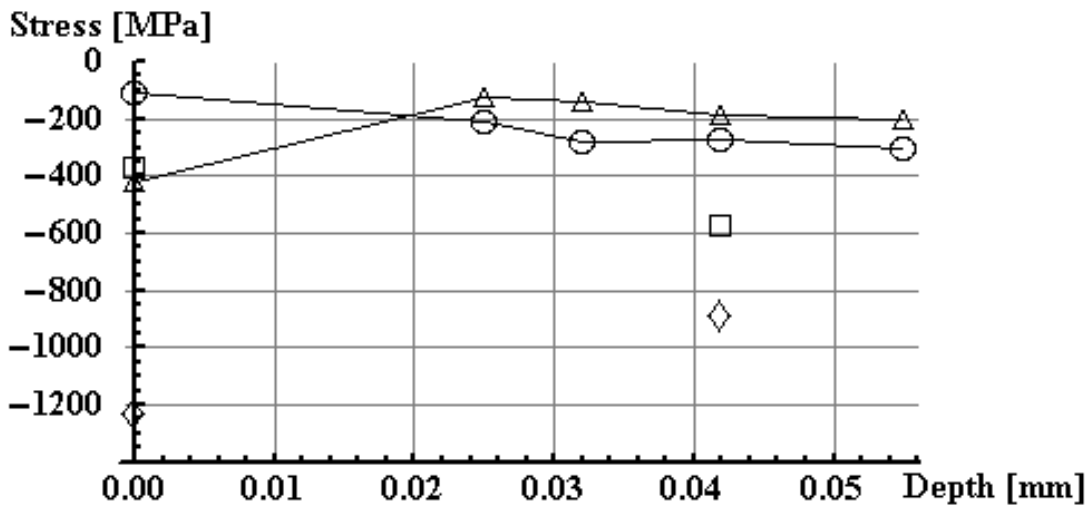


Figure 6.20. Residual stresses in Spider C-4

The reader may refer to the Appendices to see more data relative to the residual stress analysis by X-Ray diffraction. The residual stresses experimentally determined were superposed to the calculated elastic stresses. New critical shear stresses were

calculated and the corresponding curve-fitting was repeated. Results are summarized in Table 6.15

Torque [Nm]	$C = 9.345$ $C_1 = 1.02E29$	$c = 9.700$ $C_1 = 2.89E29$	Life $\times 10^6$ [cycles]	Life $\times 10^6$ [cycles]	Life $\times 10^6$ [cycles]
	τ_{max} [MPa]	τ_{oct} [MPa]	Actual	τ_{max}	τ_{oct}
272	601.1	529.6	41.49	41.47	41.50
466	747.7	664.6	4.80	5.13	4.36
816	850.8	693.3	2.19	1.47	2.78

Table 6.15. Life prediction summary, residual stresses included

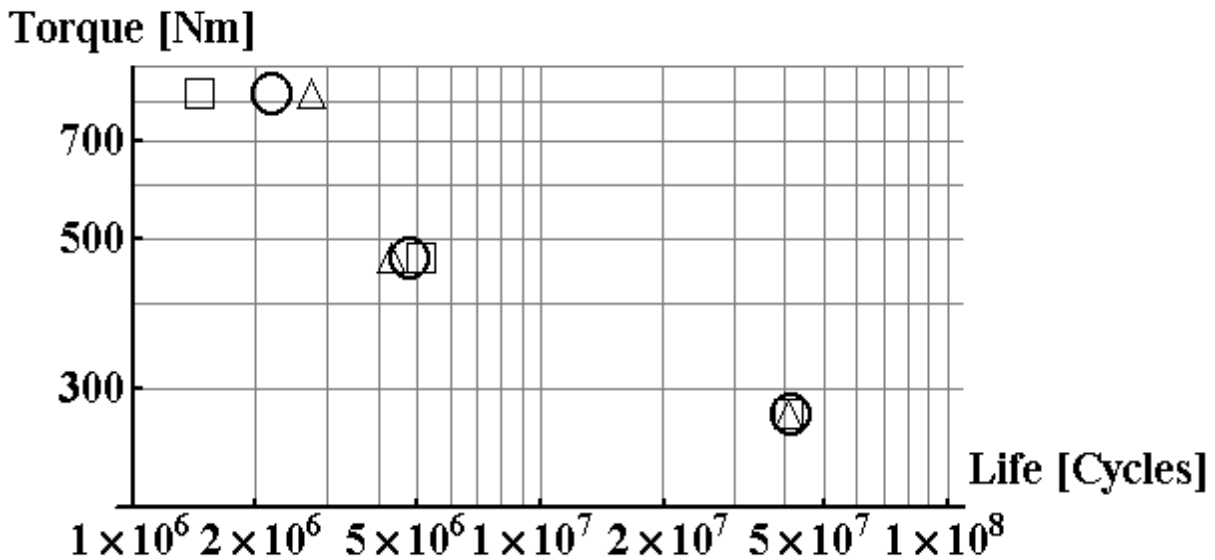


Figure 6.21. Actual versus theoretical life after superposing residual stresses

Figure 6.21 compares the life predictions after including the experimentally determined residual stresses. The circles represent the actual life, the squares

represent the maximum principal shear criterion and the triangles represent the octahedral criterion.

The life prediction using the Octahedral Shear criterion fits better actual life values than the prediction using the Maximum Shear criterion, where a better fit means a lower value of the sum of squared errors. The better fit using the Octahedral Shear criterion holds true when the residual stresses, caused by the manufacturing process used to make the trunnions, are neglected or included.

A stress-life exponent of $c = 9.7$ was reported by Baughman [42] for rolling contact fatigue of bearings, which is similar to best-fit c value determined in this work, using the Octahedral shear criterion and including residual stresses. Then, Eq (6.15) can take the form of Eq (6.34), which is the expression that will be used in the remaining portion of this work.

$$L = 2.89 \times 10^{29} C_2 \left(\frac{1}{\tau_{eff}} \right)^{9.7} \left(\frac{1}{l_{eff} \phi_{eff} \frac{t}{2}} \right)^{0.9} \quad (6.34)$$

Material analysis was performed in Part A-2, the actual chemical composition of the batch of material used to make the prototype spiders can be reviewed in the Appendices of this work. The average surface hardness before testing was measured to be 61.5HRc. After testing, Part A-2 was sectioned close to the generated pit and a hardness traverse check surface to core was performed, shown in Figure 6.22.

Hardness in the region of maximum shear was found to be 62HRc (743Hv), which supports the idea of an elastic contact for the tests at 272Nm and 466Nm.

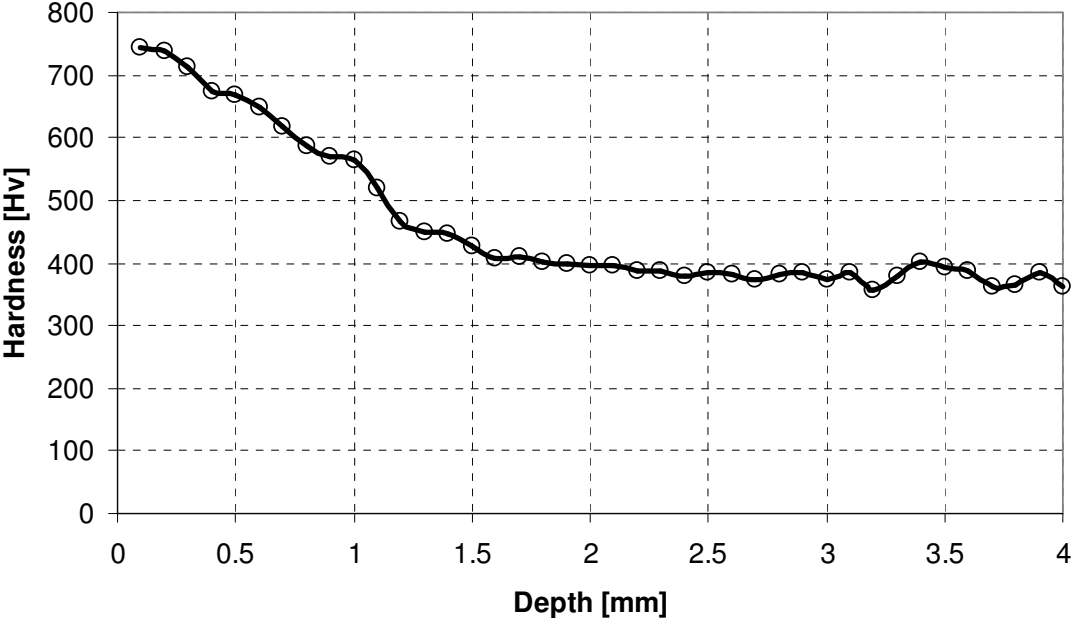


Figure 6.22. Hardness gradient in trunnion

7. TRUNNION FORM OPTIMIZATION

7.1 Introduction

It has been studied In the previous sections the way loads are transmitted inside of the Tripode Joint (Section 3) after an input torque is applied, how those loads are distributed among needle rollers (Section 4), the state of stress in the contacts because of the loads (Section 5) and the relationship between the state of stress and the wear fatigue-life of the joint (Section 6). One of the most effective ways of improving the life of a Tripode Joint, while keeping the same materials, the same packaging and similar manufacturing processes is to improve the load distribution among needles to reduce the peak load on the most heavily loaded contact. The consequence of reducing the peak load will be a reduced stress. Therefore, an increment in the number of cycles a joint can survive before spalling. This Section deals with the optimization of the trunnion form to minimize the peak load at the contacts.

7.2 Elliptical vs. Circular Trunnion

It was mentioned in Section 4 that a trunnion can be made with an elliptical shape to have a better load distribution among the needle rollers. The elliptical form was defined based on radial deviations from the minimum circumscribed circle. Eq (4.70) describes such deviations, where e_t is the elliptical ratio, defined as the ratio of the major to the minor axis of the ellipse.

$$\Omega_V = -\frac{t}{2} \left(1 - \sqrt{\cos\left(\phi_V + \frac{\pi}{2}\right)^2 + \frac{1}{e_t^2} \sin\left(\phi_V + \frac{\pi}{2}\right)^2} \right) \quad (4.70)$$

The author has tested joints made with elliptical trunnions and equivalent joints made with circular trunnions. In the author's experience parts made with elliptical trunnions perform better than parts made with circular trunnions when tested on the same durability schedule [43], which supports the idea of lower stresses due to a better distribution of contact loads. For illustration purposes, Schedule 3 of Table 6.1 will be used to show the estimated life improvement when an elliptical trunnion is used, with respect to a perfect circular trunnion.

Table 7.1 shows a comparison of the load distributions on the trunnion at an input torque of 816Nm and at a joint angle of 7°, while Table 7.2 shows a comparison of the input variables for Eq (6.34), which is used to calculate the joint life at different stress levels.

$$L = 2.89 \times 10^{29} C_2 \left(\frac{1}{\tau_{eff}} \right)^{9.7} \left(\frac{1}{l_{eff} \phi_{eff} \frac{t}{2}} \right)^{0.9} \quad (6.34)$$

ϕ_v	Circular [N]	Elliptical [N]
0°	2772	2632
10°	2386	2257
20°	1661	1589
30°	991	1018
40°	494	610
50°	146	342
60°	0	87
70°	0	0
80°	0	0

Table 7.1. Load distribution, circular vs. elliptical trunnion ($e_t = 1.003$)

The reader will notice in Table 7.1 that an extra needle carries load in the elliptical trunnion and the peak load goes down by 5%. Form errors and waviness will be ignored for the sake of illustrating the nominal differences between different trunnion geometries. Also, for the purpose of illustrating differences between trunnion profiles, it will be assumed that the trunnion is hard enough to neglect plastic deformation and only elastic contacts will be considered.

It can be observed in Table 7.2 that octahedral shear stress in the elliptical trunnion is lower than in the circular trunnion by 2.3% while there is an increment in predicted life of 24.4%, a significant improvement.

Variable	Circular	Elliptical
P_{1max} [N]	2772	2632
S_0 [MPa]	3435.0	3355.9
S_{max} [MPa]	3729.7	3646.9
α [mm]	0.010544	0.010095
ϕ_{eff}	10.75°	10.75°
l_{eff} [mm]	9.82	9.82
z_{oct} [mm]	0.042	0.041
τ_{oct} [MPa]	988.0	965.6
$L_{10} \times 10^6$ [cycles]	0.090	0.112

Table 7.2. Life comparison, circular vs. elliptical trunnion at 816Nm and 7°

7.3 Optimized vs. Elliptical Trunnion

The advantages of an elliptical trunnion over a circular trunnion are clear. Then, it is necessary to find out if there is another trunnion form that will distribute contact loads better than a perfect ellipse, an optimum shape. The computer program for the load model described in Section 4 was modified to make it compatible with commercially

available optimization tools. Two tools were selected, the SOLVER function included in a commercial spreadsheet software (Tool A) and a specialized optimization software (Tool B) [44]. The optimization problem was set up the following way.

Define a load on each needle roller as p_v , where $v = 1, 2, 3, \dots, n$. The number of needle rollers is indicated by n . The angular location of the needle roller ϕ_v is established with respect to the plane of symmetry of the load distribution, where the maximum load $p_{v\max}$ occurs when $\phi_v = 0^\circ$ and $v = 1$. The form of the trunnion is defined by the radial deviations Ω_v from the trunnion base circle.

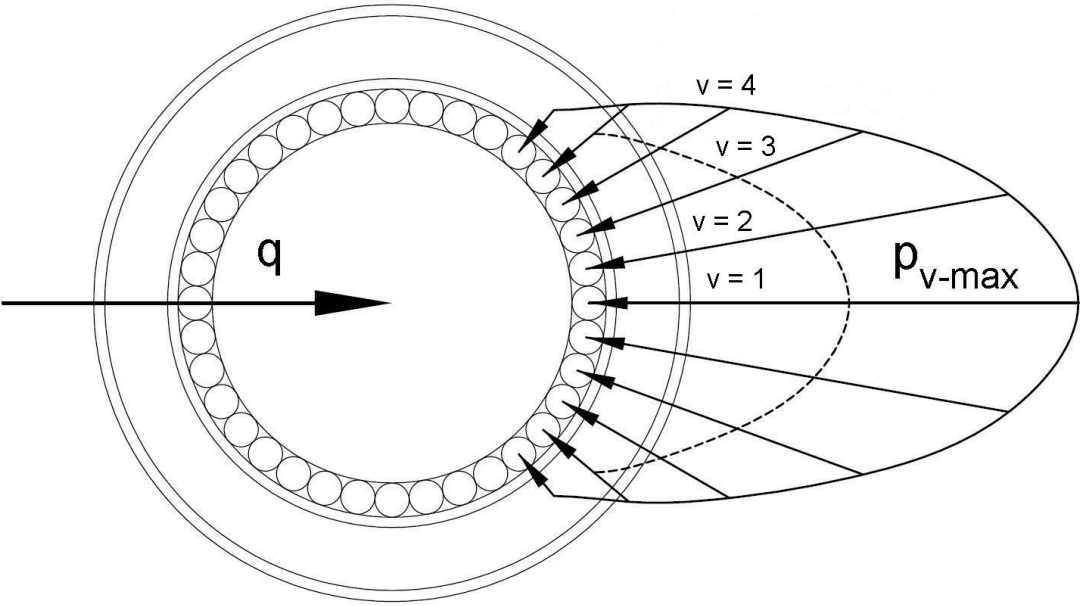


Figure 7.1. Load distribution on a trunnion

The SOLVER function of Tool A can handle optimization of only one variable. Therefore, the objective function was to minimize the difference of loads with respect to the maximum load.

$$\min \left(\sum_{v=2}^{\text{int}\left(\frac{n}{4}+1\right)} (\rho_{v\max} - \rho_v)^2 \right) \quad (7.1)$$

For $n = 36$. Subject to the trunnion having a symmetrical shape and to the constraints

$$\rho_{v\max} \geq \rho_v \geq \rho_{v+1} \quad (7.3)$$

$$\begin{aligned} \Omega_1 &= 0.031 \\ \Omega_{10} &= 0 \end{aligned} \quad (7.4)$$

Changing the values of Ω_v for $v = 2, \dots, 9$. Constraint $\Omega_1 = 0.031$ mm defines the “elliptical gap”, which is the same gap of the ellipse used to calculate Table 7.1. The elliptical gap is defined as the radial deviation from the base circle of the trunnion at the spider plane.

Tool B has the capability of doing multi-objective optimization. Therefore, two variables were targeted to be minimized: The difference of loads with respect to the maximum load and the maximum load.

$$\min \left(\sum_{v=2}^{\text{int}\left(\frac{n}{4}+1\right)} (\rho_{v\max} - \rho_v)^2 \right); \quad \min(\rho_{v\max}) \quad (7.5)$$

Subject to the trunnion having a symmetrical shape and to the constraints

$$\rho_v - \rho_{v+1} \geq 0 \quad (7.6)$$

$$\begin{aligned} \Omega_1 &= 0.031 \\ \Omega_{10} &= 0 \end{aligned} \quad (7.4)$$

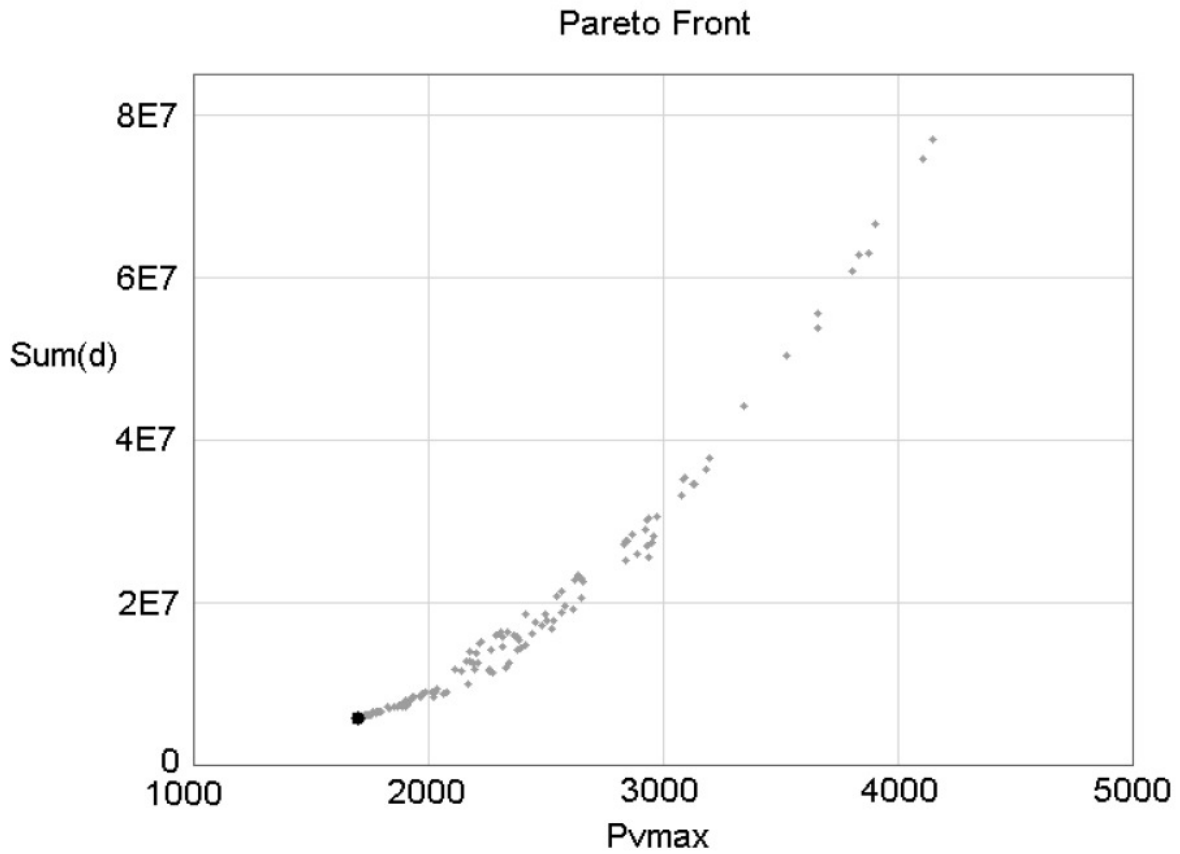


Figure 7.2. Pareto Front

A Pareto Front was generated for Eq (7.5), shown in Figure 7.2. The results of the two optimizations are shown and compared in Table 7.3.

ϕ_v	Elliptical [N]	Elliptical Ω_v [mm]	Tool A [N]	Tool A Ω_v [mm]	Tool B [N]	Tool B Ω_v [mm]
0°	2632	0.0310	1714	0.0310	1702	0.0310
10°	2257	0.0301	1714	0.0270	1698	0.0270
20°	1589	0.0274	1714	0.0181	1689	0.0179
30°	1018	0.0232	1714	0.0076	1650	0.0074
40°	610	0.0182	1315	0	1448	-0.0015
50°	342	0.0128	0	0.0082	0	0.0027
60°	87	0.0077	0	0.0047	0	0.0077
70°	0	0.0036	0	0.0044	0	0.0002
80°	0	0.0009	0	0.0014	0	0.0000

Table 7.3. Load distribution, circular vs. elliptical vs. optimized trunnion

Even though less needle rollers are loaded in the optimized profile the load is more uniformly distributed and there is a significant reduction in the peak load with respect to the elliptical trunnion, 35.3% when the best optimized solution (Tool B) is considered. If the two optimum solutions are compared it is clear that the solution

obtained using Tool B features a lower peak load and a reduced difference between adjacent loads and the peak load, which were the optimization targets. Table 7.4 shows a comparison of the pressure, critical stress and predicted life between the circular, the elliptical and the best optimized trunnion profile.

Variable	Circular	Elliptical	Optimized
P_{1max} [N]	2772	2632	1702
s_0 [MPa]	3435.0	3355.9	2763.4
s_{max} [MPa]	3729.7	3646.9	3031.1
α [mm]	0.010544	0.010095	0.007001
ϕ_{eff}	10.75°	10.75°	10.75°
l_{eff} [mm]	9.82	9.82	9.54
z_{oct} [mm]	0.042	0.041	0.034
τ_{oct} [MPa]	988.0	965.6	802.8
$L_{10} \times 10^6$ [cycles]	0.090	0.112	0.690

Table 7.4. Life comparison, different trunnion forms at 816Nm and 7°

The advantages of an optimized trunnion over an elliptical trunnion are clear. Reduction in maximum pressure of 16.8% and an increment in predicted life of more than six times, at 816Nm. It must be noted that given the non-linearity of contact stresses, with respect to torque, the optimum trunnion profile would be different if a different input torque were used.

8. CONCLUSIONS

The kinematics of a Tripode Joint has been studied in this work. A Tripode Joint is not a perfect constant velocity joint and the effective angular displacement of ball rollers changes as a function of joint angle. A higher joint angle means a higher deviation from the perfect constant-velocity behavior and an integral approach has to be followed to calculate the angular displacement of rollers.

At joint angles where the Tripode Joint is tested and validated (i.e. 7°) the non-constant velocity behavior causes very small changes in the loads that are transmitted between balls and ball bores, less than 0.1%. Such changes can be neglected for the purpose of calculating the loads that are transmitted to the needle rollers.

The effective arch ϕ_{eff} traveled by a needle roller on a trunnion can be calculated neglecting joint angle variation at joint angles where the Tripode Joint typically operates and kinematic equations, such as those used to calculate roller displacement, can be linearized.

At typical functional angles, 7° and lower, the Tripode Joint can be considered a Constant Velocity Joint even though it exhibits small deviations from constant-velocity behavior.

The main contributor to Generated Axial Force (GAF) in a Tripode joint is the sliding friction between balls and ball bores. The rolling friction between trunnions, needle rollers and balls is very small and allows modeling of the contacts between the trunnion and the needle rollers as frictionless contacts.

The state of stress in the contact between a needle roller and a trunnion can be approximated considering Hertzian line contacts. However, non-Hertzian contacts are a more complete solution. Non-Hertzian contact analysis, which can be performed meshing the contact area in small rectangles, assigning a load to each rectangle and applying superposition, allows calculation and understanding of the pressure distribution in the contact. Factors that may influence the pressure distribution in the contact between a trunnion and a needle roller, such as needle crowning, needle skewing, edge loading and asymmetrical loading, were considered in this work and its effects were individually studied.

The area in the contact where maximum pressure was calculated to occur matched the area where trunnion pitting in tested parts initiated, verifying the advantages of non-Hertzian contact analysis over traditional line-Hertzian contacts.

The pressure distribution on a contact causes sub-surface stresses. Two static failure theories for ductile materials were considered in this work to calculate the critical shear stress under the surface: The Maximum Shear Stress Theory and the Maximum Distortion-Energy Theory. The Maximum Shear Stress Theory predicts the critical shear

stress to be at a deeper point than the location predicted by the Maximum Distortion-Energy Theory.

Wear fatigue-life in a Tripode Joint is defined when spalling or pitting occurs on the surface of a trunnion due to repeated rolling contact. A pit always precedes a large spalled area. A pit forms due to a crack under the surface at the depth where the critical shear occurs. In this work it was found that the depth of a newly generated pit was in the same region where the critical shear stress was predicted to be, which validates the assumption of a pit initiating under the surface.

Residual stresses were included as part of the contact stress analysis for life prediction. Theoretical residual stresses due to shakedown of the material were calculated considering an Elastic-Perfectly Plastic model and were found to be compressive. Residual stresses in the trunnion were measured using X-Ray diffraction techniques and found to be compressive after testing in the contact area, which confirms the existence of shakedown in the material.

Theoretical residual stresses were directionally correct when compared to experimentally determined residual stresses and in a similar order of magnitude. The use of more sophisticated plasticity models would allow a better prediction of residual stresses.

Measured residual stresses were superposed to the calculated elastic state of stress. These stresses, in combination with the corresponding actual life of Tripode Joints obtained from testing, were used as data points to best-fit a stress-life exponent and a proportionality constant for the Tripode Equation proposed in this work.

The critical stress values determined using the Maximum Distortion-Energy Theory provided a better fit than the values obtained using the Maximum Shear Stress Theory. Therefore, the Maximum Distortion-Energy Theory is preferred to predict wear fatigue-life in Tripode Joints.

The final form of the Tripode Equation proposed in this work is

$$L = C_1 C_2 \left(\frac{1}{\tau_{eff}} \right)^c \left(\frac{1}{l_{eff} \phi_{eff} \frac{t}{2}} \right)^{1/\varepsilon}$$

$$C_2 = \left(\text{Ceiling} \left(\frac{\phi_{eff}}{2\pi/n} \right) \right)^{-1}$$

Where $c = 9.7$, $\varepsilon = 1.11$ and $C_1 = 2.89 \times 10^{29}$. The model can be used to predict wear life-fatigue in Tripode Joints.

The value of the constant C_1 is specific to the type of grease and manufacturing processes used to make the Tripode Joints used in this work, which cover a wide range

of automotive applications. A different grease or different manufacturing process would require the experimental determination of a new constant C_1 .

The best way to improve wear life-fatigue in a Tripode joint is to minimize the peak load at the contacts between the trunnion and the needle rollers, and at the same time minimize the load differences between adjacent needles. Optimizing for these two objective functions at the same time generated a Pareto front that converged to one point, which uncovered that the objective functions are not in contraposition.

Elliptical trunnions distribute load among needle rollers better than circular trunnions, which has the advantage of better durability.

An optimized trunnion shape can dramatically increase the wear life-fatigue in a Tripode Joint, when compared to perfectly round and perfectly elliptical trunnions. The improvement can be done without changing materials, processes and the size of the joint.

The load analysis used in this work allows the incorporation of form errors and trunnion waviness. This allows the possibility of optimizing the trunnion shape including expected manufacturing variation.

During regular operation in a vehicle, a Tripode joint will see different loads and a load history that will depend on the application (i.e. load history in city driving is different

from load history in freeway driving). The model developed in this work would allow to extend the optimization problem previously discussed to include load history, where the optimization of the trunnion is not done to minimize the contact loads for a specific torque but to minimize the size of the trunnion or to maximize the life of the joint under a series of different loads and the time the joint spends at each load. In other words, optimize the size and/or the life of a Tripode Joint for a specific load history.

The results and models developed in this work can have an immediate and direct application in the auto-industry.

APPENDICES

APPENDIX A

SURFACE FINISH INSPECTION BEFORE AND AFTER TEST

Ra = 0.18um

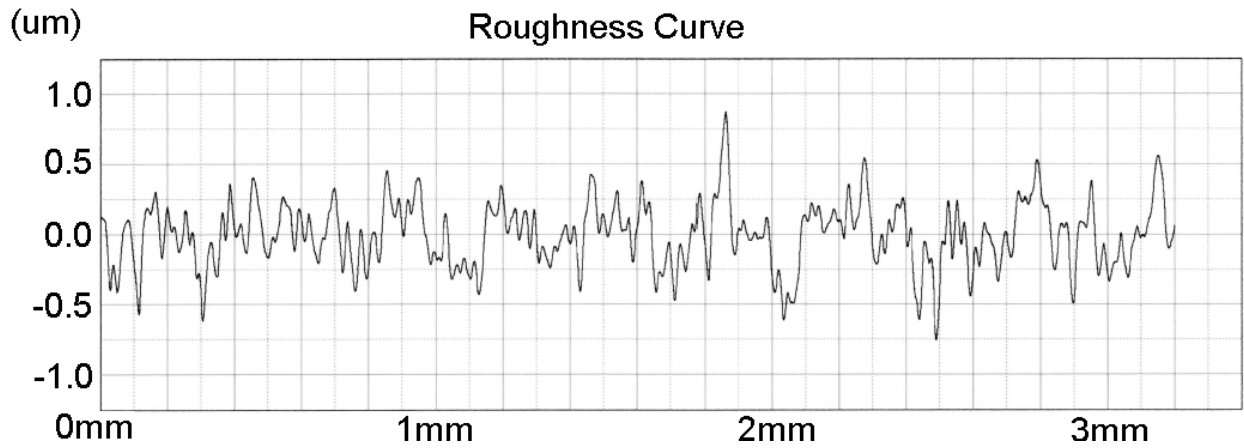


Figure A.1. Surface texture before testing

Ra = 0.09um

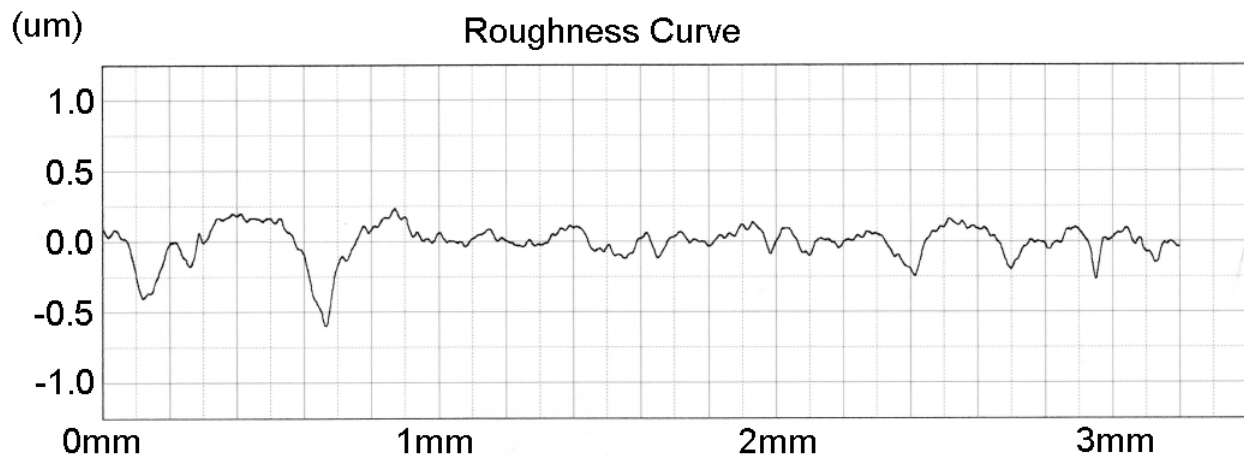


Figure A.2. Surface texture after testing

APPENDIX B
RESIDUAL STRESS ANALYSIS

Depth, [mm]	Residual Stress, [MPa]			Error, ±[MPa]	Peak Width, [°]
	As Measured	Corrected for Stress Gradient	Corrected for Layer Removal		
1. Marked Location on Trunnion, Axial					
0.000	- 375.5	- 417.6	- 417.6	21.2	5.95
0.025	-120.2	-124.5	-123.2	16.9	6.16
0.032	-164.4	-140.0	-138.6	23.3	6.40
0.042	-196.9	-188.3	-186.5	32.0	6.41
0.055	-204.1	-201.7	-199.4	21.7	6.47
2. Marked Location on Trunnion, Circumferential					
0.000	-128.1	-112.5	-112.5	21.3	5.85
0.025	-236.1	-213.2	-212.8	23.1	6.27
0.032	-295.4	-282.6	-282.0	23.7	6.23
0.042	-279.7	-275.4	-274.5	23.7	6.22
0.055	-319.2	-305.9	-304.7	24.0	6.56
3. 90° from Original Location on Trunnion, Axial					
0.000	-1206.6	-1232.8	-1232.8	27.8	4.73
0.042	-873.3	-900.4	-891.8	27.2	4.00
4. 90° from Original Location on Trunnion, Circumferential					
0.000	-385.9	-367.2	-367.2	15.5	4.74
0.042	-595.2	-576.7	-574.8	12.2	3.97

Table B.1. Residual stresses

APPENDIX C

MATERIAL ANALYSIS OF PROTOTYPE MATERIAL

TEST RESULTS:

CHEMISTRY

Specification: JIS-G4052 SCM-420H

Actual: JIS-G4052 SCM-420H

Sample	C	Mn	P	S	Si	Ni	Cr
Spider	0.20	0.80	0.027	0.009	0.223	0.11	1.03
Sample	Al	Cu	Pb	B	Nb	Zr	Ti
Spider	0.035	0.142	0.0000	0.0001	0.043	0.001	0.004
Sample	Mo	V	Ca				
Spider	0.16	0.010	0.00000				

Table C.1. Chemical composition

HARDNESS

Trunnion B was sectioned transversely adjacent to the pitting in order to determine the hardness profile. A microhardness traverse was performed from the surface to the core with the readings taken in HV500g and converted to HRC.

Specification:	*Actual:
Finished trunnion surface hardness to be 58 HRC minimum	62 HRC
Finished trunnion case depth to 50 HRC to be 0.8mm minimum	1.1mm
As a reference: finished trunnion total case depth to be 1.0mm minimum	2.0mm

Table C.2. Hardness

**Readings from taken microhardness traverse*

APPENDIX D

TRUNNION ROUNDNESS INSPECTION REPORTS AND EFFECTS OF FILTERING

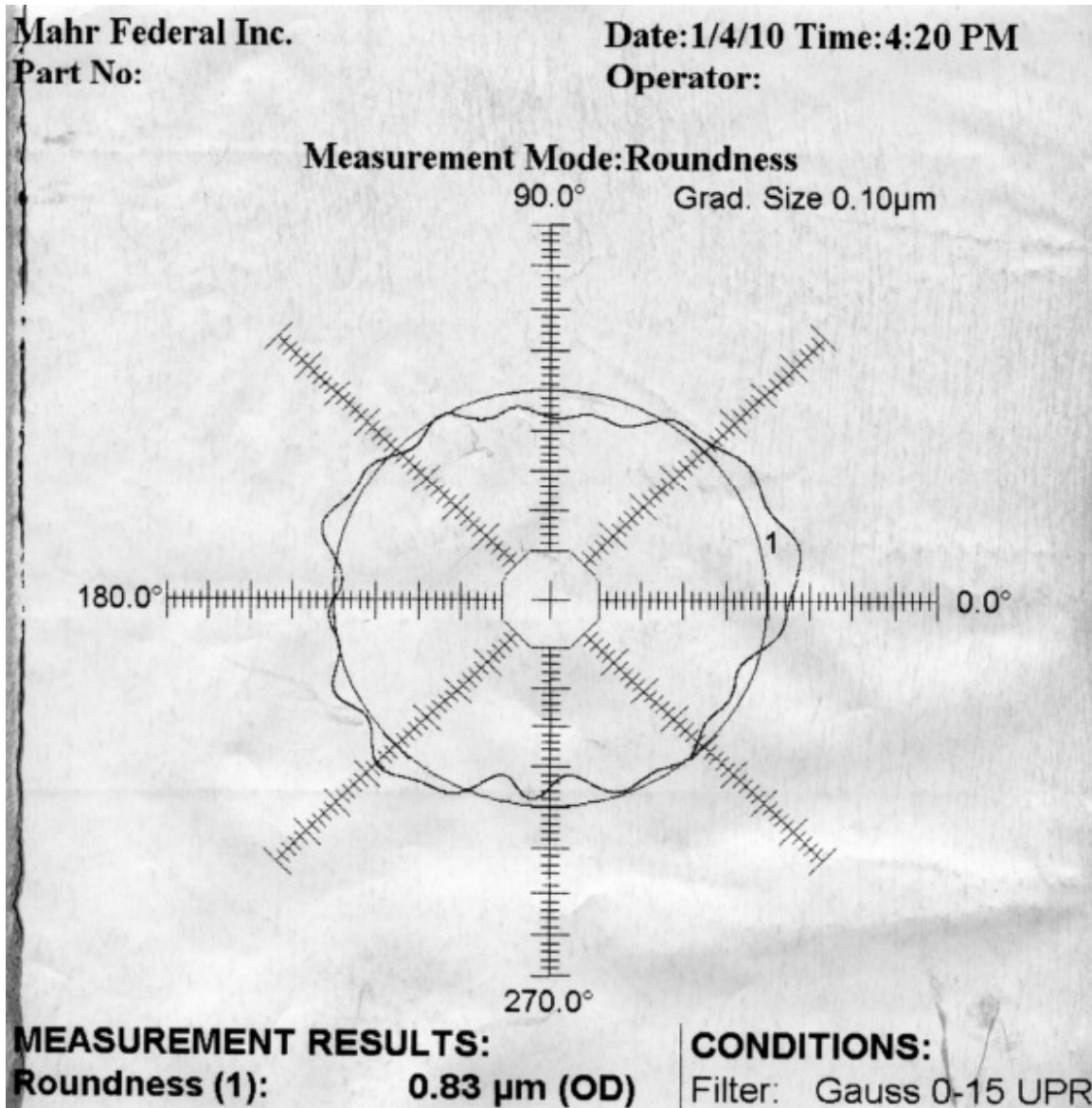
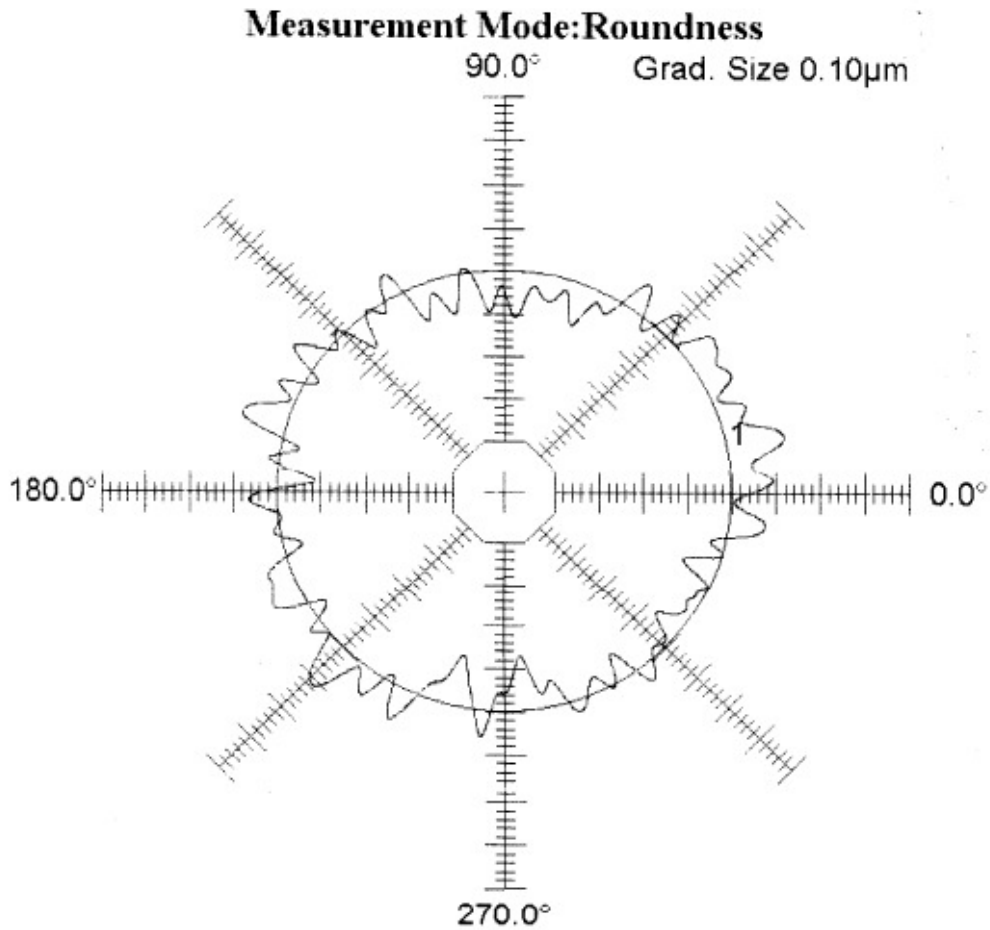


Figure D.1. Roundness with filter 0-15UPR

Mahr Federal Inc.
Part No:

Date:1/4/10 Time:4:19 PM
Operator:



MEASUREMENT RESULTS:

Roundness (1): 1.28 µm (OD)*

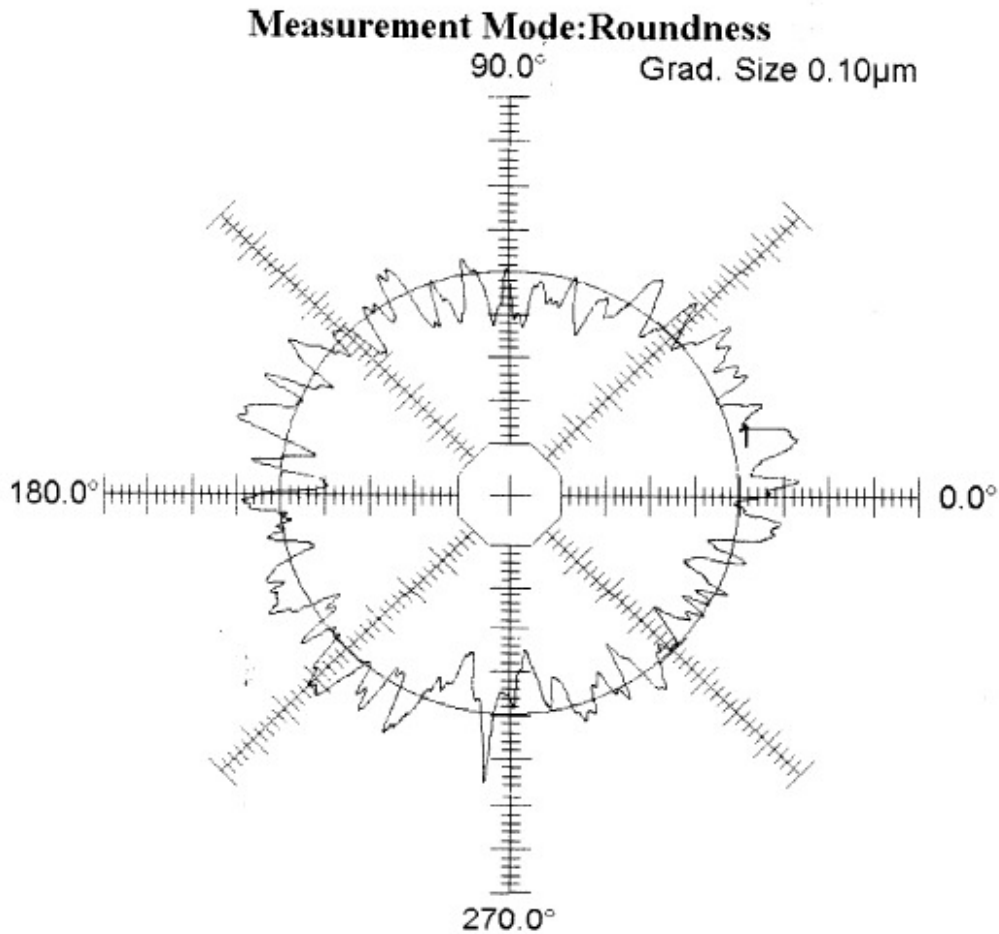
CONDITIONS:

Filter: Gauss 0-50 UPR

Figure D.2. Roundness with filter 0-50UPR

Mahr Federal Inc.
Part No:

Date:1/4/10 Time:4:18 PM
Operator:



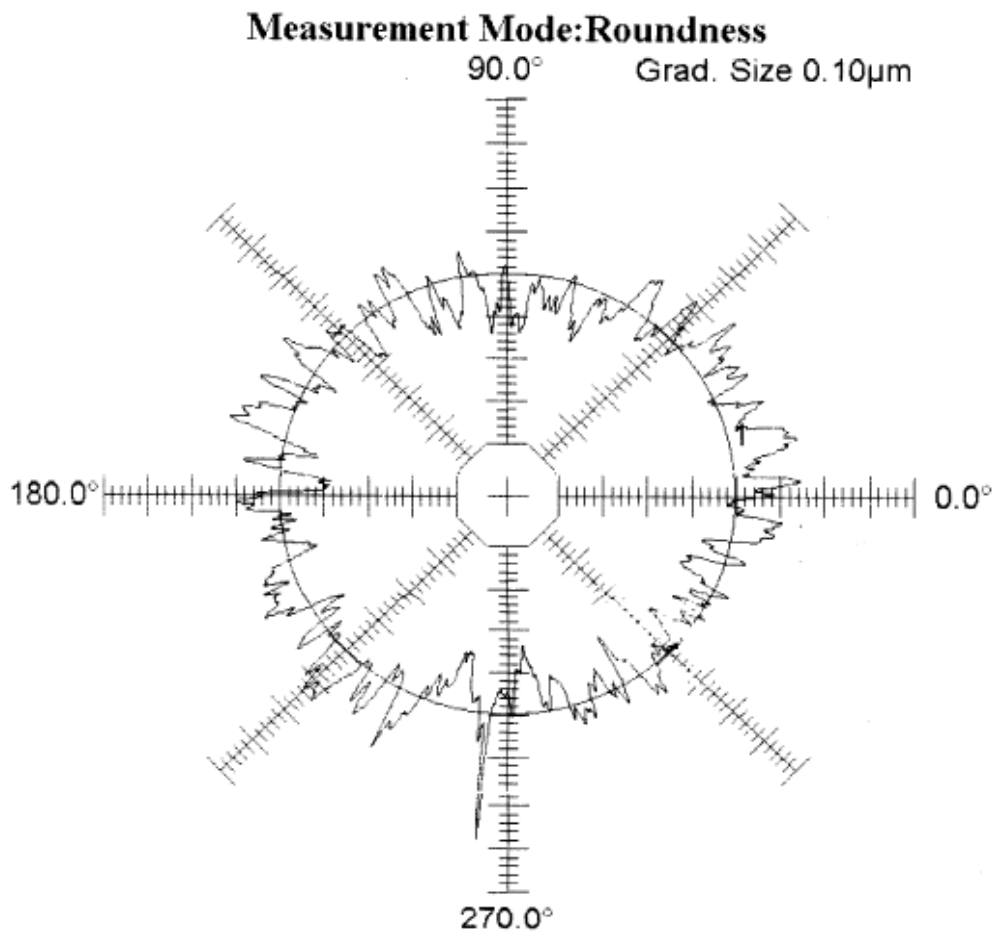
MEASUREMENT RESULTS:
Roundness (1): 1.53 μm (OD)*

CONDITIONS:
Filter: Gauss 0-150 UPR

Figure D.3. Roundness with filter 0-150UPR

Mahr Federal Inc.
Part No:

Date:1/4/10 Time:4:19 PM
Operator:



MEASUREMENT RESULTS:

Roundness (1): 2.20 µm (OD)*

CONDITIONS:

Filter: Gauss 0-500 UPR

Figure D.4. Roundness with filter 0-500UPR

REFERENCES

REFERENCES

- [1] Zaretsky, E. V., "A. Palmgren Revisited – A Basis for Bearing Life Prediction", NASA Technical Memorandum, TM-107440, May 1997.
- [2] Universal Joint and Driveshaft Design Manual, Advances in Engineering Series No. 7, SAE Publication, 1979.
- [3] Seherr-Thoss, H. C., Schmelz, F. and Aucktor E. "Universal Joints and Driveshafts, Analysis, Design, Applications", Springer, Berlin, Germany, 2nd ed, 2006.
- [4] Rzeppa, A. E., "US-Patent 2046 584", 1934
- [5] Durum, M. M., "Kinematic Properties of Tripode Joints", ASME Journal of Engineering for Industry, May 1975, pp708-713
- [6] Akbil, E. and Lee, T. W., "Kinematic Structure and Functional Analysis of Shaft Couplings Involving Pode Joint", ASME Journal of Mechanisms, Transmissions, and Automation in Design, December 1983, pp672-680
- [7] Akbil, E. and Lee, T. W., "On the Motion Characteristics of Tripode Joints. Part 1: General Case", ASME Journal of Mechanisms, Transmissions, and Automation in Design, June 1984, pp228-234
- [8] Akbil, E. and Lee, T. W., "On the Motion Characteristics of Tripode Joints. Part 2: Applications", ASME Journal of Mechanisms, Transmissions, and Automation in Design, June 1984, pp235-241
- [9] Mariot, J. P. and K'Nevez, J. K., "Kinematics of Tripode Transmissions. A New Approach", Multibody System Dynamics, 1999, 3, pp85-105
- [10] K'Nevez, J. K., Mariot, J. P., Moreau, L. and Diaby, M., "Kinematics of transmissions consisting of an outboard ball joint and an inboard generalized tripod joint", Journal of Multi-body Dynamics, 2001, 3, pp132-145
- [11] Urbinati, F., and Pennestri, E., "Kinematic and Dynamic Analyses of the Tripode Joint", Multibody System Dynamics, 1998, 2, pp355-367
- [12] Mariot, J. P., K'Nevez, J. K. and Barbedette, B., "Tripod and Ball Joint Automotive Transmission Kinetostatic Model Including Friction", Multibody System Dynamics, 2004, 11, pp127-145

- [13] Serveto, S., Mariot, J. P. and Diaby, M., "Modelling and Measuring the Axial Force Generated by Tripod Joint of Automotive Drive-Shaft", *Multibody System Dynamics*, 2007, DOI 10.1007/s11044-007-9091-1
- [14] Lee, C. H., "Dynamic Friction Characterization of Tripod Constant Velocity (CV) Joints: Experiments, Analysis and Modeling", doctoral dissertation, University of Illinois, Urbana-Champaign, Illinois, USA, 2006.
- [15] Orain, M., "General Theory and Experiment of Homokinetic Joint", doctoral dissertation, The University Pierre et Marie Curie, Paris, France, 1976, English Translation.
- [16] Perrow, S., Ritter, D. and Flaugher D., "Tripot Analyzer", Nexteer Automotive, Internal Technical Report, Saginaw, MI, USA, 2005.
- [17] Generated Axial Force Test Activities, internal test reports number: 290451, 292963, 293281 and 293286, Saginaw Steering Systems, 2007.
- [18] Harris, T. A. and Kotzalas, M. N., "Advanced Concepts of Bearing Technology", CRC, Boca Raton FL, USA, 5th ed, 2007, pp8-40
- [19] Filetti, E. G. and Rumbarger, J. H., "A General Method for Predicting the Influence of Structural Support Upon Rolling Element Bearing Performance", *ASME Journal of Lubrication Technology*, January 1970, pp121-128.
- [20] Papadopoulos, G. A., "Experimental Study of the Load Distribution in Bearings by the Method of Caustics and the Photoelasticity Method", *Journal of Strain Analysis*, 2005, Vol. 40 No. 4, pp357-365.
- [21] Zhao, H., "Analysis of Load Distributions within Solid and Hollow Roller Bearings", *ASME Journal of Tribology*, January 1998, pp134-139.
- [22] Ugural, A. C. and Fenster, S. K., "Advanced Strength and Applied Elasticity", Prentice-Hall, Upper Saddle River NJ, USA, 4th ed, 2003, pp221-227
- [23] Test Activity 290610. Nexteer Automotive, Saginaw, MI, USA, 2008.
- [24] Johnson, K. L., "Contact Mechanics", Cambridge University Press, Cambridge, U.K., 1985.
- [25] Garnham, J. E., "Constant Velocity Joint Material Performance Criteria", SAE Technical Paper Series, February 1996, SAE paper 960572.
- [26] Teutsch, R. and Sauer B., "An alternative Slicing Technique to Consider Pressure Concentrations in Non-Hertzian Line Contacts", *ASME Journal of Tribology*, July 2004, pp436-442.

- [27] Conry, T. F. and Seireg, A., "A Mathematical Programming Method for Design of Elastic Bodies in Contact", ASME Journal of Applied Mechanics, June 1971, pp387-392
- [28] Singh, K. P. and Paul, B., "Numerical Solution of Non-Hertzian Elastic Contact Problems", ASME Journal of Applied Mechanics, June 1974, 484-490
- [29] Oh, K. P. and Trachman, E. G., "A Numerical Procedure for Designing Profiled Rolling Elements", ASME Journal of Lubrication Technology, October 1976, pp547-552
- [30] Hartnett, M. J., "The Analysis of Contact Stresses in Rolling Element Bearings", ASME Journal of Lubrication Technology, January 1979, pp105-109.
- [31] Hartnett, M. J. and Kannel J. W., "Contact Stresses Between Elastic Cylinders: A Comprehensive Theoretical and Experimental Approach", ASME Journal of Lubrication Technology, January 1981, pp 40-45.
- [32] Young, W. C., "Roark's Formulas for Stress & Strain", McGraw-Hill, New York, USA, 1989, pp647-657
- [33] Love, A. E. H., "The Stress Produced in a Semi-Infinite Solid by Pressure on part of the Boundary", Proc A Royal Society (London), Vol. 228, Oct. 1929
- [34] Zaretsky, E. V., "Rolling Bearing Life Prediction – Past, Present and Future", NASA Technical Memorandum, TM-2000-210529, November 2000.
- [35] Vlcek, B. L., Hendricks R. C. and Zaretsky, E. V., "Determination of Rolling-Element Fatigue Life from Computer Generated Bearing Tests", NASA Technical Memorandum, TM-2003-212186, August 2003
- [36] Harris, T. A. and McCool, J. I., "On the Accuracy of Rolling Bearing Fatigue Life Prediction", ASME Journal of Tribology, April 1996, pp297-309
- [37] Ioannides, E. and Harris, T. A., "A New Fatigue Life Model for Rolling Bearing", ASME Journal of Tribology, July 1985, pp367-378
- [38] Zaretsky, E. V., Poplawski J. V. and Peters, S. M., "Comparison of Life Theories for Rolling-Element Bearings", Tribology Transactions, 39, 2 (1996), pp237-248, pp501-503
- [39] Pavlina E. J. and Van Tyne C. J., "Correlation of Yield Strength and Tensile Strength with Hardness for Steels", Journal of Materials Engineering and Performance, 17, 6 (2008), pp888-893
- [40] Xu, B. and Jiang, Y., "Elastic-Plastic Finite Element Analysis of Partial Slip Rolling Contact", ASME Journal of Tribology, 124, pp20-26.

- [41] Jiang, Y. and Sehitoglu H., "An analytical Approach to Elastic-Plastic Stress Analysis of Rolling Contact", ASME Journal of Tribology, 116, p577-587
- [42] Baughman, R. A., "Experimental Laboratory Studies of Bearing Fatigue", ASME Paper 58-A-235 (1958)
- [43] Wear Test Activities, internal test reports number: 290610 and 290604, Nexteer Automotive, 2009.
- [44] "HEEDS v5.3 User's Manual", Red Cedar Technologies, East Lansing, MI, USA, 2010.
- [45] Materials Analysis, internal test report number: 325638, Nexteer Automotive, 2010.
- [46] Matlock, B., "Residual Stress Analysis, TEC Report No. R-2010-231", TEC, Knoxville, TN, 2010.
- [47] Wolfram, S. "The Mathematica Book", Wolfram Research, Champaign, IL, USA, 5th ed, 2003